Mechanical Behavior and Microstructural Evolution of Lead Free Solder Alloys in Harsh Environment Applications

by

Mohammad S. Alam

A dissertation submitted to the Graduate Faculty of
Auburn University
in partial fulfillment of the
requirements for the Degree of
Doctor of Philosophy

Auburn, Alabama
August 3, 2019

Keywords: microelectronics reliability, lead-free solder, harsh environment applications, high temperature aging, mechanical testing, microstructural evolution

Approved by

Jeffrey C. Suhling, Chair, Quina Distinguished Professor of Mechanical Engineering
Hareesh V. Tippur, McWane Professor of Mechanical Engineering
Peter Schwartz, Professor Emeritus of Mechanical Engineering
Michael J. Bozack, Professor Emeritus of Physics

Abstract

Solder joints provide mechanical support, electrical and thermal interconnection between packaging levels in microelectronics assembly systems. Proper functioning of these interconnections and the reliability of the electronic packages depend largely on the mechanical properties of the solder joints. Lead free solders are common as interconnects in electronic packaging due to their relatively high melting point, attractive mechanical properties, thermal cycling reliability, and environment friendly chemical properties. However, environmental conditions, such as, operating temperature, aging temperature, and aging time significantly affect these properties due to the microstructural evolution of the solder that occurs during aging. Moreover, electronic devices, sometimes experience harsh environment applications including well drilling, geothermal energy, automotive power electronics, and aerospace engines, where solders are exposed to very high temperatures from T = 125-200 °C. Mechanical properties of lead free solders at elevated temperatures are limited. This research involves several projects to create a database of extreme high-temperature mechanical properties and the associated microstructural changes of several lead free solder alloys.

In the first project, several SAC and SAC+X lead free solder alloys, recommended for high reliability applications have been chemically analyzed and then mechanically tested in order to determine the temperature dependent mechanical properties of these alloys. The alloys include SAC305, Ecolloy (SAC_R), Cyclomax (SAC_Q), and Innolot. The mechanical behavior of these alloys have been explored at several extreme high temperatures from 125 to 200 °C. For each of 4 elevated temperatures (T = 125, 150, 175, and 200 °C), tensile stress-strain tests were performed at three strain rates (SR = 0.001,

0.0001, and 0.00001 sec^{-1}). For each alloy and testing temperature, the stress-strain curve shape and high temperature tensile properties (initial modulus, yield stress, and ultimate tensile strength) were measured and compared.

In the second project, temperature dependent stress-strain behavior of SAC305, SAC_Q, and Innolot solders subjected to high temperature aging at 125 and 200 °C have been reported. Before testing, the solder uniaxial specimens were aged (preconditioned) at the extreme high temperature of either T = 125 °C or T = 200 °C. At each of these aging temperatures, several durations of aging were considered including 0, 1, 5, and 20 days. Stress-strain and creep tests were then performed on the aged specimens. Using the measured data, the evolutions of the stress-strain and creep behaviors were determined as a function of aging temperature and aging time.

In third project, SAC305 and doped SAC solder alloys (SAC_Q and Innolot) recommended for high reliability applications have been chemically analyzed and then mechanically tested in order to determine the nine Anand parameters. Anand parameters were determined for SAC305 with both water quenched and reflowed microstructures. For SAC_Q and Innolot, only reflowed microstructures were explored to determine the Anand parameters. The nine Anand parameters were determined for each unique solder alloy from a set of uniaxial tensile tests performed at several strain rates and temperatures. Testing conditions included strain rates of 0.001, 0.0001, and 0.00001 (sec^{-1}), and temperatures of 125, 150, 175, and 200 °C.

In the fourth project, nanoindentation methods were utilized to explore the creep behavior, and aging effects of SAC305 solder joints at several extreme high testing temperatures from 125 to 200 °C. A special high temperature stage and test protocol was

used within the nanoindentation system to carefully control the testing temperature, and make the measurements insensitive to thermal drift problems. Solder joints were extracted from 14 x 14 mm PBGA assemblies (0.8 mm ball pitch, 0.46 mm ball diameter). For all the experiments, only single grain solder joints were used to avoid introducing any unintentional variation from changes in the crystal orientation across the joint cross-section. After extraction, the single grain solder joints were subjected to various aging conditions. Nanoindentation testing was then performed on the aged specimens at four different testing temperatures (T = 125, 150, 175, and 200 °C). In order to understand creep response of the solder joints at different temperatures, a constant force at max indentation was applied for 900 sec while the creep displacements were monitored. With this approach, creep strain rate was measured as a function of both temperature and prior aging conditions. Nanoindentation pile-up effects, although insignificant at room temperature, were observed during high-temperature testing and corrections were made to limit their influence on the test results.

The changes in mechanical behavior of solder alloys that occur during isothermal aging are a result of the evolution of microstructure. In the final project, the microstructural evolution of solder alloys were investigated for different aging conditions. In particular, aging was performed at T = 125, 150, and 175 °C for up to 20 days, and the topography of the microstructure of a fixed region was captured using the SEM system. This process generated several images of the microstructure as the aging progressed. These images were used to predict the microstructural evolution in SAC305 solder joints exposed to high temperature aging. Image analysis software was utilized to quantify microstructural

changes (total area, number and average diameter of IMC particles, interparticle spacing etc.) with respect to aging time.

Acknowledgments

I would like to express my deepest appreciation to my advisor Dr. Jeffrey C. Suhling for his continuous supervision and untiring support throughout my PhD study at Auburn University. I am grateful for getting the opportunity to work with a mentor like him. He is one of my role models and a source of inspiration. He continuously and convincingly convey a spirit of pursuit of excellence and perfection in research. I am really grateful that I had the opportunity to work with an exceptional mentor who taught me beyond what is expected in academia. I am also grateful to my advisory committee members including Dr. Hareesh V. Tippur, Dr. Michael J. Bozack, and Dr. Peter Schwartz for their insightful discussion about this research work. Special thanks are extended to my friends and co-workers Dr. Munshi Basit, Dr. Md. Hasnine, Dr. Nianjun Fu, Dr. Quang Nguyen, Dr. Sudan Ahmed, Dr. ChienChih Chen, Promod Chowdhury, Abdullah Fahim, Md Mahmudur Rahman Chowdhury, KM Rafidh Hasan, Jing Wu, Jun Chen, Mohd Aminul Hoque, Kamrul Hasan, Mohammad Ashraful Haq, Jason Smith, and John Marcell for their support.

I am heartily grateful to my parents and all of my family members for their support to my study and life in the United States. Finally, I solemnly dedicate this dissertation and all achievements in pursuit of doctoral degree to my wife, Nusrat Jahan, for her perseverance and support, and her understanding during my busy time at graduate school have been priceless to me.

Table of Contents

List of Figures

List of Tables

CHAPTER 1

INTRODUCTION

1.1 Overview of Solders in Microelectronics

Lead free solders provide excellent thermo-mechanical properties and commonly used as interconnections in electronic packages. As a joining material, in electronic assemblies, Solder joints provide mechanical support, electrical and thermal interconnection between packaging levels in microelectronics assembly systems. It also helps to dissipate the heat generated from the Si-chip [1].

With the emergence of the modern electronic packaging technology over the last few decades, solder alloys have been the primary interconnect material used in electronic packaging. In the past, eutectic 63Sn-37Pb has been the most extensively used soldering alloy in the packaging industries. The eutectic Sn-Pb solders were very attractive due to their relatively low melting temperature (183 °C) and excellent ductility and good reliability and for their superior wettability and compatibility with most substrates and devices [2].

There is a general trend towards products that minimize harmful effects on the environment and human health. This trend is further reinforced by the RoHS ban on harmful substances and WEEE regulations on recycling and minimizing of electronic wastes. In June 2000, the EU adopted two directives, the Waste of Electrical and Electronic Equipment (WEEE) and the Directive of the Restriction of the Use of Certain Hazardous

Substances (RoHS) [3]. The WEEE directive requires that lead has to be removed from any end-of-life electrical or electronic components. The RoHS specifically bans lead from electrical and electronic components manufactured after July 1, 2006. As a result of the enforcement of the directives, all electrical or electronic equipment and devices produced in or imported to E.U. member states must comply with these lead-free standards except those items that are exempted from the bans. In addition to legislation enforcement there are emerging detection technologies to enforce compliance. So due to the general push towards the eco-efficiency and green electronics, manufacturers are motivated for the adoption of lead free electronics. Therefore, the conversion to lead free solders in the global electronic market appears imminent [4].

In the United States, as soon as lead-free solder legislation was proposed, the lead-free solder project headed by the NCMS initiated research and development of lead-free solder in a program lasting 4 years [5]. The results of the project have been made available in a database and offer information on such matters as modifying equipment and processes for selecting alternative materials. The project initially selected for study 79 types of alloys considered at the time to be potential candidates for use in lead-free solder. Basic attributes considered included toxicity, resource availability, economic feasibility, and wetting characteristics. The selection process narrowed the field down to the final seven alloys, and these received secondary evaluation for reliability and ease of mounting manufacturing. Evaluation of the individual alloys did not result in the final selection of a single candidate, but three alloys, Sn–58Bi, Sn–3.5Ag–4.8Bi, and Sn–3.5Ag, were recommended as candidates. Screening comments indicated that the Sn–58Bi eutectic alloy was not suitable for use as standard solder due to the scarcity of Bi resources. However,

since this material can be used for mounting at less than 200 °C, and has chalked up a 20-year plus record of use in mainframe computers, this solder was deemed suitable for special applications. These results were used to construct a database on lead-free solder that includes the information in these tables along with other items such as (1) recommended applications for lead-free solder, (2) alloy composition guidelines reflecting price and availability, (3) database of the 7 selected alloys and comparison with Sn–Pb eutectic alloy, (4) data on the characteristics of the other 70 eliminated alloys, (5) optimal process conditions using various test PWBs, (6) strength evaluation and metallurgical reaction analysis for the selected alloys and various surface mounting process reactions, (7) predicted life (using NCMS Project proprietary life prediction software) and thermal fatigue evaluation for 4 of the selected alloys, and (8) assessment of nontoxicity and alloy composition.

1.2 Lead Free Solders Choices

In selecting suitable alternative of Sn-Pb soldering materials, it is important to take into consideration that the properties of the alternative solders are comparable or superior to Sn-Pb solders. Compatible candidates of the Sn-Pb solders must have the following behaviors [6]:

- melting temperature similar to eutectic Sn-Pb for a similar reflow profile
- sufficient wettability for good metallization process
- good electrical properties for transmitting electrical signals
- strong mechanical properties for good fatigue resistance and reliability
- inexpensive and easier manufacturability

Among various alloy systems that are considered as lead-free solder candidates, Sn-Ag-Cu alloys have been recognized as the most promising because of their relatively low melting temperature (compared with the Sn-Ag binary eutectic lead free solder), superior mechanical properties, and good compatibility with other components [7-9]. Sn-Ag-Cu alloys are widely used as lead-free solutions for ball-grid-array (BGA) interconnection in the microelectronic packaging industry as solder balls and pastes. Although no "drop in" replacement has been identified that is suitable for all applications, Sn-Ag, Sn-Ag-Cu (SAC), and other alloys involving elements such as Sn, Ag, Cu, Bi, In, and Zn have been identified as promising replacements for standard 63Sn-37Pb eutectic solder. Industries have proposed several SAC alloys which include 96.5Sn-3.0Ag-0.5Cu (SAC 305) in Japan, 95.5Sn-3.8Ag-0.7Cu (SAC 387) in the EU, and 95.5Sn-3.9Ag-0.6Cu (SAC 396) in the USA. The International Printed Circuit Association has suggested that 96.5Sn-3.0Ag-0.5Cu (SAC305) and Sn-3.9Ag- 0.6Cu (two near-eutectic alloys) will be the most widely used alloys in the future [10]. This prediction is attributed to their good mechanical properties, acceptable wetting properties, and suitable melting points [8, 11, 12].

A relatively large number of lead free solder alloys have been proposed so far, including binary, ternary and even quaternary alloys. More than 70 alloys have been identified in the literature. Among them, the majority of the alloys are Sn-based alloys, that is, Sn is the preferred major constituent. In fact, Sn-rich lead free alloys have occupied more than 80% in the wave solder market share and more than 90% in the reflow solder market share (Figure 1.1). The main benefits of the various SAC alloy systems are their relatively low melting temperatures compared with the 96.5Sn–3.5Ag binary eutectic

alloy, as well as their superior mechanical and solderability properties when compared to other lead-free solders. There are some major challenges for the current series of lead-free solders. SAC series alloys have a higher melting temperature, around 217 °C, compared to 183 °C for the eutectic Sn-Pb solders. They thus require higher reflow temperature during the manufacturing process, which can lead to reliability problems. The excessive buildup of intermetallic formed at the interface between the solder joints and the copper pad can also cause reliability problems. High costs are another issue for lead-free solders.

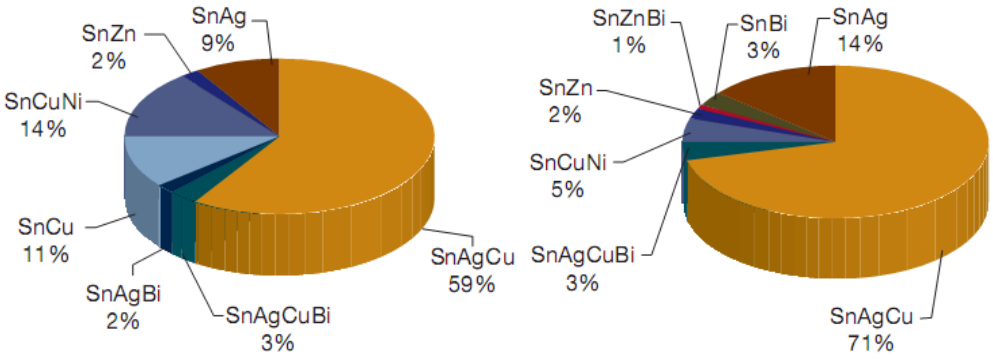

(a) Wave Solders (b) Reflow Solders

Figure 1.1 Lead Free Solder Market Share

1.3 Candidates for Alternative Lead Free Solders

About 70 different alloys were proposed as an alternative to the Sn-Pb solder. Most of these are Sn based solder where Sn is the main constituent along with one, two or even three other minor elements. These minor elements are added mainly to 1) decrease the melting temperature and 2) improve wetting and reliability of the solder [1]. The properties of Sn and the effects of different alloying elements on the Sn based solder alloys are described below:

1.3.1 Tin

The melting temperature of elemental Sn is 231 °C. One of the main reasons of choosing Sn as the principle component in the lead free solder for electronic applications is its ability to spread and wet a number of various different substrates. In the solid state, tin can have two different phases or crystal structures 1) white or β-Sn with tetragonal crystal structure and 2) gray or α-Sn with diamond cubic crystal structure. At the room temperature the thermodynamically stable phase is β-Sn. Upon cooling, when the temperature goes below 13 °C (allotropic transformation temperature), α-Sn becomes the thermodynamically stable phase. The allotropic transformation of β-Sn to α-Sn, results a significant volume change (around 27%) causing blistering of the tin surface, cracking or disintegration. This phenomenon is mainly a surface event and often referred as 'tin pest'. The low ductility of α-Sn is another reason of causing blistering and cracking of the tin after the transformation [1, 13, 14]. Although the equilibrium temperature for β-Sn to α-Sn is 13 °C, the transformation occurs only after a significant undercooling and an extensive incubation period as long as several years. For example, no 'tin pest' was found on a SAC387 bulk sample after storing at -40 °C for 5 years [14]. Presence of heterogeneous nuclei, also known as seeding, can considerably accelerate the kinetics of the transformation. The possibility of $\beta \rightarrow \alpha$ transformation in a actual solder joint is even limited due to the constraints (component and substrate) on the both side of the joint [13, 14].

Addition of other elements, as an impurity, can affect the allotropic transformation. For example, the presence of Pb, Bi, Sb, Cu, Ge and Si inhibit $\beta \rightarrow \alpha$ transformation while the presence of As, Zn, Al and Mg promote the transformation [13, 14].

Sn has a body centered tetragonal crystal structure (β-Sn), at room temperature, which is anisotropic. Hence, tin shows an anisotropic thermal (e.g. CTE) and mechanical (e.g. elastic modulus) properties as shown in Figure 1.2. As a result, during thermal cycling experiment, cracking occurs along the grain boundaries [1].

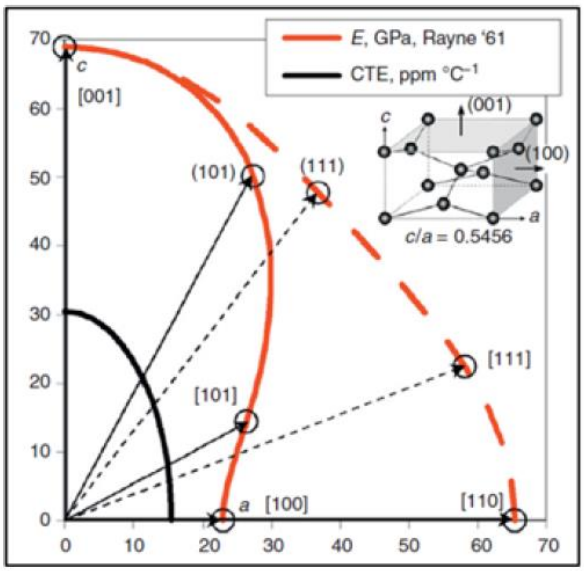

Figure 1.2 Elastic Modulus and Coefficient of Thermal Expansion (CTE) of Tin as a Function of Crystal Orientation [1]

1.3.2 Chromium (Cr)

Cr helps to improve shear ductility after long term aging. Besides, it also suppress kirkendall void formation in the solder joints [15].

1.3.3 Nickel (Ni)

Among all the micro-alloy additives, Ni is one of the most common element. Addition of Ni improves fluidity of SAC solders. Ni also improves the high strain rate properties of solder joints. For example, the drop strength of SAC alloys can be significantly improved by Ni addition. Although Ni does not have any significant influence

on the creep properties of the solder, it inhibits Cu diffusion and thus reduce the thickness of Cu_3Sn intermetallic compound (IMC). The Ni addition greater than 0.01 wt% could suppress the growth of Cu_3Sn IMC even after long term (2000 hours) aging. Since Cu_3Sn IMC is very brittle, the growth of Cu_3Sn layer is very critical for the brittle failure of the solder joints. Addition of Ni on SAC solder causes to form more stable $(Cu, Ni)_6Sn_5$ IMC which act as a barrier layer and suppress the growth of Cu_3Sn layer. Therefore, by reducing the thickness of brittle Cu_3Sn layer, Ni helps to improve strength of the solder joints. Ni also helps to improve strength by refining solder microstructure [16].

1.3.4 Zinc (Zn)

While Ni reduces only the formation Cu_3Sn, Zn doping can retard both Cu_3Sn and Cu_6Sn_5 IMC's in SAC solders. Zn also helps to improve the interface quality after multiple reflow and high temperature aging. Addition of 1.5% Zn in SAC207 solder could refine Ag_3Sn and Cu_6Sn_5 IMC's and hence increase strength by dispersion strengthening [15].

1.3.5 Cobalt (Co)

Co helps to reduce the growth of Cu_3Sn layer during high temperature aging. Addition of small amount of Co (<0.1 wt%) can improve the properties of SAC solders. Co increases the number of nucleation sites and hence significantly refine the grains of SAC305 solder. Thus it helps to improve shear strength of the solder joints [15].

1.3.6 Bismuth (Bi)

If added in small amount, Bi can improve the wetting ability and reduce melting temperature of lead free solder alloys. It also increases strength of the bulk solder and inhibit the large Ag_3Sn formation in the bulk solder. It is recommended to avoid Pb contamination in the solder before using Bi as an additive. Because Bi can react with Pb to form a brittle IMC at the grain boundary and reduce strength significantly. If present in excess amount, Bi can cause solidification crack due to the increase in the gap between solidus and liquidus temperature [15].

1.3.7 Antimony (Sb)

Sb improves mechanical properties of lead free solders but it is toxic in nature. A small percentage (0.5 wt%) of Sb can improve drop test reliability of SAC solder joints [16]. Besides, Sb also helps to enhance strength of the solder by solid solution strengthening [17].

1.3.8 Germanium (Ge)

Ge doped solders shows low Cu dissolution from the Cu pad and hence suitable for the wave soldering process. Ge significantly improve wetting properties of the lead free solders and refine the solder microstructure. As a result, Ge addition improves the strength and ductility of the lead free solder [16].

1.3.9 Sn-Ag-Cu System

As shown in Figure 1.1, Sn-Ag-Cu (SAC) has been the most popular, widely used lead free solder in today's market. Although they are still not identified as the "drop in" replacement for all applications, a variety of SAC alloys with different chemical compositions have been the proposed by various user groups and industry experts. These include: SAC105 (98.5Sn-1.0Ag-0.5Cu), SAC205 (97.5Sn-2.0Ag-0.5Cu), SAC305 (96.5Sn-3.0Ag-0.5Cu), and SAC405 (95.5Sn-4.0Ag-0.5Cu), known as the SACN05 series; SAC387 (95.5Sn-3.8Ag-0.7Cu), SAC396 (95.5Sn-3.9Ag-0.6Cu), and SAC357 (95.2Sn-3.5Ag-0.7Cu), identified as near eutectic SAC choices; SAC3810 (95.2Sn-3.8Ag-1.0Cu), SAC3595 (95.55Sn-3.5Ag-0.95Cu), SAC0307 (9Sn-0.3Ag-0.7Cu), and SAC107 (98.3Sn-1.0Ag-0.7Cu), designed for special needs such as high temperature application, drop and shock optimization, etc. The main benefits of the various SAC alloy systems are their relatively low melting temperatures compared with the 96.5Sn-3.5Ag binary eutectic alloy, as well as their superior mechanical and manufacturability properties when compared to other lead free solders [18].

Figure 1.3 shows a typical 3-D ternary phase diagram. The contours on the top surfaces of the figure represent the isothermal lines. Each of the 3 sectors represents the binary phase diagram of two of the three elements. The center of the diagram, where the isothermal lines reach the common, lowest point, is the eutectic point of the ternary system. Figure 1.4 is the top view (2-D) of the ternary phase diagram of Sn-Ag-Cu.

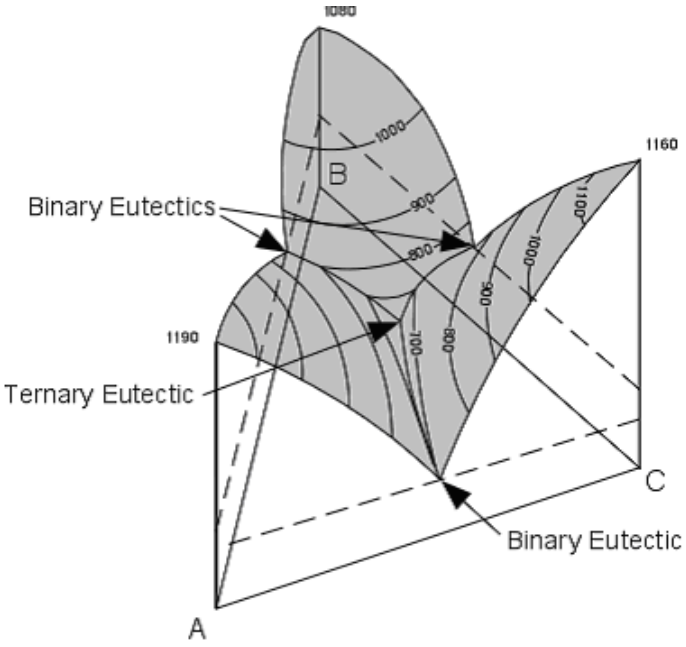

Figure 1.3 Typical 3-D Ternary Phase Diagram

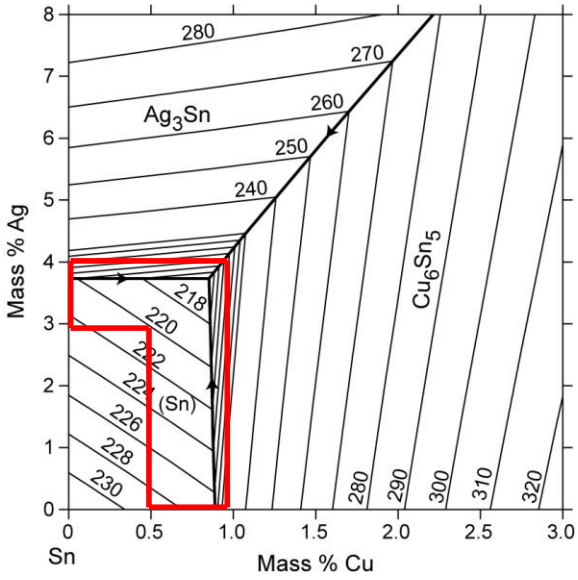

Figure 1.4 Sn-Ag-Cu Ternary Phase Diagram

The area indicated in the red box is the near eutectic region. Most of the SAC alloy compositions currently on the market are within this region. The eutectic and near eutectic

melting temperature has been determined to be 217 °C, although the precise eutectic point is not known [19].

In SAC alloys, the formation of intermetallic compounds between the primary elements Sn and Ag, and Cu affect all the properties of the alloys. There are three possible intermetallic compounds that may be formed: Ag_3Sn forms due to the reaction between Sn and Ag (Figure 1.5) and Cu_6Sn_5 forms due to the Sn and Cu reaction. The compound Cu_3Sn will not form at the eutectic point unless the Cu content is high enough for the formation of Cu_3Sn at higher temperatures, so in bulk specimens Cu_3Sn is not presented. There is no reaction between Ag and Cu to form any kind of intermetallic compounds. The particles of intermetallic compounds possess much higher strength than the bulk material. Fine intermetallic particles in the Sn matrix can therefore strengthen the alloys. The intermetallic compounds can also improve the fatigue life of the solders, as SAC alloys are reported to be 3-4 times better fatigue properties than the Sn-Pb eutectic solders. The higher fatigue resistance is believed to be contributed by the interspersed Ag_3Sn and Cu_6Sn_5 particles, which pin and block the movement of dislocations. The many patents that have been granted for SAC systems have limited their use and hindered research on several of the SAC alloys. However, many familiar alloy such as SAC305 and SAC405 are not patented to avoid excessive licensing and fees [18].

Despite the benefits mentioned above, SAC family solders sometimes are still questionable as complete substitutes for eutectic Sn-Pb because of costs, some patent issues (particularly outside Europe), aesthetic consideration (dross problem of SAC solders), and relatively high melting temperature (217 °C vs. 183 °C).

1.3.10 Sn-Ag-Cu + X System

Sn-Ag-Cu alloys have shown potential to be successful substitutes for eutectic Sn-Pb, however, the industry is still looking for a "perfect" solution. According to the results of many recent studies, performance characteristics of solder alloys are able to be optimized by doping, that is, by adding a small amount of other alloying elements into the SAC solder alloys.

The proposed doping element candidates include Bi, Ni, Co, Ge, Zn, La, Mg, Mn, Ce, Ti, Fe, In, B, etc. For example, adding 0.05% (wt.) Ni can successfully stabilize the microstructure, inhibit the excessive consumption of metal base and thus increase the reliability of the solder joints [20-22]. In addition, doping rear earth (RE) elements can significantly enhance wettability, refine microstructure and improve ductility of SAC alloys [23-26].

Even though dopants can greatly alter the mechanical, electrical and physical behavior of SAC solders, the effect on melting temperature, however, is found to be negligible. This is another advantage for doped solder alloys because manufacturers can still use the same processing conditions as conventional SAC alloys.

Meanwhile, the known issues for SAC-X solders are also apparent. For instance, the material properties and interfacial behavior of solder alloys have been demonstrated to be very sensitive to the quantity of the X-additive. As a result, it takes much more time and cost to figure out the optimal composition levels for the dopants.

1.4 Characteristics and Applications of Sn-Ag-Cu Solder Material

The advantages of SAC series over other Pb-free systems include relatively low melting temperatures, superior mechanical and solderability properties, and good tolerance for Pb contamination. These characteristics give SAC alloys good compatibility with existing electronics packaging infrastructure. In fact, there is a long history of using 95.5Sn–4.0Ag–0.5Cu (SAC405) to form solder joints for BGA packages. The high market share (≈ 70%) by SAC series alloys on a global scale provides strong evidence of its world-wide acceptance. Also, nanoscale lead-free solders ("nano-solders") have been proposed and investigated in the development of nano-soldering technique for nanoscale assembly and integration. Tin (Sn)-based and indium (In)-based lead-free nano-solders have been synthesized directly onto multisegmented nanowires using electro deposition method in nanoporous templates. Furthermore, high temperature lead free solders are being used in medical industries today where a variety of intrusive procedures used requiring tools, instruments, sensors and components in materials that are inert with respect to reactions with the body [27]. Also, new surgical techniques have been developed to improve the quality of operations, reduce the risk to patients and reduce the pain experienced by patients. Environmental concerns and the concern about toxicity and health hazards indicate that there is a drive to develop and use lead-free solders.

1.5 Mechanical Properties of Lead Free Solders

In an electronic device, a number of different types of engineering materials exists in a close proximity. For example, a printed circuit board (PCB) is typically a glass fiber reinforced polymer (composite material), a die is a semiconductor material which is often

encapsulated in a plastic or a ceramic, and the tracking and the solder joints are metallic materials. Solder joints are used to create an electrical circuit by mounting chips and components on the PCB. Hence an ideal solder joint should have a good conductivity to transmit electrical signals and at the same time, adequate strength to provide mechanical support and connection. Hence, mechanical properties of solder joints are critically important to ensure reliability of the electronic products. Among all the mechanical properties, tensile, fatigue, and creep performance of the solder are critically important. Thus an accurate measurement of mechanical properties and development of constitutive equations for solder materials are required in mechanical design, process optimization and reliability assessment.

1.5.1 Tensile Properties (Stress-Strain Behavior)

Under the action of an increasing stress, metals usually exhibit elasticity, plasticity, and a maximum in stress is followed by necking and fracture. The slope of the linear elastic portion of the stress vs. strain plot is the modulus, and the stress at termination of elastic behavior is the yield stress. The extent of deformation prior to fracture is known as ductility. Ceramics display only elastic behavior until fracture, which is associated with cracking and very limited deformation (brittleness). Polymers may exhibit both characteristics above according to the temperature. Above the glass transition temperature, T_g, extensive deformation due to mechanisms quite unlike those in metals may follow a small degree of elasticity. Below this temperature, polymers exhibit ceramic-like behavior. In all material categories, the maximum stress attained is the tensile/compressive/shear strength according to the mode of stressing employed. Composites are physical mixtures

and exhibit the average properties of their components, taking into account the proportions of each. These characteristic features of monotonic behavior are summarized in Figure 1.5. The fracture strains of brittle materials and the yield strains of metals are generally less than 1% (the yield strain of solders is around 0.1–0.2%). The amount of deformation prior to the attainment of maximum strength is between about 3% and 7% for common solder alloys.

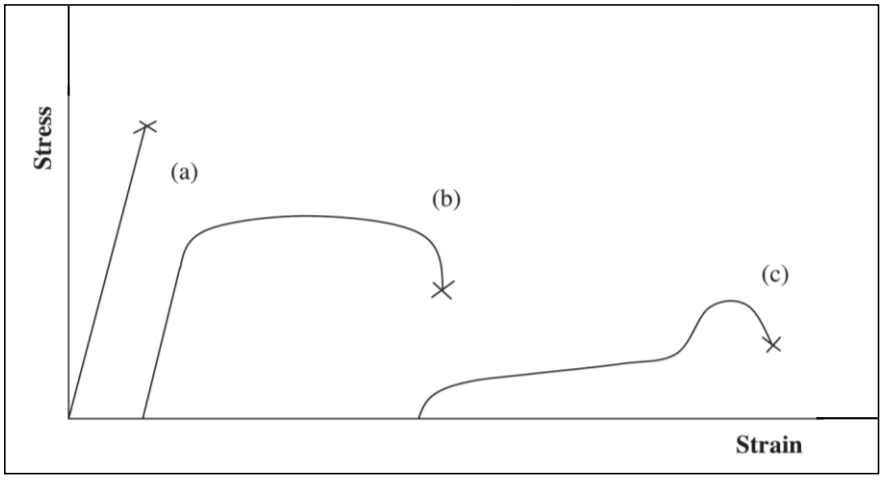

Figure 1.5 Schematic Overview of Mechanical Behavior of a) Ceramics, Polymers below their Glass Transition Temperature (Tg) and Non Ductile Material b) Ductile Materials c) Polymers above Tg

Tensile properties indicate how the material will react to forces being applied in tension. Although solder joints are rarely under pure tensile/compressive loading, tensile properties are still crucial indicators for design purposes. Through tensile tests, several material properties can be determined, such as effective modulus, yield stress (YS), ultimate tensile strength (UTS), elongation, etc. In most of the cases that engineering stress-strain curves are employed by neglecting the change in cross sectional area.

Tensile properties are generally described by stress-strain curves. Figure 1.6 shows a typical engineering stress strain curve. A typical engineering stress-strain curve for solder alloys consists of an elastic region and a plastic region. In the elastic region, when the stress is reduced, the material will return to its original shape. In this linear region, the material obeys the relationship defined by Hooke's Law. However, since the effective modulus includes small inelastic deformations or time-dependent deformations such as creep, it is usually smaller than the dynamic modulus measured by the acoustic or ultrasonic wave method, which largely eliminates the inelastic deformation due to rapid wave propagation [28-30]. Also, Ralls, et al. showed that the elastic modulus of metal will decrease with increasing temperature [31]. The underlying reason for this is because the distance between adjacent atoms increases at higher temperatures which in turns decrease the elastic modulus.

When the load is high enough to exceed the elastic limits the material will experience plastic deformation, which is permanent. At this stage the material is undergoing a rearrangement of its internal molecular or microscopic structure, in which atoms are being moved to new equilibrium positions. Specimens subject to plastic deformation will simultaneously elongate and decrease in diameter. The Yield Stress (YS) is defined as just enough stress to cause the onset of plastic deformation. However, YS is difficult to determine. In engineering practice, a specified small amount of plastic deformation is used, with 0.2% being the widely accepted value [32]. This is determined by a parallel line drawn at 0.2% of the strain to the elastic slope (Figure 1.6). When the load is removed at a point above the yield stress, the stress-strain curve will be approximately parallel to the initial modulus.

The ultimate tensile strength (UTS) is the maximum engineering stress level reached in a stress-strain test. In ductile materials similar to solders, the UTS are usually well outside of the elastic portion and the elastic strain is very small comparing to the plastic strain. When necking occurs, the engineering stress decreases and the specimen eventually fail.

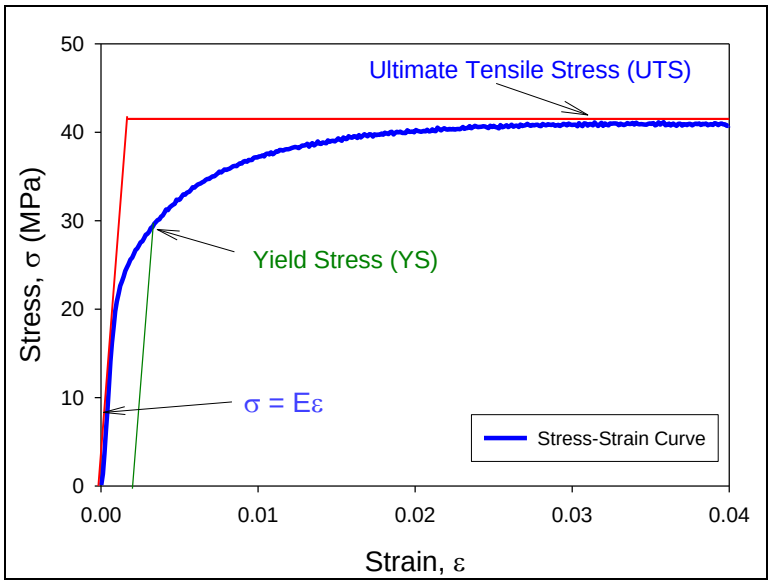

Figure 1.6 Typical Stress-Strain Curve.

1.5.2 Creep Properties

Creep deformation refers to the time dependent plastic flow or deformation of a material that occurs when the material is exposed to a constant load, typically below yield stress, for a long period of time. Creep deformation becomes significant when the material operates at a high homologous temperature (T_h), which is defined by the ratio of operating temperature (T) and the melting temperature (T_m) of the material.

$$T_h = \frac{T}{T_m} \tag{1.4}$$

Creep deformation becomes the dominant failure mode in a metallic material if T_h is greater than $0.5T_m$ [33]. The melting temperature of lead free SAC solder is around 217 °C (490 K) causing T_h for the alloys, for room temperature (298 K) operating conditions, is $0.61T_m$. As a result, lead free SAC solder alloys display creep deformation even in room temperature operating condition. Due to the mismatches of the coefficient of thermal expansion (CTE) of silicon chip and other assembly materials used in an electronic package, solder joints are remain under mechanical stress. These mechanical stresses can cause time dependent creep deformation of solder materials. In microelectronic packaging, creep deformation is regarded as one of the major failure mechanisms of solder joints [34].

Creep test is typically conducted by applying a constant uniaxial load on the test specimen at a particular temperature. During the test, deformation of the test specimen is recorded as a function of test time and the result of the creep test is presented as a 'creep strain' vs. 'time' plot. The extent of creep deformation significantly depends on the applied stress level and the test temperature. Figure 1.7 represents a typical creep curve which consists of three distinct regions, after the initial jump, namely, primary, secondary, and tertiary regions.

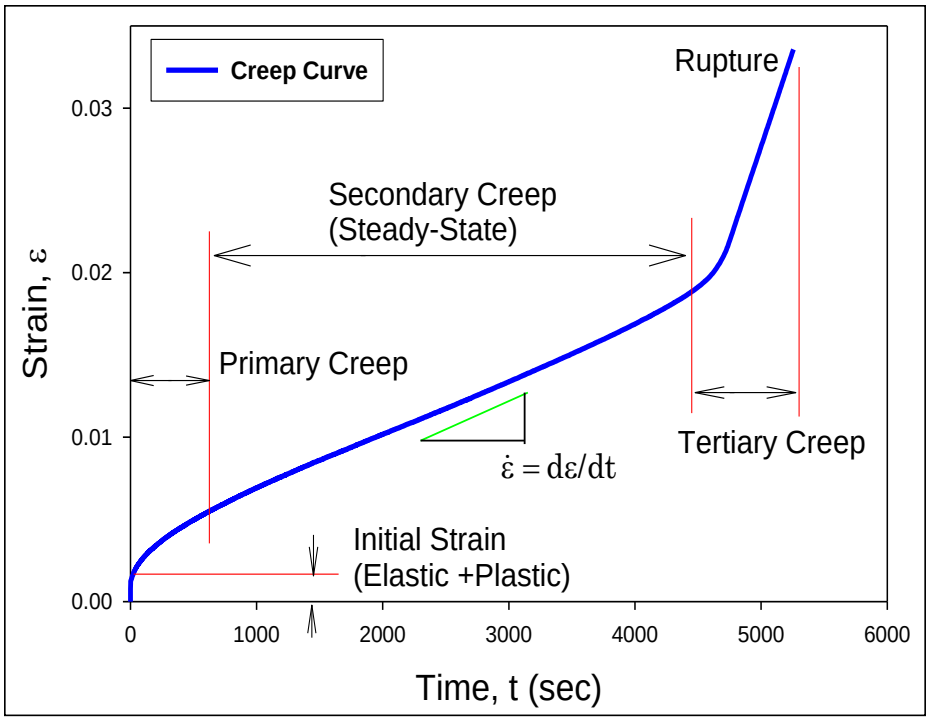

Figure 1.7 Typical Creep Curve.

Every creep test begins with an initial strain which corresponds to the instantaneous response (mostly elastic) of the material due to the applied force/load. In the primary creep stage, the material starts to deform with at a high strain rate (high slope at the beginning of the primary region) and then the strain rate decrease gradually with increasing time. This is due to the work hardening of the material which resists deformation. Eventually, with increasing test time, the creep strain rate reaches to a steady state stage which is known as steady state creep or secondary creep region. The constant creep rate, in the secondary stage, is due to the dynamic balance between strain hardening and recrystallization [32]. The strain rate in the secondary stage is very important since very often researchers use this parameter in the finite element simulations to predict reliability of the solder joints under different test conditions. After secondary creep, the material enter into the tertiary

creep region followed by an immediate rupture. Tertiary region begins when the strain rate start increasing abruptly from the constant value.

1.5.3 Mechanisms of Creep Deformation

Several creep mechanisms have been proposed such as dislocation glide, dislocation creep, grain boundary diffusion, and lattice diffusion which can be summarized in a creep deformation map, as shown in Figure 1.8 [35, 36]. The deformation diagram was first introduced by Ashby in 1972 [36], and has been widely accepted and studied by other researchers in the area. In the deformation map show in Figure 1.8, the abscissa is the homologous temperature and the ordinate is normalized tensile or shear stress. The top of the map is bounded to the theoretical or ideal stress, below which is the onset of dislocation glide. *Dislocation glide* occurs at high stress levels over the entire homologous temperature range. In this case, the dislocation moves along the slip planes [37]. Dislocation creep is characterized by a high-temperature deformation mechanism with homologous temperatures greater than $0.5T_m$ and requiring intermediate high stress. The deformation results from diffusion controlled dislocation movement, with dislocations climbing away from barriers.

Coble proposed a *grain boundary based diffusion* mechanism, which involves the atomic or ionic diffusion along the grain boundaries [38]. The deformation occurs at intermediate low stress levels over an intermediate to low temperature range. Nabarro-Herring Creep or *lattice or bulk diffusion* occurs at low stress level and high temperature. In this case, interstitial atoms and lattice vacancies along the gradient of a grain boundary migrate in reversed directions in the presence of tension or compression pressure. Lattice

or bulk diffusion becomes the primary deformation mechanism under this circumstance [39]. If there is no pressure, interstitial atoms and lattice vacancies will migrate in proportion to the gradient of their concentrations. Under pressure, the lattice defects tend to move in directions to relieve the imbalance of pressure. The movement will eventually cause creep deformation.

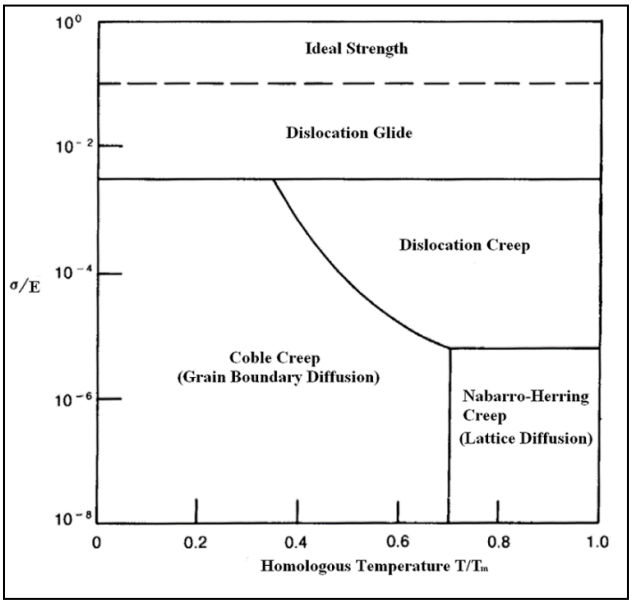

Figure 1.8 A Typical Creep Deformation Map

Grain-boundary sliding may also be involved in the creep deformation at high temperatures [30] where the displacement of grains can be induced by stress at high temperatures. However, this is not an independent deformation mechanism, but may accompany one or more of the above deformation mechanisms.

Due to the high homologous temperature ($> 0.5T_m$) of most solder alloys under normal operating conditions, the stress level determines the creep deformation mechanism. At low stress levels, the controlling mechanism is lattice diffusion and grain-boundary

diffusion. As the stress rises to intermediate levels, dislocation creep takes over, and at high stress level, dislocation gliding becomes dominant. Additionally, the contribution of grain boundary gliding to creep deformation should be taken in account at all stress levels.

1.6 Nanoindentation

Indentation testing is a technique where a hard tip, with known mechanical properties, is pressed into the surface of a test sample to extract the test sample's properties. The load applied on the indenter tip caused it to penetrate into the test sample surface. When the applied load reaches to the user specified value, it can be held for a certain period of time (for creep properties) or remove instantaneously (for hardness and elastic modulus). Removal of the applied load leaves an impression or indent on the sample surface.

Nanoindentation (NI) is a kind of indentation testing where the penetration length is measured in nanometer. The development of the NI technique has been motivated by the miniaturization of the engineering materials as well as the development of the nanostructured materials. Since the area of the indenter tip is well defined (known geometry), the indent area can be easily determined from the tip penetration depth from the sample surface. Elastic modulus, hardness and creep properties of a material can be obtained from indentation load displacement data [40].

Because of having very high hardness and elastic modulus, diamond is typically used to make indenter tip Indenter tips are available in different shape and the choice of indenter tip shape depends on the type of required information from a NI test. Berkovich tip is used in this study (Figure 1.9).

This is the most common indenter tip and used to measure mechanical properties using a NI technique. The shape of a Berkovich tip is similar to a three sided pyramid where the faces meet at a single point (Figure 1.5). The tip can maintain its self-similar geometry to a significantly small scale. The center to face angle of the tip is 65.3^{o}.

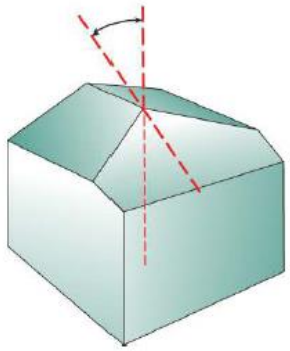

Figure 1.9 Berkovich Tip.

1.7 Harsh Environment applications of Electronics

The reliability of electronics used in various devices depends on the environmental conditions experienced during field use. In oil and gas exploration, avionics, automotive, and defense applications, electronics typically experience very harsh environments compared to consumer electronics [41, 42]. The electronic systems used in under-the-hood automotive applications can be operated at temperatures over 150 °C [43, 44]. For example, engine control modules mounted directly onto the engine experiences high-temperature excursions while in operation. In vehicles, when the engine is turned on, it continues to ramp up to the maximum operating temperature from the ambient temperature while the engine continues to be in operational state. Electronics experience extremely high temperatures during this period, and there can be fluctuation in the temperature conditions.

The electronic systems used in oil and gas exploration applications, also experiences ambient temperatures above 150 °C, even in some applications, 200 °C or higher [45]. Wireline logging represents a typical application in oil and gas drilling where the electronics are exposed to very high temperatures. During this application, the logging tool is lowered into the wellbore, and the electronics experience extremely low or high temperatures depending on the location and type of the oil well. The reliability of electronics is an important concern here since the wireline logging usually lasts 2 to 6 hours.

Electronics used in commercial and defense aircrafts and ground military vehicles also experience extremely high temperatures. In high-speed civil transport and supersonic aircraft, the highest ambient temperature experienced by actuator-mount electronics (without cooling) are ≈ 193 °C and 200 °C respectively [41]. Also, temperatures in electric propulsion system in the battle tank and other mobile ground defense applications can reach up to 200 °C.

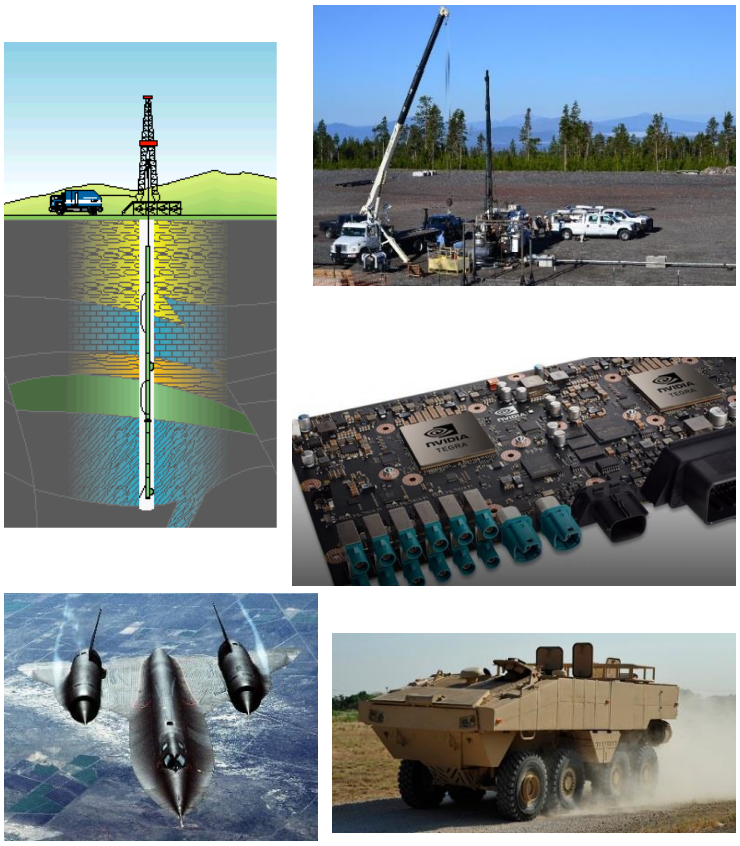

Figure 1.10 High Temperature Application of Electronics

1.8 Objectives of This Research

The motivation of this research is to explore the extreme high temperature mechanical behavior of lead free solder alloys for harsh environment applications, and to develop new constitutive equations and reliability models that include aging effects to predict solder joint reliability in microelectronic packaging. The Primary objectives of this research involve:

(1) Investigate the uniaxial tensile properties of SAC305 and doped SAC solders at very high temperatures (up to 200 °C).

(2) Compare the tensile properties of the solder alloys to examine the effect of the dopants.

(3) Explore high temperature creep behavior and determine secondary creep strain rate for different lead free solders.

(4) Study the effects of extreme high temperature aging on the mechanical behavior (tensile and creep) of lead free solders.

(5) Determine sets of Anand model parameters applicable for high temperature range (such as, 125 to 200 °C) and investigate the correlation of Anand model predicted results and experimental results.

(6) Determine the effects of test temperature and aging time on the creep properties of SAC305 solder joints using Nanoindentation method.

(7) Investigate the effects of different aging temperature and aging time on the microstructure of lead free solders using Scanning Electron Microscopy system.

(8) Perform quantitative analysis of the microstructural evolution of SAC and SAC+X alloys subjected to extreme high temperature aging.

1.9 Organization of the Dissertation

This dissertation mainly focuses on investigating the aging dependent Mechanical behavior and microstructural evolution of lead-free Solder alloys and is presented in the following chapters:

Chapter 1: Introduction to lead free solders alloys and mechanical properties of solder materials.

Chapter 2: Literature review on isothermal aging effects, mechanical properties, nanoindentation on SAC solder joints, nanoindentation at elevated temperature, microstructural evolution during aging of SAC alloys, life

prediction and reliability models of electronic packages that consist of lead free solder materials based on coarsening of IMC particles.

Chapter 3: Description of experimental procedure, sample preparation, uniaxial tensile and nanoindentation creep tests, data processing and quantitative analysis.

Chapter 4: Characterization of uniaxial tensile properties of different lead free solder alloys and comparison of the properties to examine the effect of the dopants.

Chapter 5: Study on the mechanical behavior of lead free solder alloys subjected to extreme high temperature aging.

Chapter 6: Study on the applicability of Anand viscoplastic model for high temperatures.

Chapter 7: Investigation on the effects of test temperature and aging time on the nanoindentation creep response of lead free SAC305 solder joints

Chapter 8: Study on the evolution of the microstructure of lead free solders as a function of aging time and aging temperature.

Chapter 9: Summary and conclusions of the dissertation.

CHAPTER 2

LITERATURE REVIEW

2.1 Introduction

As the electronic industries transition to lead free soldering by the motivation of environmental concerns, legislative mandates, and market differentiation, great efforts have been undertaken to develop desirable lead free solders and establish a corresponding database of material properties. Many researchers have attempted to measure the key mechanical properties of lead free solders. However, large discrepancies have been found in the published data from various groups. There are several reasons for these discrepancies. Firstly, the differences in specimen preparation methods among the researchers cause different microstructures in the specimens that directly affect the experimental results significantly. Secondly, the testing methods and the test conditions may also be different which will again affect the results. Thirdly, mechanical properties obtained from the bulk solders might be different from the measured properties of solder joints. Finally, the lack of standardization in the data acquisition and processing of mechanical properties makes it difficult to obtain good laboratory-to-laboratory comparisons.

Apart from the above mentioned reasons for the discrepancies in solder material properties, another critical factor is aging effects. Aging is mostly neglected in the majority of prior studies, which will further exacerbate these problems. It has been observed from

recent studies that isothermal aging leads to large reductions (up to 50%) in several key material properties for lead free solders including stiffness (modulus), yield stress, ultimate strength, and strain to failure [33]. Even more dramatic evolution has been observed in the creep response of aged lead free solders, where up to 100X increases were found in the steady state (secondary) creep strain rate (creep compliance) of SAC solders that were simply aged at room temperature [46, 47]. For elevated temperature aging at 125 °C [48], the creep strain rate was observed to change even more dramatically (up to 10,000X increase for SAC105).

In real applications, solder joints are continuously exposed to aging/thermal cycling during service. It has been well documented that the microstructure, mechanical response, and failure behavior of solder materials are constantly evolving under such circumstances [49-84]. It has also been demonstrated that aging effects are universally detrimental to reliability and cause reductions in stiffness, yield stress, ultimate strength, and strain to failure, as well as highly accelerated creep. Solder joints with highly degraded microstructure and material properties are so vulnerable that the service life of the package is often severely shortened.

2.2 Aging Effects on Tensile Properties

Studies on the effects of aging on solder material properties are primarily divided into two groups, which are aging effects on bulk solders and aging effects on solder joints. These are described in subsequent sub-sections.

2.2.1 Aging Effects on Bulk Solders

Evolution of mechanical properties with aging in both Sn-Pb and lead free solders has been reported in recent years. Researchers have done numerous studies on the effects of aging on bulk solder properties as well as some studies on solder joints in actual components. Most studies show aging has significant effects on the mechanical properties of solder materials. In 1956, Medvedev [62] reported a 30% loss of tensile strength for bulk Sn-Pb solder after 450 days of room temperature (RT) aging, and a 23% loss in tensile strength for solder joints under a similar exposure. Room temperature aging effects on solder alloys has been presented by Lampe [60]. He showed that after 30 days of room temperature aging, the shear strength and the hardness of Sn-Pb and Sn-Pb-Sb solders reduced by approximately 20%. Miyazawa [77] reported reduction of hardness and microstructural coarsening for Sn-Pb solders aged at 25 and 100 °C for 1000 hours.

Xiao, et al. [66] investigated the stress-strain behavior of SAC396 solder alloy which were subjected to aging at 25 and 180 °C for various amount of time. They have shown that the strength reduces by 25% for aging at room temperature for 35 days and a 33% reduction for aging at 180 C for 9 days. Ding, et al. investigated the influence of aging on fracture behavior of Sn-Ag solder in tensile tests [56]. They have shown that the solder samples tensile strength reduce very quickly for isothermal aging at 180 °C for 120 hours. Ma, et al. [85] studied the evolution of Young's modulus, yield stress, and ultimate tensile strength of SAC305 and SAC405 solder alloys under various aging conditions. A linear-exponential model was developed to describe the material property evolution. They have shown that the material properties decreased dramatically in the first 20 days for both

room temperature aging as well as elevated temperature aging. After 20 days of aging, the properties change slowly and linearly and it continues for longer aging time.

Zhang, et al. [86] also studied the aging effects on tensile properties of SACN05 (N = 1%, 2%, 3% and 4% silver) series solders for different amount of aging at temperatures 25-125 °C. They have demonstrated that the mechanical properties degraded more dramatically when the aging temperature was increased. The data also shows that the degradation becomes linear with longer aging time. Cai, et al. [51] have also shown that the aging effects are significant for lead free solders (SAC105, SAC205, SAC305 and SAC405) for room temperature aging as well as elevated temperature aging. They have also shown that the aging effects can be reduced by using certain dopants to (e.g. Bi, In, Ni, La, Mg, Mn, Ce, Co, Ti, Zn, etc.) SAC solder alloys to enhance the reliability of lead free solders. Finally, Mustafa, et al. [78] have demonstrated that the hysteresis loop area in cyclic (tension/compression) loading of various SAC solder alloys changes significantly with aging. For strain controlled tests, the hysteresis loop area deceases and for the stress controlled tests, the loop area increases with aging time.

2.2.2 Aging Effects on Solders Joints

Isothermal aging effects have also been reported to lower the strength and to reduce reliability of solder joints. The mechanical response of solder joints to external loading can be different from the bulk solders due to fine microstructure, grain orientation (single grain/ multigrain), and the presence of intermetallic compounds at joint boundaries.

Coyle, et al. [87] reported 20% shearing strength reduction of BGA solder joints after 240 hours of aging at room temperature. A 10% shearing strength reduction has been

reported by Lee, et al. [88] for the BGA packages just after 3 days room temperature aging. Chilton, et al. [89] reported a 15% fatigue strength reduction of Sn-Pb solder joints of a SMD test package which were aged for 60 days at room temperature. Li, et al. [90] studied the elevated temperature aging effects on flip-chip packages with SAC solders. They have shown that the shear strength of solder bumps subjected to aging at 80 °C decreased gradually with aging. Also for the aging temperatures 150 and 175 °C, the degradation of shear strength of the bumps were much faster. They also reported that the fracture of the solder bumps occurred at the bulk solder. Koo, et al. [91] found that 63Sn-37Pb solder joint strength on electroplated Ni/Au BGA substrate was significantly affected by aging at 170 °C for up to 21 days, while the deterioration of shear properties of Sn-3.5Ag was much smaller. Darveaux [92] indicated that after 24 hours of aging at 125 °C, all alloys showed a 10% to 30% reduction in solder joint strength. All of the solder joints failed within the bulk solder and exhibited high ductility. In addition, the ductility of all of the Pb-free solder joints decreased with increased aging [66]. Oliver et al. [93] reported that the joint strength of Sn-3.5Ag and SAC325 solder on both Ni/Au and Sn/Pb pad metallizations were unchanged after aging at room temperature as well as elevated temperature for 1000 hours. However they found reduction in shear strength of solder joint in Sn-Pb solders.

Pang, et al. [94] studied the aging effects on the mechanical properties and fatigue life of Sn-Pb solder joint specimens that were subjected to thermal cycling conditions from -40 to 125 °C. They have shown that the shear strength reduces significantly for specimens that were subjected to 1000 thermal cycles. They have also shown that the fatigue life of the specimens dropped by 6 times compared to non-cycled specimens. Zhou, et al. compared the joint strengths of SAC387 on both Cu and Ag substrates at an aging

temperature of 170 °C, and concluded that aging had little effect on the SAC/Ag interface, but dramatically softened the SAC/Cu joint. The softening difference was said to be due to lower residual stresses at the SAC/Ag joint interface. Chen, et al. [73] studied the effects of aging on the solder bump shear strength for both Sn-Pb and Sn-3.5Ag solders. They reported that shear strength for both solder materials decreases after aging at 150 °C for 1500 hours, 8.9% for Sn-Pb solder bumps and 5.3% for Sn-3.5Ag. Kim, et al. [59] also reported similar results in which they reported an average 5% decrease in joint strength in stud bump samples for aging at 150 °C for 300 hours.

The degradations of the stiffness, strength, and creep compliance with aging are expected to be universally detrimental to reliability of solder joints in lead free assemblies. This has been demonstrated explicitly in the recent investigation of Lee and coworkers [88], where aging has been shown to degrade the Thermal Cycling Reliability (TCR) of lead free Plastic Ball Grid Array (PBGA) assemblies subjected to Accelerated Life Testing (ALT). They have shown dramatic degradation in fatigue life of BGA components with SAC 305 solders, which were subjected to thermal cycling from 0 to 100 °C with prior aging at either 100 or 150 °C. The amount of life degradation was found to be dependent on the surface finish of the PCB substrates, with 44% degradation observed for ENIG surface finish and 20% degradation observed for OSP surface finish under the most severe aging conditions (1000 hours at 150 °C) prior to thermal cycling accelerated life testing.

In a similar study, Lee, et al. [95] showed that the lifetime of wafer-level chip scale packages with SAC305 solder interconnects was reduced by 29% for 500 hours of aging at 150 °C. Zhang, et al. [81] have investigated the correlation between the effects of isothermal aging on the reliability of PBGA components. They have shown that for 6

months aging at 125 °C that the reliability of SAC105 components dropped by 53%. Smetana, et al. [96] have performed an extensive study on the effects of prior isothermal preconditioning (aging) on the thermal cycling lifetime for a variety of components. Similar to the investigations discussed above, it was observed that prior aging reduced the thermal cycling characteristic life of SAC BGA assemblies subjected to 0 to 100 °C cycling. It was also found that changes occurred in the Weibull slope, suggesting other failure modes were created by aging. They also found that prior aging increased the thermal cycling reliability of certain components (e.g. 2512 chip resistors and certain QFNs). Similar results of improved reliability with aging were found for components subjected to a smaller thermal cycling range of 20 to 80 °C. This led them to conclude that aging does not universally reduce solder joint fatigue life.

The effects of aging on the degradation of the thermal cycling reliability of lead free BGA assemblies have been studied recently by Zhang, et al. [81]. In their studies, PBGA daisy chain test assemblies were subjected to up to 2 years of aging (25, 55, 85, and 125 °C), followed by thermal cycling from -40 to 125 °C or -40 to 85 °C to failure. They have shown that for all component sizes and lead free solder alloys, the solder joint thermal cycling reliabilities of the BGA components were severely reduced by prior aging. For up to 12 months prior aging for the components with Im-Ag PCB surface finish and thermal cycling from -40 to 125 °C, they have observed clear degradation in life for aged components relative to non-aged components and the amount of degradation was exacerbated with higher aging temperatures. Using the 63.2% Weibull characteristic life (η) as a failure metric, the reliability was observed to decrease by 37% (6 months aging)

and 53% (12 months aging) for the 19 mm BGA components subjected to aging at 125 °C prior to thermal cycling.

Gradual aging also occurs during thermal cycling tests due to the high temperature dwells at the top of each thermal cycle. Several recent studies [97-101] have demonstrated that there is a strong dwell time effect on thermal cycling reliability for lead free electronics; with longer dwell times leading to reductions in the thermal cycling life.

2.3 Aging Effects on Creep Properties

It has been found in the literature that aging at room temperature as well as elevated temperatures have significant effects on creep deformation of lead free solder alloys. Darveaux, et al. [92] reported a faster creep rate for aged solder specimens than non-aged specimens. For both SAC305 and SAC405 solders and for aging at 125 °C for 1 day, they found 20 times increase in the creep rate for aged specimens. Xiao, et al. [66] found that SAC396 showed much lower absolute creep rates compared with eutectic Sn-Pb and ascribed this increase in creep resistance to the finely dispersed intermetallic compound (IMC) precipitates in the Sn matrix. Wiese, et al. [65, 102] investigated the creep behavior of SAC 387 solder with short (1 day at 125 °C) and long (49 days at 125 °C) thermal storage times. They found that the creep rate of solder increase significantly for short time aging at 125 C but relatively smaller changes occurred for longer aging times.

Ma, et al. [103] studied the evolution of secondary creep rate with aging for SAC305 and SAC405 solders. They showed that the secondary creep rates for SAC solders increase with aging at either room temperature or elevated temperature. Also, for both SAC solders exposed to elevated temperature aging, the effects were much higher than

those for room temperature aging. A more detailed investigation was conducted by Zhang, et al. [86] on aging effects on the creep behavior of lead free solders. They reported that for 6 months aging at 125 °C, the secondary or steady state creep rate of SAC105 solder increased by about 10000 times. Also, for other aging temperatures (25 to 125 °C), they found that the both the primary and secondary creep rates increase with 6 months aging. Finally, Cai, et al. [51] demonstrated that by using certain types of dopants in SAC solders, the aging effects on steady state creep rate can be reduced. They showed that for no aging the creep rates of doped solders were higher than SAC105 and SAC205 due to lower silver contents of the doped solders compared to SAC105. However, with 6 months aging at temperatures 25 to 125 °C, the secondary creep rates of the doped solders were smaller than the creep rates of SAC105.

2.4 Constitutive Modeling for Solder Materials

In microelectronics packaging, complex stresses and strains are usually generated in the components due to the CTE mismatch of different materials. Solder interconnects are usually subjected to deformations that lead to three-dimensional stress and strain states. The solder material constitutive law plays an important role in the development of thermo-mechanical models for microelectronic assemblies. Under thermo-mechanical loading, the solder material undergoes elastic and in-elastic deformations. Elastic deformations are recoverable, while inelastic deformations consist of time-independent plastic deformations and time-dependent creep deformations, which are not recoverable. Solder constitutive behavior can be represented by a combination of elastic, plastic (isotropic or kinetic hardening), and viscoplastic/creep models.

2.4.1 Constitutive Modeling for Stress-Strain Tests

The linear elastic region in a uniaxial stress-strain curve can be modeled by Hooke's law where stress and strain are related by an elastic modulus (E). The plastic strain hardening region can be modeled by a time-independent non-linear stress-strain relationship based on either isotropic or kinematic strain hardening. Isotropic hardening assumes that the origin of the von Mises yield surface remains stationary in the stress space and the size of its yield surface expands resulting from strain hardening. In kinematic hardening, the von Mises yield surface does not change in size, but the origin of the yield surface is allowed to translate in the stress space to model strain hardening effects of increasing plastic flow stress. For solder materials, the tensile stress and strain curves are dependent on the test temperature and strain rate. The elastic modulus (E), yield stress (YS) and the tensile strength (UTS) properties vary with temperature and strain rate.

For a typical thermal cycling temperature range from -40 to 125 ^{o}C, these mechanical properties reduce with the increase in temperature. The solder material has a homologous temperature from 0.5 to 0.8 for this temperature range. Also, the creep deformation in a solder material is highly dependent on the stress and temperature state. Thus, a time-dependent elastic-plastic-creep constitutive model, or viscoplastic constitutive model, is needed to facilitate finite element modeling for simulation of solder joint reliability during thermal cycling tests. High temperatures induce transitions in macroscopic fracture, and these transitions parallel the changes in the strength and ductility of materials [104]. Materials lose strength at higher temperatures. Hertzberg stated that the material strength increases with the testing strain rate, following a form similar to

Holloman's Equation [104], where stress is related to strain rate through some strain hardening exponent.

Solder alloys possess very high homologous temperatures. The properties of solder alloys are strongly dependent on both the temperature and strain rate. Jones, et al. [105, 106] have observed an approximately linear relationship between the strength and temperature. Pang, Shi and co-workers [107] have observed similar experimental results, with a near linear relationship with temperature and a power law relation with the strain rate. Several other studies have also observed similar material behavior for both Sn-Pb eutectic and lead-free solder alloys [108-111].

The Ramberg-Osgood model describes the elastic-plastic behavior of materials, and can be used to describe to describe the stress-strain curve of solder materials [112]. In prior work, the Ramberg-Osgood model hardening exponent n and the stress coefficient σ_o were modified to be temperature and strain rate dependent. The temperature and strain-rate dependent modified Ramberg-Osgood model was also applied by Pang, et al. [112].

2.4.2 Constitutive Modeling for Creep

In general, the creep behavior of materials consists of three different stages: primary creep, secondary creep, and tertiary creep. In the primary creep regime, the material undergoes strain hardening, resulting in a decreasing strain rate with time. In the secondary stage, also known as steady-state creep regime, the creep strain rate is essentially constant, showing a very slow decrease. In tertiary stage, strain rate increases with time and ultimately results in failure of the material. Solder alloys are often subjected to steady-state creep regime under typical thermo-mechanical loading conditions. Constitutive modeling

of creep deformation is needed to predict the end-of-life of electronic components by using finite element analysis. A constitutive creep model is established by conducting creep tests at different temperatures and stress levels. The materials constants are important in determining the accuracy of end-of–life predictions for solder joints using finite element analysis. Large discrepancies between the creep model and experimental data would degrade the accuracy of these predictions.

The minimum creep rate may be linked with the applied stress, σ, by a series of equations according to the dominant creep mode. There are mainly three types of creep modes, namely, power law creep, exponential creep, and combination creep. Creep is highly sensitive to both applied stress level and to test temperature. As a thermally activated process, the creep rates increase exponentially with temperature. The effect of stress is dependent upon the controlling creep mechanism. The two widely used creep models are the Dorn power law model [113], and the Garofalo hyperbolic sine model [114]. In logarithmic coordinates, the Dorn power law model yields a linear relationship between the creep strain rate and applied stress for a specified temperature. Nonlinear experimental curves for creep, however, have been found over the entire stress range. The high stress regime exhibits the largest stress exponent n, and the low stress regime exhibits the smallest n value for any given temperature. This phenomenon is referred to as "power law break down" and indicates that the Dorn model is not suitable for fitting data obtained over large stress ranges.

The Garofalo model was established for matching creep behavior at both low and high stresses. At low and medium stresses, the creep strain rate depends on stress to the power n. At high stresses, the creep strain rate is an exponential function of stress. The

model is able to predict the creep deformation over intermediate temperature regimes for the entire stress range, but it underestimates the creep deformation at both low (-40 °C) and high (125 and 150 °C) temperatures.

Ma and Suhling [33] have evaluated the creep parameters in the two models for various Pb-containing and Pb-free solder alloys and found large discrepancies in the creep data for solder alloys of the same chemical composition. There are several reasons that could explain the differences, including the specimen design, variations in testing method and test conditions used by different researchers, and storage time and temperature before the creep test. Moreover, it is important to recognize that the creep behavior of bulk solder significantly differs from solder in a joint due to the effects of microstructure evolution, intermetallic compound formation, and constraint due to different methods of assembly. Since creep modeling is often to be incorporated in finite element analysis to predict the end-of-life of electronic package, the discrepancies in material constants will directly affect the accuracy of prediction.

A third widely used creep constitutive model was proposed by Weise, et al. [102], and is often referred to as the double power law. They identified two mechanisms for steady state creep deformation for the bulk and PCB samples. They attributed them to climb controlled (low stress process) and combined gliding/climbing (high stress process) behavior and represented steady state creep behavior using two power law terms. In electronic packages, thermal mismatch induced stresses can result in extensive plastic deformation at solder joints, which is responsible for the low cycle thermal fatigue failure of solder materials. An expression for the strain was proposed by Yang, et al. [100] where total strain was divided into elastic, plastic, and creep strains.

Apart from these models, several other creep constitutive models have been proposed by researchers. Shi, et al. [101] established a unified dislocation-controlled creep constitutive model that described the creep deformation of solder alloy over a wide temperature range (-40 to 150 °C) and explained the temperature dependencies of the stress exponent n and activation energy Q. For creep strain rates at very low stress levels, they further developed a unified diffusion-controlled creep constitutive model to describe low temperature Coble creep and high temperature Nabarro-Herring creep. Clech [99] established obstacle-controlled creep models for both Pb-containing and Pb-free solder alloys. Creep deformation is impeded by discrete obstacles (phases, precipitates, grain boundaries, and other defects) distributed throughout the Sn-matrix in Sn-based solders. By taking these impeding elements into consideration, the rate-dependent obstacle-controlled creep models are able to resolve the anomalies observed in the classical analysis of creep data including stress and/or temperature dependences of activation energies and stress exponents in the Power Law or Hyperbolic Sine models.

2.5 Application of Anand Model for Solder Joint

In the electronic packaging industry, it is important to be able to make accurate predictions of board level solder joint reliability during thermal cycling exposures. The Anand viscoplastic constitutive model is often used to represent the material behavior of the solder in finite element simulations. This model is defined using nine material parameters, and the reliability prediction results are often highly sensitive to the Anand parameters. The viscoplastic constitutive equations proposed by Anand [115] have become popular for rate-dependent deformation of metals at high temperatures. They were initially

developed for structural metals, but have been adopted for microelectronic solders (Sn-Pb and lead free) for homologous temperatures in excess of $0.5T_m$. The so-called Anand model has been widely applied for the solder stress-strain relations in finite element simulations of electronic packages, where solders undergo small elastic deformations and large viscoplastic deformations. For example, Che, et al. [116] have considered multiple constitutive theories, and then demonstrated that the Anand equations were well matched with predictions of lead free solder fatigue life. In addition, Pei and coworkers [117] have calculated the nine parameters of the Anand model by conducting tensile testing of Sn3.5Ag and Sn3.8Ag0.7Cu lead free solders at several temperatures and strain rates.

Mysore, et al. [118] have found the Anand material parameters for SAC305 (Sn3.0Ag0.5Cu) lead free solder alloy by performing double lap shear tests. They suggested that the Anand parameters for solder joint samples are significantly different than those measured by testing of bulk solder specimens. In addition, Motalab, et al. [119] have evaluated the Anand parameters for SAC305 solder using two approaches, including stress-strain testing and creep testing. Bai and coworkers [120] suggested a modified approach for SAC305 (Sn3.0Ag0.5Cu) lead free solder where strain rate and temperature dependent values were included for Anand model parameter h_o. The Anand model constants for SAC105 (Snl.0Ag0.5Cu) lead free solder have been reported by Amagai, et al. [121] and Kim, et al. [122].

2.6 Reduction of Aging Effect by Dopant

Addition of 4th element in the SAC solder is known as doped SAC alloy. Dopants play an important role to control microstructure and mechanical properties of the alloy.

Dopants have been found to strongly influence the properties and behaviors of lead free solders. For example, addition of Bismuth (Bi) as a dopant has been demonstrated to have several beneficial effects. Bi helps to reduce solidification temperature, increases strength by means of precipitation hardening, and also helps to reduce IMC (Intermetallic Compound) layer thickness in lead free solder materials [123]. The Effect of Bi on the mechanical properties of a SAC (Sn3.5Ag0.9Cu) alloy was investigated by Matahir and coworkers [124]. They reported that the shear strength increased with increasing Bi addition up to 2 wt%. Beyond that point, the shear strength decreased with increasing Bi%. Improved shear strength might attribute to the role of Bi on the morphology of microstructure and distribution of dominant IMC (Ag_3Sn). Reduction of strength at higher Bi content was due to the evolution of Bi rich phase and fragmentation of the IMC. Pandher, et al. [125] also reported that addition of 2% Bi in SAC alloys improves wetting and alloy spreading.

Zhao, et al. [126] found that addition of 0.02% Ni to SAC105 increased the formation of NiCuSn IMC and reduced the localized grain size at solder/NiAu pad interface. In addition, the effects using various doped elements (i.e. Co, Fe, In, Ni, Zn and Cu) in SAC305 BGA solder joints on Cu pads were studied by Sousa, et al. [127]. They concluded that addition of low levels of Zn had a significant beneficial effect on the interfacial IMC. Lee and coworkers [128] found that micro-alloying SAC alloys with Ni and Bi improved thermal fatigue life and drop impact resistance. Yeung, et al. [129] studied a novel lead-free solder SAC_Q. Based on drop test, thermal cycling, and finite element simulation, they conclude that the doped alloy has improved board level reliability

when compared to SAC105. Additional literature publications on the effects of dopants have been reviewed in reference [51].

Sun et. al. [130]reviewed the effects of different alloying elements (Mn, Fe, Bi, Ni, In, Zn, Ga, Sb, Mg), Rear Earth (RE) Elements (Ce, La, Y, Er, Pr, Nd, Yb), and nanoparticles (Al_2O_3, Al, TiO_2, ZnO, ZrO_2, CNT, Graphene, CeO_2, TiB_2, Ni-Coated CNT, Mo, SiC, $SrTiO_3$, Co) on melting temperature, wettability, mechanical properties, microstructure, interfacial reaction and Sn whiskers.

For SAC305 solder, average width of eutectic region was found as 6.8±2.8 μm and grain size of β-Sn was 24.8±5.9 μm. Indium (In), helps to refine IMC and Sn-rich phase as well as makes the microstructure more uniform. Titanium (Ti) can significantly reduce Sn grain size and width of eutectic region by heterogeneous nucleation of IMC's. Iron (Fe) forms large $FeSn_2$ IMC which has a weak interface with β-Sn matrix. Magnesium (Mg) helps to coarsen eutectic region. Addition of Al in SAC105 refines β-Sn dendrites and enlarge eutectic regions. Besides, it also prevent Ag_3Sn and Cu_6Sn_5 and forms two new IMC Ag_3Al and Al_2Cu. Zn also helps to refine β-Sn dendrites significantly. Ni was found to reduce the size of Sn-rich phase and refine the microstructure. Since Antimony (Sb) has higher affinity towards Sn, presence of Sb reduces the driving force to form Cu-Sn IMC's resulting a narrow IMC layer in the solder joint. Sb also helps to refine IMC grain size.

RE elements can significantly refine the microstructure of SAC solders. Er can reduces the particle size of Ag_3Sn and Cu_6Sn_5 whereas Pr and Nd refine β-Sn dendrites and IMC particle size by forming uniformly dispersed fine $RESn_3$. These fine particles act as heterogeneous nucleation sites during solidification. However, excessive amount of RE

elements will cause to form bulk $RESn_3$ phase which has a negative effect on mechanical properties. La, Ce, and Y also have a similar effect on solder microstructure.

Al and Ni nanoparticle was found to reduce IMC particle size, spacing and IMC layer thickness by forming very fine and uniformly dispersed Sn-Ni-Cu and Sn-Sg-Al IMCs. Addition of small amount of Fe nanoparticles refine the microstructure and forms $FeSn_2$ phase. Al_2O_3 nanoparticles increase the size of eutectic region and reduce Ag_3Sn particle size. TiO_2 and SiC nanoparticle reduces the size and spacing between Ag_3Sn particles. $SrTiO_3$ nanoparticle reduces the size of Ag_3Sn and Cu_6Sn_5 particles by promoting the rate of nucleation during solidification. ZnO suppresses Ag_3Sn and Cu_6Sn_5 IMC formation and reduces β-Sn grain size by 22%.

The Effect of dopants on the aging induced changes in microstructure was also studies by a number of scientists. Sadiq et al. [131] worked with different Lanthanum (La) doped SAC305 alloys and recorded the changes in microstructure and mechanical properties during isothermal aging at 150 °C for 6 different aging conditions (i.e. 0 , 10, 25, 50, 100 and 200 hours). They reported that La drastically reduces the IMC particle size and also significantly inhibit the growth of IMC particles during isothermal aging. Based on polarized light image they found that in as cast condition, grain size of SAC305 was ~8 mm and was significantly reduced (~1 mm) after La addition. From the graph presented in that paper, it is also clear that aging doesn't have any significant influence in average grain size.

In another study, Lee et al. [132] studied the effect of Lanthanum (La) addition and high temperature storage on the microstructure and microhardness of Sn-3.5Ag solder joints. Their experimental results confirms that addition of La refine the solder

microstructure. They explained that during solidification of the solder, $LaSn_3$ compounds form at the beginning and provide extra nucleation sites for Ag_3Sn IMC to grow resulting a refine microstructure. Addition of La was also found to reduce the thickness of IMC layer after soldering as well as isothermal aging. They also reported that La addition helps to improve microhardness and thermal resistance of solder joints.

Hao et al. [133] studied the effects rare earth element Er addition on the evolution of microstructure of lead free eutectic SAC (Sn-3.8Ag-0.7Cu) solder joints during isothermal aging. Aging was conducted at 170 °C for 4 different holding periods (i.e. 0, 200, 500 and 1000 hours). The authors measured the thickness of IMC layer of Sn-3.8Ag-0.7Cu and Sn-3.8Ag-0.7Cu-0.15Er alloy after different aging duration. They found that Er addition reduces the thickness of IMC layer in as reflowed condition and also significantly reduces the growth during aging. They argued that Er combines with Sn to form $ErSn_3$ IMC and reduces the activity of Sn which subsequently suppress the formation of Cu_6Sn_5 IMC layer. They also observed that $ErSn_3$ IMCs formed during solidification of solder act as a heterogeneous nucleation site for Ag_3Sn and Cu_6Sn_5 precipitates. The increase in nucleation sites results a refinement of Ag_3Sn and Cu_6Sn_5 particles. Addition of Er also found to make the microstructure more uniform and reduce the coarsening rate of the IMCs during isothermal aging.

Witkin [134] and Delhaise et al. [135] studied the effect of aging of Bi doped SAC alloys. In both study, the authors reported an elimination or at least reduction of aging induced degradation in SAC-Bi alloys.

2.7 Nanoindentation on SAC Solder Joints

Most prior work on solder mechanical behavior and aging effects has involved tension, compression, and shear testing of miniature bulk solder specimens. Sample geometries have included traditional uniaxial tensile specimens, small cylinders in compression, lap shear specimens, and Iosipescu shear specimens. A more limited number of researchers have examined aging effects by mechanical loading of solder joints [57, 64, 65, 92]. These studies have involved shearing of custom fabricated solder ball arrays [64, 65, 92], as well as impression creep experiments [57].

Nanoindentation techniques [40] have recently become popular for measuring mechanical properties and creep deformation behavior of extremely small material samples, and several investigators [75, 136-148] have applied them to lead free solders. Early solder nanoindentation studies included room temperature measurements of the elastic modulus E and hardness H of β-Sn dendrites, eutectic phases, and individual Ag_3Sn and Cu_6Sn_5 intermetallic compounds [136, 137, 146, 148]. Hasnine et al. [75, 140-142], have examined aging effects in SAC solder joints extracted from PBGA assemblies using nanoindentation. Their results showed that the aging induced degradations of the room temperature mechanical properties (modulus, hardness) of single grain SAC joints were of similar magnitudes to those seen previously by testing of larger "bulk" solder specimens with hundreds of grains. However, the degradation of the creep response, while still significant (15-100X increase), was less in the solder joints relative to larger uniaxial tensile specimens (200-7500X increase). This was due to the single grain nature of the joints considered, and the lack of the grain boundary sliding creep mechanism. They also

tested very small tensile specimens (10 mm long) with 10-20 grains, and the creep degradation results were similar to the single joint specimens.

Knowledge of elevated temperature behavior, especially creep behavior, is critical to understanding solder joint reliability in thermal cycling and accelerated life testing. Elevated temperature nanoindentation measurements of modulus and hardness of bulk SAC305 and SAC357 solder samples were performed by Gao, et al. [138], and Han and coworkers [139]. In addition, the latter authors also examined the sensitivity of the creep response of lead free solder to temperature. Sadiq, et al. [147]have investigated the nanoindentation elastic modulus and hardness of β-Sn and eutectic phases within a SAC305 solder joint at temperatures ranging from 45-85 °C. Another solder nanoindentation study over a larger temperature range (25-150 °C) was performed by Lotfian, et al. [143], where they reported the mechanical properties of the constituent phases of SAC397 solder joints. Marques, et al. [144, 145] used nanoindentation to study mechanical properties and creep behavior of SAC305 solder joints over a wide temperature range (25-175 °C). Based on finite element simulations, they also developed a method to correlate nanoindentation creep results with uniaxial creep data.

Nanoindentation pile-up, defined by an uplift of material near the edges of an indent, is often observed in testing of solders [136, 137, 143, 147, 148]. Pile-up depends significantly on the work hardening ability of the material [149]. For a material that easily work hardens, the top surface near the indent will be hardened during the deformation and thus will prevent pile up by resisting upward flow of the material. Prior researchers have used different techniques to include the pile-up area in their measurement. Kese, et al. [150] proposed a semi ellipse method for pile up correction, which was based on the

assumption that the pile-up contact area had a semi-elliptical shape. While some researchers [147, 148, 151] have used the Kese, et al. method, others [137] have used FEA simulations to guide pile-up corrections.

2.8 Effects of Aging on the Microstructure of Solder

Due to their low melting temperatures, solders are exposed to high homologous temperatures in most product applications. Thus, there is a continuous state of active diffusion processes in the solder alloys, and their microstructures are inherently unstable and will continually evolve during normal operating temperature conditions of electronic packaging assemblies. High temperature storage, which is also known as isothermal aging, of the solder alloys causes a significant change in the microstructure leading to a degradation of mechanical properties. Chou [152] studied the effect of isothermal aging on microstructure of Sn-Pb and lead free SAC solder joints. He reported a significant phase coalescence of eutectic Sn-Pb solder joint after aging.

Xu et al. [61] measured the thickness of IMC layer of different Sn-Pb alloys with different surface finishes after isothermal and thermal cycling aging. Based on their experimental results they had proposed an integrated model to predict the IMC layer growth under different isothermal aging and thermal cycling environment.

Ubachs et al. [153] developed a model to predict microstructural evolution during isothermal aging of Sn-Pb alloy by numerical simulation. They focused their study on a fixed region and compared experimental observation of phase growth during isothermal aging at 150 °C, for 0 to 15 hours, with the predicted phase growth by simulation.

In recent days, electronic industries are moving towards lead free solders due to the growing concern about environment. Effect of aging in lead free solder is even more significant. Sahaym et al. [154] examined the evolution of microstructure of bulk SAC105 and SAC305 solder during isothermal aging at 150 °C. They observed the changes of identical region after 4 different aging durations (0, 110, 194, and 310 hours). In as reflowed condition, they found that the microstructure is consisted of several pro-eutectic colonies of β-Sn grains surrounded by eutectic regions. Most of the grains in a pro-eutectic colony has low angle ($<15^{o}$) boundaries with the neighboring grains. They reported that after 310 hours of aging, the average size of IMC precipitates has increased from 0.35 μm to 2.5 μm and the average grain size has increase from 4.5 μm to 7.5 μm.

The authors also observed that a small percentage (~10%) of β-Sn grains, especially those near the eutectic region, has went through recrystallization during isothermal aging. They claimed the stress on the β-Sn grains, due to the growth of IMC particle, is responsible for the recrystallization. The extent of recrystallization was less in SAC105 than in SAC305 due to the relative difference in IMC volume fraction. Although not mentioned clearly in the text, it is evident from their graph that the number of high angle grain boundary has been reduced and low angle grain boundary has been increased after aging for 100 hours.

Maleki et al. [155] studied the evolution of microstructure of SAC405 and pure Sn during isothermal aging at 150 °C after 144 hours and 296 hours. They also performed Mechanical testing (shear test) to correlate changes in microstructure and mechanical properties. Sample size was approximately 1 × 0.3 × 0.3 mm and it was attached to Cu-pad. They reported that in as-reflowed condition, the microstructure of SAC405 was

consisted of ~70 vol% of eutectic phase and ~30 vol% of β-Sn dendrite, whereas the mean diameter of IMC particles and interparticle distance was ~250nm and ~630 nm, respectively. Average particle size increases with aging time due to Ostwald ripening. During IMC growth, they attributed bulk diffusion to be the main rate controlling mechanism. On the other hand, aspect ratio decreases and interparticle spacing increases with aging due to the driving force to reduce surface energy. Electron backscatter diffraction (EBSD) analysis confirmed the presence of large grains (~200 μm) in SAC405 solder before aging. After 296 hours of aging at 150 °C they didn't find any significant change in grain size and orientation. On the other hand, pure tin has a fine grain (~10 μm) microstructure before aging which grows significantly during aging and become ~200 μm after aging. They attributed the reduction of mechanical properties during aging for SAC 405 to the IMC's coarsening whereas for pure Sn to the grain coarsening.

Telang et al. [156] worked on the effects of aging at 150 °C on microstructure, especially grain size and grain-boundary misorientation, of several alloys including Pure Sn (ingot and reflowed), Eutectic Sn-3.5Ag (ingot), Eutectic Sn-3.8Ag-0.7Cu (ingot), Sn-1.6Ag (solder ball), Sn-3.0Ag (solder ball), and Sn-3.0Ag-0.6Cu (solder ball). For Sn-3.5Ag alloy they studied three different aging conditions (i.e. 0, 200, and 400 hours.) whereas for rest of the alloys they studied two different aging conditions (i.e. 0. and 200 hours). Before aging, grain size of pure Sn ingot and Reflowed Pure Sn was 50-150 μm (equiaxed) and 100-250 μm (equiaxed), respectively. After aging for 200 hours, the grain size of pure Sn for both condition was >500 μm with irregular shape. They found ledges, in SEM image, along the grain boundary (confirmed by polarized light microscopy) of sample after aging. According to the authors, these ledges were formed due to anisotropic

nature of thermal expansion coefficient (CTE) of Sn grain. After aging, when the sample was taken out from the oven, different grains contracted with different magnitudes leading to the ledges. They also argued that the extent of contraction depends on the size and the orientation of the grain. Before aging, the sample had smaller grain size. As a result, when the sample was kept inside the oven, difference in expansion of different grains was relatively small. This resulted small ledges along the grains of as reflowed sample. Although the grain boundaries moved during the aging process, these ledges were retained throughout the experiment.

After comparing the microstructure of eutectic Sn-Ag (3.5% Ag) ingot with pure Sn ingot, they found that Sn-Ag alloy has a much finer (10-30 μm) grain size, which was very stable. Aging of Ag-Sn alloy did not cause any significant grain growth due to the pinning effect of Ag_3Sn IMC particles. On the other hand, the grain size of SAC (Sn-3.8Ag-0.7Cu) ingot was similar to that of Sn-Ag ingot (10-30 μm). But, aging for 200 hours caused a significant growth in the grain size (~120 μm) of the alloy. Although not stated clearly in the text, it is evident from the misorientation histogram that the extent of misorientation, among the grains, for the both alloys decrease with increasing aging time. From their experimental observations the authors also have discussed the effect of Ag and Cu on preferred grain orientation and grain size.

Allen et al. [70] studied two near eutectic lead free SAC solders (bulk Sn-3.5Ag-0.9Cu and SAC405 joint). They used 3 different aging temperatures (152, 177, and 201 °C) and 5 different aging durations (0, 1, 2, 4, and 8 weeks). They measured the density of IMC particle after different aging conditions and based on their experimental results they conclude that the rate controlling mechanism for coarsening is volume diffusion (n=3).

They also reported that the coarsening kinetics of eutectic SAC solder is slower than that of eutectic Sn-Pb solders.

Kumar et al. [157] worked with SAC105 and SAC305 alloys. For isothermal aging experiments, they polished a bulk reflowed solder samples and then aged the samples at 150 °C in high vacuum (to prevent oxidation). After different aging intervals (i.e. 0, 110, 194, 220, and 330 hours) they captured the SEM image of the same region, of any particular sample, to quantify the coarsening behavior of the IMC's. They found that the growth rate of Cu_6Sn_5 particles are much faster than Ag_3Sn particles, due to the higher diffusivity of Cu than Ag in Sn matrix. Besides, the fraction of Ag_3Sn particles was significantly higher than Cu_6Sn_5 particles. Hence, they decided to focus their study on the coarsening of Ag_3Sn particles only. The authors introduced a new parameter named as explicit parameter '$C_{Ag}D_{Ag}t/T$', where C_{Ag} and D_{Ag} are solubility and diffusivity of Ag in Sn matrix, respectively, to capture the thermomechanical history of a lead free solder during isothermal aging. Utilizing this parameter, they predicted coarsening rate of Ag_3Sn particles, during isothermal aging, and then compared with the experimental observations. They conclude that the model could efficiently measure thermomechanical history during isothermal aging and thermomechanical cycling (TMC) below 200 cycles. After 200 cycles the IMC particles undergo dissolution and re-precipitation/redistribution which can't be captured properly by this model. In addition to coarsening, during isothermal aging, they also had observed recrystallization near the eutectic region. They explained that the growth of IMC particles might play an important role in recrystallization.

Besides bulk solder samples, researchers have also explored the effect of aging on the actual solder joints. Chauhan et al. [158] monitored the effect of isothermal aging at

100 ^{o}C on phase coarsening and evolution of SAC305 solder joint. They used image processing software to quantify size, interparticle spacing and volume fraction of Ag_3Sn and Cu_6Sn_5 IMC's. Impact of these changes on secondary creep response was modeled using multiscale creep model. The authors performed their experiments in 4 different aging conditions (0, 24, 600, and 1000 hours.) and presented average results of 3 samples (solder joint) for each aging condition. They found that the size of Ag_3Sn increases monotonically with increasing aging time whereas the size of Cu_6Sn_5 decreased after 600 hours of aging. They didn't find any significant change in Sn grain morphology after 1000 hours (41 days) of aging.

Yang et al. [159] prepared solder joints using 2 different soldering methods (laser and infrared soldering) and captured the evolution of microstructure during aging up to 190 ^{o}C for times up to 300 days. They reported that the evolution is consisted of the growth of IMC's and the Cu-Sn layer near the interface. Although they had studied two different initial microstructure, obtained from 2 different soldering methods, aging at 190 ^{o}C caused the final microstructures to be the same.

Chiu et al. [160] examined the effect of aging time and temperature on the board level reliability during the drop test of lead free SAC solder joints. They reported that kirkendall void formation, at the interface of Cu pad and Cu_3Sn IMC, is the main reason for getting lower drop reliability during drop test.

Fix et al. [79] explored the effect of aging time (0 to 1000 hours) and temperatures (125 to 175 °C) on the microstructure of SAC405 solder joint. They have confirmed a significant growth of Ag_3Sn and Cu_6Sn_5 IMCs with aging time. The authors modeled phase growth based on Ostwald ripening mechanism. They conclude that a growth exponent n =

3, which indicated volume diffusion as the growth rate controlling mechanism, matches very well with the experimental growth rate data.

The effect of aging at 150 °C on the evolution of eutectic Sn-Ag solder joint for up to 800 hours was studied by Ahat et al. [161]. From experimental results, they conclude that the thickness of IMC layer increases linearly with square root of aging time. Choi et al. [162] investigated the effect of different soldering and aging time on the interface layer of Sn-3.5Ag solder and Cu substrate. They used the same solder joint to age at 130 °C for different time duration up to 800 hours They found that thickness of IMC layer continue to grow with increasing aging duration. However, the growth behavior of IMC layer during aging strongly depends on the initial morphology and hence on the soldering time.

Akhtar et al. [163] studied the evolution of microstructure near the interface of a solder joint during isothermal aging at 150 °C, for four different aging duration (0, 250, 500, and 1000 hours). They used SAC305 solder joint (ball diameter 500 µm) with two different surface finish (Immersion Gold (ImAu) and Immersion Tin (Sn)). Image analysis software ImageJ was used to measure the thickness of the IMC layer. They also calculated the activation energy based on the measured thickness data. They found that the thickness of the IMC layer increases with increasing aging time. Besides, the morphology of the IMC layer, for both surface finishes, change from scallop type to layer type after the aging treatment. Based on their calculations they found that the activation energy of SAC305/ImSn system was less than SAC305/ImAu system resulting a higher IMC layer growth rate in SAC305/ImSn system.

A comparative study was performed by Berthou et al. [164] where the authors compared the failure mechanism of BGA packages with SAC305 solder joints subjected

to two different conditions: (a) accelerated thermal cycling (ATC) between -55 to 125 °C and (b) thermal storage at 80, 125, and 150 °C for 1000 hours. During ATC, they found recrystallization of big Sn grains to small grains in the regions of high stress accumulation. Cracks initiates and grows at interface of the new recrystallized grains. On the other hand, thermal storage for 1000 hours caused a significant growth of IMC layer near the interface as well as the IMCs in the bulk. They didn't reported any recrystallization after thermal storage.

2.9 Summary

In this chapter, the existing literature on the effects of aging on the mechanical properties and the microstructure of lead free solder was extensively discussed. The mechanical properties of a solder are strongly influenced by its microstructure, which is controlled by its thermal history including its solidification rate and thermal exposures after solidification. Aging of lead free solders leads to degradations in their constitutive and failure behaviors. For example, research in the literature has shown that aging leads to large reductions in solder material properties including shear strength, elastic modulus, nanoindentation joint modulus and hardness, high strain rate mechanical behavior, creep response, and Anand model parameters. Other studies have shown that aging causes severe degradations in uniaxial cyclic stress-strain curves and fatigue life, shear cyclic stress-strain curves and fatigue life, fracture behavior, drop reliability, and thermal cycling reliability.

Dopants have been found to strongly influence the properties and behaviors of lead free solders. For Example, Bi helps to reduce solidification temperature, increases strength

by means of precipitation hardening, helps to reduce IMC (Intermetallic Compound) layer thickness, and also reduce aging induced degradation of mechanical properties in lead free solder materials. Ni helps to improve thermal fatigue life and drop test performance by refining Sn grain size and reducing the IMC layer formation near the Cu pad. The effects of rear earth (RE) elements and nanoparticle addition on the properties of lead free solder was also discussed in this chapter.

Nanoindentation methods have shown great potential for characterizing solder materials and aging effects at the joint scale. Nanoindentation is mainly used to extract elastic modulus and hardness of solder joints. Some of the prior works have also used nanoindentation technique to characterize the creep properties although most of the nanoindentation experiments, on solder joints, were conducted at room temperature.

The changes in solder mechanical behavior are a result of the evolution of the SAC solder microstructure that occurs during aging. The most well-known and widely observed changes are coarsening of the Ag_3Sn and Cu_6Sn_5 intermetallic compounds (IMCs) present in the eutectic regions between beta-Sn dendrites. Several researchers have proposed empirical models to describe the growth of these secondary phase particles as a function of aging temperature and aging time, and related this growth to mechanical property changes.

CHAPTER 3

EXPERIMENTAL PROCEDURE

3.1 Introduction

The specimen preparation and testing techniques are presented in this chapter. Micro-scale uniaxial tensile specimens were prepared in a rectangular shaped hollow glass tube using a vacuum suction method. The test specimens were then cooled either by a water quenched profile or an industry standard reflow profile. Typical dimension of the uniaxial tensile specimens were 80 (length) X 3 (width) X 0.5 (height) mm. Uniaxial tensile tests were performed using a micro tension torsion testing system.

Solder joints were typically extracted from 14 x 14 mm PBGA assemblies (0.8 mm ball pitch, 0.46 mm ball diameter) that are part of the iNEMI Characterization of Pb-Free Alloy Alternatives Project. After extraction, a typical sample mounting and polishing procedure was followed to make the solder joints suitable for nanoindentation tests. Since the properties of SAC solder joints are highly dependent on crystal orientation, polarized light microscopy techniques was utilized to determine the orientation of the tested joints. For all the experiments, only single grain solder joints were used to avoid introducing any unintentional variation from changes in the crystal orientation across the joint cross-section.

3.2 Uniaxial Test Sample Preparation

Initially, bulk solder material is melted in a quartz crucible using circular heating elements (see Figure 3.1). The heater in the melting process is excited using a digital controller, which uses feedback from a thermocouple attached on the crucible. The solder is drawn into the glass tube by inserting one end into the molten solder in the crucible, and then applying suction to the other end using a rubber tube connected to a vacuum source. The amount of solder drawn into the tube is controlled using a regulator on the vacuum line. After the desired amount of solder fills the tube, it is solidified by quenching in a room temperature water bath.

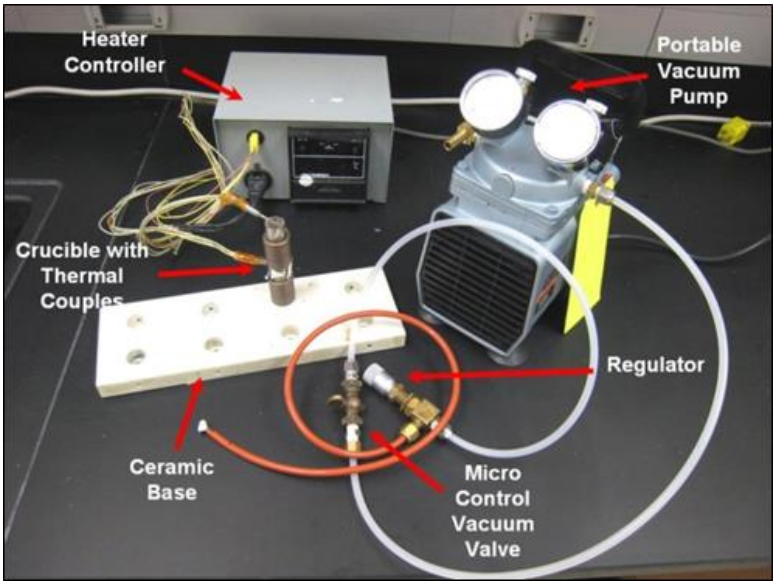

Figure 3.1 Equipment used for Specimen Preparation

Tensile specimens were prepared using two different solidification profiles.

1) Water quenched (WQ) solidification profile, leading to fine microstructures and the upper limits of the mechanical properties for each alloy.

2) Reflowed (RF) solidification profile, leading to a coarse microstructure very similar to an actual solder joints. The solder test specimens were passed through a controlled heating and cooling chamber using a SMT (surface mount technology) reflow oven.

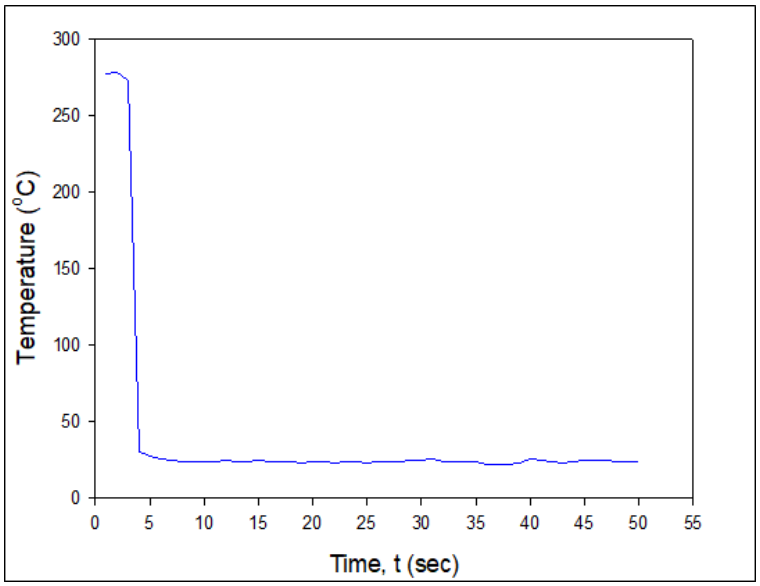

Figure 3.2 Water Quenched (WQ) Cooling Profiles

The temperature vs. time variations for the WQ profile is shown in Figure 3.2. For the samples with reflowed profile, test specimens were initially prepared using WQ profile and then the samples within the glass tubes were sent through a 9 zone Heller 1800EXL reflow oven (Figure 3.3).

Figure 3.3 Heller 1800EXL Reflow Oven

Inside the oven, solder samples were re-melted and experienced to a pre-set temperature profile which is very similar to that used for the actual solder joints. The reflow temperature profile used in this study is presented in Figure 3.4.

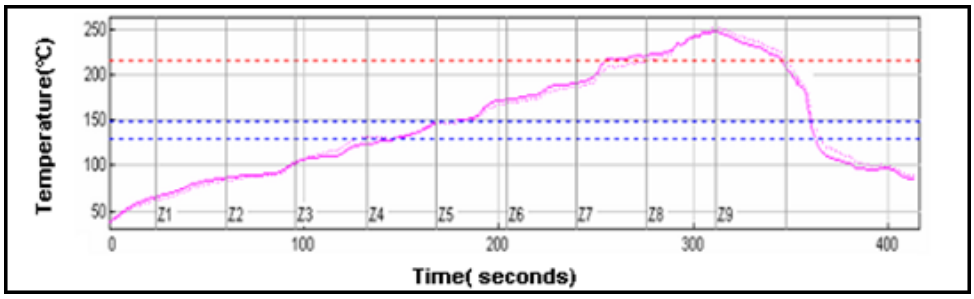

Figure 3.4 Reflow (RF) Cooling Profiles

A typical glass tubes filled with solder and final solder samples after extraction from the glass tubes are shown in Figure 3.5. Glass has lower coefficient of thermal expansion (CTE) compared to solder. As a result, for some solder alloy and cooling rate

combinations, solidified solder samples were easily pulled out from the glass tube due to the difference is the CTE of glass and solder. Another way followed to extract the solder sample from the glass tube is by carefully breaking the glass. The tubes in this work had a length of 120 mm, and a cross-sectional area of 3.0 x 0.5 mm. A thickness of 0.5 mm was chosen since it matches the height of typical BGA solder joints. The nominal dimensions of the final test samples were 80 x 3 x 0.5 mm. The specimens were stored in a low temperature freezer after the water quenched/reflow process to minimize any aging effects. The solder microstructure has been verified to be consistent throughout a specimen volume, and from specimen to specimen by cross-sectioning. A micro-focus x-ray system was used to inspect the samples for the presence of flaws (e.g. notches and external indentations) and/or internal voids (non-visible). Specimens with no flaws and voids were generated using proper experimental techniques, and Figure 3.6 illustrates x-rays scans for good and poor specimens.

(a) Within Glass Tubes

(b) After Extraction

(c) Cross-Section

Figure 3.5 Solder Uniaxial Test Specimens

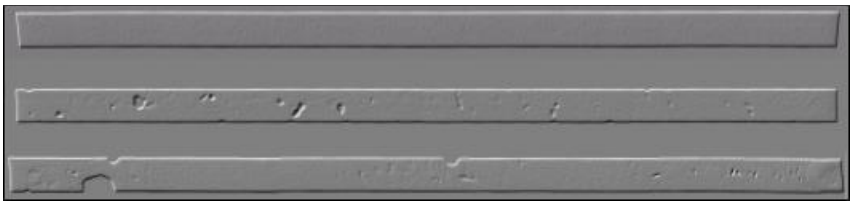

Figure 3.6 X-Ray Inspection of Solder Test Specimens (Good and Bad Samples)

3.3 Uniaxial Tensile Testing System

The tension/torsion thermo-mechanical test system (Wisdom Technology MT-200) used to perform the stress-strain tests in this study is presented in Figure 3.7. This instrument is optimized for loading small specimens such as thin films, solder joints, gold wire, fibers, etc. It provides an axial displacement resolution of 0.1 micron. Samples can be tested over a temperature range of -185 to +300 °C using supplemental environmental chambers added to the system. However, the high temperature system has been calibrated to accurately control the specimen temperature. Appendix A.1 represents the variation in set temperatures and specimen temperatures. The calibrated temperature table has also been included in Appendix A.1.

(a)

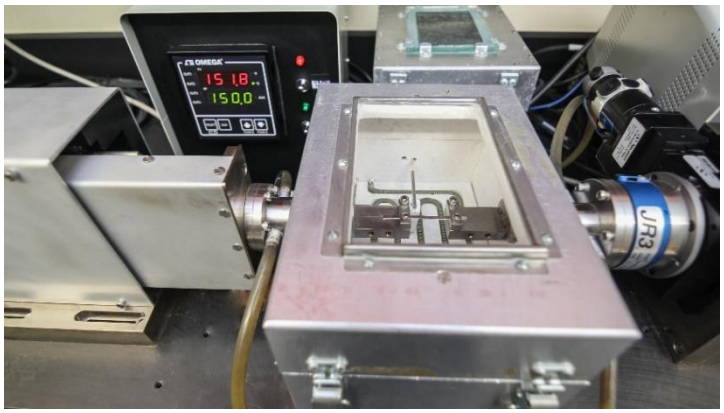

(b)

Figure 3.7 Mechanical Test System with Uniaxial Sample

Forces and displacements were measured in the uniaxial tests, and the axial stress and axial strain were calculated using

$$\sigma = \frac{F}{A} \qquad \varepsilon = \frac{\Delta L}{L} = \frac{\delta}{L} \tag{3.1}$$

where F is the measured uniaxial force, δ is the measured crosshead displacement, σ is the uniaxial stress, ε is the uniaxial strain, A is the original cross-sectional area, and L is the chosen specimen gage length (initial length between the grips). The gage length of the specimen was kept as 60 mm (thus the length to width ratio was 20 to 1).

3.4 Typical Testing Data and Data Processing

3.4.1 Typical Test Data

A typical SAC solder tensile stress strain curve is illustrated in Figure 3.8. The standard material properties are labelled on the graph including the effective elastic modulus E (initial slope of the stress-strain curve). This effective modulus is rate dependent since solder behavior is viscoplastic. The value of the effective modulus will become the true elastic modulus as the testing speed is increased to the limit of infinite

strain rate. The yield stress σ_Y (YS) is defined using the typical definition of the stress level that results in a permanent strain of $\varepsilon = .002 = 0.2\%$ upon unloading. The maximum (saturation) stress on the stress-strain curve is the ultimate tensile strength σ_u (UTS). As shown the figure, the stress-strain curve for the solder material has an elastic region at the beginning, a small transition region followed by a plastic region. As the strain becomes significantly high, localized deformation takes place which is also known as necking. Necking causes a visible reduction in cross-sectional area and a drop in the applied load, near the end of the stress strain curve, leading towards a rupture.

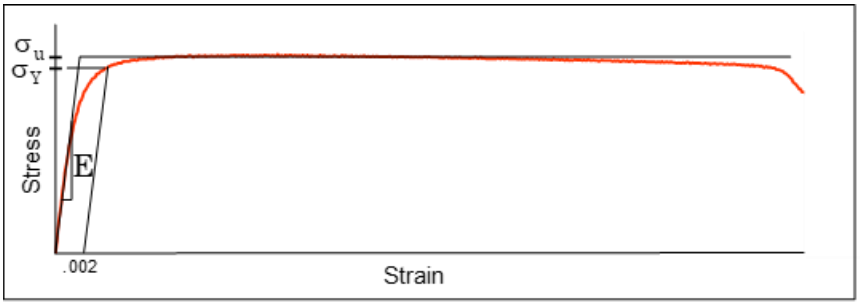

Figure 3.8 SAC Stress-Strain Curve and Material Properties

3.4.2 Stress-Strain and Creep Data Processing

Figure 3.9 illustrates a typical set of 5 solder stress strain curves measured for the same alloy under similar environmental and aging conditions. In this work, a four parameter hyperbolic tangent empirical model

$$\sigma = C_1 \tanh(C_2\varepsilon) + C_3 \tanh(C_4\varepsilon) \tag{3.2}$$

has been used to represent the "average" stress-strain curve through a set of experimental data (red curve in Figure 3.9). Material constants C_1, C_2, C_3, and C_4 are determined through

regression fitting of the model to experimental data. The effective elastic modulus E at zero strain is calculated from the model constants using

$$E = \sigma'(0) = C_1 C_2 + C_3 C_4 \tag{3.3}$$

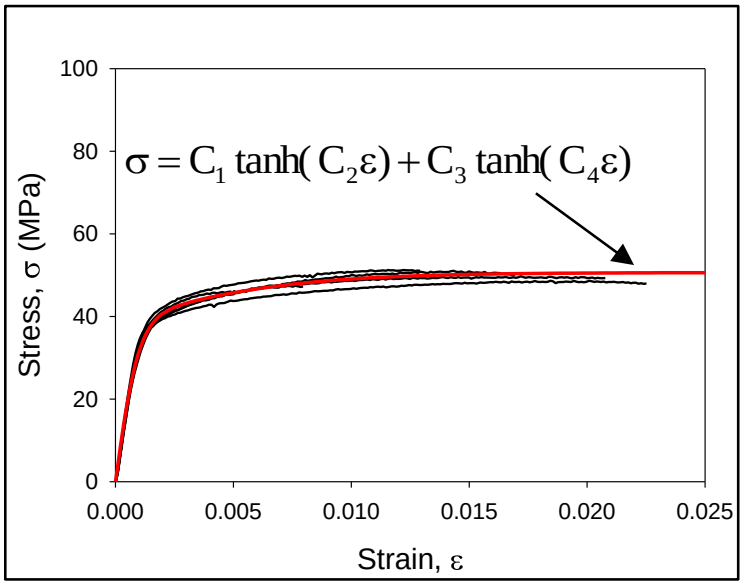

Figure 3.9 Empirical Model Fit to Solder Stress-Strain Curves

For the creep testing, 5 constant load/stress tests were performed for each leg of the test matrix. The four parameter Burger's (spring-dashpot) model given by

$$\varepsilon = C_0 + C_1 t + C_2(1 - e^{-C_3 t}) \tag{3.4}$$

was used to fit the average raw experimental data, where C_0, C_1, C_2, and C_3 are fitting constants. Constant C_1 represents the "steady state" creep strain rate.

3.5 Microstructure Study

For microstructure analysis, the fabricated solder samples were cut into small pieces and potted in epoxy. Details of the preparation process included mechanical grinding with several SiC papers (#320 to #400, #600, #800 and #1200) in a rotating metallographic disc as shown in Figure 3.10. The final polishing was conducted with 0.02 μm colloidal silica suspensions (BUEHLER MasterMet 2) and BUEHLER ChemoMet polishing cloth. This procedure resulted in mirror finish samples suitable for optical microscopy, Scanning Electron Microscopy (SEM), as well as nanoindentation. Microstructure analysis of the solder alloys was performed on the mounted and polished testing coupons by using an OLYMPUS BX60 Optical Microscope (Figure 3.11), Zeiss Polarized Light Microscope (Figure 3.12), and a JEOL JSM 7000F Field Emission SEM (Figure 3.13). In addition, EDS (Energy-Dispersive X-ray Spectroscopy) was employed to explore the chemical composition of different phases in the microstructure.

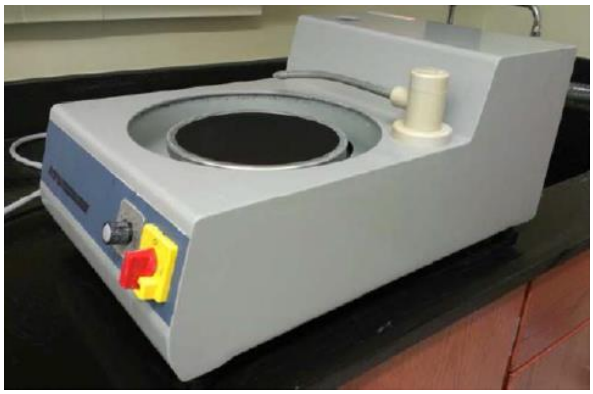

Figure 3.10 Grinding and Polishing Machine

Figure 3.11 OLYMPUS BX60 Optical Microscope

Figure 3.12 Zeiss Polarized Light Microscope

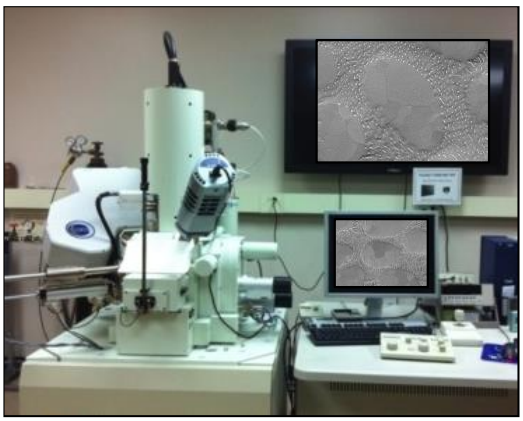

Figure 3.13 JEOL JSM-7000F Field Emission SEM

3.6 Nanoindentation Method for Creep Tests on Solder Joints

3.6.1 Sample Preparation for Nanoindentation

SAC305 (96.5Sn-3.0Ag-0.5Cu) lead free solder joints were extracted from PBGA assemblies (Amkor CABGA, 14 x 14 mm, 192 balls, 0.8 mm ball pitch, 0.46 mm ball diameter) that were assembled for the iNEMI Characterization of Pb-Free Alloy Alternatives Project (Figure 3.14). Prior to cross sectioning, the PBGA test assemblies were stored in a freezer at T = -10 °C to minimize any aging effects after board assembly. The assembled PBGA components were cut out from the test boards and then cross-sectioned using BUEHLER IsoMet 1000 Precision Cutter (Figure 3.15). The space inside the high temperature stage, attached with the nanoindentation system, is limited. The maximum allowable sample height is around 3 mm, which impose a restriction of using an epoxy mounted sample inside the high temperature stage. As a result, an alternative approach was developed to polish solder joint samples without any epoxy encapsulate. As shown in Figure 3.16, cross-sectional samples were mounted on a cylindrical epoxy preform by double-sided tape to facilitate polishing. The polished solder joint array cross-sections were then carefully extracted from the preform.

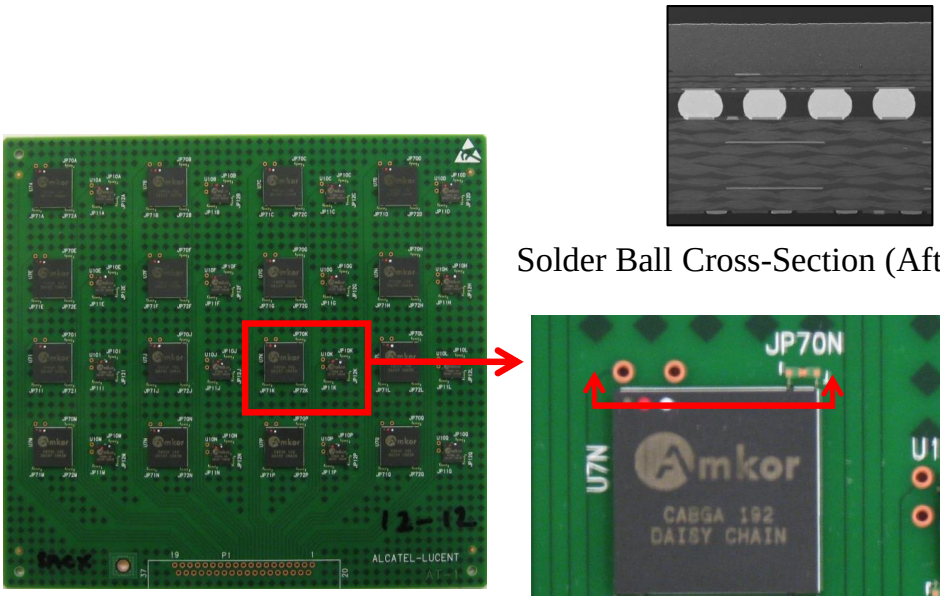

Figure 3.14 iNEMI Test Board and BGA Package

Figure 3.15 IsoMet 1000 Precision Cutter

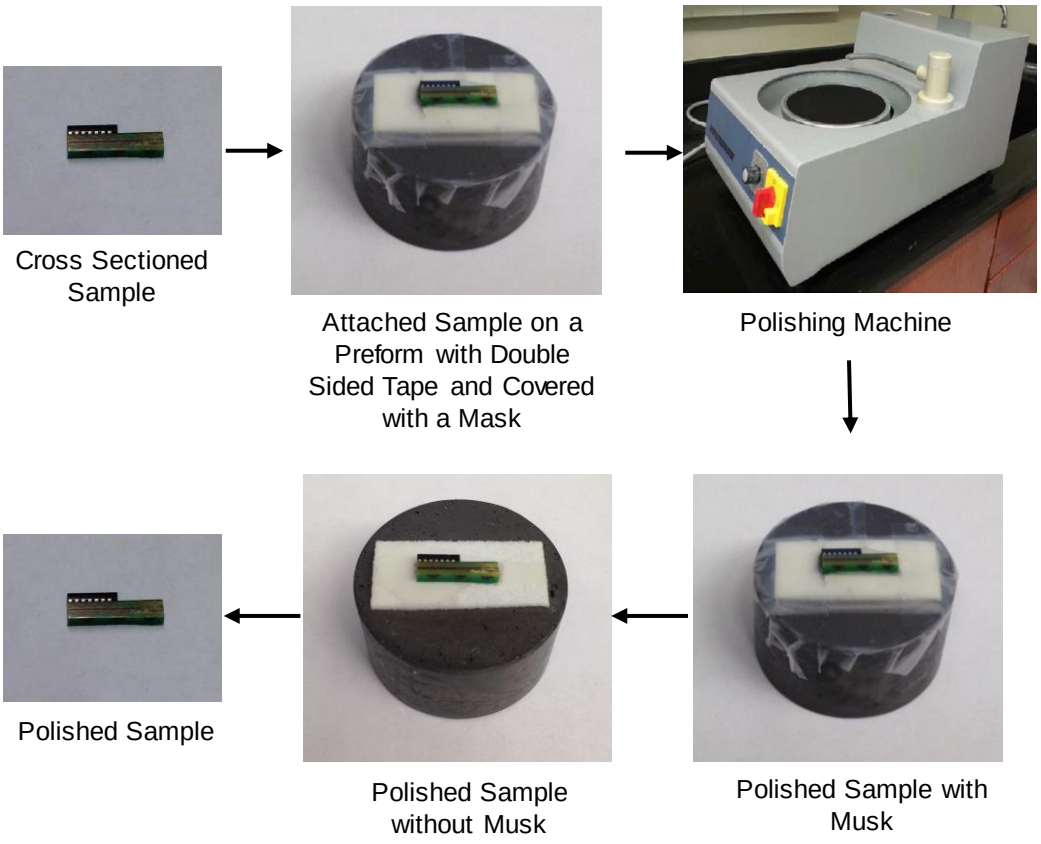

Figure 3.16 Sample Preparation Procedure for High Temperature Nanoindentation

3.6.2 Nanoindentation Machine and Test Procedures

The nanoindentation tests in this work were performed using an instrumented Hysitron TI 950 nanoindentation system (Figure 3.17) and a Berkovich indenter tip. During each indentation experiment, load versus indentation displacement response of the test samples in the direction normal to the cross-sectional surface was measured.

Figure 3.17 Hysitron TI950 TriboIndenter

Figure 3.18 shows a typical cross-sectioned SAC305 lead free solder joint sample after nanoindentation testing. A set of 10-30 indents were made, and the measured test data were averaged to obtain statistically relevant results and consistency of inspection. The indents in a set were positioned at least 3b apart, where b is the width of a single indent, to avoid interactions between the plastic zones created by the indentations. Figure 3.19 shows a typical example of loading profile used during nanoindentation, for hardness and modulus testing. The loading profile has three segments 1) loading from 0 mN to 10 mN force, 2) holding 10 mN force for a few seconds, and 3) unloading from 10 mN to 0 mN. Depending on the type of the test material, the different parameters in the loading profile was adjusted to get an accurate measurement.

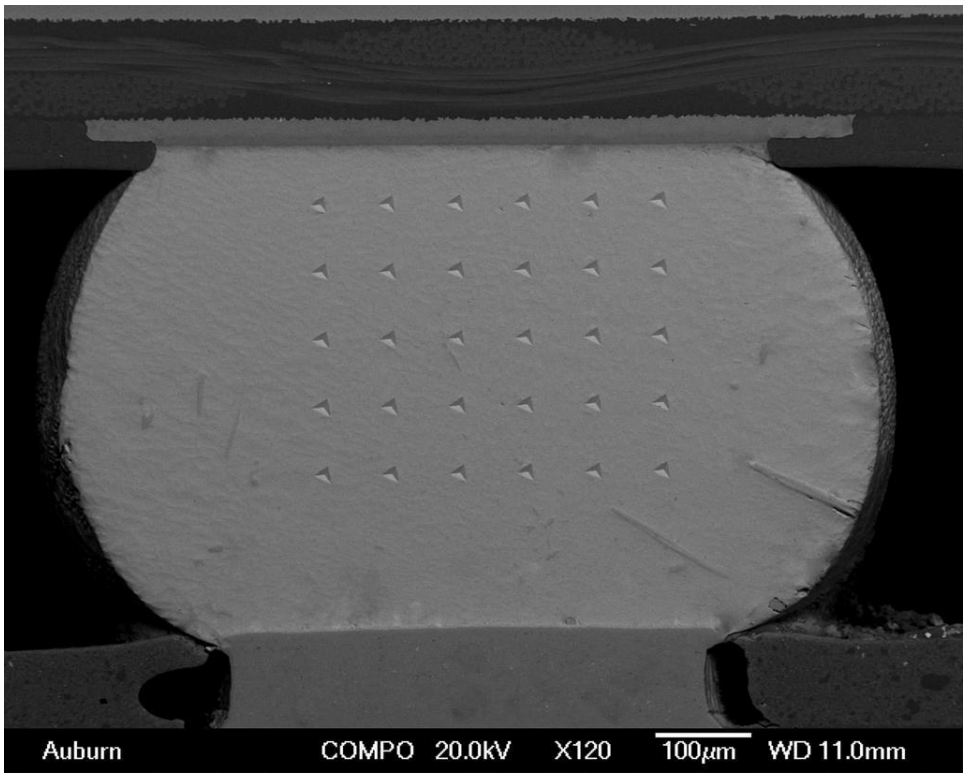

Figure 3.18 SAC305 Solder Joint after Nanoindentation Testing

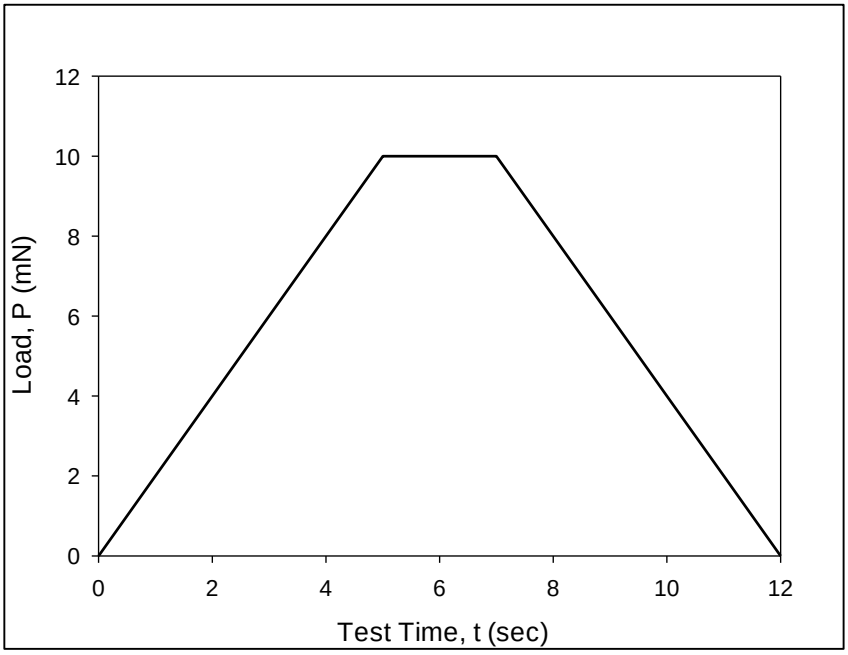

Figure 3.19 An example of the loading profile used during nanoindentation testing

3.6.3 Measurement of Elastic Modulus and Hardness

A typical load (P) versus displacement (h) curve, obtained after a nanoindentation test, is presented in Figure 3.20. This curve has three different segments where the first, second, and third segments represent the displacements during the loading, holding and unloading period, respectively.

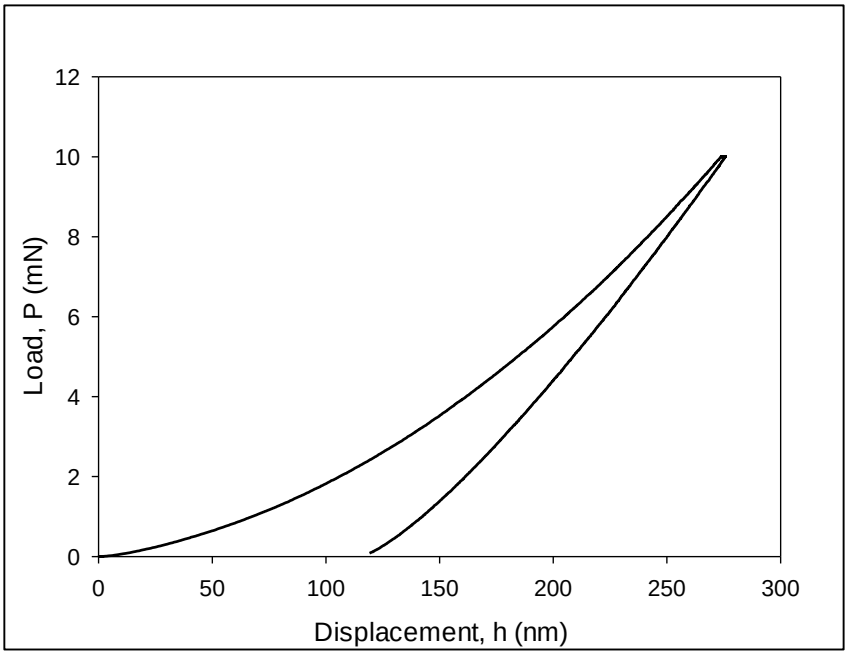

Figure 3.20 An example of load-displacement curve obtained after nanoindentation Test

During a nanoindentation experiment, the effects of the non-rigidity of an indenter, during a nanoindentation experiment, can be addressed by introducing a term called reduced modulus (E_r) through the following equation:

$$\frac{1}{E_r} = \frac{(1-\nu^2)}{E} + \frac{(1-\nu_i^{\,2})}{E_i} \tag{3.5}$$

where E is the elastic modulus of the test specimen, E_i is the known elastic modulus of the indenter tip material, ν and ν_i are the Poisson's ratio of the test specimen and the

indenter tip, respectively. Typically reduced modulus was measured from an indentation experiment using the following equation

$$E_r = \frac{\sqrt{\Pi}}{2} \times \frac{S}{\sqrt{A}} \tag{3.6}$$

where S is the stiffness of the test specimen at the maximum load and A is the projected contact area at the maximum load. Stiffness was determined from the initial slope $(\frac{dP}{dh})$ of the unloading segment of a load displacement curve. The contact area A was measured following the technique proposed by Oliver and Pharr [165] where they assumed the contact area to be a function of contact depth. For an ideal Berkovich tip, it can be expressed as

$$A(h_c) = 24.5h_c^2 \tag{3.7}$$

In order to address any deviation from the ideal Berkovich geometry due to tip blunting, a modified version of Equation 3.7 was utilized.

$$A(h_c) = 24.5h_c^2 + C_1h_c^1 + C_2h_c^{1/2} + C_3h_c^{1/4} + C_4h_c^{1/8} + C_5h_c^{1/16} \tag{3.8}$$

where C_1, C_2, C_3, C_4, and C_5 are fitting constants. In order to determine the values of these constants, multiple indents were made at multiple depths on a quartz sample with known elastic modulus (69.6 GPa). The contact areas at the different known depths were determined from Equation 3.7 and these values were plotted to get a A versus h_c plot. The values of constants C_1 to C_5 were determined by fitting the plot by Equation 3.8. Once the values of the constants are known for a particular tip geometry, Equation 3.6 was used to determine the value of reduced modulus (E_r) for any unknown material and Equation 3.5 was used to convert E_r to elastic modulus E.

Hardness is a material property that defines the resistance of the surface against plastic deformation. During a nanoindentation experiment, hardness H was determined by dividing the maximum load by the projected contact area.

$$H = \frac{P_{max}}{A} \tag{3.9}$$

Tabor [166] developed an approximate relationship between hardness and yield stress of which is true for many metals.

$$H \approx 3\sigma_Y \qquad \text{or} \qquad \sigma_Y \approx \frac{H}{3} \tag{3.10}$$

The above equation was used to determine stress during nanoindentation experiments.

3.7 Summary and Discussion

All the experimental procedures and the data processing steps were presented in this chapter. Micro-scale uniaxial tensile specimens were prepared in a rectangular shaped hollow glass tube using a vacuum suction method. Typical dimension of the uniaxial tensile specimens were 80 (length) × 3 (width) × 0.5 (height) mm. Uniaxial tensile tests were performed using a micro tension torsion testing system. Nanoindentation experiments were conducted on actual solder joints which were typically extracted from 14 x 14 mm PBGA assemblies (0.8 mm ball pitch, 0.46 mm ball diameter). Nanoindentation experiments were performed using Hysitron TI950 TriboIndenter.

CHAPTER 4

HIGH TEMPERATURE MECHANICAL BEHAVIOR OF SAC AND SAC+X LEAD FREE SOLDERS

4.1 Introduction

Solder joint reliability in harsh environment applications are big concerns in the electronic packaging industry. The reliabilities of electronic packages used in various products depend on the environmental conditions experienced during field use. Consumer electronics are typically designed using maximum operating temperatures of 100 °C or less. However, there are several important harsh environment uses of electronic packaging, where electronics can be exposed to temperatures up to 200 °C. This leads to reduced values of the solder mechanical properties due to the normal temperature dependencies exhibited by metals. It is important to make accurate predictions of solder joint reliability at extreme high Temperatures.

In this chapter, several SAC and SAC+X lead free solder alloys, recommended for high reliability applications have been chemically analyzed and then mechanically tested in order to determine the temperature dependent mechanical properties of these alloys. The alloys include SAC305, Ecolloy (SAC_R), Cyclomax (SAC_Q), and Innolot. The mechanical behavior of these alloys have been explored at several extreme high temperatures from 125 to 200 °C. For each of 4 elevated temperatures (T = 125, 150, 175, and 200 °C), tensile stress-strain tests were performed at three strain rates (SR = 0.001,

0.0001, and 0.00001 sec^{-1}). For each alloy and testing temperature, the stress-strain curve shape and high temperature tensile properties (initial modulus, yield stress, and ultimate tensile strength) of the solder alloys were measured and compared. Test specimens were initially solidified with both water quenched (WQ) and reflowed (RF) cooling profiles.

4.2 Chemical Composition of the Solder Alloys

Chemical compositions of the SAC305 and doped solder alloys (SAC+X) are presented in Table 4.1. SAC305 is consisted of tin, silver and copper with 96.5 %, 3.41% and 3.80%, respectively. Innolot is an engineering alloy with 6-element target composition having additional bismuth, nickel, and antimony. The compositions of SAC_R (also known as Ecolloy) and SAC_Q (also known as Cyclomax) are unpublished. Energy Dispersive X-Ray Spectroscopy (EDX) was used to explore the compositions of these doped alloys. All three alloys were found to employ Bismuth (Bi) as the primary X-additive. SAC_R alloy does not have any measureable silver (Ag) content, contrary to all other SAC alloys. This is most likely the reason it is marketed as a low cost (economy) material. The silver contents of SAC_Q and Innolot are similar to SAC305, with 3.41% and 3.80%, respectively. Nickel (0.15%) and antimony (1.4%) are present in Innolot.

Table 4.1 Chemical Compositions of the Solder Alloys

Alloy	Sn	Ag	Cu	Bi	Ni	Sb
SAC 305	96.50	4.00	0.50	0.00	0.00	0.00
SAC_R	96.62	0.00	0.92	2.46	0.00	0.00
SAC_Q	92.77	3.41	0.52	3.30	0.00	0.00
Innolot	90.95	3.80	0.70	3.00	0.15	1.40

4.3 Stress-Strain Data for Various Temperature and Strain Rates

The measured high temperature stress-strain curves for SAC305, SAC_R, SAC_Q, and Innolot alloys are shown in Figures 4.1-4.5. For each alloy, results are given for three strain rates of 0.001, 0.0001, and 0.00001 sec-1. Each colored curve is the "average" experimental stress-strain curve for a particular strain rate and temperature. They were determined by performing nonlinear regression fits of the empirical model in Equation 3.2 (chapter 3) to the experimental data (ten recorded stress-strain curves for each alloy and set of conditions). The colors of the curves represent the testing temperature with blue = 125 °C, green = 150 °C, orange = 175 °C, and red = 200 °C. Again, in each plot, the top curve represents the average stress-strain curve at 125 °C, and the bottom curve is the average stress-strain curve at 200 °C For each alloy, the initial elastic modulus, yield stress, and UTS decrease with increasing temperature. In addition, they also decrease with decreasing strain rate.

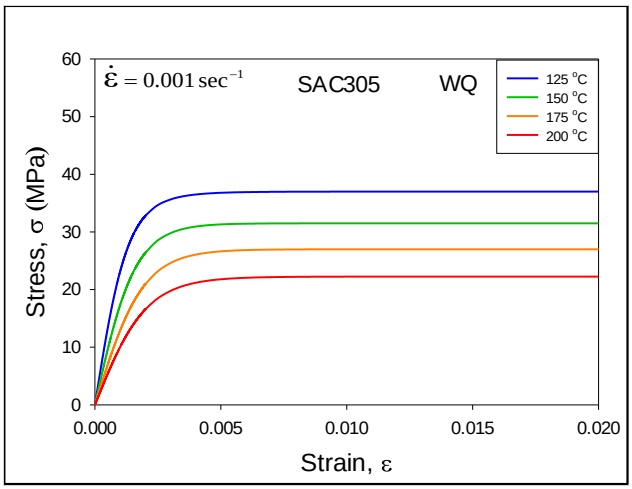

(a)

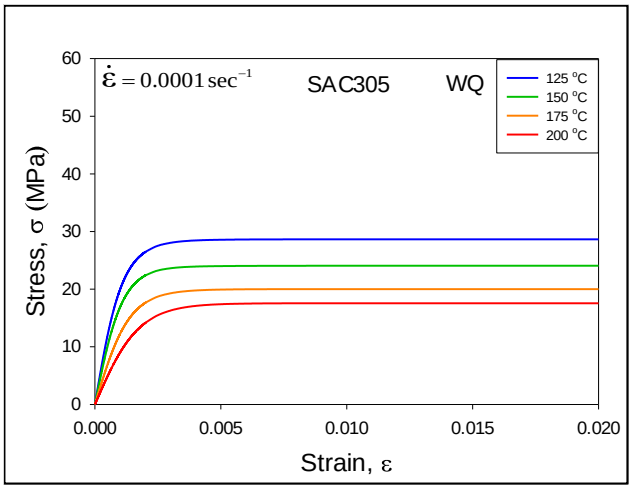

(b)

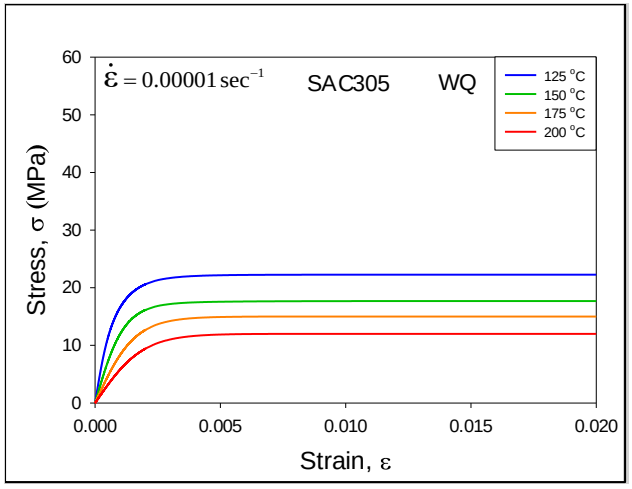

(c)

Figure 4.1 Stress-Strain Curves for SAC305 (WQ)

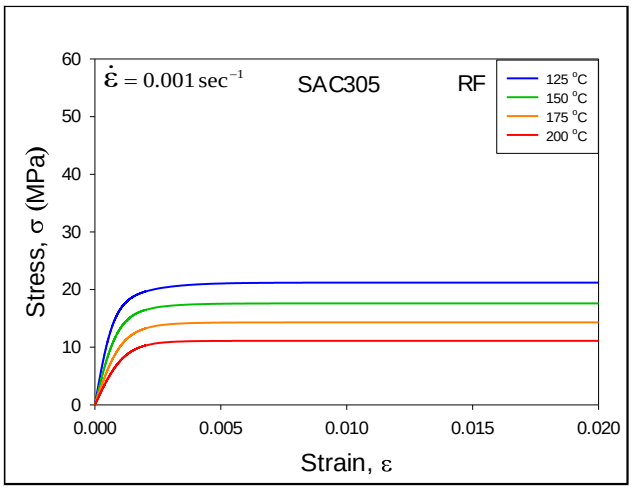

(a)

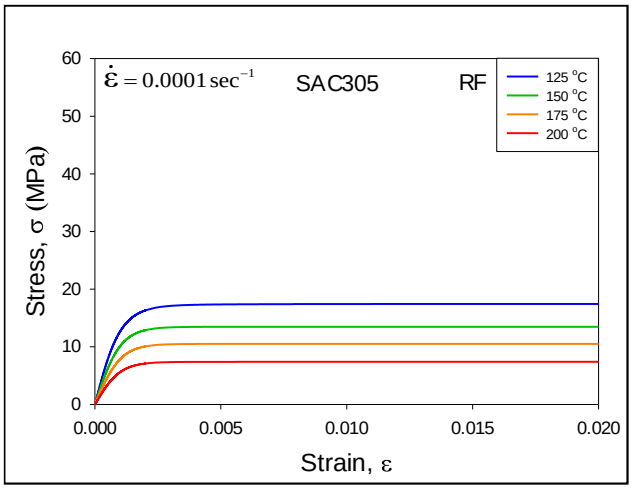

(b)

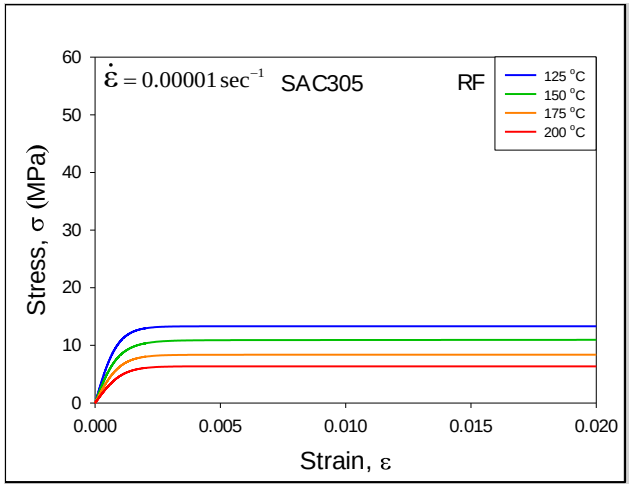

(c)

Figure 4.2 Stress-Strain Curves for SAC305 (RF)

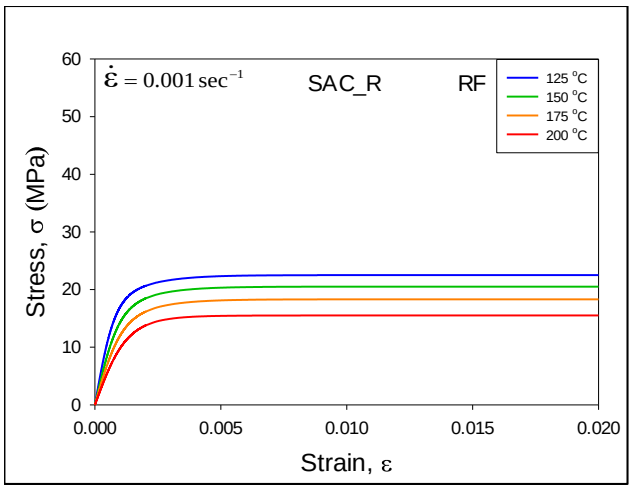

(a)

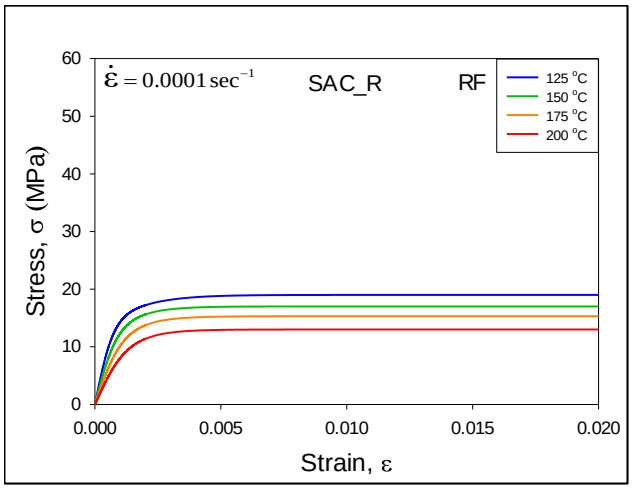

(b)

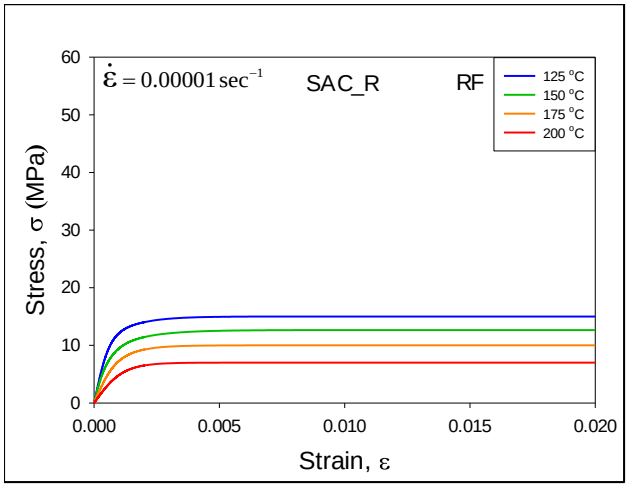

(c)

Figure 4.3 Stress-Strain Curves for SAC_R (RF)

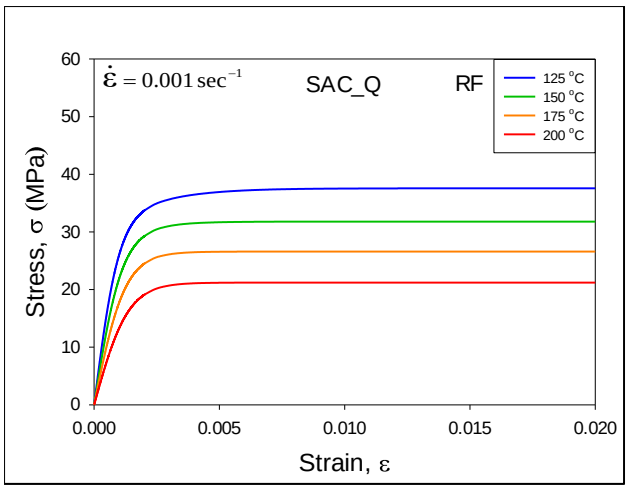

(a)

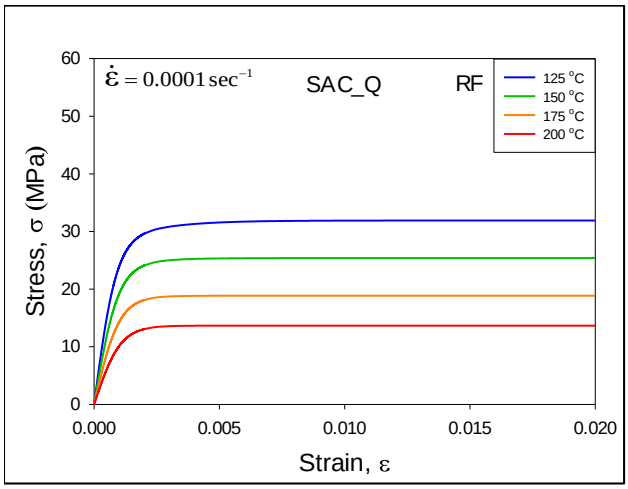

(b)

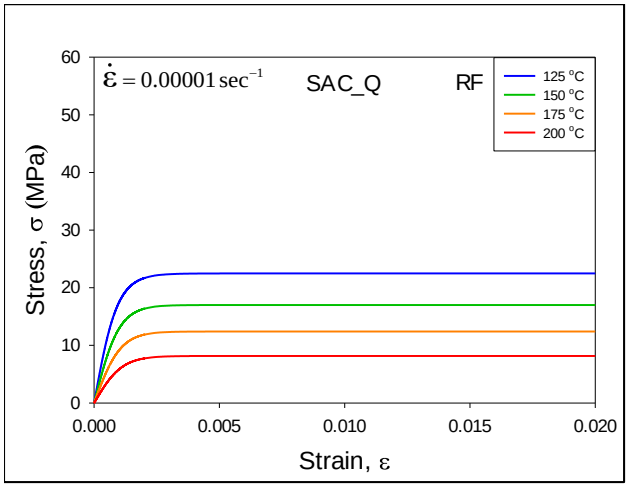

(c)

Figure 4.4 Stress-Strain Curves for SAC_Q (RF)

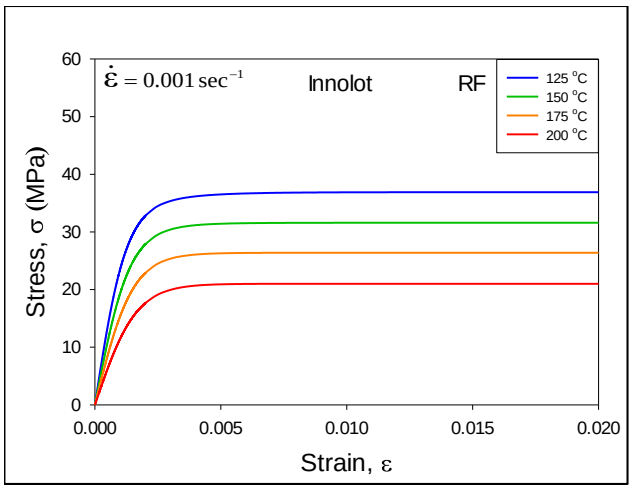

(a)

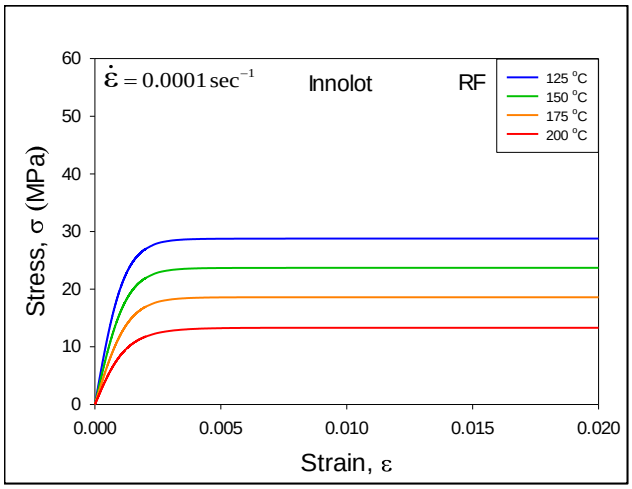

(b)

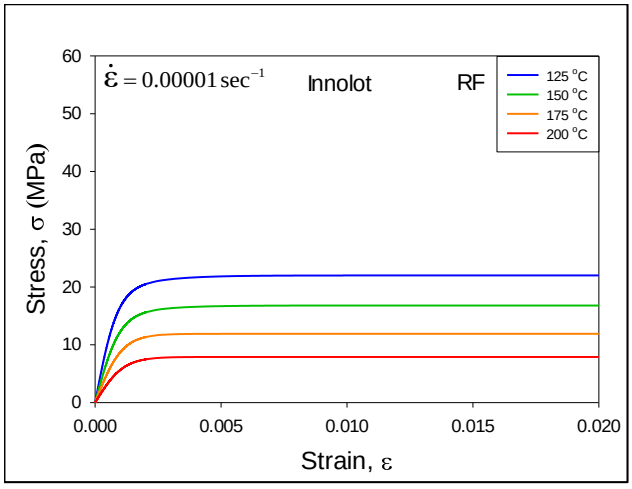

(c)

Figure 4.5 Stress-Strain Curves for SAC_Q (RF)

4.4 Comparison of Mechanical Behavior of Solder Alloys at Various Temperature and Strain Rates

Comparisons of the uniaxial tensile test results for the four solder alloys at different test temperature and strain rate are shown in Figures 4.6-4.8. Figure 4.6 represents comparison at 0.001 sec^{-1} strain rate. Figures 4.7 and 4.8 correspond to the comparison of similar results obtained at 0.0001 and 0.00001 sec^{-1} strain rate respectively. In each plot, different color curve represents different alloy with blue = SAC_Q, green = Innolot, orange = SAC_R and red = SAC305. It can be easily seen that both the SAC_Q and Innolot alloys strongly outperform SAC305 and SAC_R at all strain rates at a particular temperature, with much higher ultimate tensile strength (UTS) and superior initial elastic modulus. The stress-strain curves for SAC_Q and Innolot are very similar at each strain rate, but SAC_Q exhibits slightly higher mechanical properties. The strength of SAC_R is slightly higher than SAC305, even though SAC_R does not contain any Ag. Similar results were found for all testing temperatures.

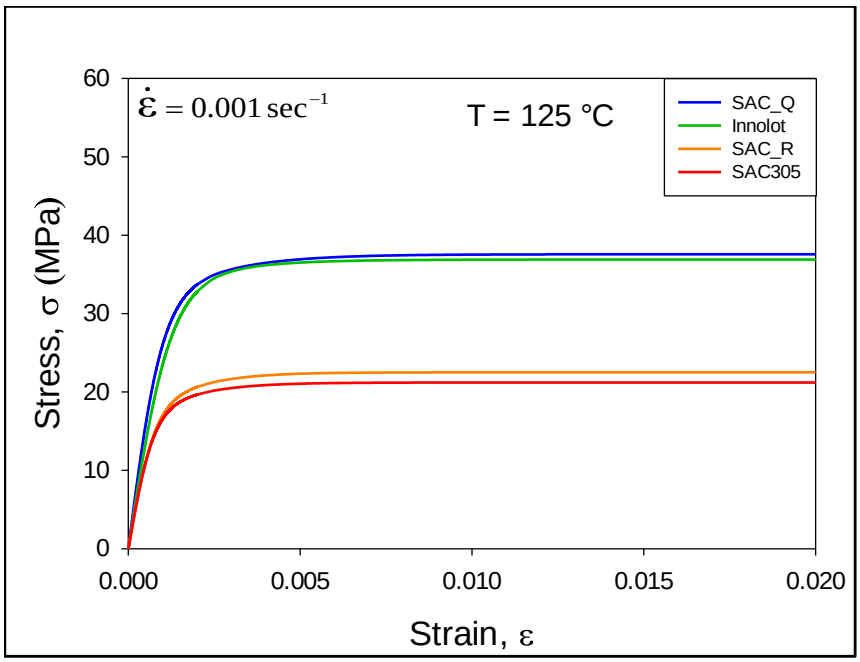
$\dot{\varepsilon} = 0.001\,\mathrm{sec}^{-1}$
T = 125 °C
SAC_Q
Innolot
SAC_R
SAC305
Stress, σ (MPa)
Strain, ε
0
10
20
30
40
50
60
0.000
0.005
0.010
0.015
0.020

(a)

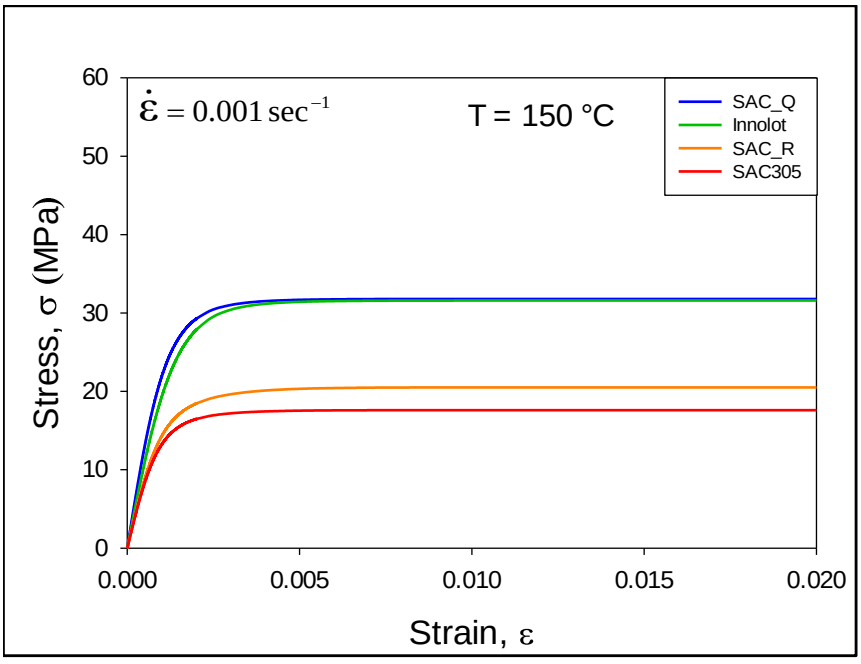
$\dot{\varepsilon} = 0.001\,\mathrm{sec}^{-1}$
T = 150 °C
SAC_Q
Innolot
SAC_R
SAC305
Stress, σ (MPa)
Strain, ε
0
10
20
30
40
50
60
0.000
0.005
0.010
0.015
0.020

(b)

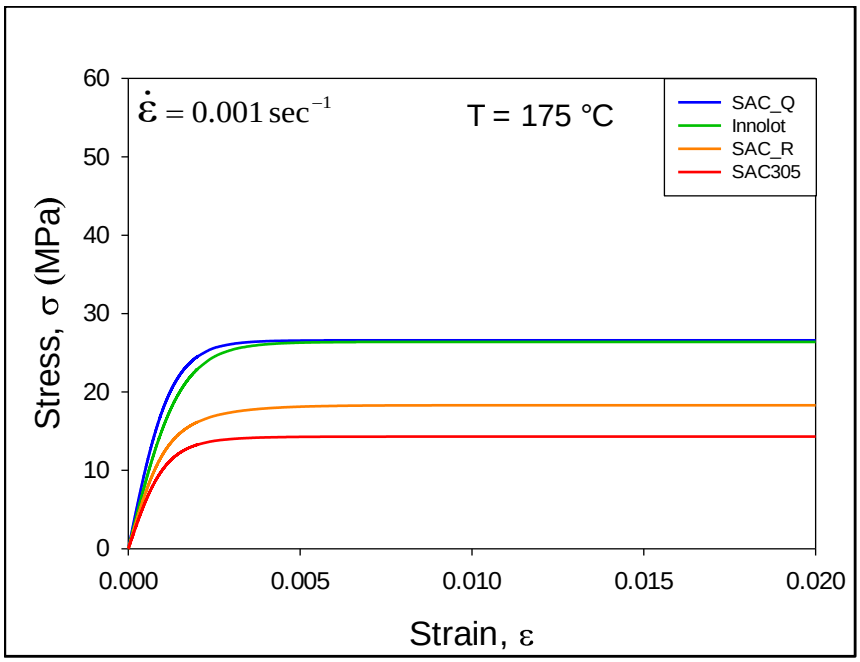

(c)

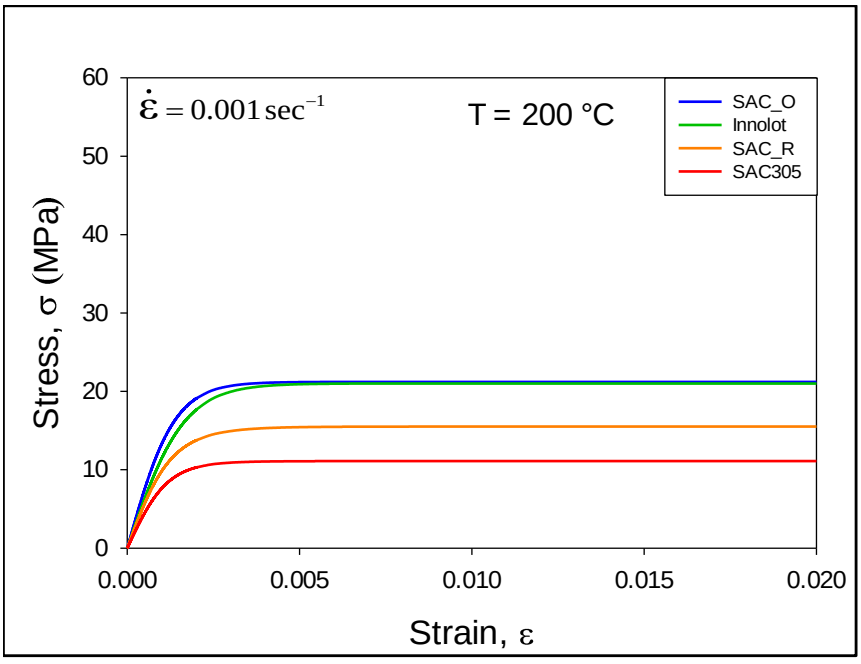

(d)

Figure 4.6 Comparison of Average Stress-Strain Curves ($\dot{\varepsilon}$ = 0.001 sec^{-1})

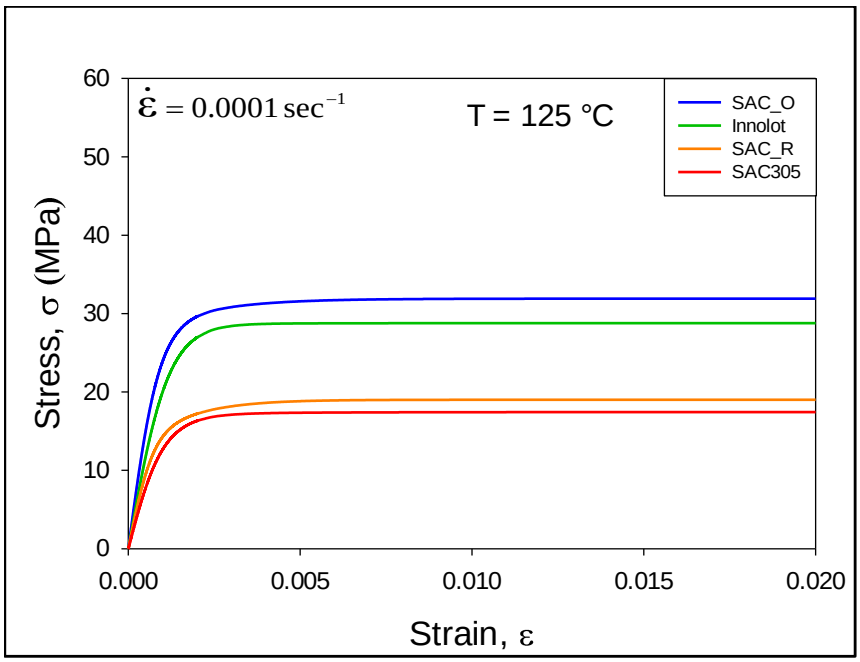
$\dot{\varepsilon} = 0.0001\,\mathrm{sec}^{-1}$
T = 125 °C
SAC_O
Innolot
SAC_R
SAC305
Stress, σ (MPa)
Strain, ε
0
10
20
30
40
50
60
0.000
0.005
0.010
0.015
0.020

(a)

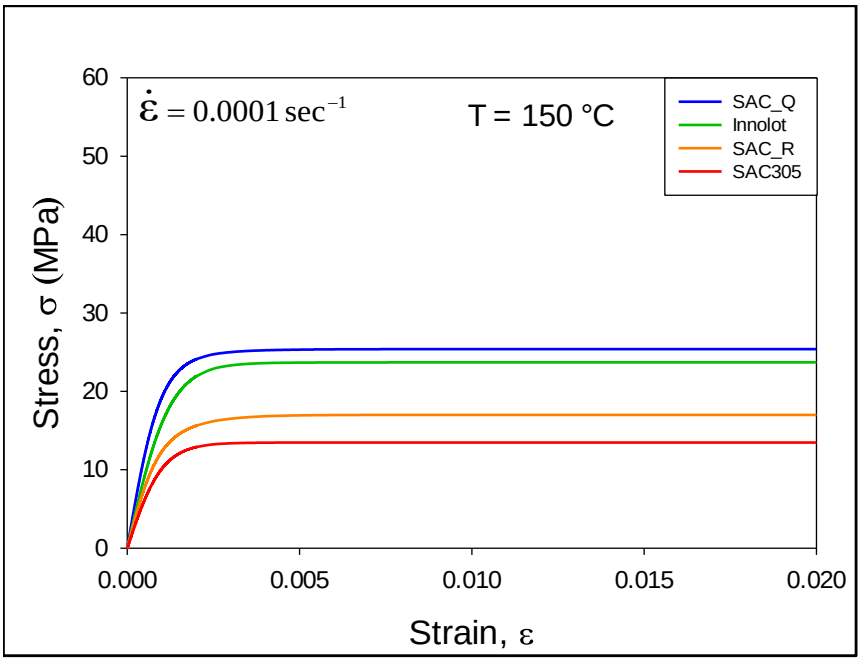
$\dot{\varepsilon} = 0.0001\,\mathrm{sec}^{-1}$
T = 150 °C
SAC_Q
Innolot
SAC_R
SAC305
Stress, σ (MPa)
Strain, ε
0
10
20
30
40
50
60
0.000
0.005
0.010
0.015
0.020

(b)

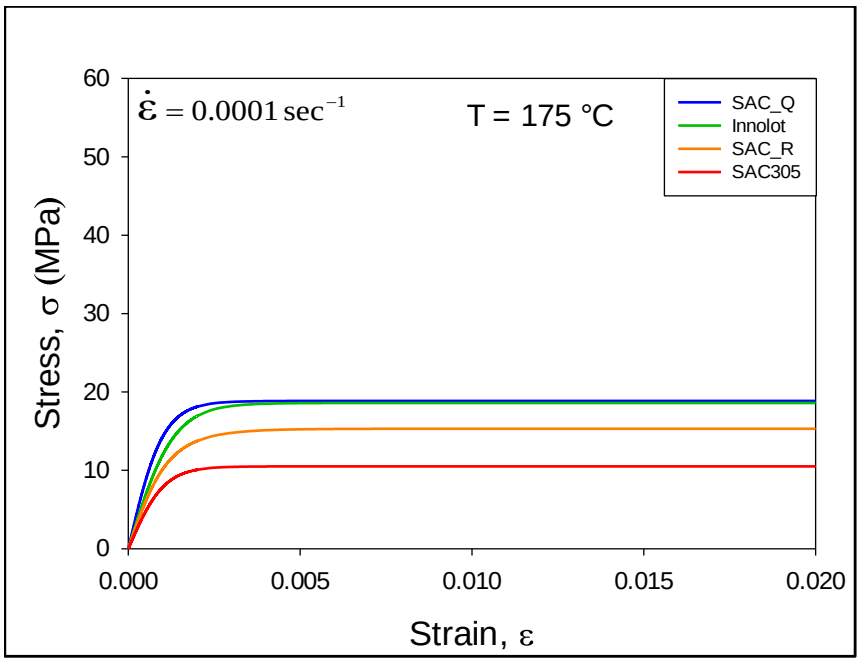

(c)

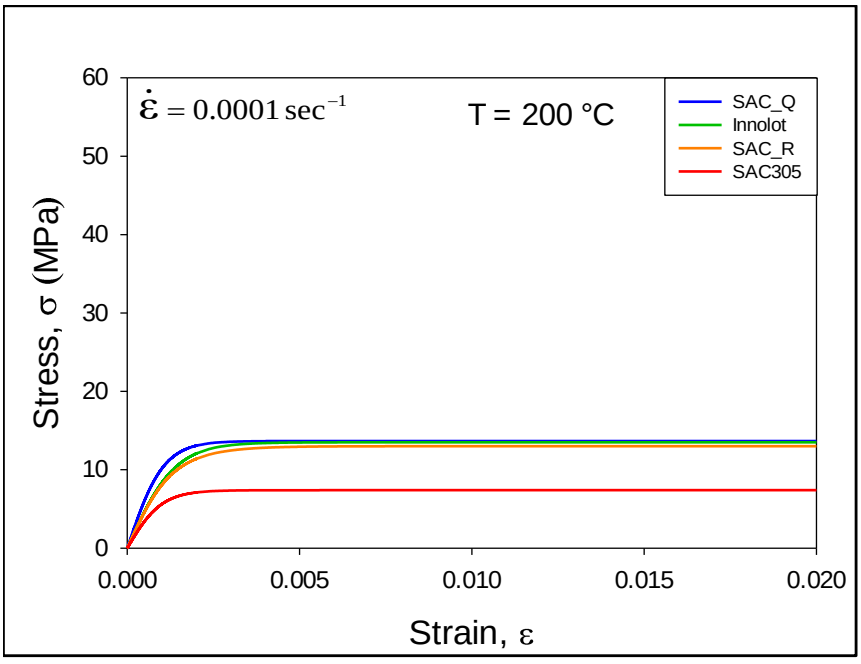

(d)

Figure 4.7 Comparison of Average Stress-Strain Curves ($\dot{\varepsilon}$ = 0.0001 sec^{-1})

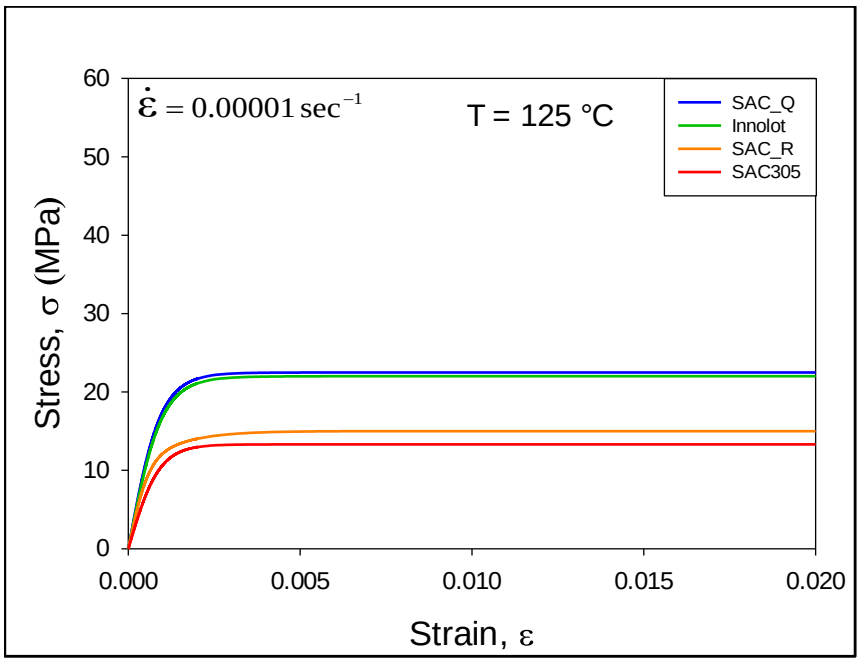
$\dot{\varepsilon} = 0.00001\,\mathrm{sec}^{-1}$
T = 125 °C
SAC_Q
Innolot
SAC_R
SAC305
Stress, σ (MPa)
Strain, ε
0
10
20
30
40
50
60
0.000
0.005
0.010
0.015
0.020

(a)

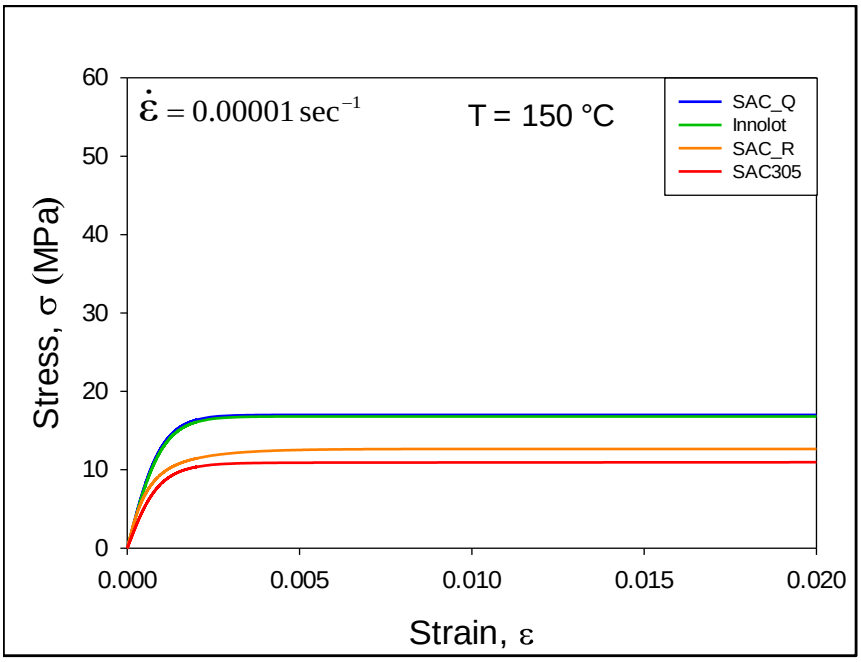
$\dot{\varepsilon} = 0.00001\,\mathrm{sec}^{-1}$
T = 150 °C
SAC_Q
Innolot
SAC_R
SAC305
Stress, σ (MPa)
Strain, ε
0
10
20
30
40
50
60
0.000
0.005
0.010
0.015
0.020

(b)

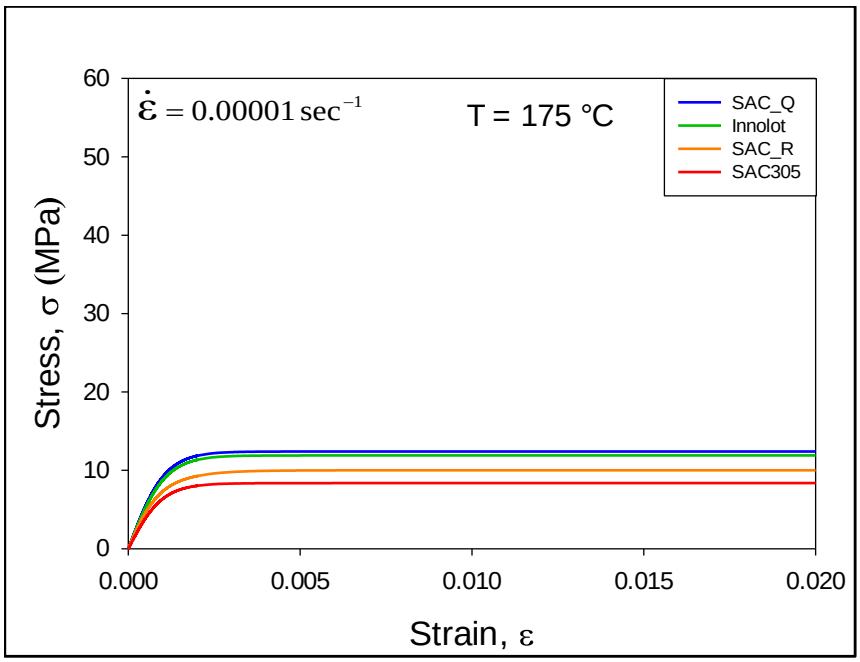

(c)

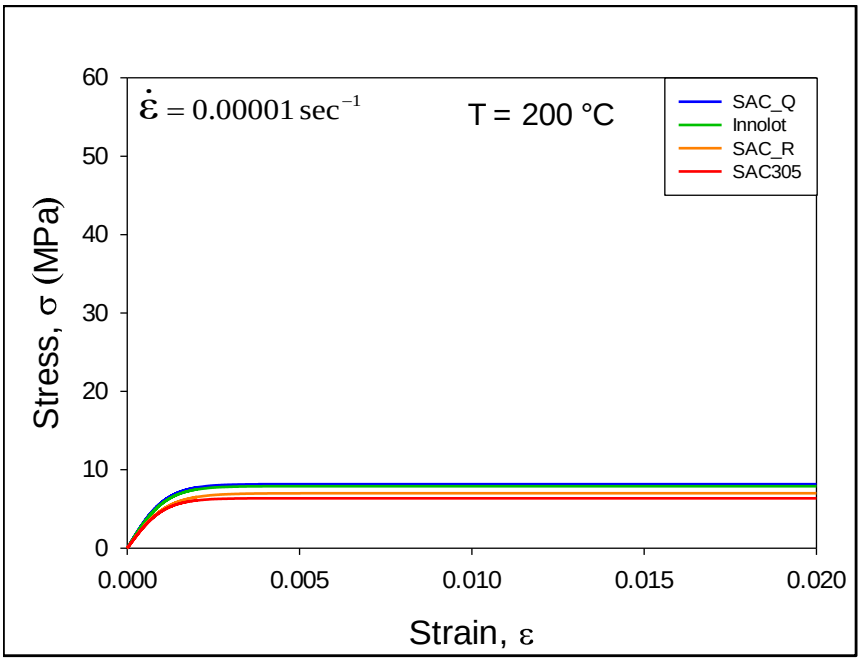

(d)

Figure 4.8 Comparison of Average Stress-Strain Curves ($\dot{\varepsilon}$ = 0.00001 sec^{-1})

4.5 Mechanical Properties

The mechanical properties of the three alloys have been extracted from the measured stress-strain data and tabulated in Tables 4.2-4.4. These properties, such as, initial effective elastic modulus, ultimate tensile strength, and yield stress have been plotted in Figures 4.9-4.11 as a function of temperature at each of the three strain rates. In each plot, different color curve represents different alloy with blue = SAC_Q, green = Innolot, orange = SAC_R and red = SAC305. Large reductions in the properties were observed to occur between T = 125 °C and T = 200 °C. For example, ultimate tensile strength dropped 40-50% for each alloy and strain rate. Linear variations in the properties with temperature were observed. By comparing the analogous results for the same temperature and alloy, but different strain rates, it has also been observed that as the strain rate decreases, the effective elastic modulus, ultimate tensile strength, and yield stress also decrease.

Table 4.2 Comparison of Effective Modulus

Alloy	Strain Rate (sec^{-1})	Effective Modulus, E (GPa)			
		125 (°C)	150 (°C)	175 (°C)	200 (°C)
SAC_Q	0.001	34.0	27.5	21.5	15.6
	0.0001	32.8	25.7	18.8	13.1
	0.00001	23.9	17.4	12.2	7.7
Innolot	0.001	28.4	22.7	17.6	12.9
	0.0001	24.8	19.3	14.3	9.7
	0.00001	22.6	16.5	11.0	6.8
SAC_R	0.001	26.2	20.9	16.6	12.2
	0.0001	23.6	19.0	13.8	8.6
	0.00001	20.5	16.2	10.2	6.1
SAC305	0.001	25.1	18.4	13.0	7.6
	0.0001	15.7	13.3	10.1	7.4
	0.00001	14.9	11.6	8.5	4.6

Table 4.3 Comparison of Ultimate Tensile Strength (UTS)

Alloy	Strain Rate (sec^{-1})	Ultimate Tensile Strength, UTS (MPa)			
		125 (°C)	150 (°C)	175 (°C)	200 (°C)
SAC_Q	0.001	37.6	31.7	26.5	21.2
	0.0001	31.7	25.4	18.9	13.7
	0.00001	22.6	17.0	12.4	8.2
Innolot	0.001	36.9	31.6	26.4	21.0
	0.0001	29.8	24.4	18.5	13.3
	0.00001	22.0	16.8	11.9	7.9
SAC_R	0.001	22.4	20.2	17.2	14.5
	0.0001	18.6	16.7	15.5	12.9
	0.00001	15.7	13.1	10.0	7.5
SAC305	0.001	21.2	17.9	14.3	10.9
	0.0001	16.5	13.2	10.7	7.5
	0.00001	14.5	10.9	8.4	6.4

Table 4.4 Comparison of Yield Stress (YS)

Alloy	Strain Rate (sec^{-1})	Yield Stress, YS (MPa)			
		125 (°C)	150 (°C)	175 (°C)	200 (°C)
SAC_Q	0.001	36.0	30.5	25.5	19.7
	0.0001	30.5	23.9	17.2	11.9
	0.00001	21.0	15.9	11.1	7.2
Innolot	0.001	34.8	29.7	24.5	19.2
	0.0001	29.5	23.0	16.2	11.2
	0.00001	20.0	14.8	10.5	6.5
SAC_R	0.001	21.5	18.9	15.8	13.0
	0.0001	17.5	15.2	14.0	11.7
	0.00001	14.2	11.7	8.9	6.3
SAC305	0.001	19.7	16.0	12.2	8.5
	0.0001	16.0	13.4	10.2	7.4
	0.00001	13.3	10.8	8.3	5.2

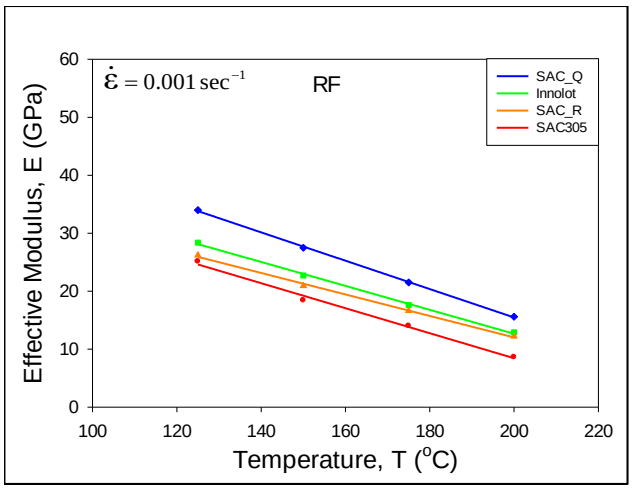

(a)

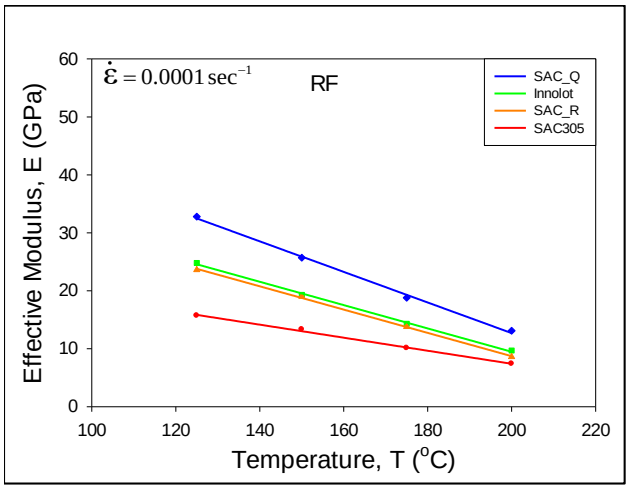

(b)

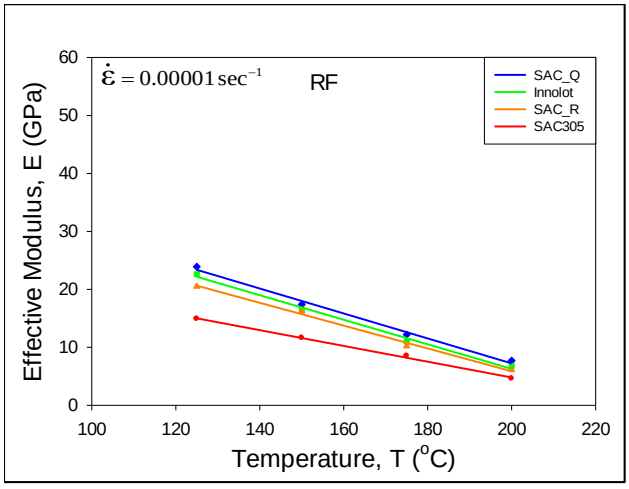

(c)

Figure 4.9 Comparison of Effective Modulus

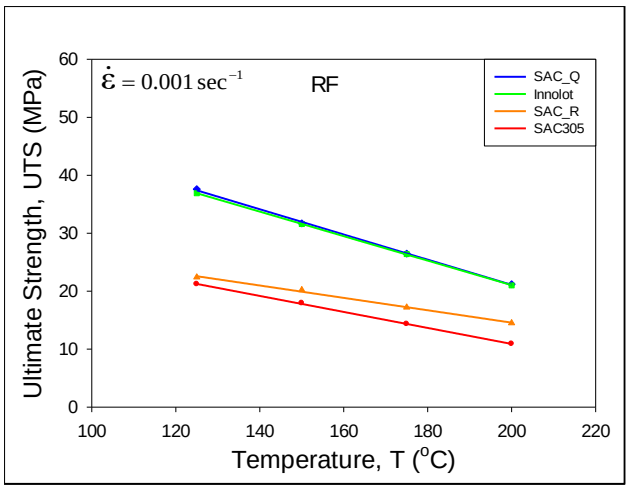

(a)

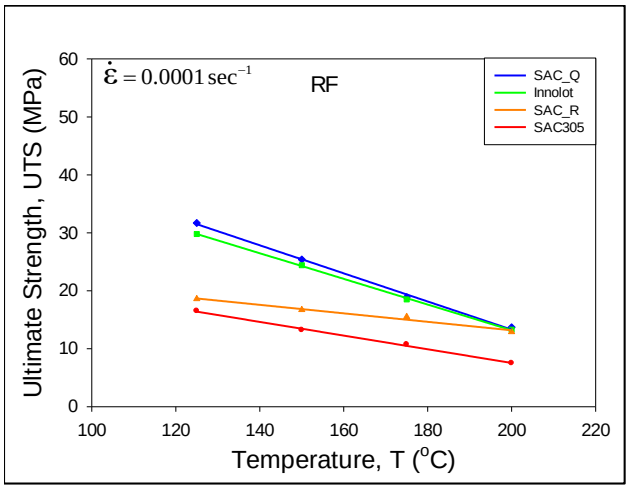

(b)

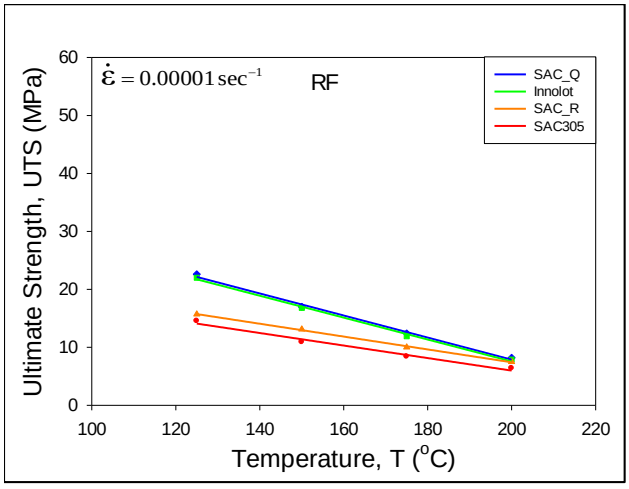

(c)

Figure 4.10 Comparison of Ultimate Tensile Strength (UTS)

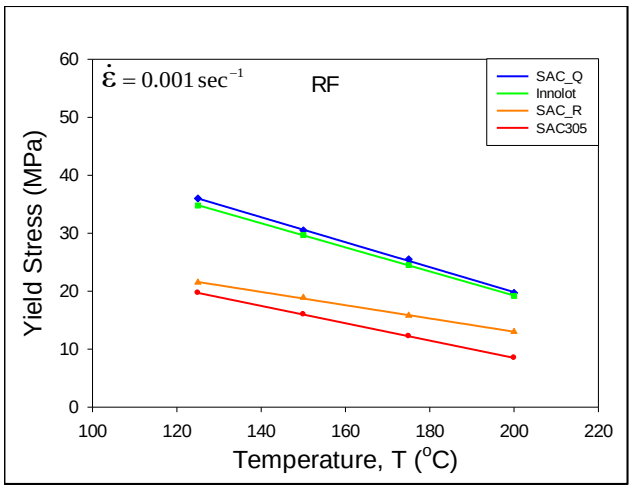

(a)

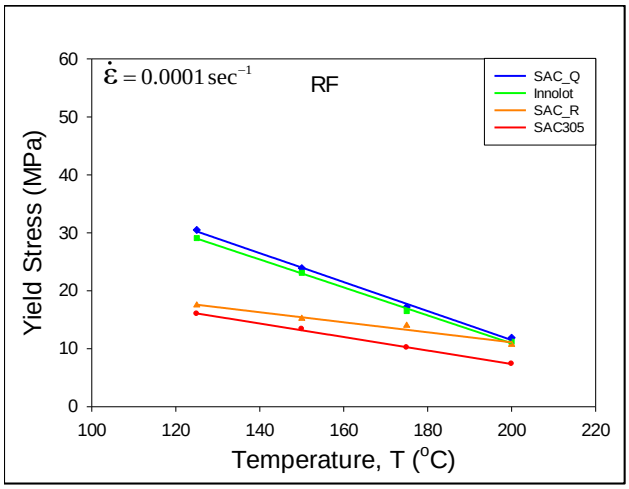

(b)

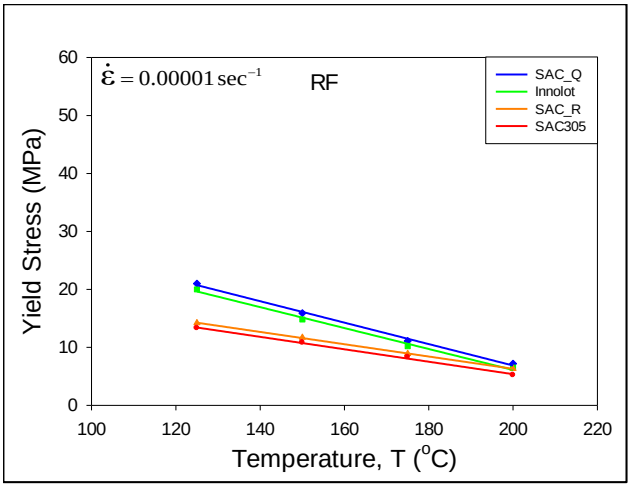

(c)

Figure 4.11 Comparison of Yield Stress (YS)

4.6 Discussion

In this work, the mechanical behavior of several SAC and SAC+X lead free solder alloys at extreme high temperatures up to 200 °C has been investigated. The studied alloys included SAC305 (96.5Sn-3.0Ag-0.5Cu), SAC_R (96.6Sn-0.9Cu-2.5Bi), SAC_Q (92.8Sn-3.4Ag-0.5Cu-3.3Bi), and Innolot (90.95Sn-3.8Ag-0.7Cu-3.0Bi-0.15Ni-1.4Sb). The solder uniaxial test specimens were formed in high precision rectangular cross-section glass tubes using a vacuum suction process. The samples were initially cooled in a water bath and were later reflowed. The reflow profile was chosen to closely mimic profiles used for BGA assemblies, so that the obtained microstructures were similar to those found in typical solder joints.

For each of 4 elevated temperatures (T = 125, 150, 175, and 200 °C), tensile stress-strain tests were performed at three strain rates (SR = 0.001, 0.0001, and 0.00001 sec-1). For each alloy and testing temperature, the stress-strain curve shape and high temperature tensile properties (initial modulus, yield stress, and ultimate tensile strength) of the solders were measured and compared. As expected, the results have shown significant degradations of the mechanical properties of lead-free solders at higher temperatures. However, it was found that the addition of dopants (e.g. Bi, Ni, and Sb) in the SAC+X alloys improved their high temperature properties significantly. Both SAC_Q and Innolot alloys significantly outperformed SAC305 and SAC_R at all temperature levels.

CHAPTER 5

EFFECTS OF EXTREME HIGH TEMPERATURE AGING ON THE MECHANICAL BEHAVIOR OF SAC AND SAC+X SOLDER ALLOYS

5.1 Introduction

Prolonged exposures of lead free solders at high temperatures will cause aging effects, which involve evolution (coarsening) of the intermetallic compound (IMC) particles in microstructure resulting in further degradations of their mechanical properties. Most prior researches on lead free solder have been restricted to testing temperatures and aging temperature at or below T = 125 °C. Extreme high temperatures properties up to T = 200 °C are relatively unexplored. Mechanical behaviors of lead free solder alloys at such extreme high temperatures are necessary to support several harsh environment electronics applications. In chapter, we have reported the temperature dependent stress-strain behavior of SAC305, SAC_Q, and Innolot solders subjected to high temperature aging at 125 and 200 °C. Before testing, the solder uniaxial specimens were aged (preconditioned) at the extreme high temperature of either T = 125 °C or T = 200 °C. At each of these aging temperatures, several durations of aging were considered including 0, 1, 5, and 20 days. Stress-strain and creep tests were then performed on the aged specimens. Using the measured data, the evolutions of the stress-strain and creep behaviors were determined as a function of aging temperature and aging time.

5.2 Stress-Strain Data for Various Test Temperatures and Aging Conditions

The recorded experimental tensile test results for SAC305 solder alloy with different test temperatures and aging durations (Aging T = 125 °C) are plotted in Figure 5.1. Graphs in each plot shows the temperature dependent uniaxial stress-strain behavior of SAC305 solder alloy at a particular aging duration (0, 1, 5, or 20 days.), with the various colored curves representing the different test temperature with blue= 125 °C, green= 150 °C, orange= 175 °C, and red= 200 °C. Again, in each plot, top curve corresponds to 125 °C and bottom curve represents 200 °C test result. Similar results for SAC_Q and Innolot are shown in Figures 5.2 and 5.3. We found a significant degradation of mechanical properties with the increase in test temperature at each aging condition for all the alloys. Similar behavior has been observed at extreme high temperature aging as well (aging at T= 200 °C). Uniaxial tensile test results correspond to 200 °C aging for all the alloys are shown in Figures 5.4 to 5.6.

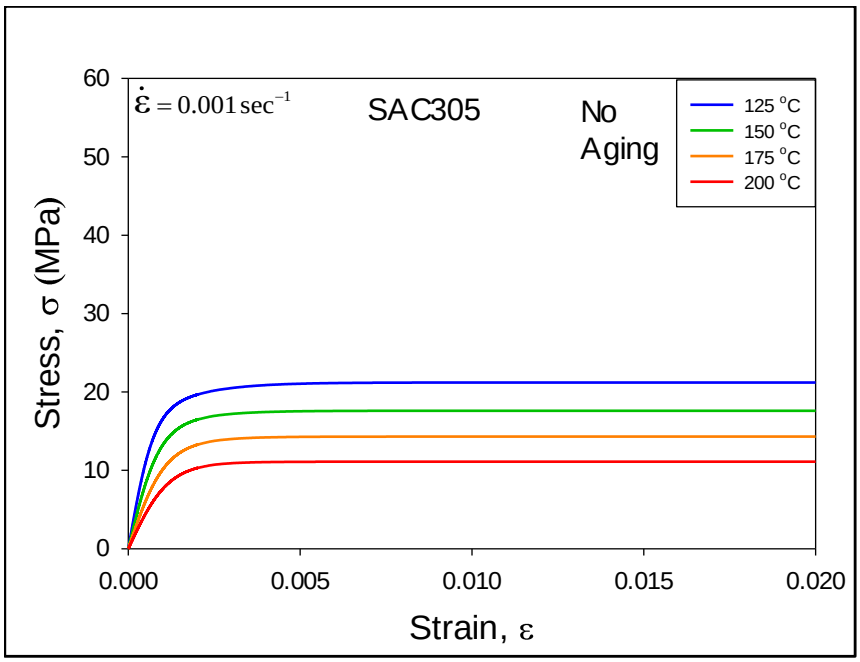
$\dot{\varepsilon} = 0.001\,\mathrm{sec}^{-1}$
SAC305
No Aging
125 °C
150 °C
175 °C
200 °C
Stress, σ (MPa)
Strain, ε
0
10
20
30
40
50
60
0.000
0.005
0.010
0.015
0.020

(a)

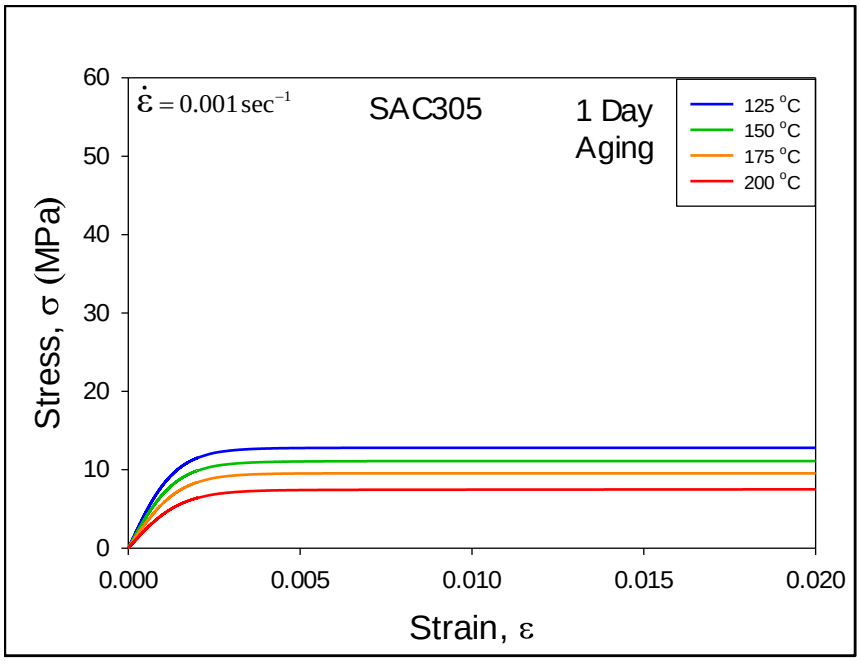
$\dot{\varepsilon} = 0.001\,\mathrm{sec}^{-1}$
SAC305
1 Day Aging
125 °C
150 °C
175 °C
200 °C
Stress, σ (MPa)
Strain, ε
0
10
20
30
40
50
60
0.000
0.005
0.010
0.015
0.020

(b)

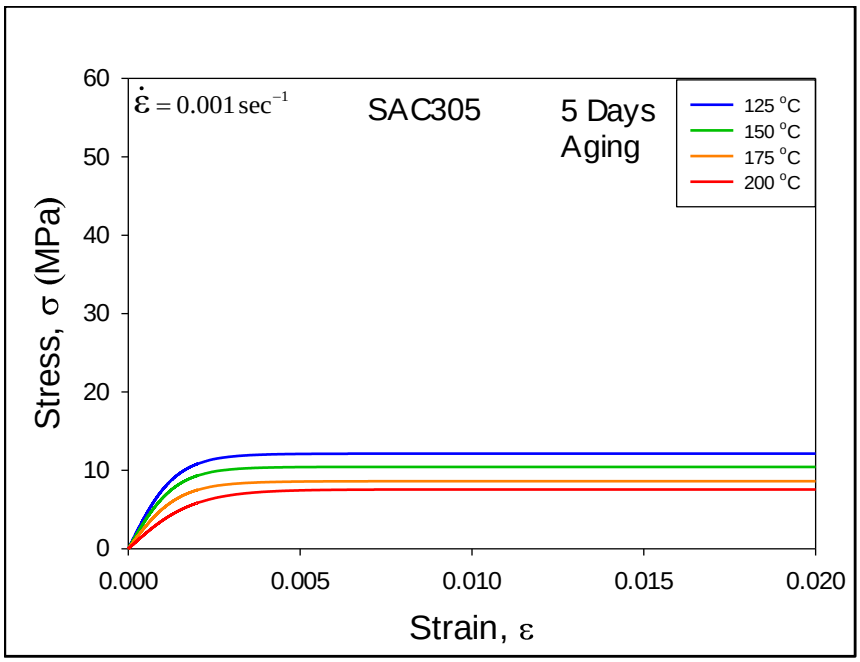

(c)

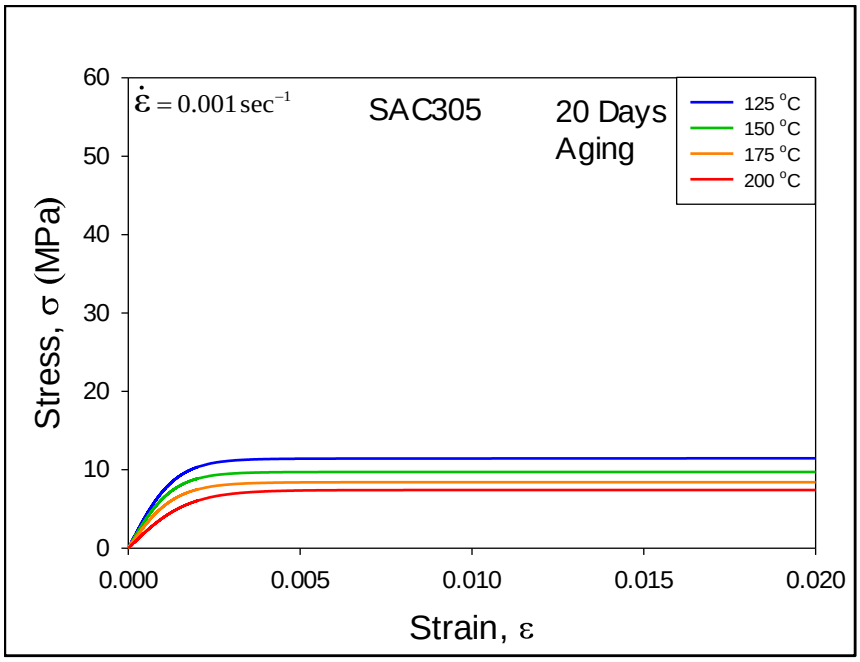

(d)

Figure 5.1 Stress-Strain Curves for SAC305 (Aging T = 125 °C)

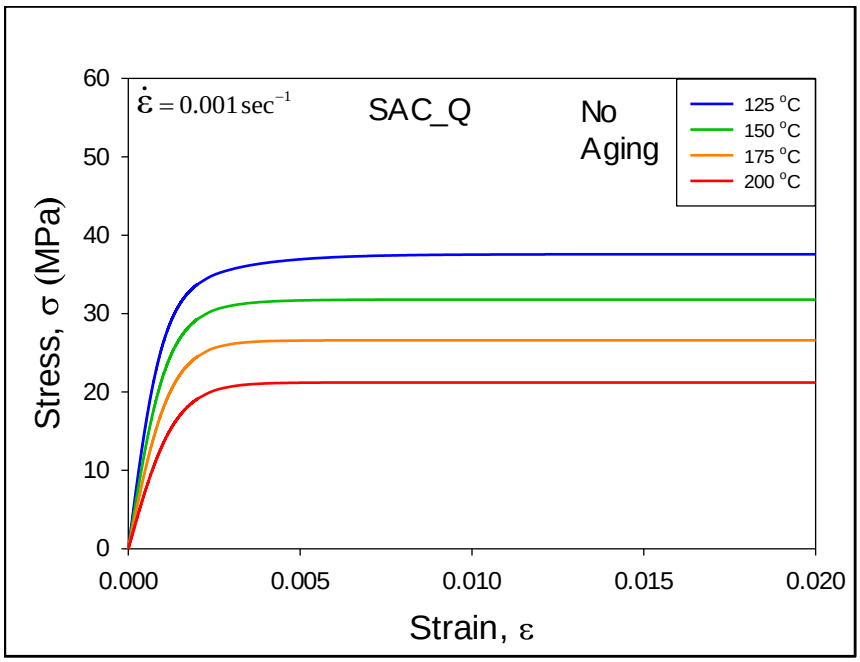
$\dot{\varepsilon} = 0.001\,\mathrm{sec}^{-1}$
SAC_Q
No Aging
125 °C
150 °C
175 °C
200 °C
Stress, σ (MPa)
Strain, ε
0
10
20
30
40
50
60
0.000
0.005
0.010
0.015
0.020

(a)

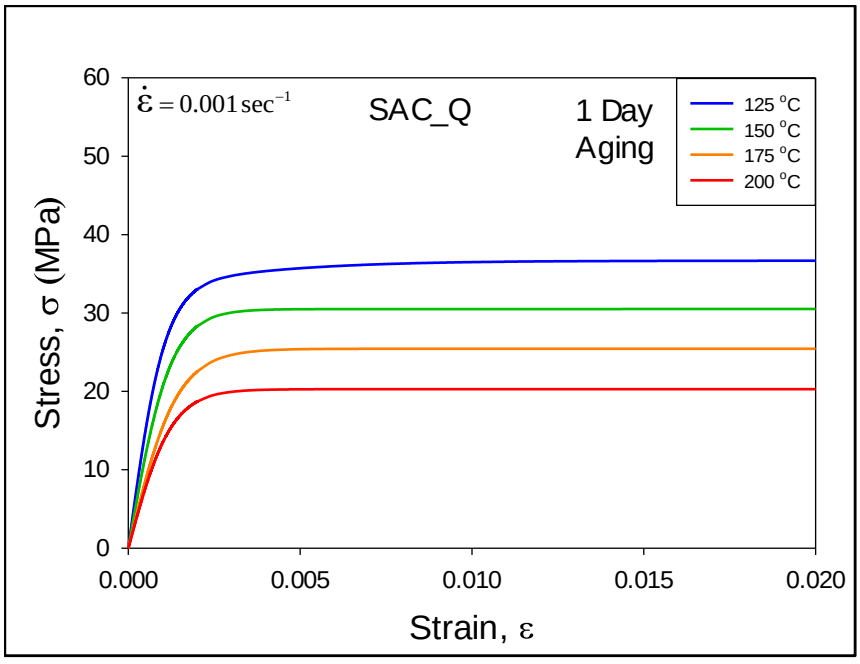
$\dot{\varepsilon} = 0.001\,\mathrm{sec}^{-1}$
SAC_Q
1 Day Aging
125 °C
150 °C
175 °C
200 °C
Stress, σ (MPa)
Strain, ε
0
10
20
30
40
50
60
0.000
0.005
0.010
0.015
0.020

(b)

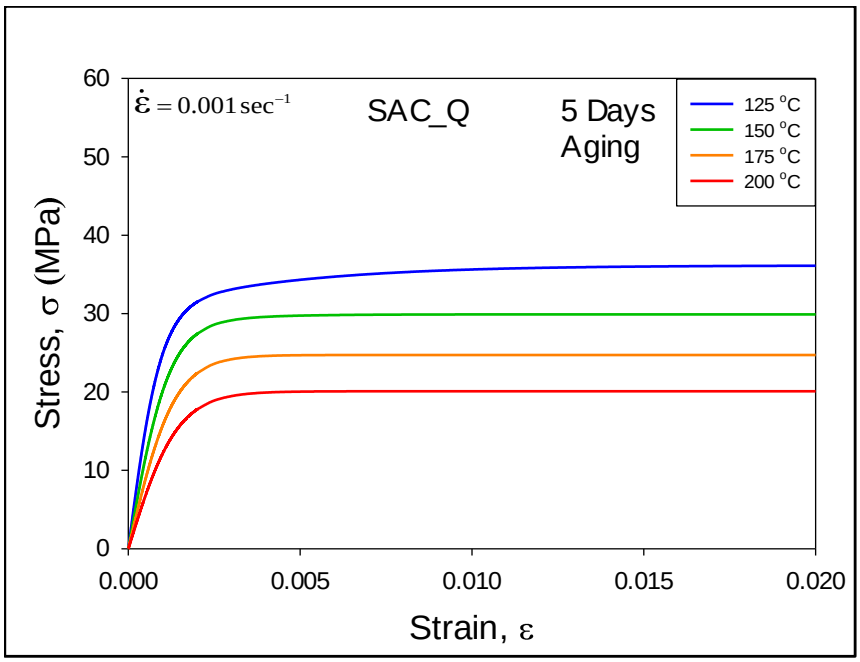

(c)

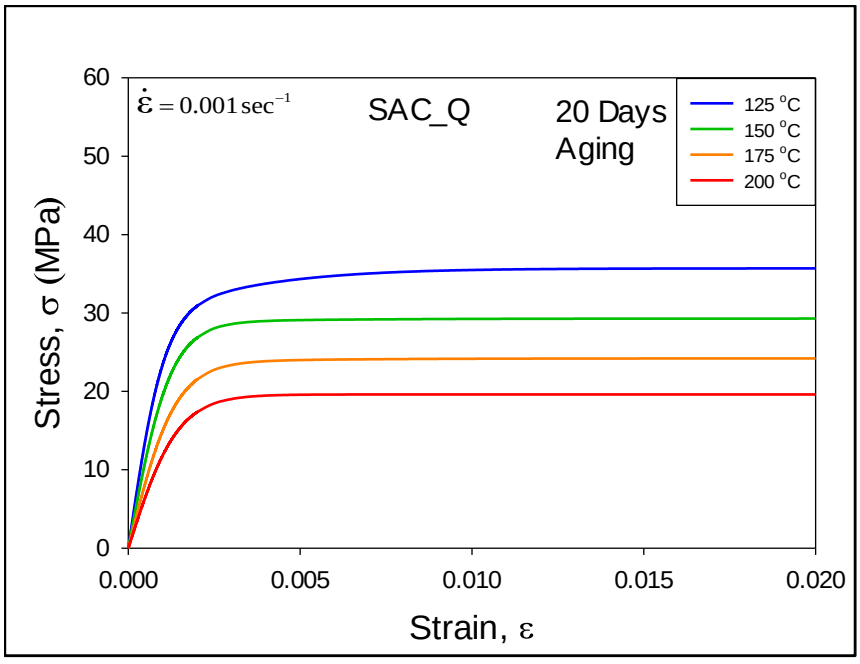

(d)

Figure 5.2 Stress-Strain Curves for SAC_Q (Aging T = 125 ℃)

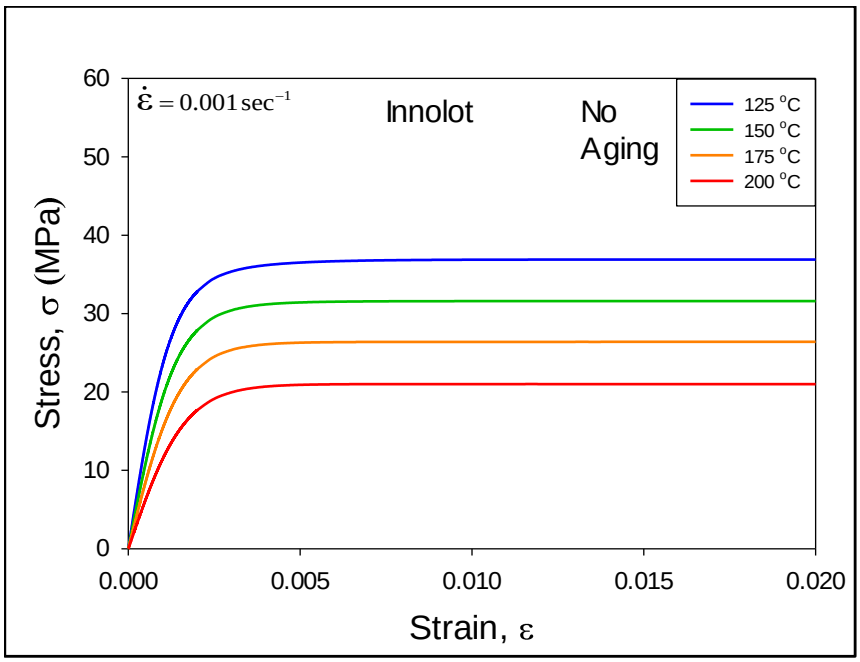
$\dot{\varepsilon} = 0.001\,\mathrm{sec}^{-1}$
Innolot
No Aging
125 °C
150 °C
175 °C
200 °C
Stress, σ (MPa)
Strain, ε
0
10
20
30
40
50
60
0.000
0.005
0.010
0.015
0.020

(a)

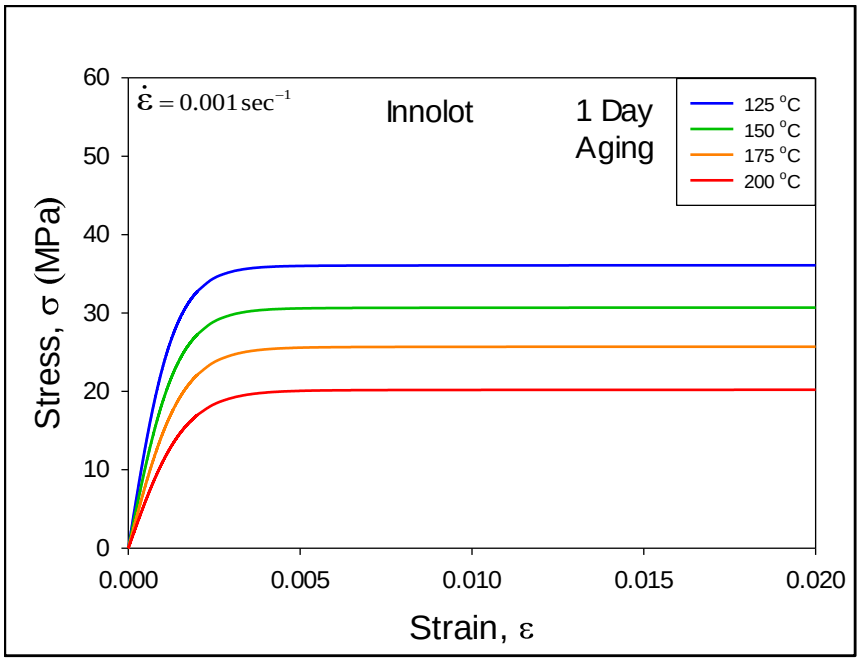
$\dot{\varepsilon} = 0.001\,\mathrm{sec}^{-1}$
Innolot
1 Day Aging
125 °C
150 °C
175 °C
200 °C
Stress, σ (MPa)
Strain, ε
0
10
20
30
40
50
60
0.000
0.005
0.010
0.015
0.020

(b)

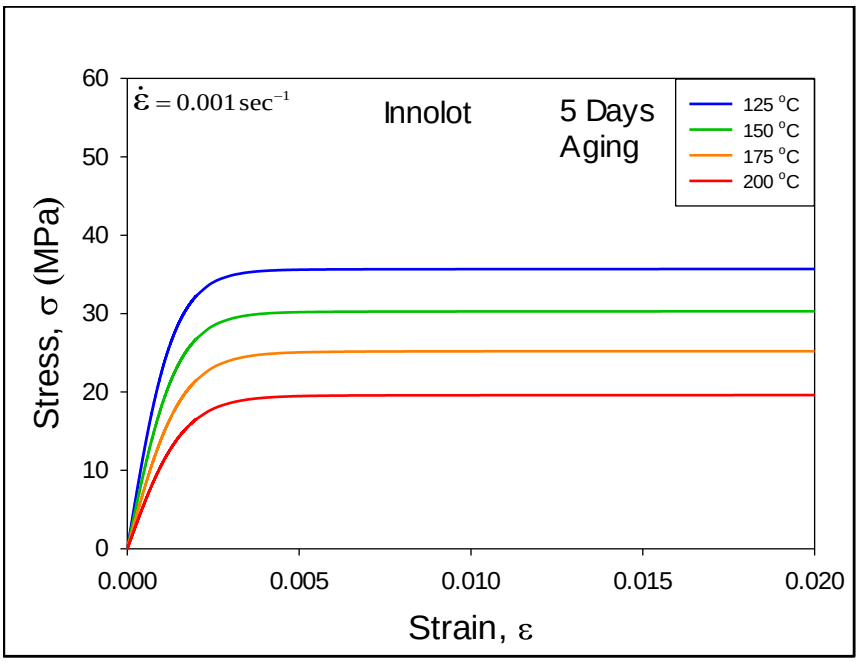

(c)

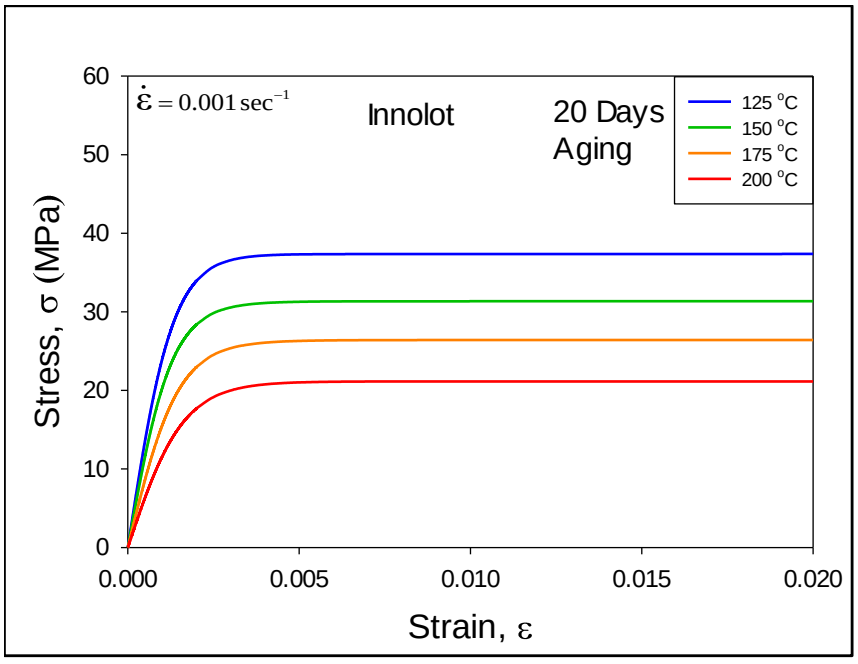

(d)

Figure 5.3 Stress-Strain Curves for Innolot (Aging T = 125 °C)

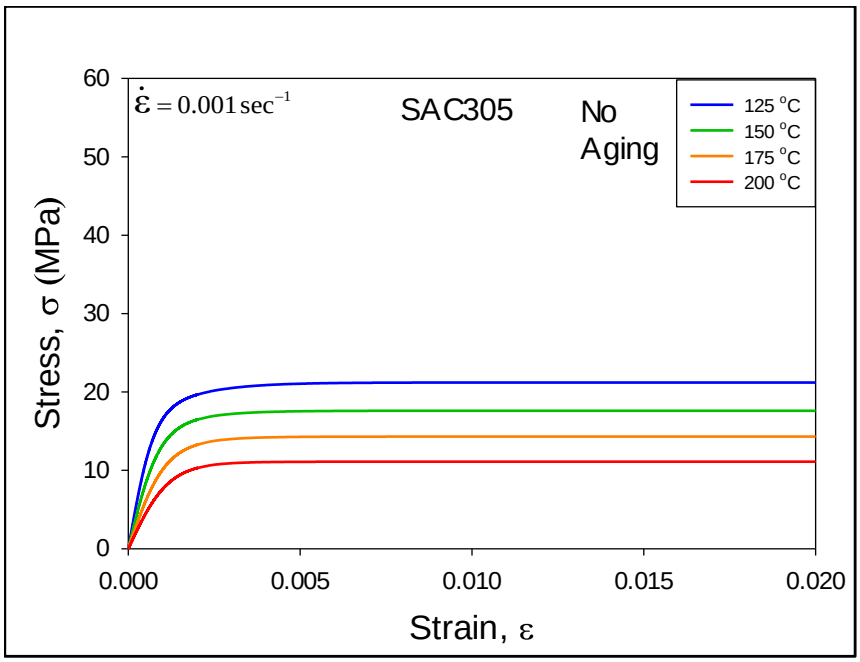
$\dot{\varepsilon} = 0.001\,\mathrm{sec}^{-1}$
SAC305
No Aging
125 °C
150 °C
175 °C
200 °C
Stress, σ (MPa)
Strain, ε
0
10
20
30
40
50
60
0.000
0.005
0.010
0.015
0.020

(a)

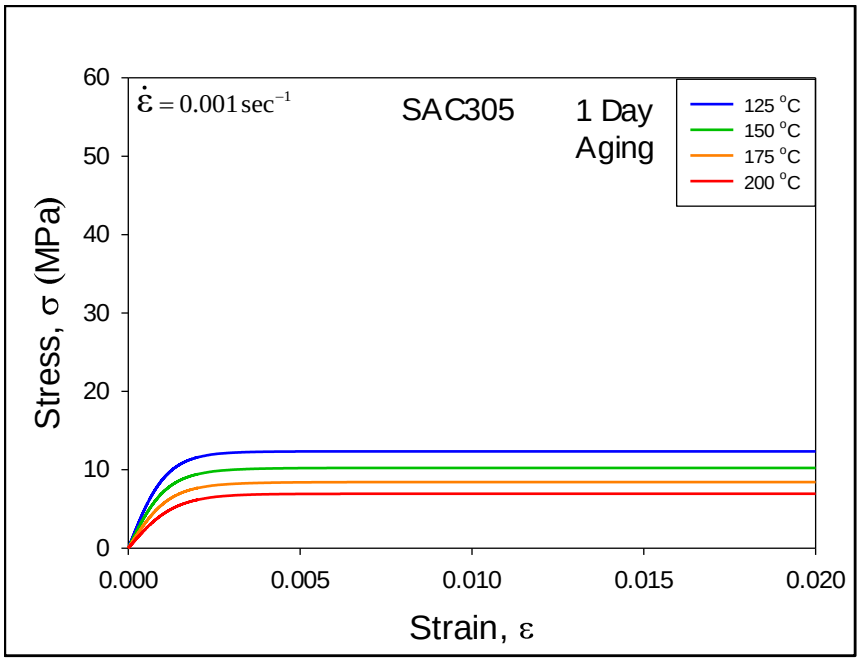
$\dot{\varepsilon} = 0.001\,\mathrm{sec}^{-1}$
SAC305
1 Day Aging
125 °C
150 °C
175 °C
200 °C
Stress, σ (MPa)
Strain, ε
0
10
20
30
40
50
60
0.000
0.005
0.010
0.015
0.020

(b)

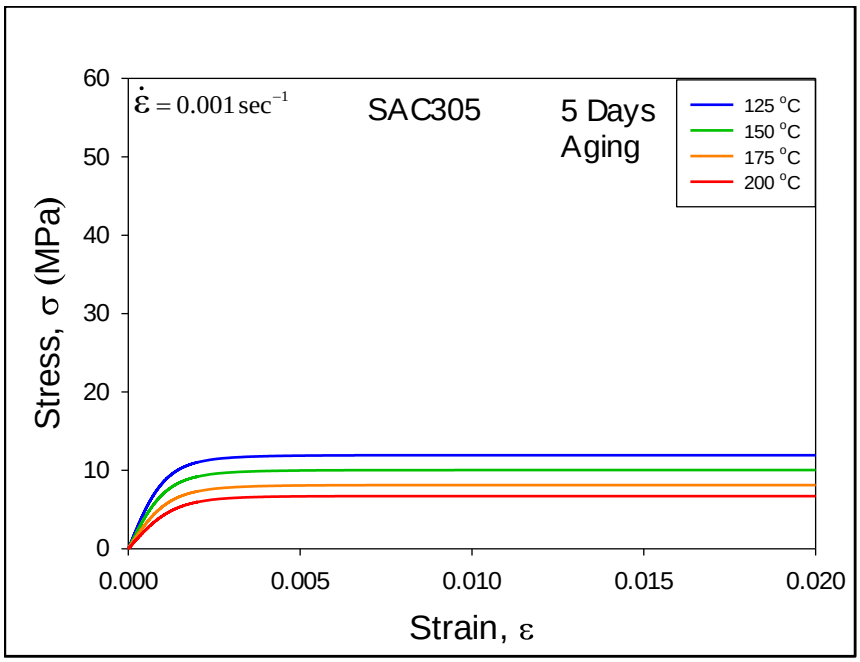

(c)

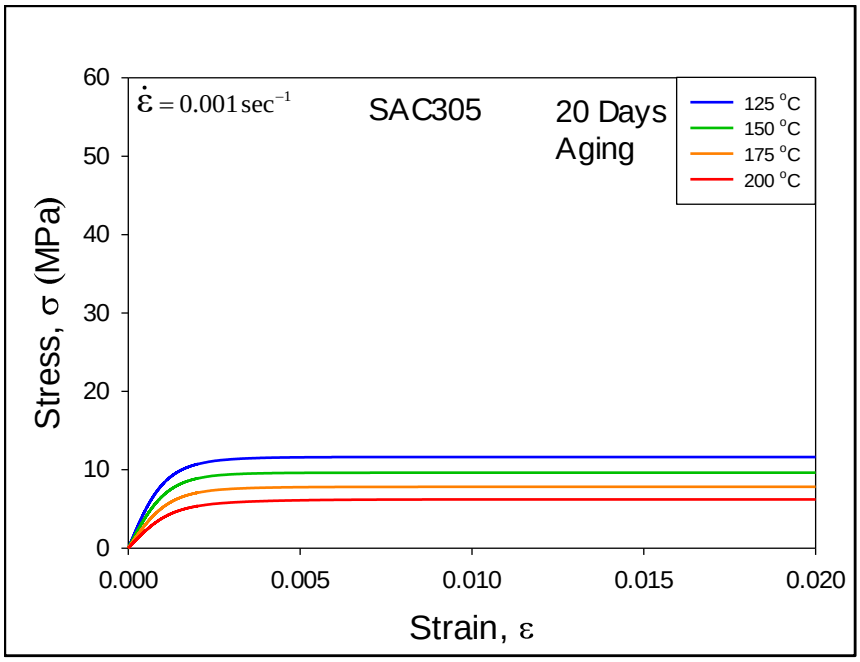

(d)

Figure 5.4 Stress-Strain Curves for SAC305 (Aging T = 200 °C)

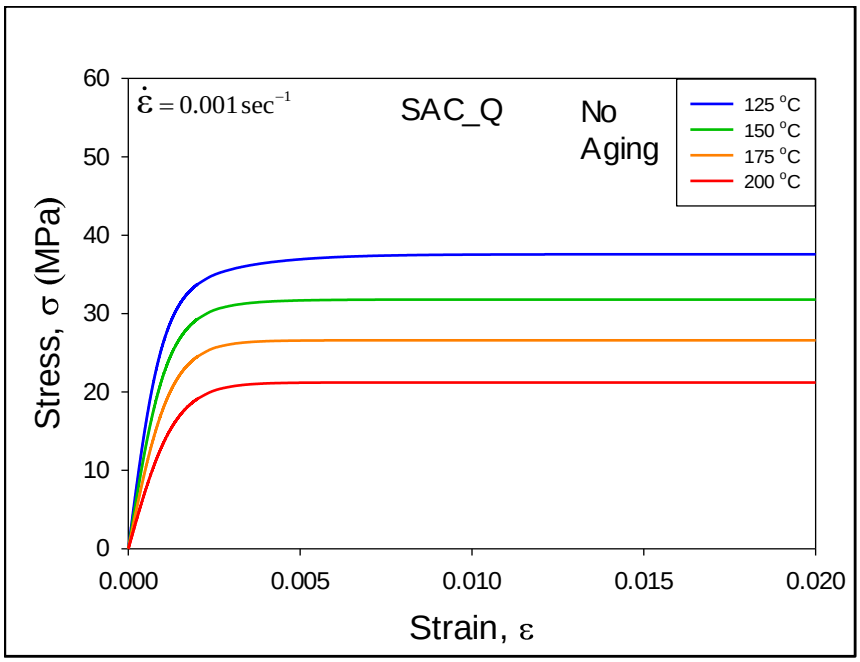
$\dot{\varepsilon} = 0.001\,\mathrm{sec}^{-1}$
SAC_Q
No Aging
125 °C
150 °C
175 °C
200 °C
Stress, σ (MPa)
Strain, ε
0
10
20
30
40
50
60
0.000
0.005
0.010
0.015
0.020

(a)

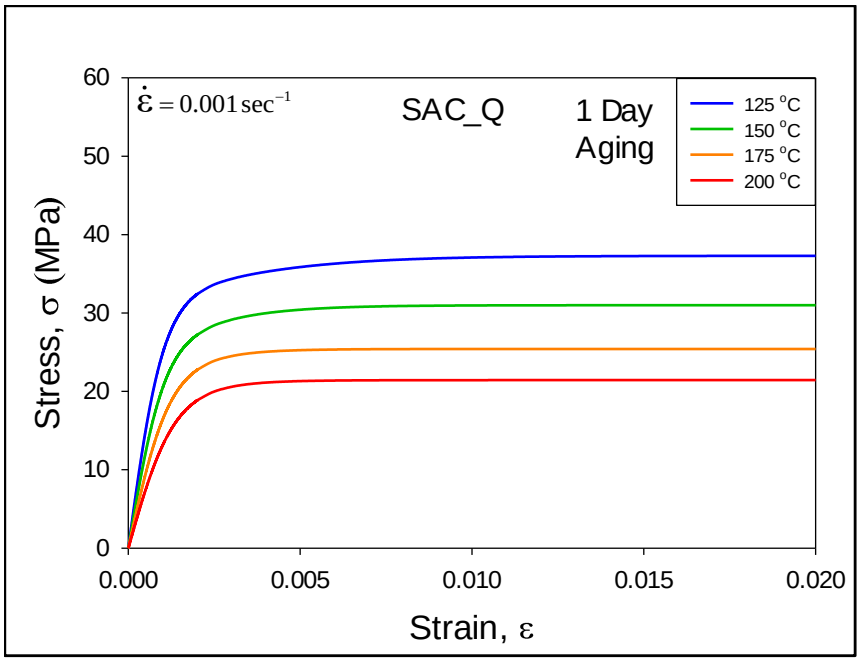
$\dot{\varepsilon} = 0.001\,\mathrm{sec}^{-1}$
SAC_Q
1 Day Aging
125 °C
150 °C
175 °C
200 °C
Stress, σ (MPa)
Strain, ε
0
10
20
30
40
50
60
0.000
0.005
0.010
0.015
0.020

(b)

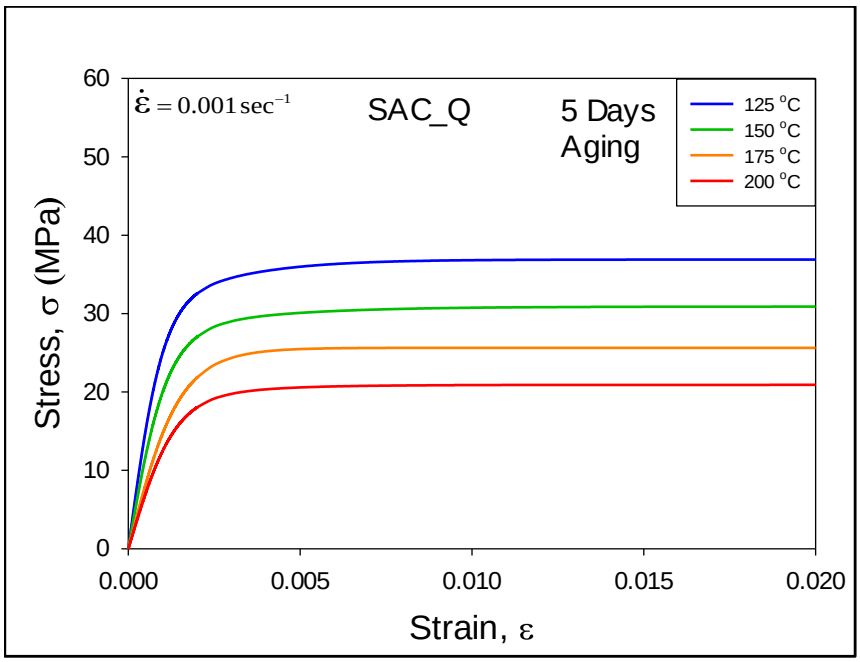

(c)

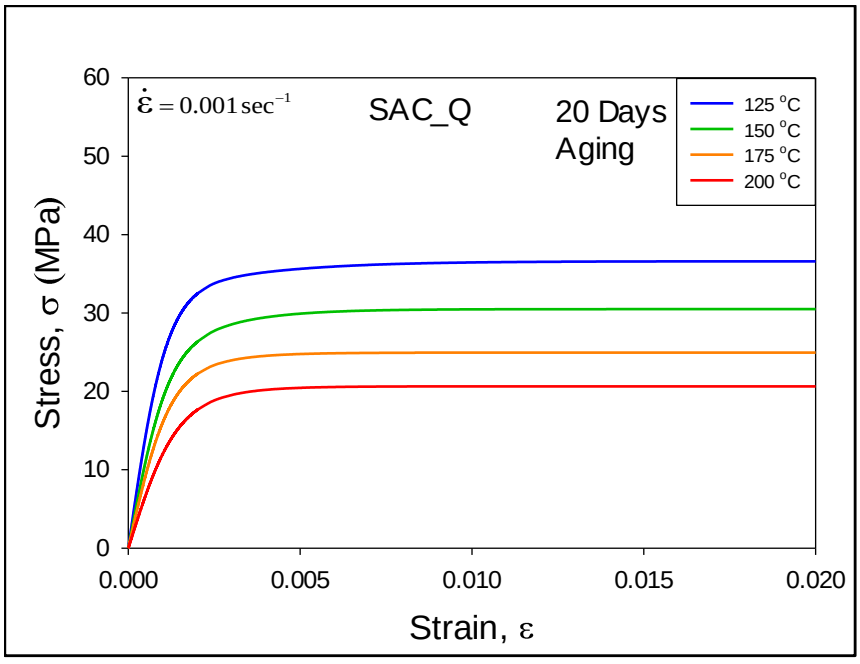

(d)

Figure 5.5 Stress-Strain Curves for SAC_Q (Aging T = 200 °C)

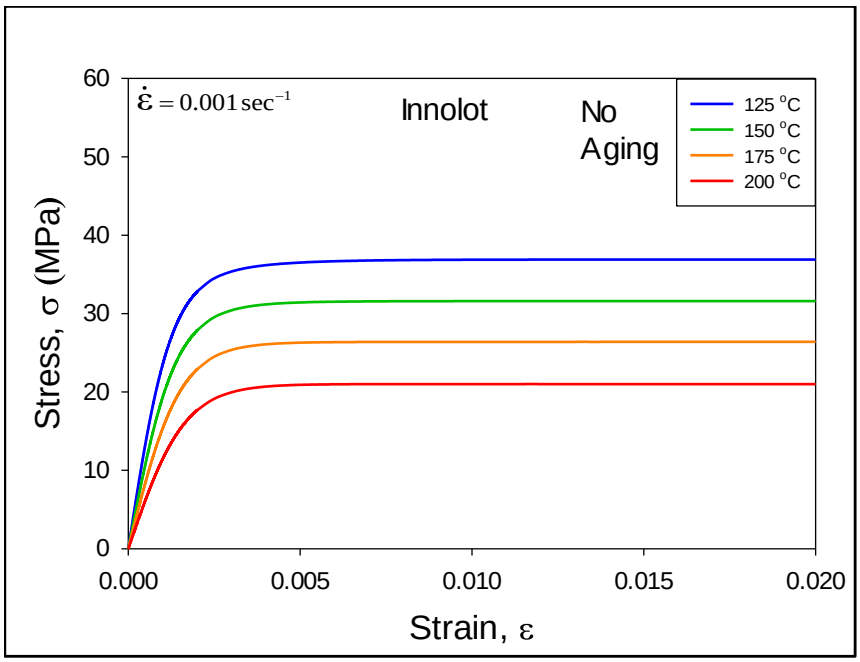
$\dot{\varepsilon} = 0.001\,\mathrm{sec}^{-1}$
Innolot
No Aging
125 °C
150 °C
175 °C
200 °C
Stress, σ (MPa)
Strain, ε
0
10
20
30
40
50
60
0.000
0.005
0.010
0.015
0.020

(a)

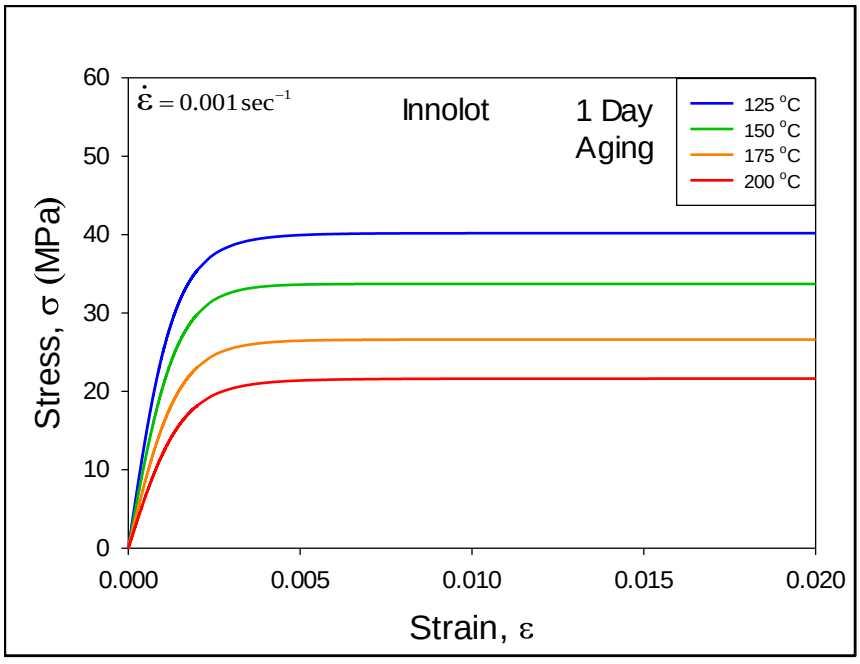
$\dot{\varepsilon} = 0.001\,\mathrm{sec}^{-1}$
Innolot
1 Day Aging
125 °C
150 °C
175 °C
200 °C
Stress, σ (MPa)
Strain, ε
0
10
20
30
40
50
60
0.000
0.005
0.010
0.015
0.020

(b)

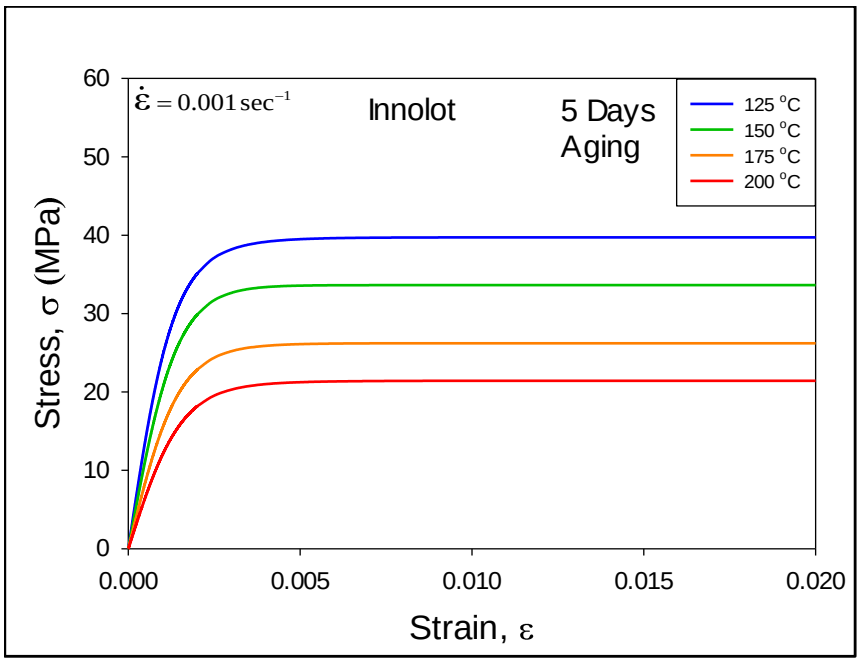

(c)

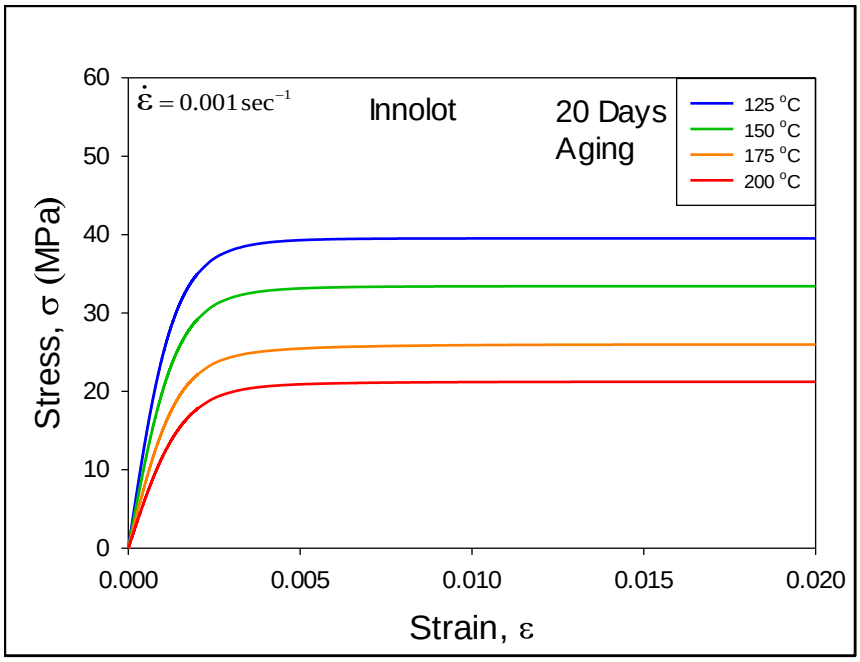

(d)

Figure 5.6 Stress-Strain Curves for Innolot (Aging T = 200 °C)

5.3 Comparison of Average Stress-Strain Results between SAC305 and SAC_Q

The uniaxial tensile test results between SAC305 and SAC_Q have been shown in the same plot for comparison (Figure 5.7). Each of the graphs shows a comparative analysis of the uniaxial stress-strain behavior of both alloys at a particular test temperature, with the various colored curves representing the different aging durations with blue= no aging, green= 1 day aging, orange= 5 days aging, and red= 20 days aging at T = 125 °C).

As mentioned before, the curves in the plots are the "average" stress-strain curves found by fitting the raw experimental data with the empirical model in Equation 3.2. The results are grouped in two sets of curves in each graph. The first set (top four curves) shows the aging dependent stress-strain behavior of SAC_Q, and the second set (bottom four curves) represents the same for SAC305. For each material, the top (blue) curve represents the average stress-strain curve for no aging, and the bottom (red) curve shows the average stress-strain curve at 20 days of aging.

At each test temperature, SAC_Q exhibited the best mechanical properties, and typically both the ultimate tensile strength (UTS) and effective elastic modulus (E) of SAC_Q were twice as large of the corresponding values for SAC305. Furthermore, the SAC305 alloy demonstrated large aging induced degradations with significant drop in mechanical properties after only 1 day of high temperature aging, while the SAC_Q alloy appeared to have negligible aging effects for all aging durations. Similar behavior is observed at extreme high temperature aging (aging ay T= 200 °C), shown in Figure 4.8.

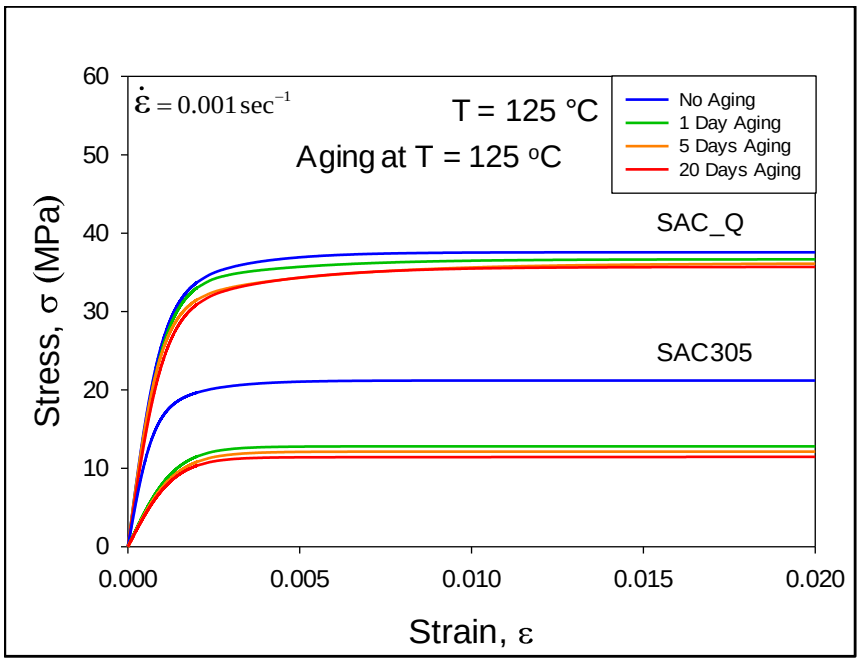
$\dot{\varepsilon} = 0.001\,\mathrm{sec}^{-1}$
T = 125 °C
Aging at T = 125 °C
No Aging
1 Day Aging
5 Days Aging
20 Days Aging
SAC_Q
SAC305
Stress, σ (MPa)
Strain, ε
0
10
20
30
40
50
60
0.000
0.005
0.010
0.015
0.020

(a)

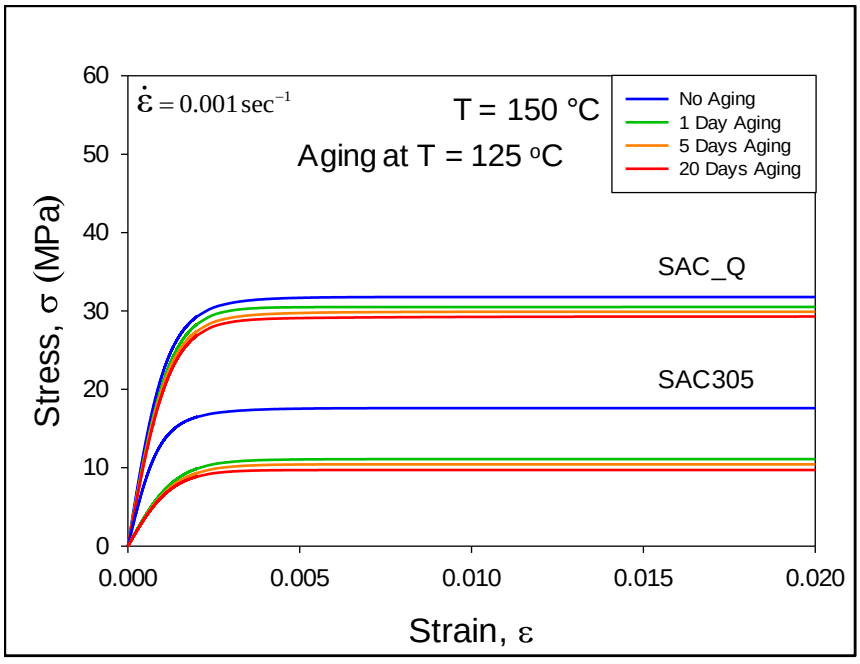
$\dot{\varepsilon} = 0.001\,\mathrm{sec}^{-1}$
T = 150 °C
Aging at T = 125 °C
No Aging
1 Day Aging
5 Days Aging
20 Days Aging
SAC_Q
SAC305
Stress, σ (MPa)
Strain, ε
0
10
20
30
40
50
60
0.000
0.005
0.010
0.015
0.020

(b)

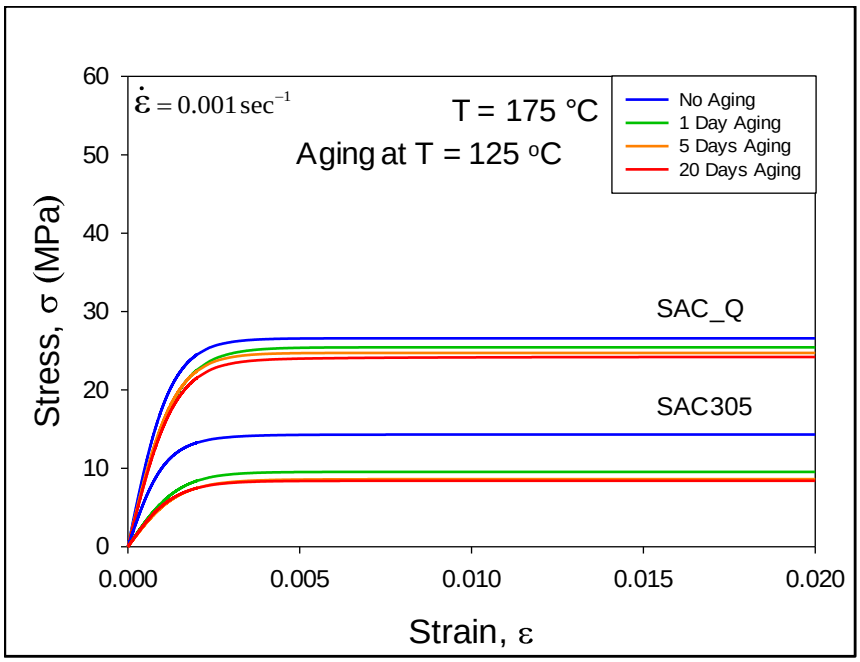

(c)

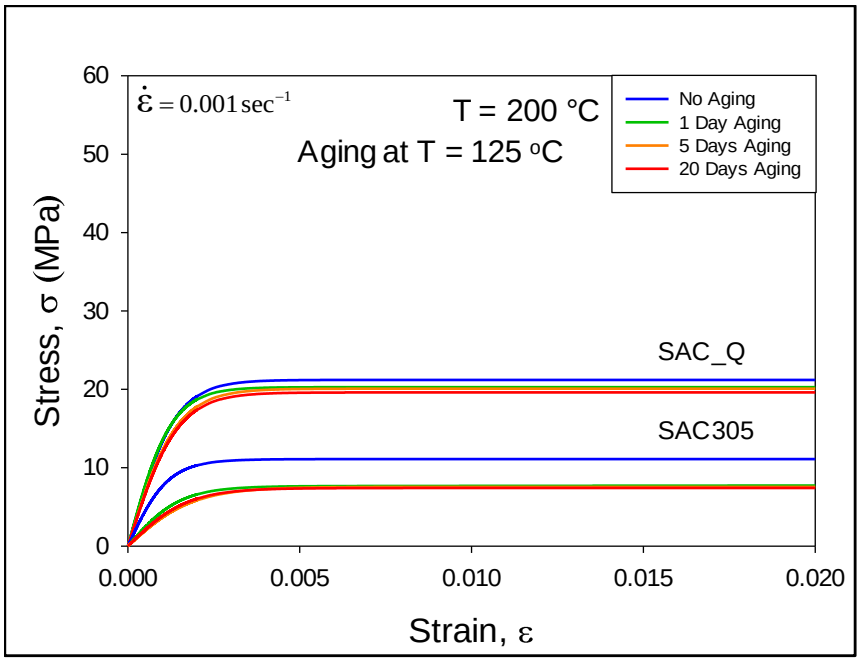

(d)

Figure 5.7 Comparison of Stress-Strain Curves (SAC305 and SAC_Q, Aging T= 125 °C)

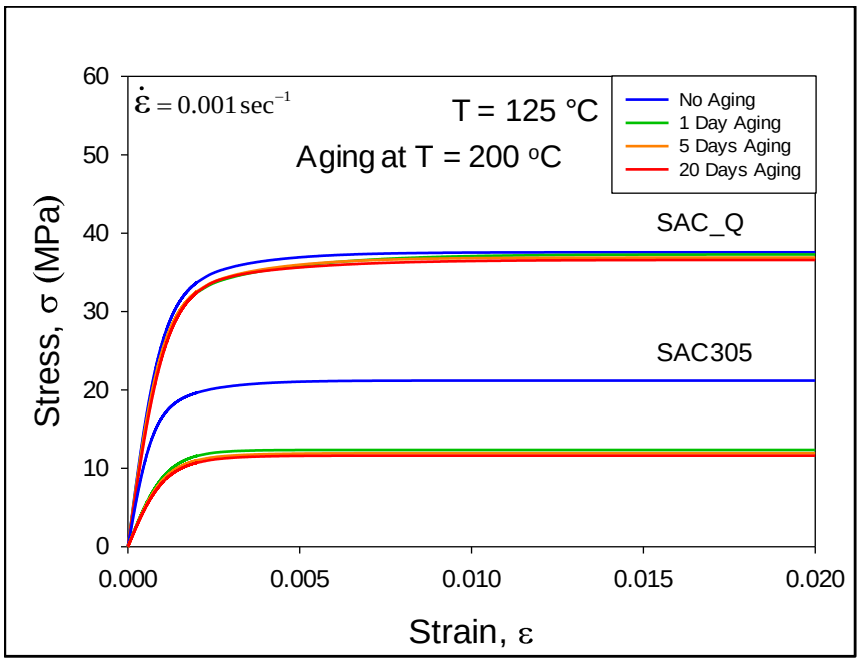
$\dot{\varepsilon} = 0.001\,\mathrm{sec}^{-1}$
T = 125 °C
Aging at T = 200 °C
No Aging
1 Day Aging
5 Days Aging
20 Days Aging
SAC_Q
SAC305
Stress, σ (MPa)
Strain, ε
0
10
20
30
40
50
60
0.000
0.005
0.010
0.015
0.020

(a)

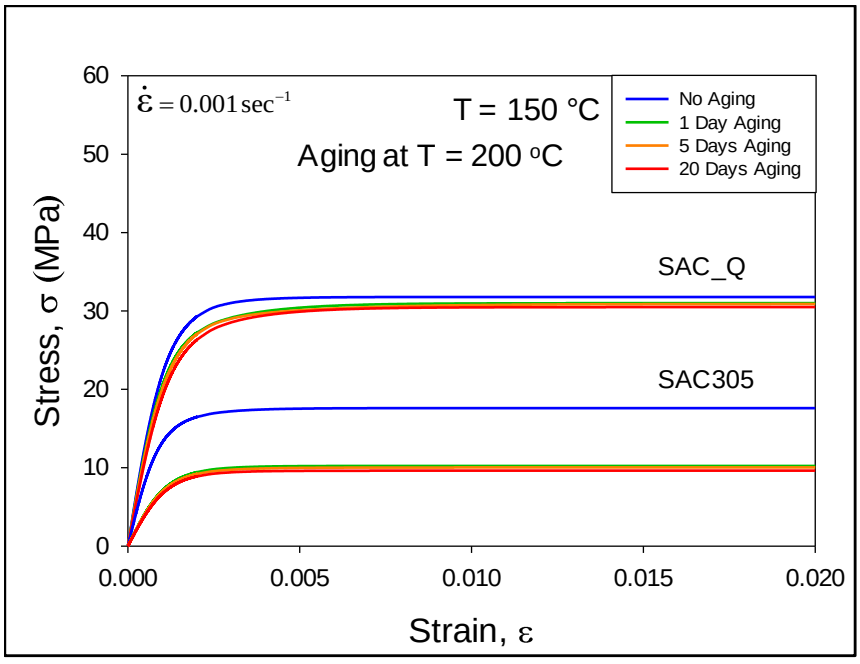
$\dot{\varepsilon} = 0.001\,\mathrm{sec}^{-1}$
T = 150 °C
Aging at T = 200 °C
No Aging
1 Day Aging
5 Days Aging
20 Days Aging
SAC_Q
SAC305
Stress, σ (MPa)
Strain, ε
0
10
20
30
40
50
60
0.000
0.005
0.010
0.015
0.020

(b)

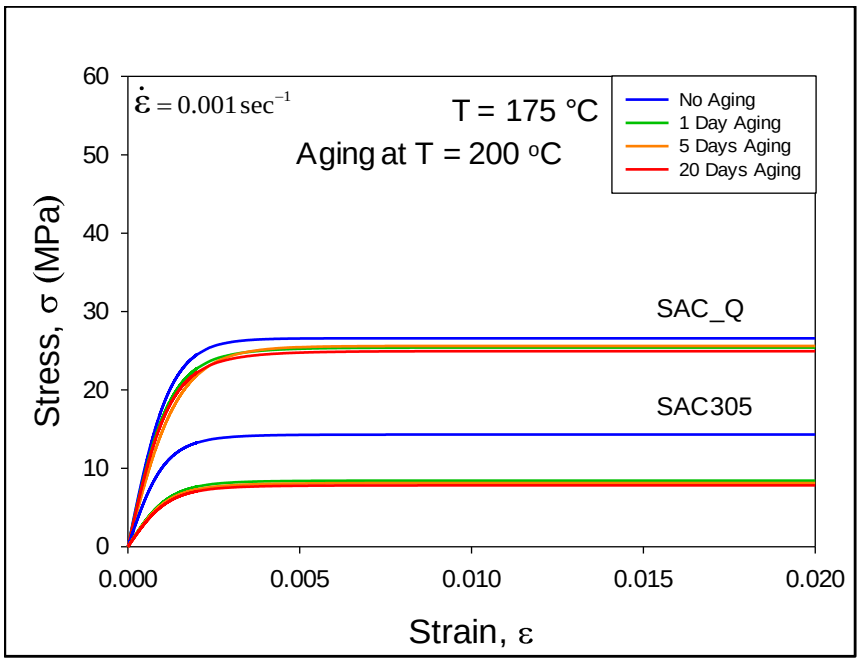

(c)

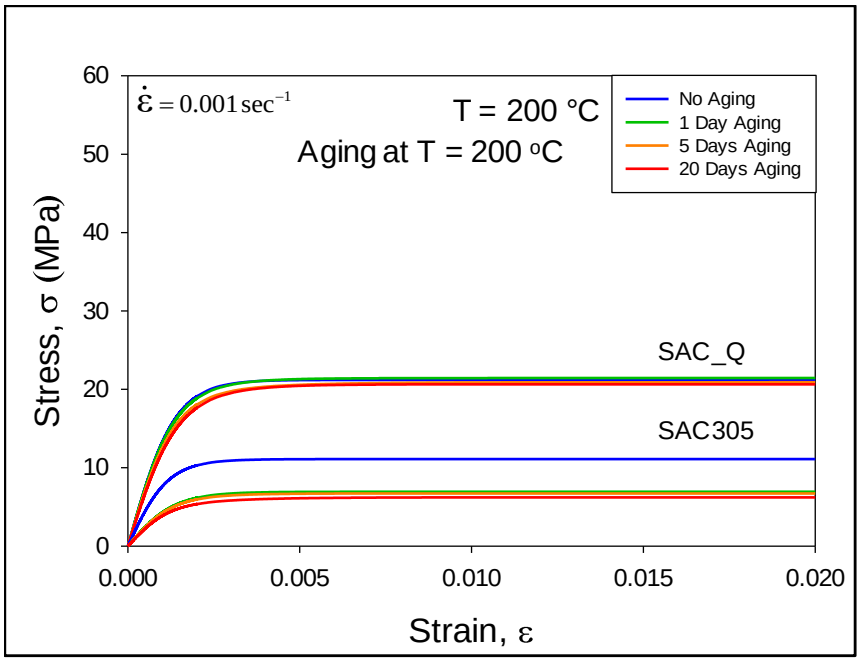

(d)

Figure 5.8 Comparison of Stress-Strain Curves (SAC305 and SAC_Q, Aging T= 200 °C)

5.4 Comparison of Mechanical Properties between SAC305 and SAC_Q

Table 5.1 and 5.2 show the aging dependent mechanical properties of SAC 305 and SAC_Q solder alloys for aging at 125 and 200 °C. Variation of Effective Elastic Modulus are shown in Table 5.1 and Ultimate Tensile Strength (UTS) in Table 5.2. These properties have been extracted from the average stress-strain data, and plotted as a function of test temperature in Figure 5.9 (aging T= 125 °C) and Figure 5.10 (aging T= 200 °C). Again, these properties are plotted as a function of aging duration in Figure 5.11 (aging T= 125 °C) and Figure 5.12 (aging T= 200 °C). As mentioned before, the results are grouped in two sets of curves in each graph. The first set (top four curves) shows the aging dependent mechanical properties of SAC_Q, and the second set (bottom four curves) represents the same for SAC305. For each material, the top (blue) curve represents the average stress-strain curve for no aging, and the bottom (red) curve shows the average stress-strain curve at 20 days of aging.

Large aging induced degradations are evident for SAC305 with a significant drop in properties after 5 days of aging at both 125 and 200 °C. After that point, the properties degrade at a much slower rate. Conversely, the properties of SAC_Q were found to degrade very slowly or remain nearly constant at all aging conditions.

Table 5.1 Comparison of Effective Elastic Modulus between SAC305 and SAC_Q

Alloy	Aging Temperature (°C)	Test Temperature (°C)	Effective Modulus, E (GPa)			
			No Aging	1 Day Aging	5 Days Aging	20 Days Aging
SAC305	125	125	25.1	9.4	9.0	8.6
		150	18.4	8.1	7.6	7.6
		175	14.0	6.6	6.4	6.2
		200	8.6	5.1	4.7	4.4
	200	125	25.1	11.2	10.8	10.5
		150	18.4	9.0	8.8	8.4
		175	14.0	6.9	6.7	6.4
		200	8.6	5.2	5.0	4.7
SAC_Q	125	125	34.0	32.9	32.0	30.0
		150	27.5	26.0	24.7	23.7
		175	21.5	19.7	18.8	17.6
		200	15.6	14.9	14.4	13.7
	200	125	34.0	32.2	32.4	30.5
		150	27.5	26.1	25.2	23.4
		175	21.5	20.0	19.4	18.3
		200	15.6	15.5	14.7	14.0

Table 5.2 Comparison of Ultimate Tensile Strength between SAC305 and SAC_Q

Alloy	Aging Temperature (°C)	Test Temperature (°C)	Ultimate Tensile Strength, UTS (MPa)			
			No Aging	1 Day Aging	5 Days Aging	20 Days Aging
SAC305	125	125	21.2	12.8	12.1	11.6
		150	17.9	11.1	10.4	9.7
		175	14.3	9.5	8.8	8.4
		200	10.9	7.7	7.6	7.4
	200	125	21.2	12.3	11.9	11.6
		150	17.9	10.2	10.0	9.6
		175	14.3	8.4	8.1	7.8
		200	10.9	6.9	6.7	6.2
SAC_Q	125	125	37.6	36.7	36.1	35.7
		150	31.8	30.6	29.9	29.3
		175	26.5	25.4	24.7	24.2
		200	21.2	20.5	20.0	19.7
	200	125	37.6	37.3	36.9	36.6
		150	31.8	31.0	30.9	30.5
		175	26.5	25.4	25.6	24.9
		200	21.2	21.4	20.9	20.6

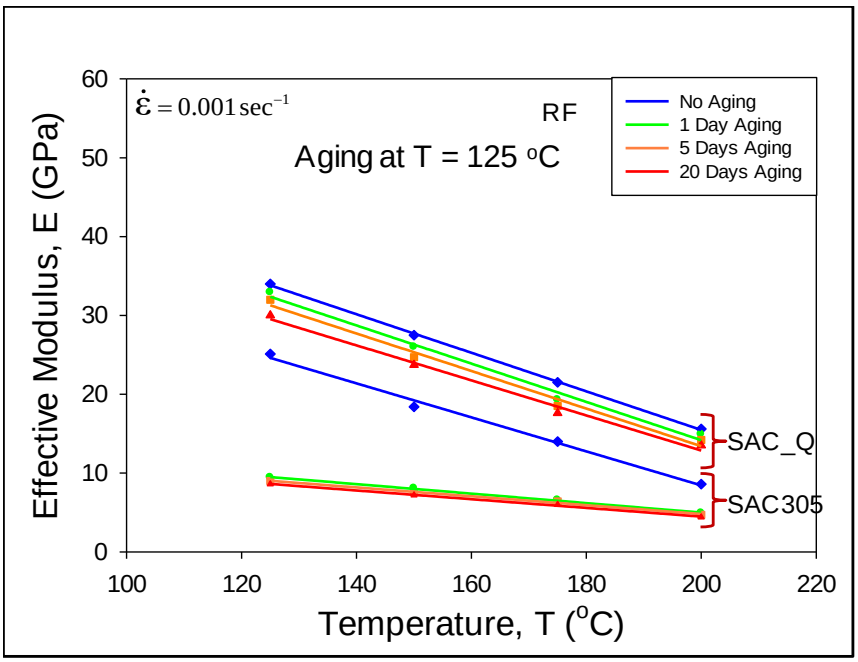

(a)

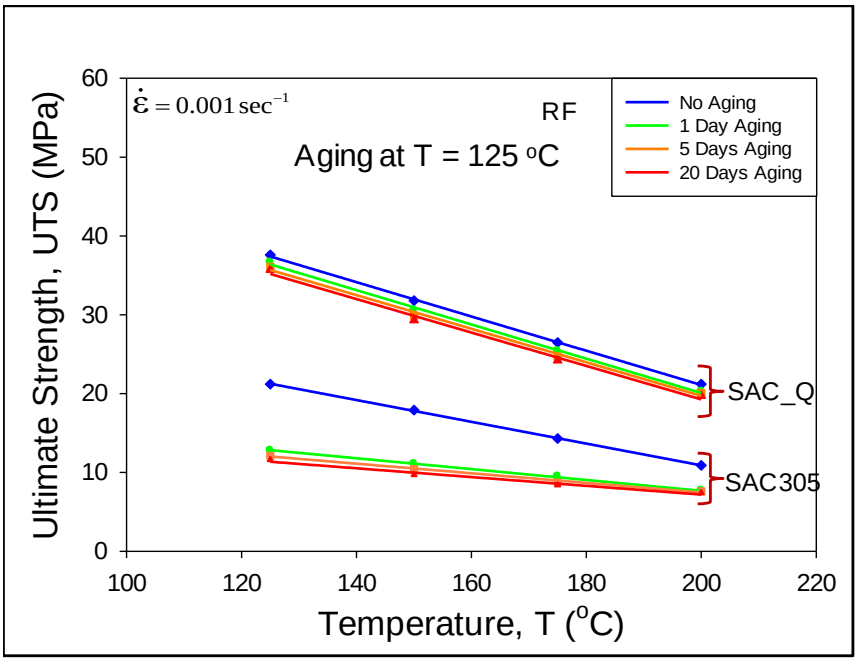

(b)

Figure 5.9 Variation of Mechanical Properties with Temperature (Aging T = 125 °C)

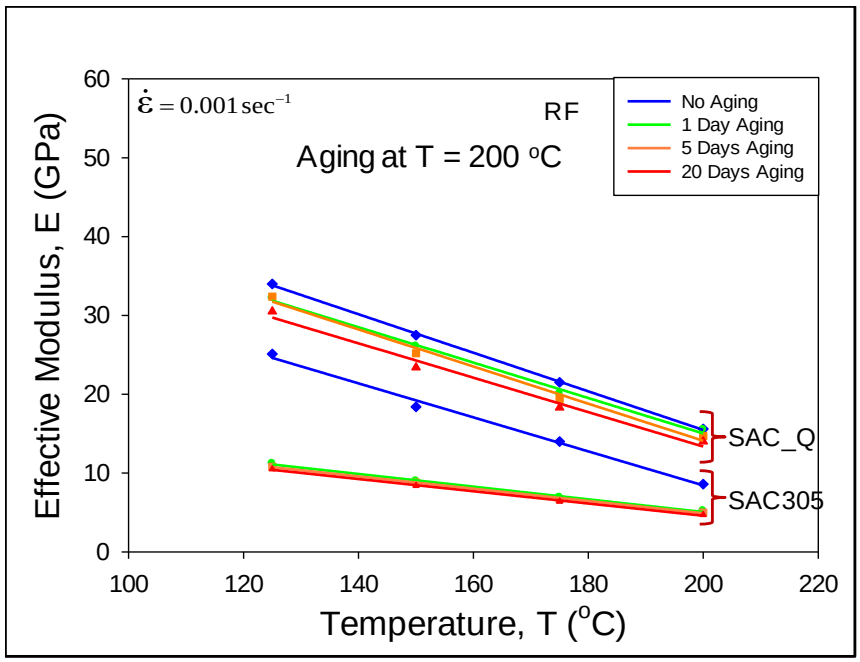

(a)

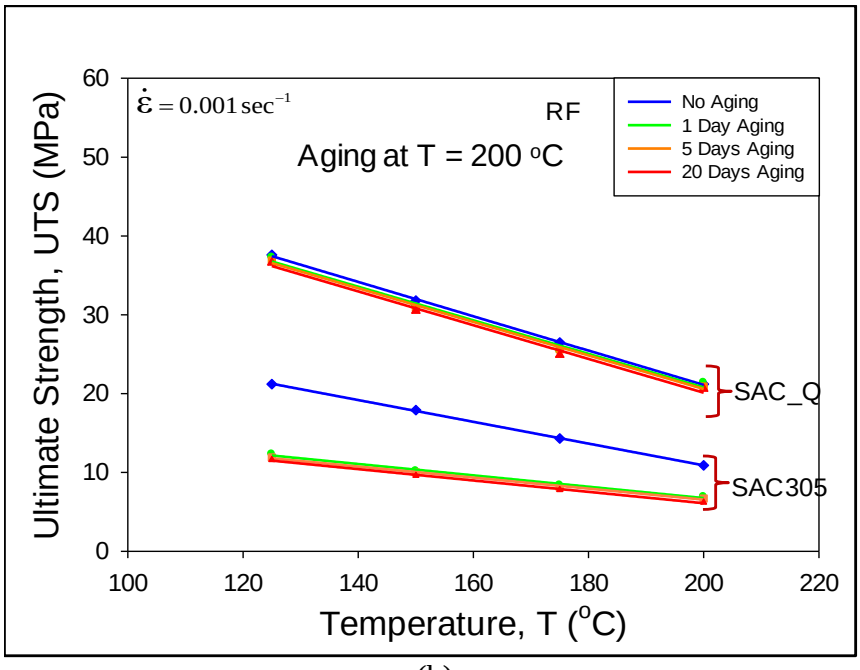

(b)

Figure 5.10 Variation of Mechanical Properties with Temperature (Aging T = 200 °C)

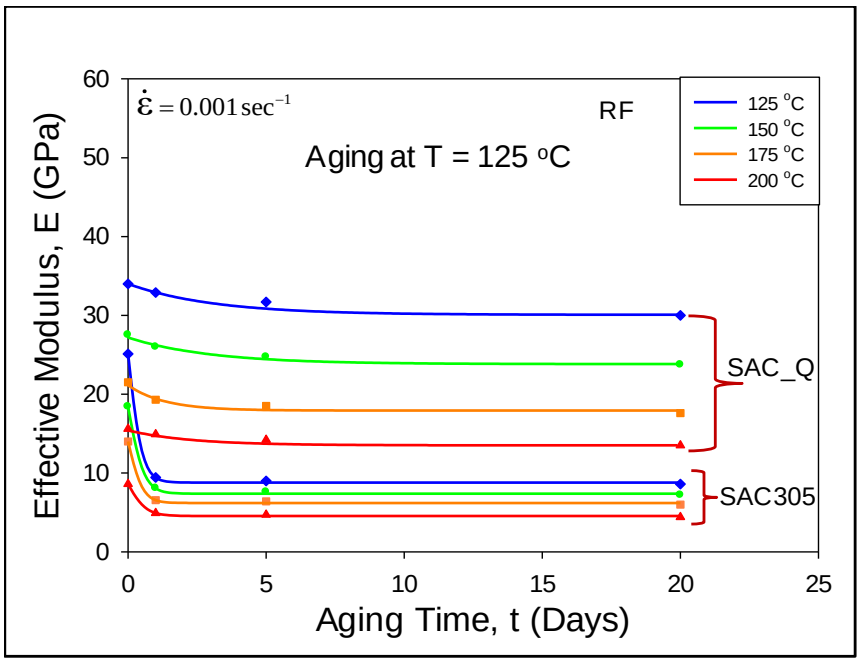

(a)

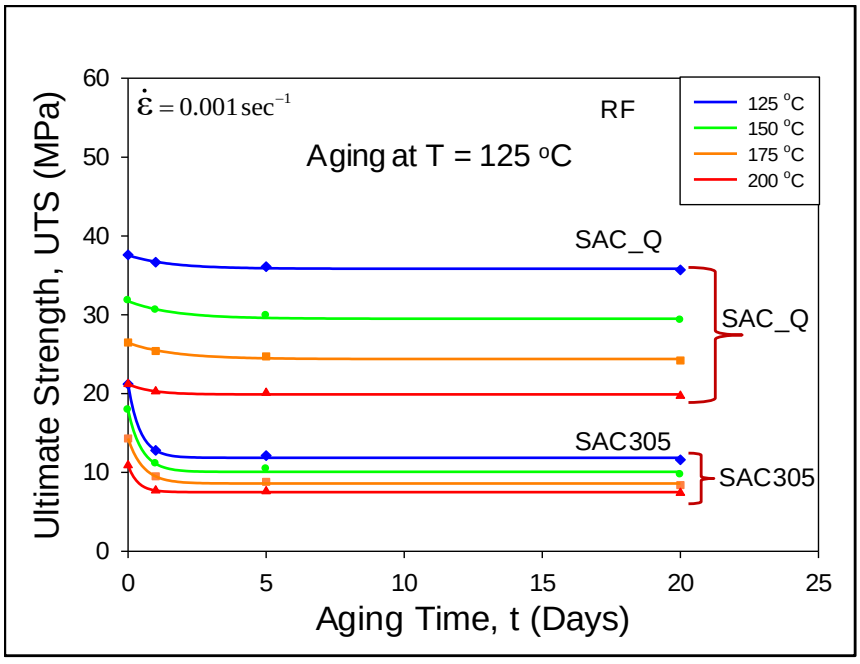

(b)

Figure 5.11 Variation of Mechanical Properties with Aging Time (Aging T = 125 °C)

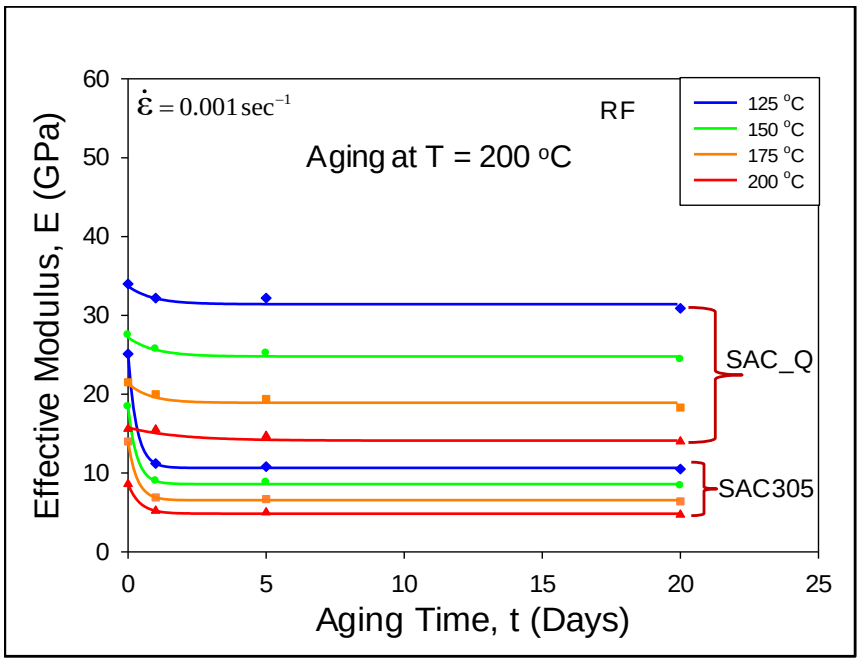

(a)

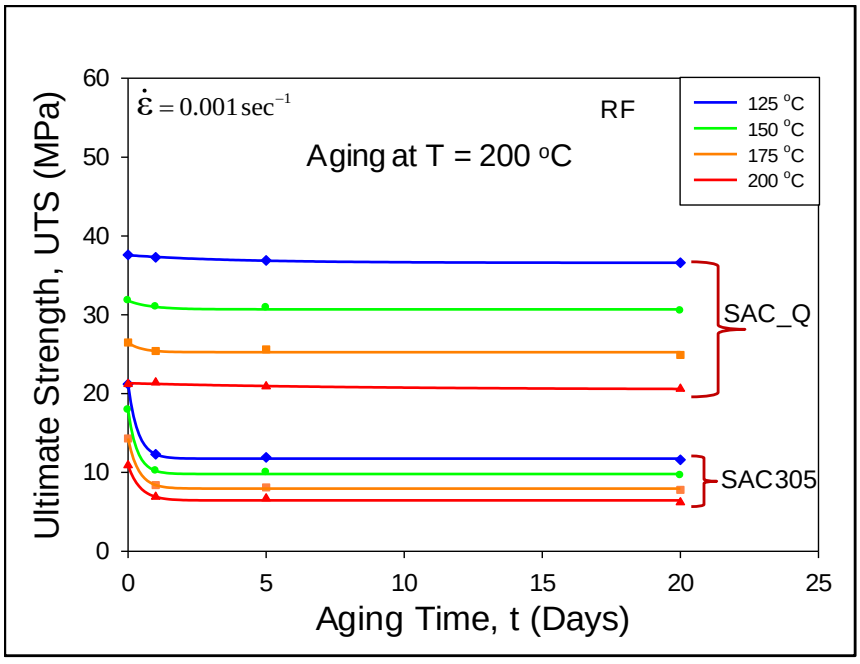

(b)

Figure 5.12 Variation of Mechanical Properties with Aging Time (Aging T = 200 °C)

5.5 Comparison of Average Stress-Strain Results between SAC305 and Innolot

Figure 5.13 shows the comparison of stress-strain behavior between SAC305 and Innolot. Each of the graphs shows comparison of the uniaxial stress-strain behavior of both alloys at a particular test temperature, with the various colored curves representing the different aging durations with blue= no aging, green= 1 day aging, orange= 5 days aging, and red= 20 days aging at T = 125 °C).

As mentioned before, the results are grouped in two sets of curves in each graph. The first set (top four curves) shows the aging dependent stress-strain behavior of Innolot, and the second set (bottom four curves) represents the same for SAC305. For each material, the top (blue) curve represents the average stress-strain curve for no aging, and the bottom (red) curve shows the average stress-strain curve at 20 days of aging.

At each test temperature, Innolot exhibited the best mechanical properties, and typically both the ultimate tensile strength (UTS) and effective elastic modulus (E) of Innolot were twice as large of the corresponding values for SAC305. Moreover, SAC305 alloy demonstrated large aging induced degradations with significant decrease in mechanical properties after only 1 day of aging at high temperature, while the Innolot showed negligible aging effects in all aging durations. Similar behavior is observed at extreme high temperature aging (aging ay T= 200 °C), shown in Figure 5.14.

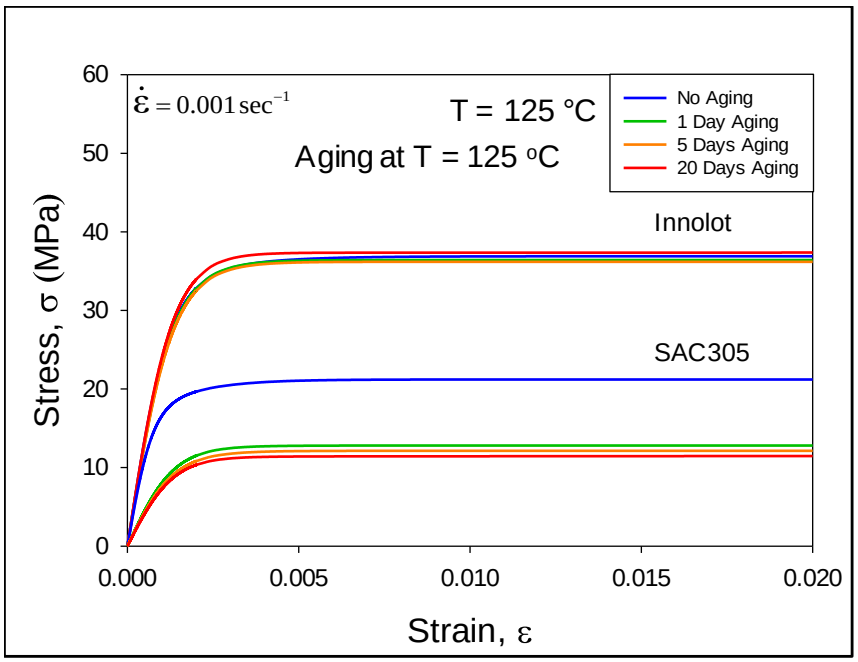
$\dot{\varepsilon} = 0.001\,\mathrm{sec}^{-1}$
T = 125 °C
Aging at T = 125 °C
No Aging
1 Day Aging
5 Days Aging
20 Days Aging
Innolot
SAC305
Stress, σ (MPa)
Strain, ε
0
10
20
30
40
50
60
0.000
0.005
0.010
0.015
0.020

(a)

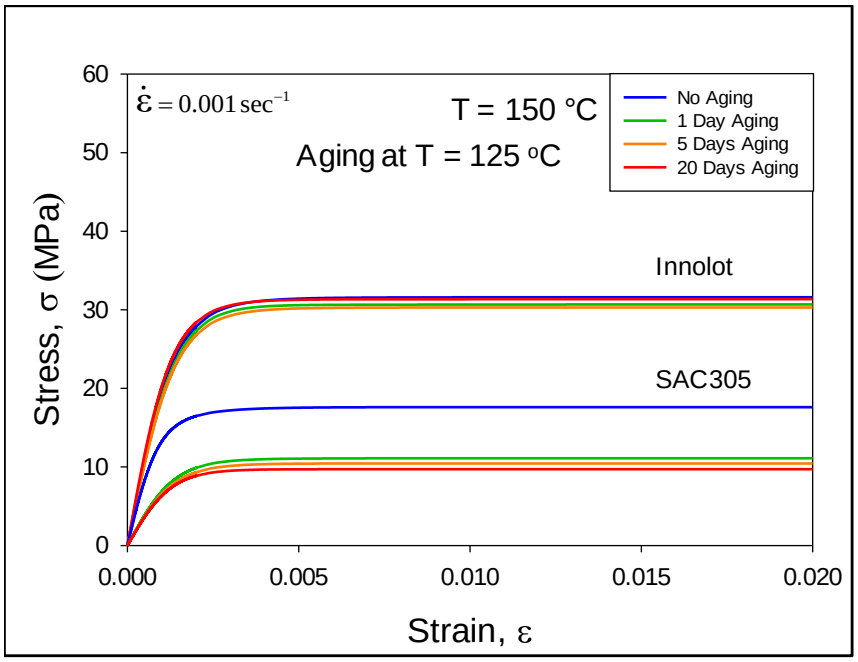
$\dot{\varepsilon} = 0.001\,\mathrm{sec}^{-1}$
T = 150 °C
Aging at T = 125 °C
No Aging
1 Day Aging
5 Days Aging
20 Days Aging
Innolot
SAC305
Stress, σ (MPa)
Strain, ε
0
10
20
30
40
50
60
0.000
0.005
0.010
0.015
0.020

(b)

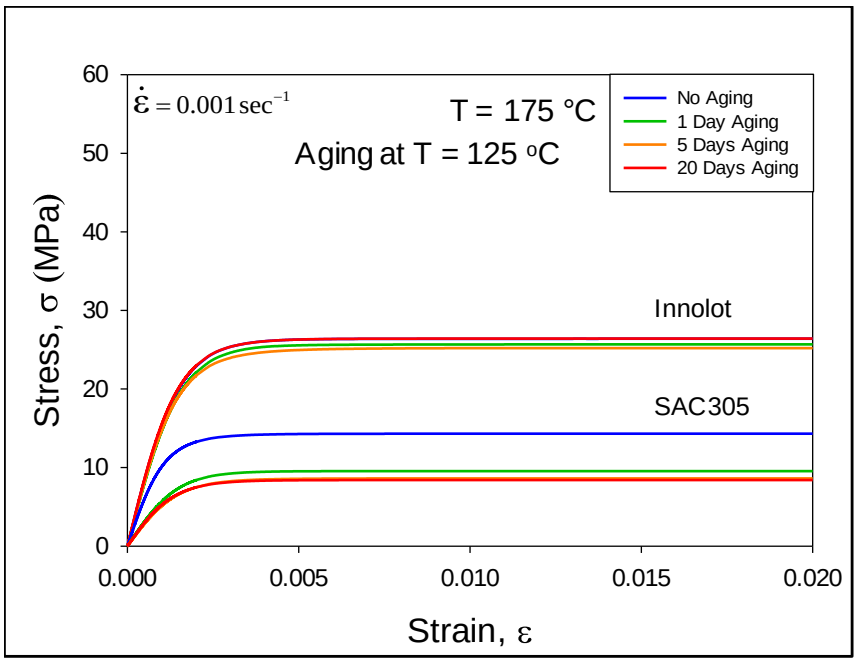

(c)

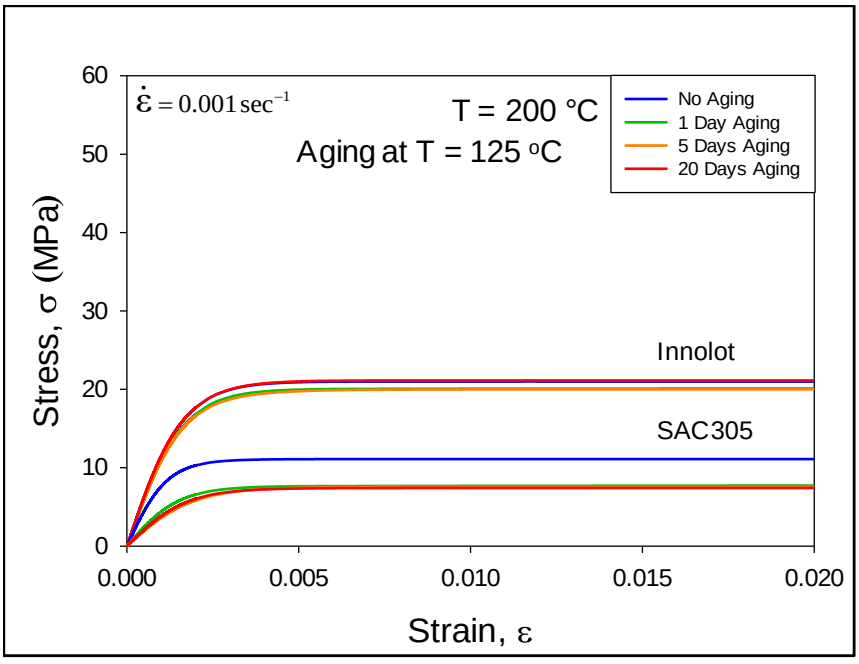

(d)

Figure 5.13 Comparison of Stress-Strain Curves (SAC305 and Innolot, Aging T = 125 °C)

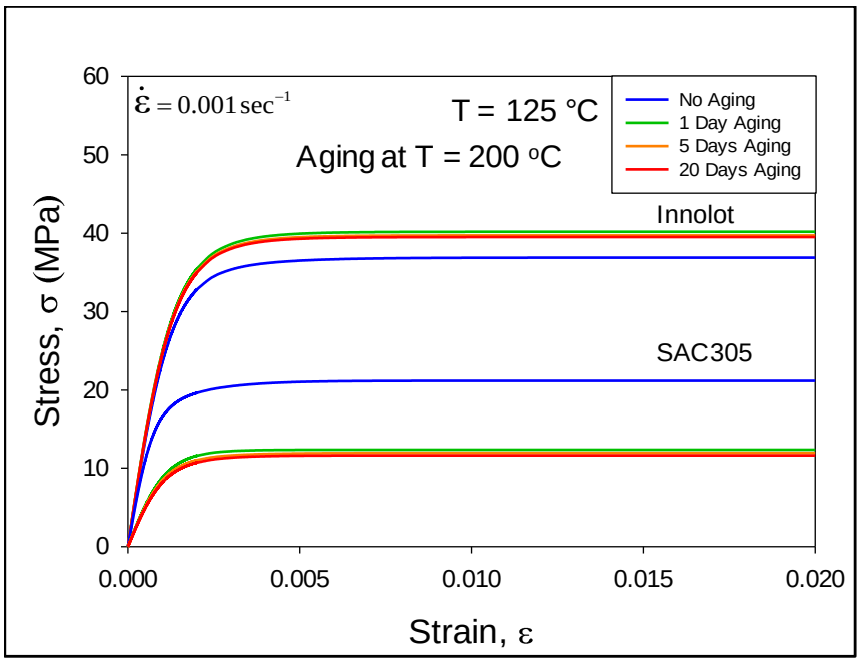
$\dot{\varepsilon} = 0.001\,\mathrm{sec}^{-1}$
T = 125 °C
Aging at T = 200 °C
No Aging
1 Day Aging
5 Days Aging
20 Days Aging
Innolot
SAC305
Stress, σ (MPa)
Strain, ε
0
10
20
30
40
50
60
0.000
0.005
0.010
0.015
0.020

(a)

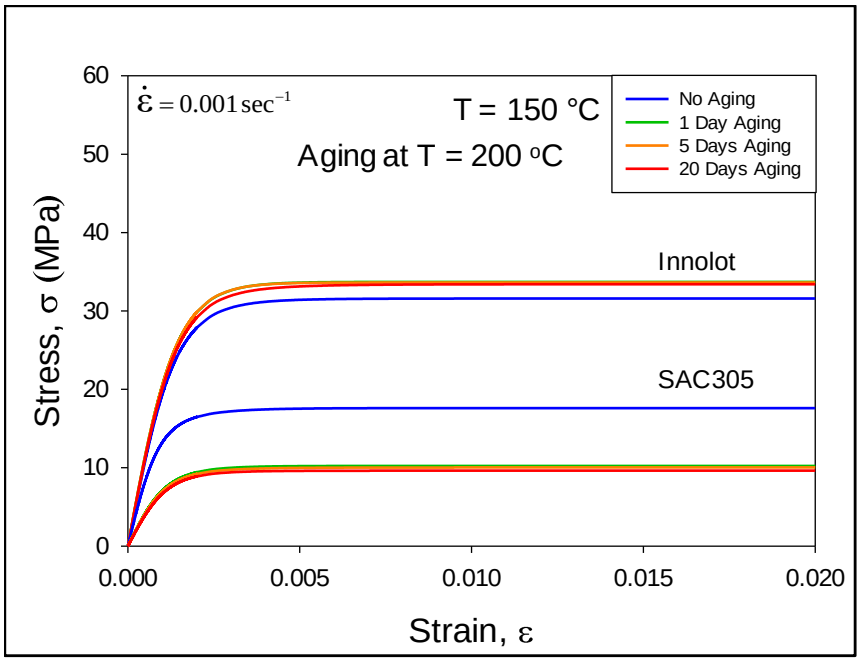
$\dot{\varepsilon} = 0.001\,\mathrm{sec}^{-1}$
T = 150 °C
Aging at T = 200 °C
No Aging
1 Day Aging
5 Days Aging
20 Days Aging
Innolot
SAC305
Stress, σ (MPa)
Strain, ε
0
10
20
30
40
50
60
0.000
0.005
0.010
0.015
0.020

(b)

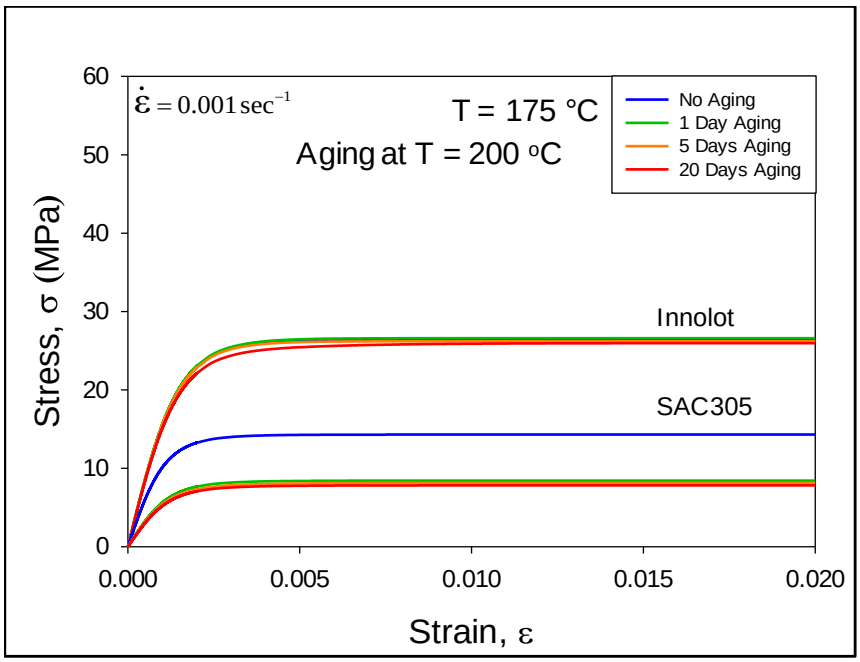

(c)

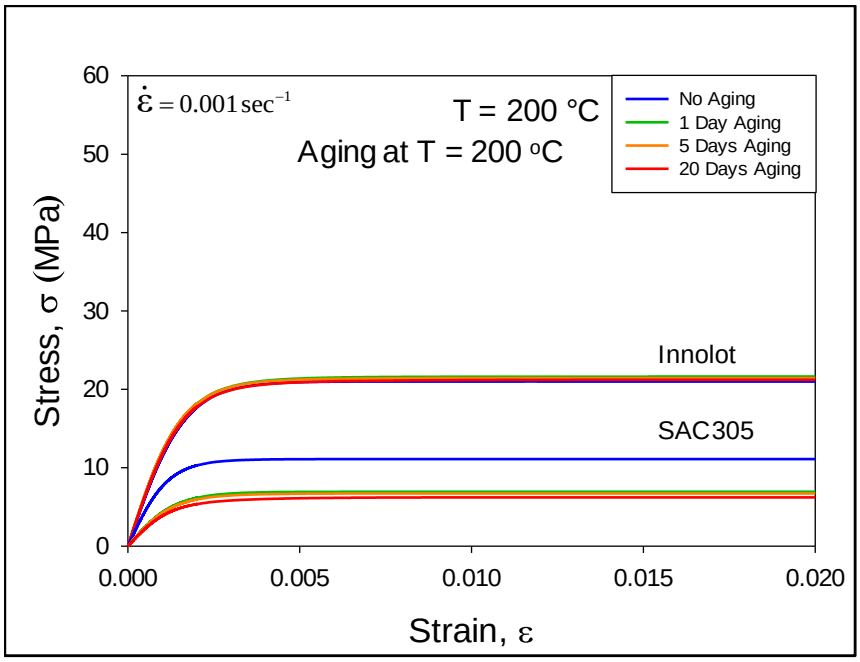

(d)

Figure 5.14 Comparison of Stress-Strain Curves (SAC305 and Innolot, Aging T = 200 °C)

5.6 Comparison of Mechanical Properties between SAC305 and Innolot

The aging dependent mechanical properties of SAC 305 and Innolot solder alloys were shown in Table 5.3 and 5.4. Variation of Effective Elastic Modulus are shown in Table 5.3 and Ultimate Tensile Strength (UTS) in Table 5.4. These properties have been extracted from the average stress-strain data at different test and aging conditions, and plotted as a function of test temperature in Figure 5.15 (aging T= 125 °C) and Figure 5.16 (aging T= 200 °C). Again, these properties are plotted as a function of aging duration in Figure 4.17 (aging T= 125 °C) and Figure 5.18 (aging T= 200 °C). As mentioned before, the results are grouped in two sets of curves in each graph. The first set (top four curves) shows the aging dependent mechanical properties of Innolot, and the second set (bottom four curves) represents the same for SAC305. For each material, the top (blue) curve represents the average stress-strain curve for no aging, and the bottom (red) curve shows the average stress-strain curve at 20 days of aging.

Large aging induced degradations are evident for SAC305 with a significant drop in properties after 5 days of aging at both 125 and 200 °C. After that point, the properties degrade at a much slower rate. Conversely, the properties of Innolot were found to degrade very slowly or remain nearly constant at all aging conditions.

Table 5.3 Comparison of Effective Elastic Modulus between SAC305 and Innolot

Alloy	Aging Temperature (°C)	Test Temperature (°C)	Effective Modulus, E (GPa)			
			No Aging	1 Day Aging	5 Days Aging	20 Days Aging
SAC305	125	125	25.1	9.4	9.0	8.6
		150	18.4	8.1	7.6	7.6
		175	14.0	6.6	6.4	6.2
		200	8.6	5.1	4.7	4.4
	200	125	25.1	11.2	10.8	10.5
		150	18.4	9.0	8.8	8.4
		175	14.0	6.9	6.7	6.4
		200	8.6	5.2	5.0	4.7
Innolot	125	125	29.6	28.9	28.8	29.9
		150	24.3	23.9	23.7	24.5
		175	17.6	17.3	17.1	18.0
		200	12.9	12.6	12.3	13.1
	200	125	28.4	29.6	29.3	29.2
		150	22.7	24.0	23.9	23.5
		175	17.6	18.1	17.9	17.5
		200	12.9	13.7	13.7	13.3

Table 5.4 Comparison of Ultimate Tensile Strength between SAC305 and Innolot

Alloy	Aging Temperature (°C)	Test Temperature (°C)	Ultimate Tensile Strength, UTS (MPa)			
			No Aging	1 Day Aging	5 Days Aging	20 Days Aging
SAC305	125	125	21.2	12.8	12.1	11.6
		150	17.9	11.1	10.4	9.7
		175	14.3	9.5	8.8	8.4
		200	10.9	7.7	7.6	7.4
	200	125	21.2	12.3	11.9	11.6
		150	17.9	10.2	10.0	9.6
		175	14.3	8.4	8.1	7.8
		200	10.9	6.9	6.7	6.2
Innolot	125	125	36.9	36.4	36.2	37.2
		150	31.6	30.8	30.6	31.3
		175	26.4	25.9	25.6	26.6
		200	21.0	20.5	20.3	21.1
	200	125	36.9	40.2	39.7	39.5
		150	31.6	33.7	33.6	33.4
		175	26.4	26.6	26.2	25.9
		200	21.0	21.6	21.4	21.2

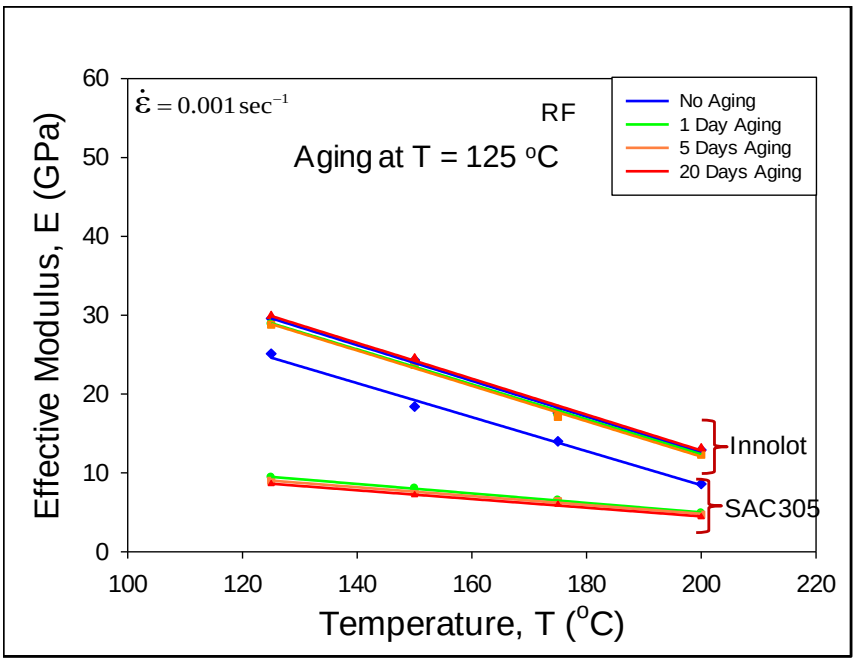

(a)

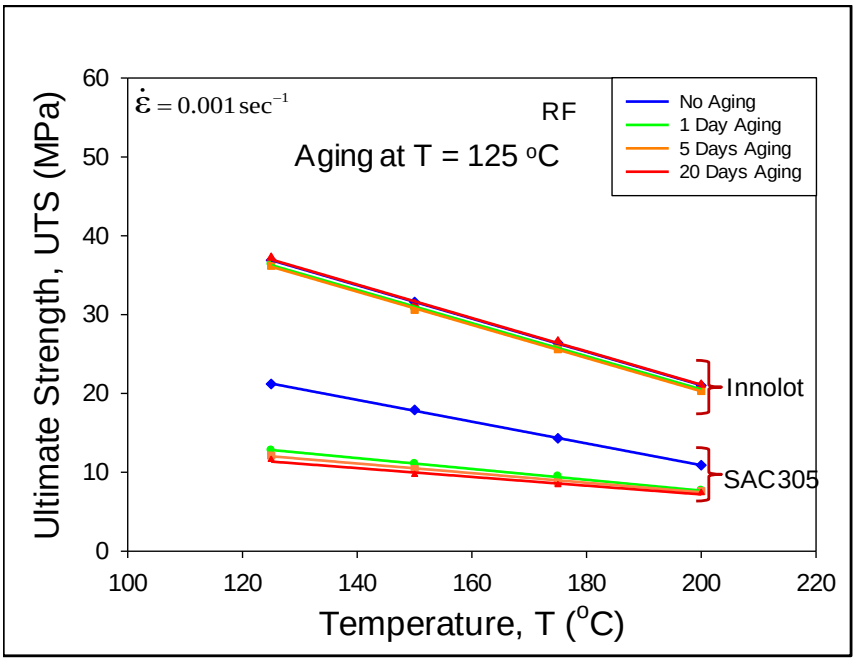

(b)

Figure 5.15 Variation of Mechanical Properties with Temperature (Aging T = 125 °C)

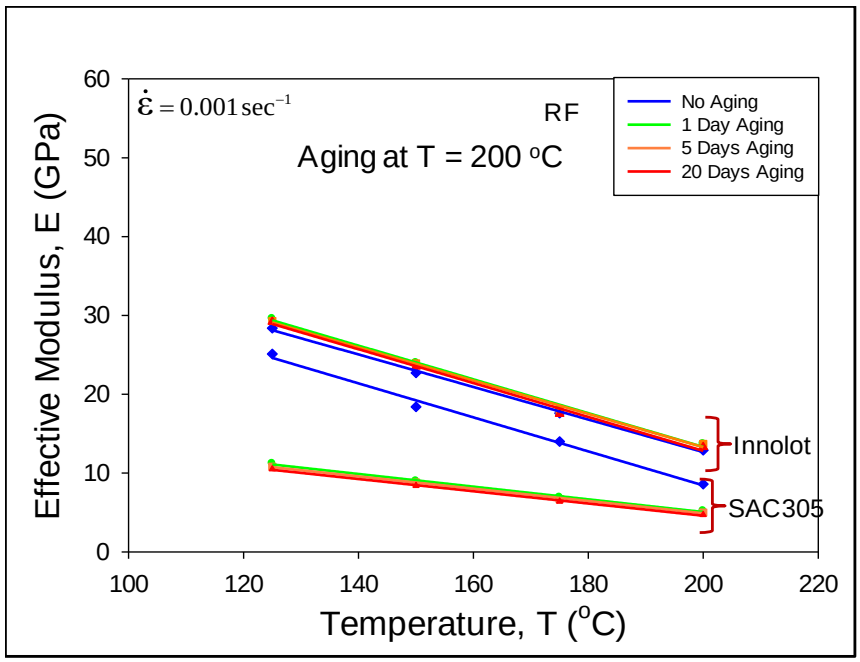

(a)

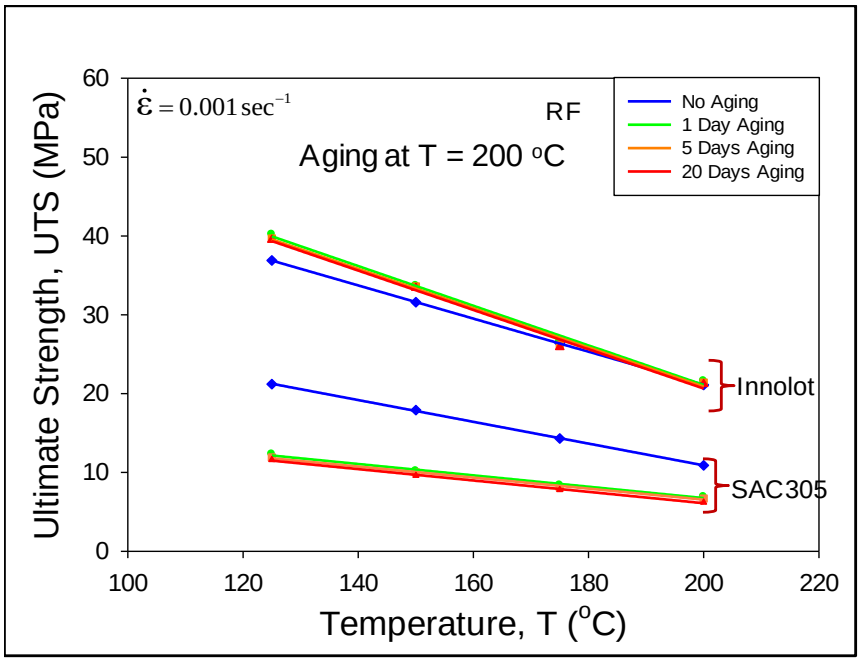

(b)

Figure 5.16 Variation of Mechanical Properties with Temperature (Aging T = 200 °C)

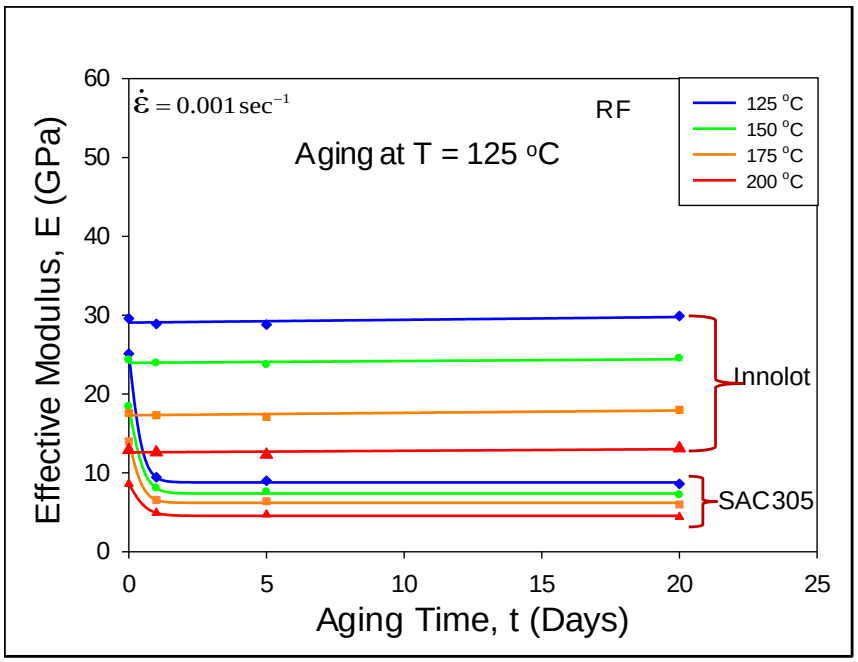

(a)

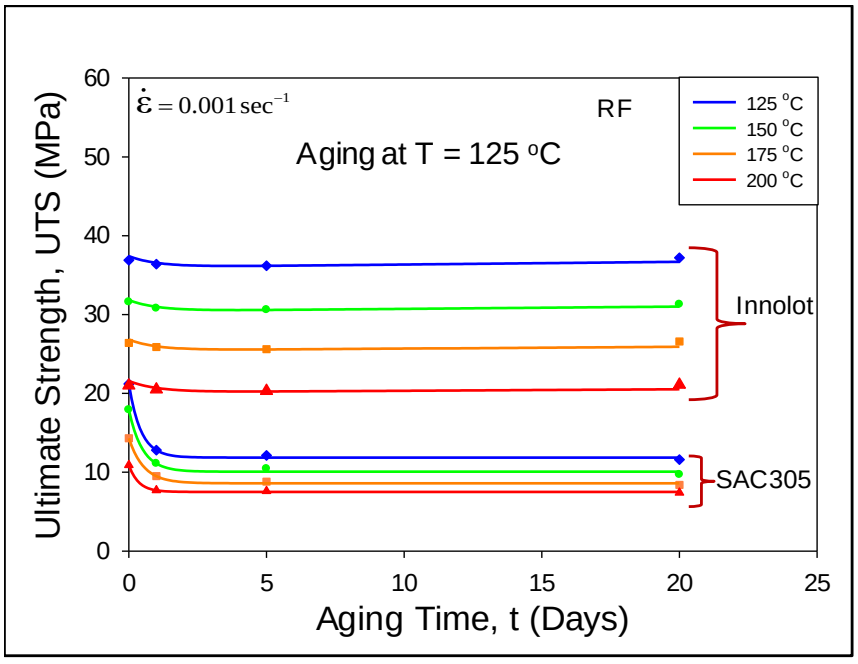

(b)

Figure 5.17 Variation of Mechanical Properties with Aging Time (Aging T = 125 °C)

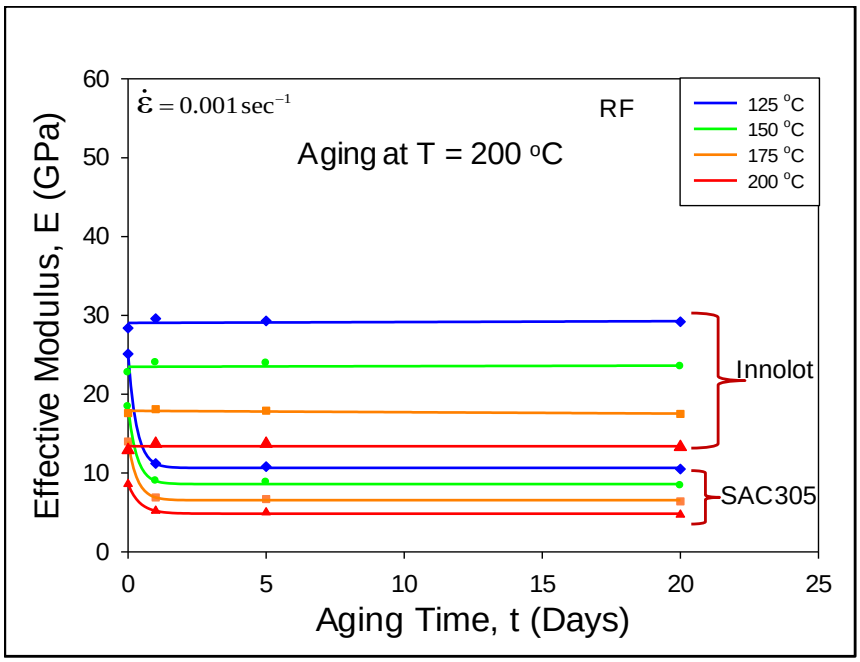

(a)

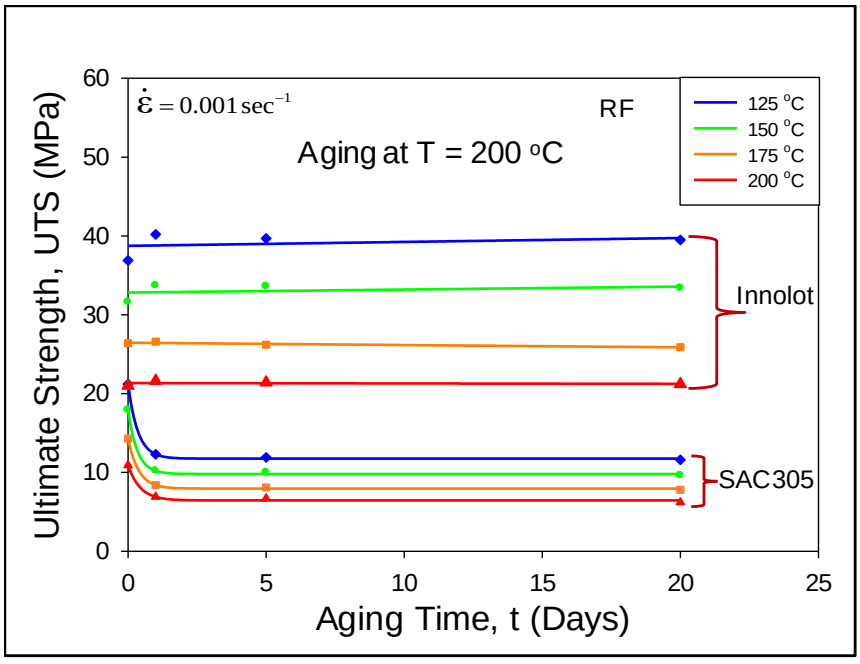

(b)

Figure 5.18 Variation of Mechanical Properties with Aging Time (Aging T = 200 °C)

5.7 High Temperature Creep Behavior of SAC305 Solder

Aging effects on the creep behavior of SAC305 solder alloys were examined by performing creep tests with a test matrix of different stress levels, testing temperatures, and aging conditions. Both water quenched (WQ) and reflowed (RF) specimens were explored. The stress levels for the creep tests were determined according to the UTS of the solders.

5.7.1 High Temperature Creep Behavior of Water Quenched SAC305 Solder

In one study, SAC305 uniaxial test specimens were formed by water quenched solidification profile and kept at room temperature for 10 days. Creep tests were performed in these aged specimens at two stress levels, such as, 7.5 and 10 MPa. The creep tests were conducted at 100, 125, 150, 175, and 200 °C. Figure 5.19 illustrates creep curves of SAC305 (WQ) under fixed stress levels of σ= 7.5 and 10 MPa. The five colored curves in each plot represent five different testing temperatures (T = 100, 125, 150, 175, and 200 °C). In each plot, we can see variations of secondary creep strain rate as temperature changes. However, the variations appear to be more significant at higher stress levels. For example, in Figure 5.19b, the creep rate increases dramatically at higher temperatures of 150-200 °C. At T = 200 °C, the samples experiences tertiary creep when the load was applied for about 2 hours. Increased dislocation movements occur for the higher creep rates at higher stress levels. At higher temperatures, the dislocation movements occur more easily, resulting in more creep for the same applied loading.

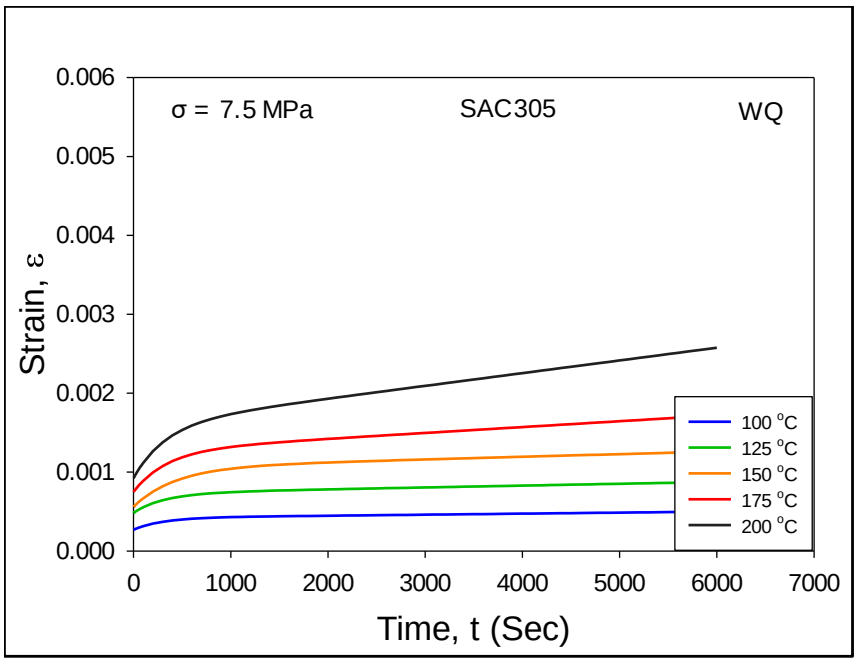

(a)

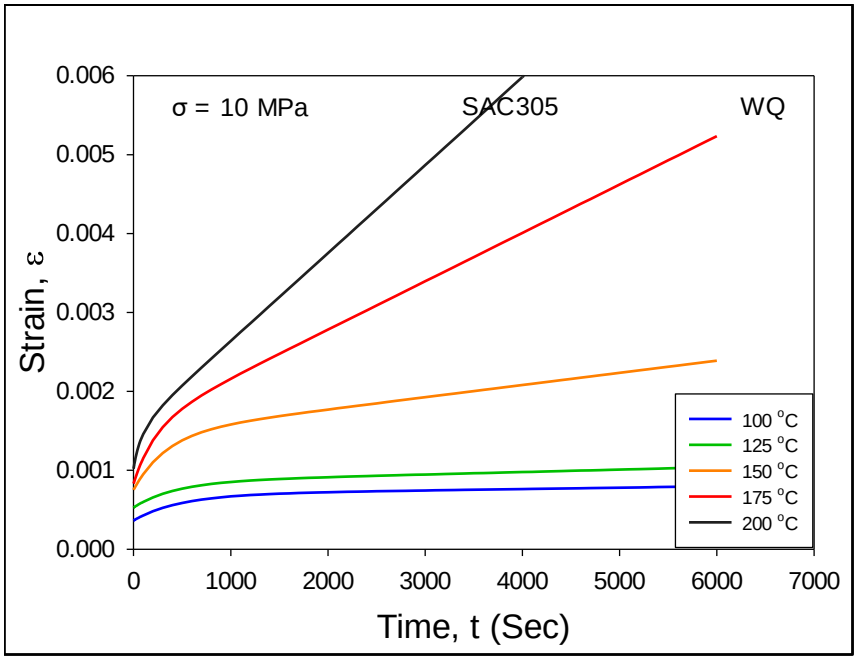

(b)

Figure 5.19 Variation of Creep Behavior with Test Temperature and Applied Stress

The average secondary creep strain rates have been extracted from the fitting equation and tabulated in Table 5.5. Also, the variations of creep rate with temperature and stress level are shown in Figure 5.20.

Table 5.5 Secondary Creep Strain Rate of SAC305 (WQ)

Temperature (°C)	Strain Rate ($x10^{-8}$ sec^{-1})	
	7.5 MPa	10 MPa
100	1.3	1.8
125	2.3	3.1
150	3.9	15.5
175	7.5	61.0
200	18.6	114.0

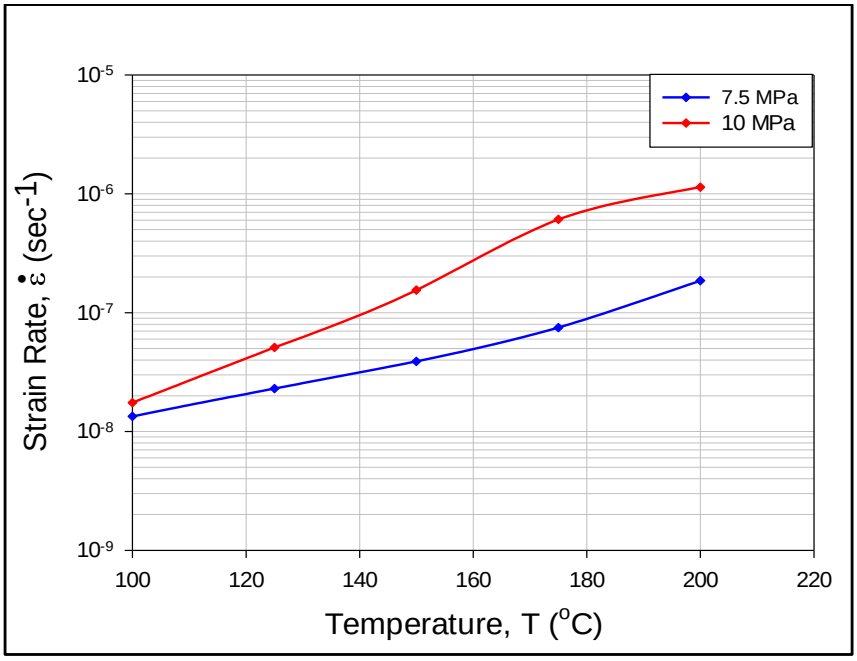

(d)

Figure 5.20 Variation of Creep Strain Rate with Test Temperature and Applied Stress

5.7.2 High Temperature Creep Behavior of Reflowed SAC305 Solder

In this study, SAC305 specimens were reflowed with a controlled reflow cooling profile described in earlier sections. The creep study in this work involved specimens with prior aging at T = 125 °C for similar aging intervals (0, 1, 5, and 20 days aging) to the aging studies for the stress-strain specimens. The creep tests were conducted at four test temperatures (125, 150, 175, and 200 °C) under 4 MPa stress level.

Figure 5.21 illustrate the recorded creep curves for the reflowed SAC305 solder specimens. Each curve represents the average of four/five creep curve fitted with four parameter Burger's (spring-dashpot) model in 3.4. In this figure, there are four graphs for the four different aging conditions. In each graph, the various creep curves are for different testing temperatures, illustrating the variation of the creep response with testing temperature at a particular aging condition. For example, in Figure 4.4 (a), the blue curve at the bottom is the creep response for non-aged specimens at a testing temperature of 125 °C, and the top red curve shows the creep response at a testing temperature of 200 °C. As expected, it is observed from the figures that creep rates are much higher at elevated temperatures than at room temperature at each aging condition.

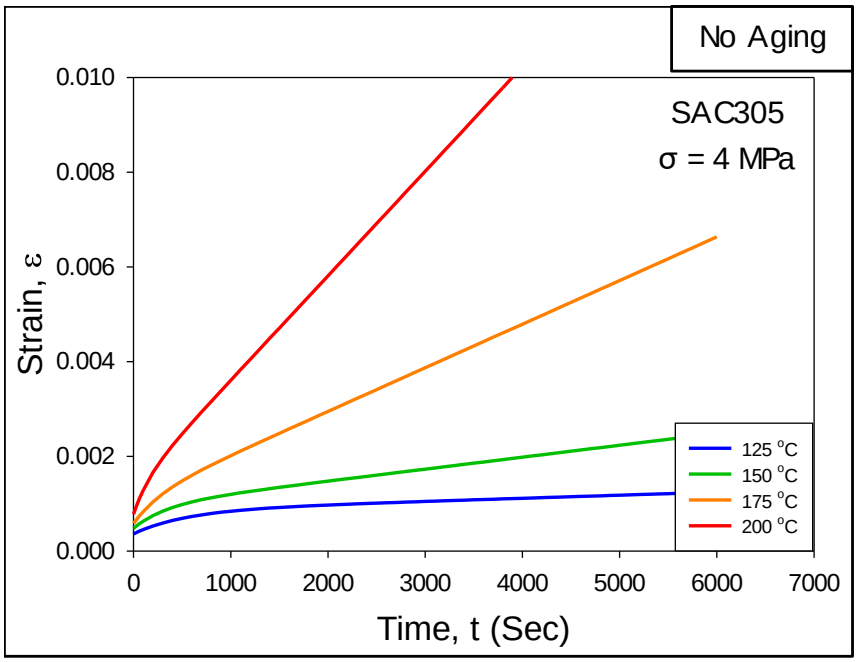
No Aging
SAC305
σ = 4 MPa
Strain, ε
0.010
0.008
0.006
0.004
0.002
0.000
0
1000
2000
3000
4000
5000
6000
7000
Time, t (Sec)
125 °C
150 °C
175 °C
200 °C

(a)

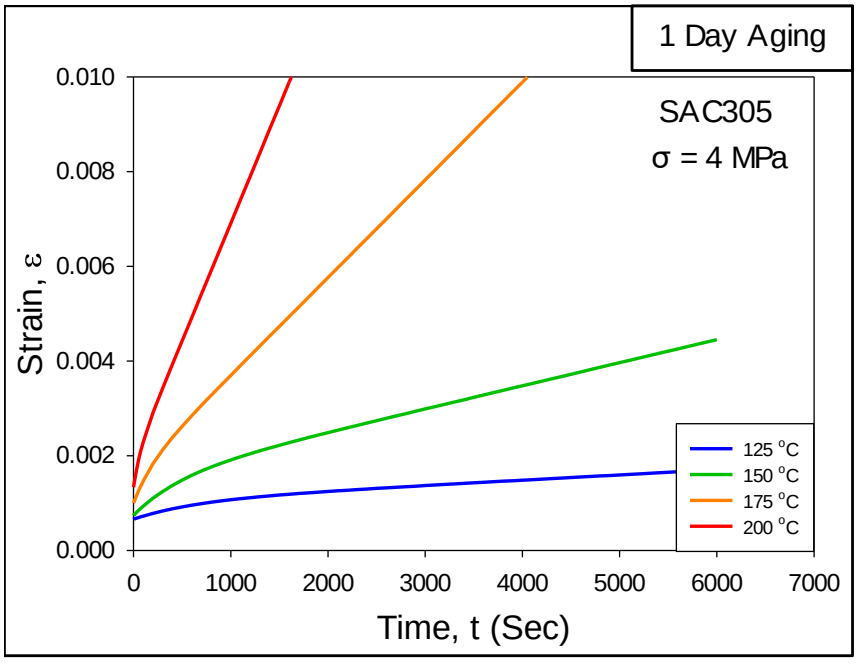
1 Day Aging
SAC305
σ = 4 MPa
Strain, ε
0.010
0.008
0.006
0.004
0.002
0.000
0
1000
2000
3000
4000
5000
6000
7000
Time, t (Sec)
125 °C
150 °C
175 °C
200 °C

(b)

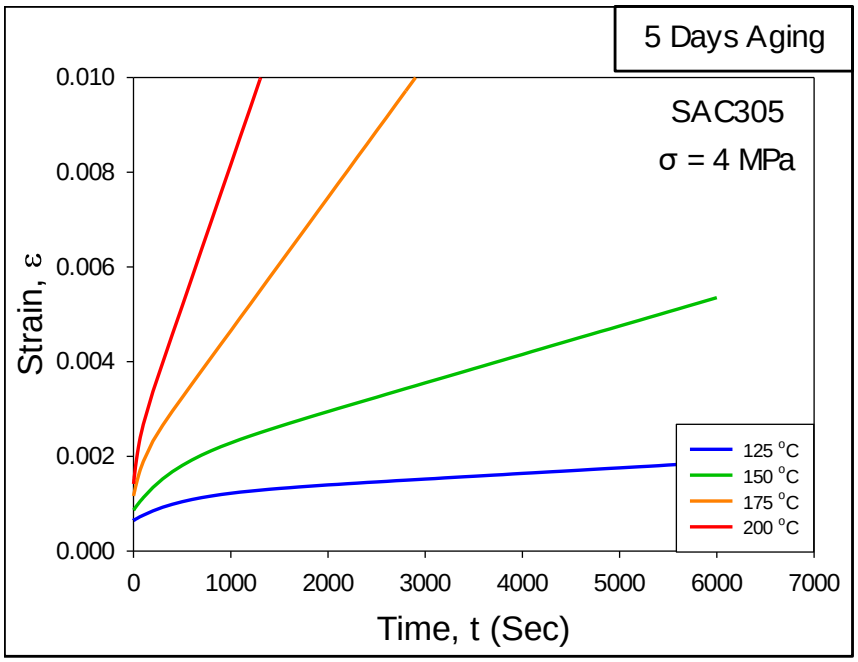

(c)

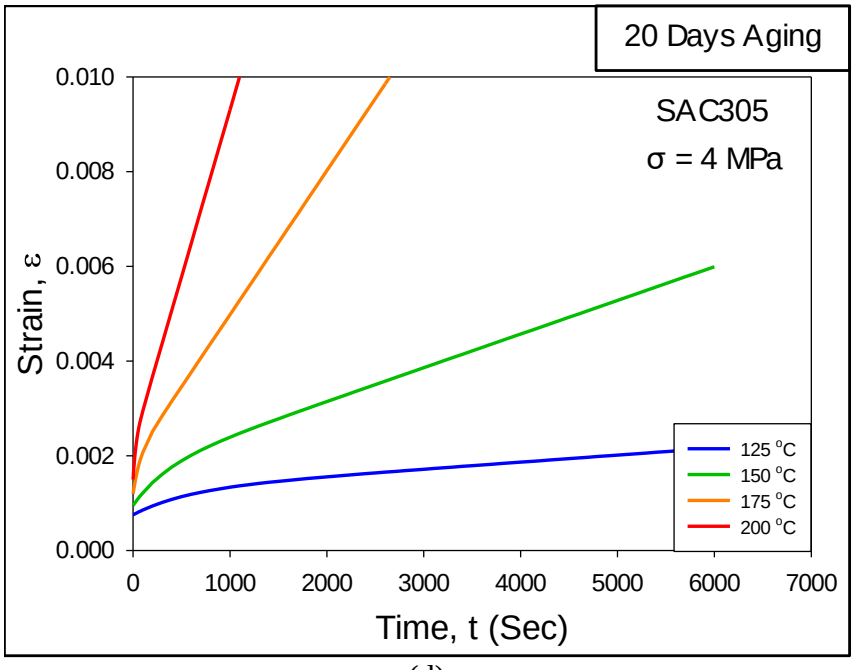

(d)

Figure 5.21 Variation of Creep Behavior with Aging Time (SAC305)

5.7.3 High Temperature Creep Behavior of SAC_Q Solder

In this study, SAC_Q specimens were reflowed with a controlled reflow cooling profile described in earlier sections. The creep study in this work involved specimens with prior aging at T = 125 °C for similar aging intervals (0, 1, 5, and 20 days aging) to the aging studies for the stress-strain specimens. The creep tests were conducted at four test temperatures (125, 150, 175, and 200 °C) under 4 MPa stress level.

Figure 5.22 illustrate the recorded creep curves for the reflowed SAC_Q solder specimens. Each curve represents the average of four/five creep curve fitted with four parameter Burger's (spring-dashpot) model in 3.4. In this figure, there are four graphs for the four different aging conditions. In each graph, the various creep curves are for different testing temperatures, illustrating the variation of the creep response with testing temperature at a particular aging condition. For example, in Figure 5.22 (a), the blue curve at the bottom is the creep response for non-aged specimens at a testing temperature of 125 °C, and the top red curve shows the creep response at a testing temperature of 200 °C. As expected, it is observed from the figures that creep rates are much higher at elevated temperatures than at room temperature at each aging condition.

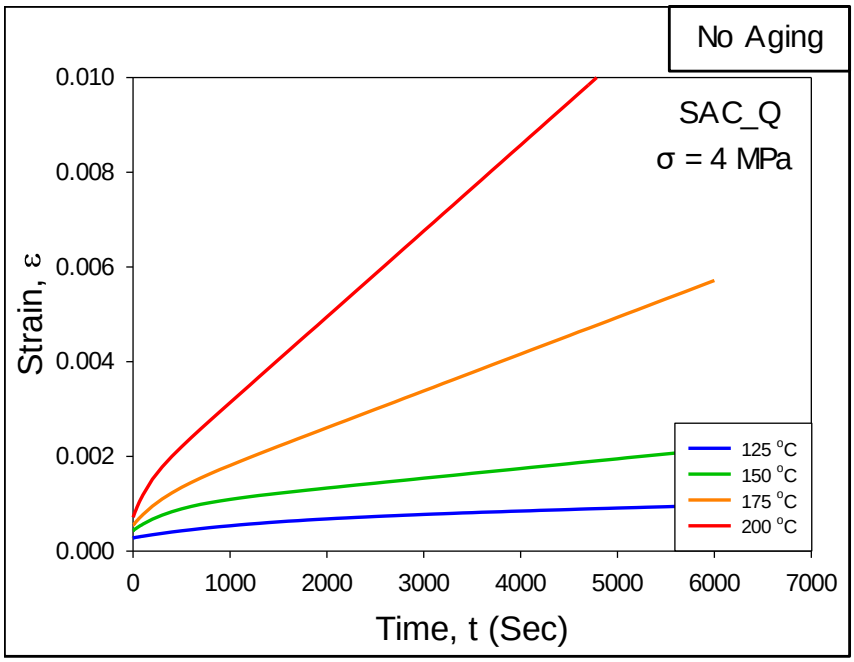
No Aging
SAC_Q
σ = 4 MPa
Strain, ε
0.010
0.008
0.006
0.004
0.002
0.000
0
1000
2000
3000
4000
5000
6000
7000
Time, t (Sec)
125 °C
150 °C
175 °C
200 °C

(a)

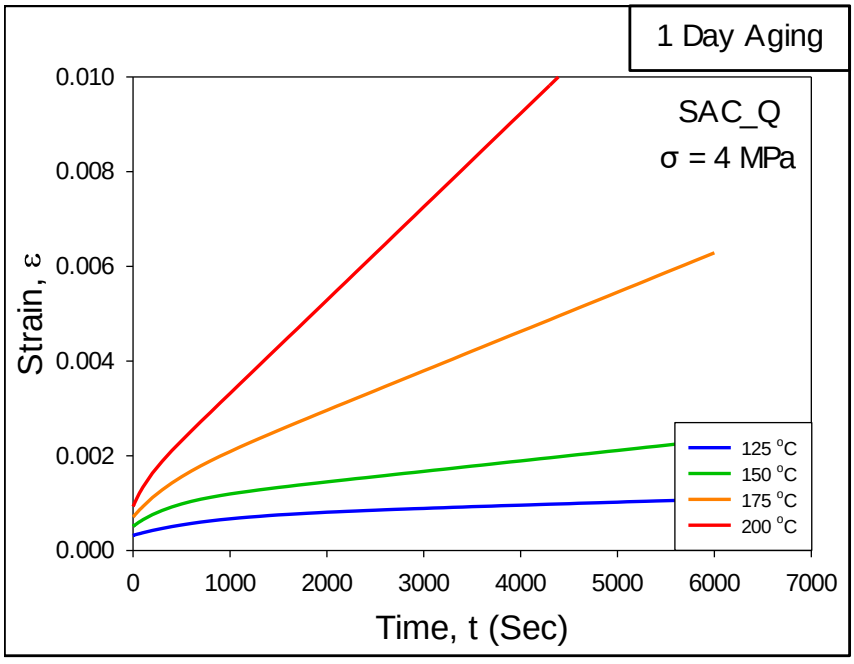
1 Day Aging
SAC_Q
σ = 4 MPa
Strain, ε
0.010
0.008
0.006
0.004
0.002
0.000
0
1000
2000
3000
4000
5000
6000
7000
Time, t (Sec)
125 °C
150 °C
175 °C
200 °C

(b)

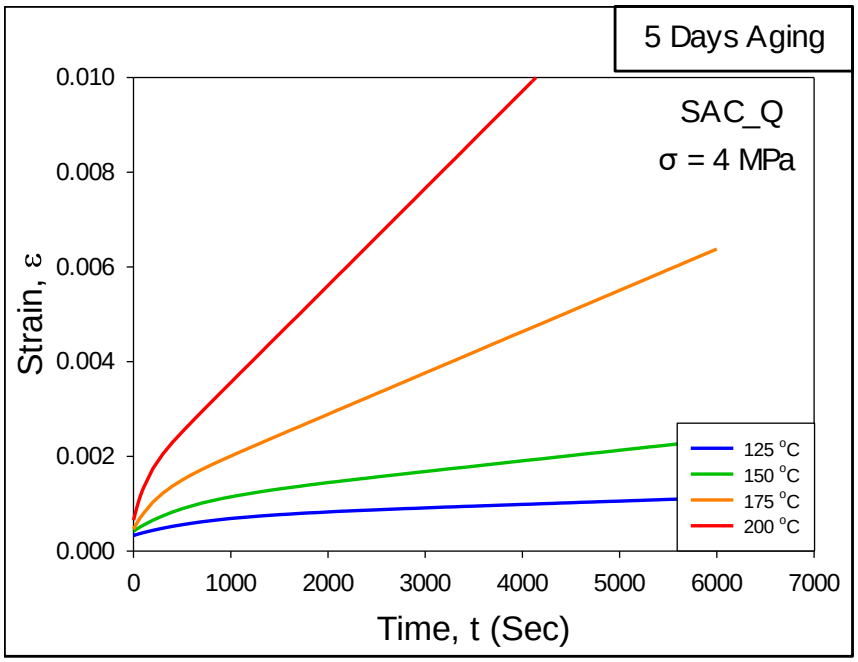

(c)

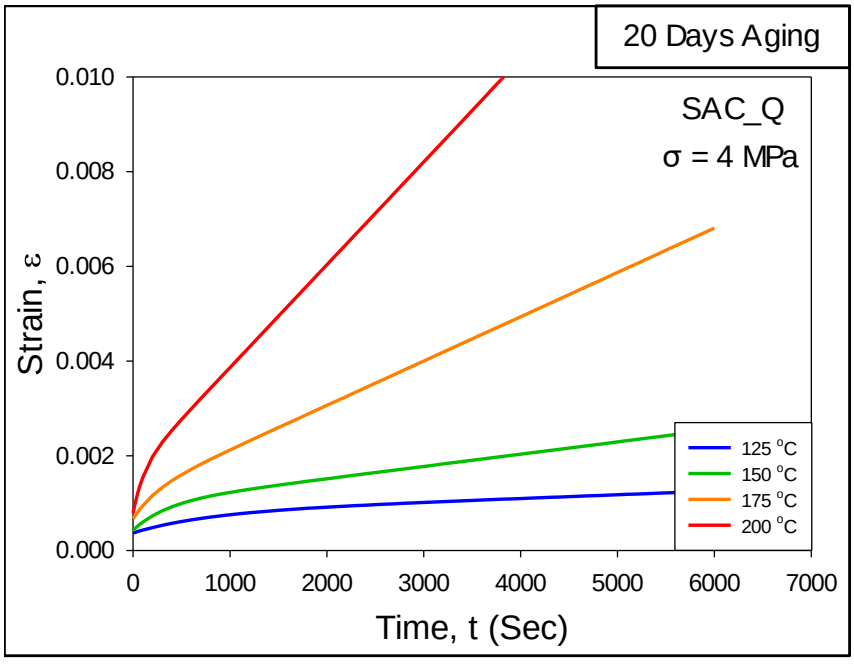

(d)

Figure 5.22 Variation of Creep Behavior with Aging Time (SAC_Q)

5.7.4 High Temperature Creep Behavior of Innolot Solder

High temperature creep behavior of Innolot solder alloys has also been explored in this study. The experimental and aging conditions were kept similar to the SAC305 and SAC_Q alloys.

The recorded creep curves of Innolot solder specimens have been presented in Figure 5.23 in a similar way as other two alloys. For example, in Figure 5.23 (a), the blue curve at the bottom is the creep response for non-aged specimens at a testing temperature of 125 °C, and the top red curve shows the creep response at a testing temperature of 200 °C. As expected, creep rates are much higher at elevated temperatures than at room temperature at each aging condition.

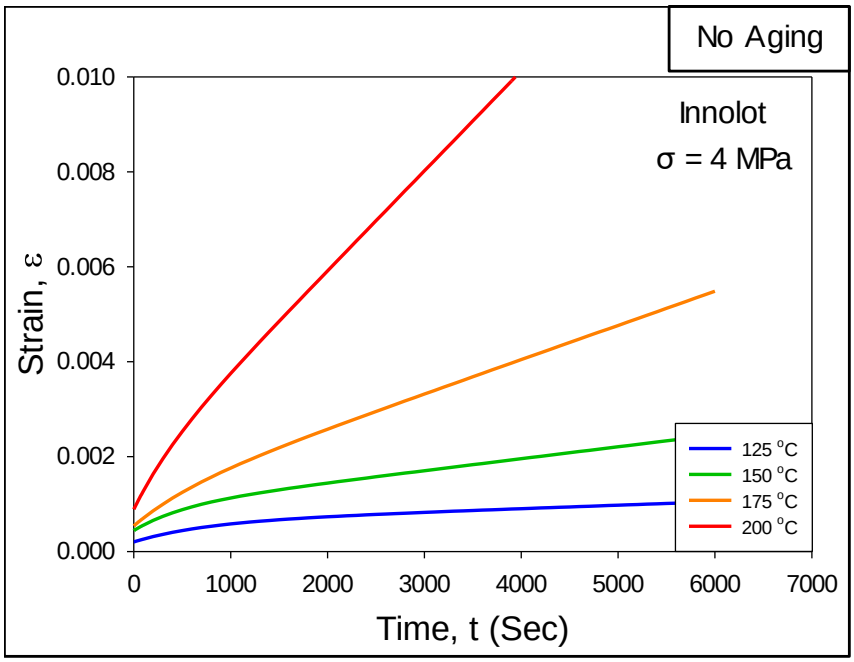
No Aging
Innolot
σ = 4 MPa
Strain, ε
0.010
0.008
0.006
0.004
0.002
0.000
0
1000
2000
3000
4000
5000
6000
7000
Time, t (Sec)
125 °C
150 °C
175 °C
200 °C

(a)

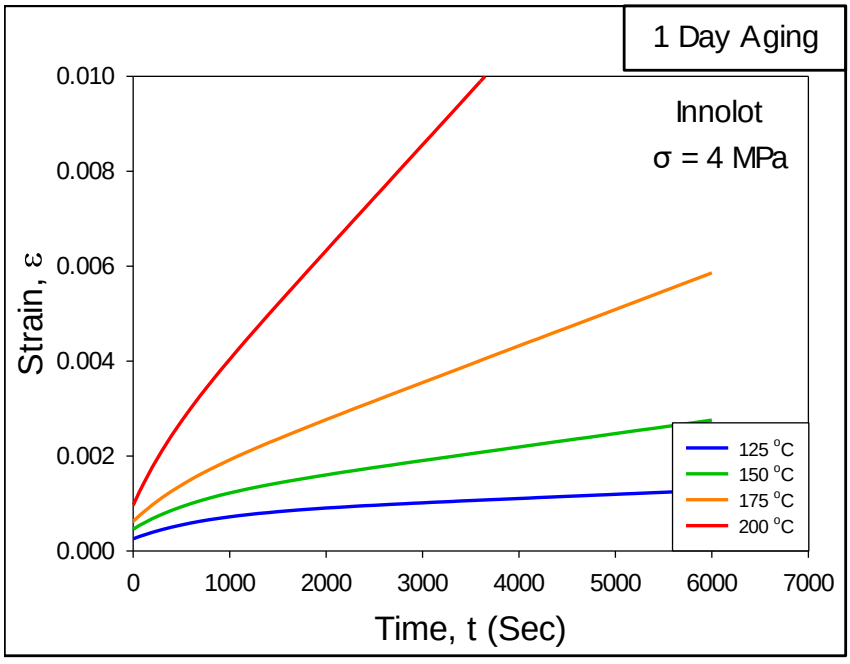
1 Day Aging
Innolot
σ = 4 MPa
Strain, ε
0.010
0.008
0.006
0.004
0.002
0.000
0
1000
2000
3000
4000
5000
6000
7000
Time, t (Sec)
125 °C
150 °C
175 °C
200 °C

(b)

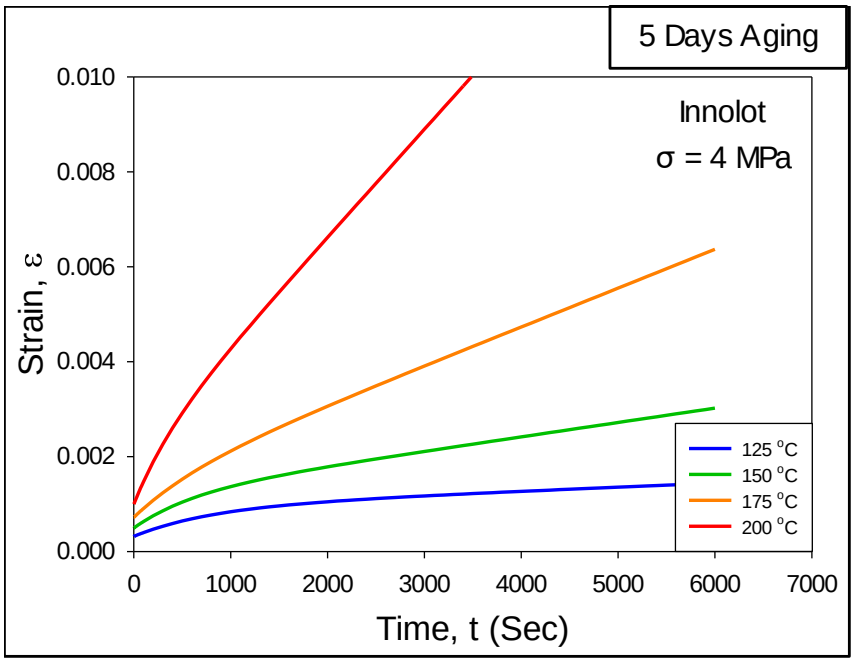

(c)

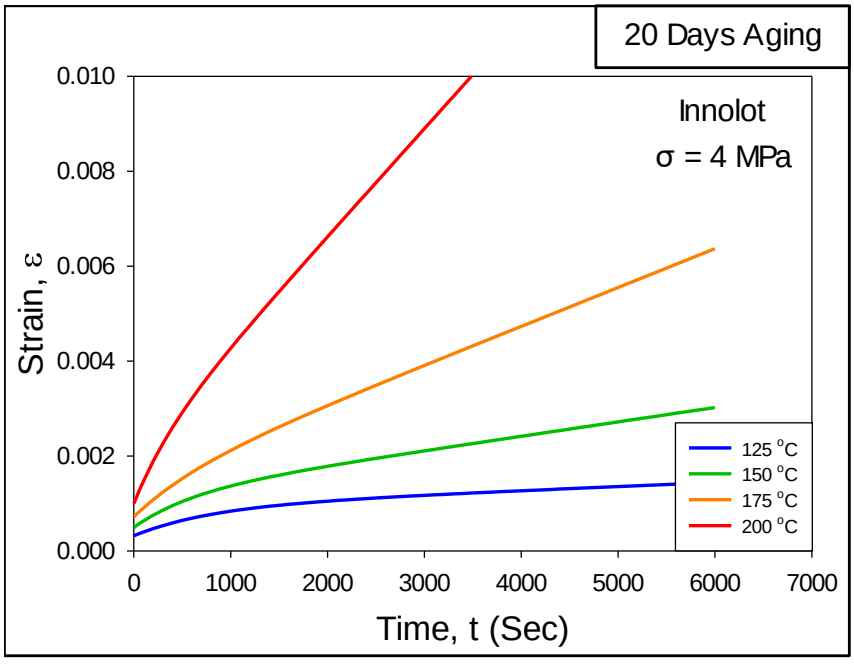

(d)

Figure 5.23 Variation of Creep Behavior with Aging Time (Innolot)

5.7.5 Comparison of Creep Behavior of SAC305 and SAC_Q

Figure 5.24 illustrates the aging dependent creep curves for SAC305 and SAC_Q under a fixed stress level of 4 MPa. Each of the graphs shows a comparative analysis of the creep behavior of both alloys at a particular test temperature, with the various colored curves representing the different aging durations (no aging, and 1, 5, and 20 days of aging at T = 125 °C). The solid curves represent average creep curves for SAC305 and the dashed curves correspond to SAC_Q. In all cases, the creep rates for SAC_Q are lower than those for SAC305 under comparable test conditions. Comparing the different graphs, we can see significant increases in the secondary creep strain rate for both alloys as the temperature increases. For testing at T = 200 °C, the samples experienced tertiary creep when the load was applied for about 2 hours. Increased dislocation movements occur for the higher creep rates at higher temperatures.

It is observed that SAC305 shows a significant degradation in its creep properties (sharp increase of the secondary creep strain rate) as the aging time increases. However, the creep rate for SAC_Q varied only slightly with aging, similar to the small changes observed in the tensile test properties with aging time. In addition, the creep behaviors of SAC_Q for all aging conditions were comparable to the creep behavior of SAC305 with no aging (the solid blue curve is within all the dashed curves at each test temperature).

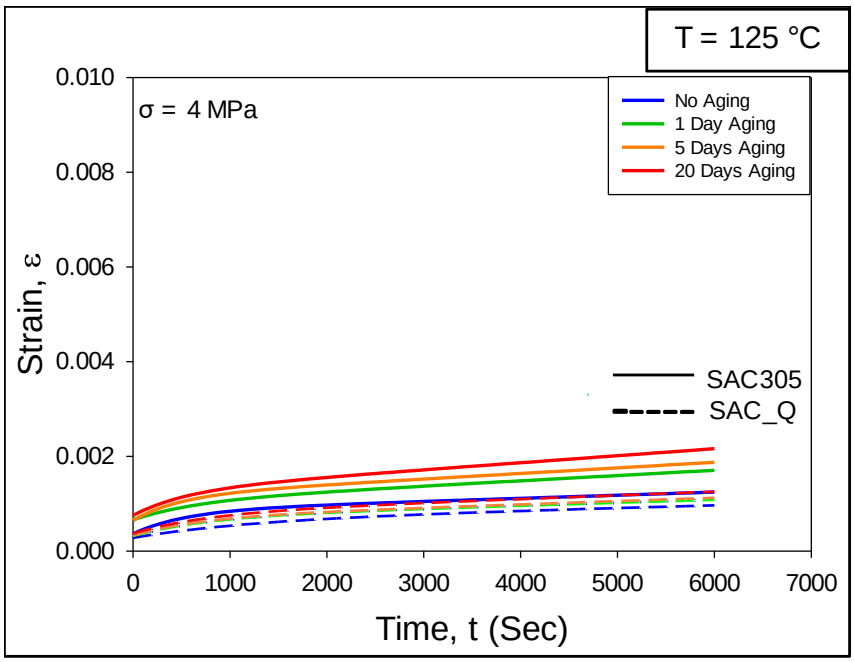
T = 125 °C
σ = 4 MPa
No Aging
1 Day Aging
5 Days Aging
20 Days Aging
SAC305
SAC_Q
Strain, ε
Time, t (Sec)
0.010
0.008
0.006
0.004
0.002
0.000
0
1000
2000
3000
4000
5000
6000
7000

(a)

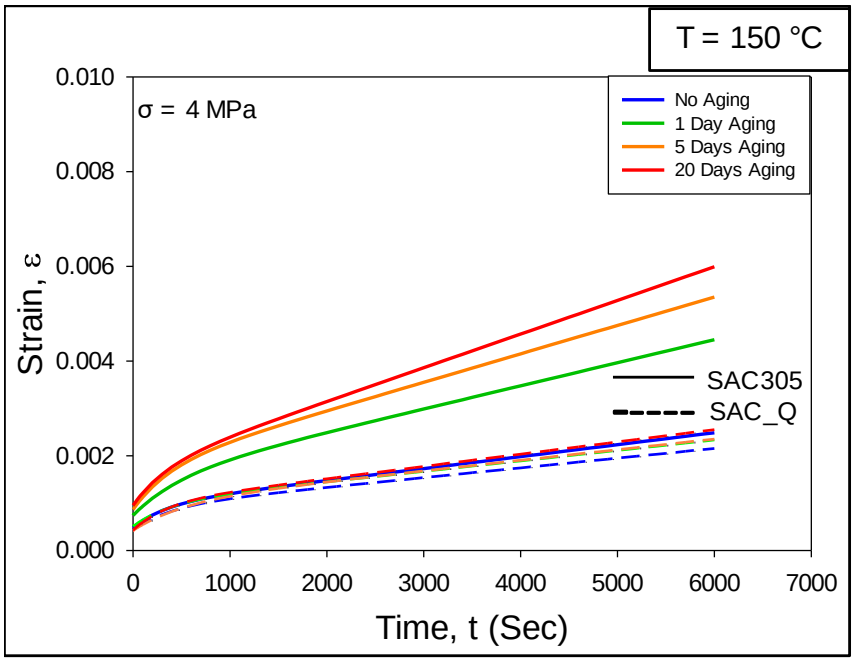
T = 150 °C
σ = 4 MPa
No Aging
1 Day Aging
5 Days Aging
20 Days Aging
SAC305
SAC_Q
Strain, ε
Time, t (Sec)
0.010
0.008
0.006
0.004
0.002
0.000
0
1000
2000
3000
4000
5000
6000
7000

(b)

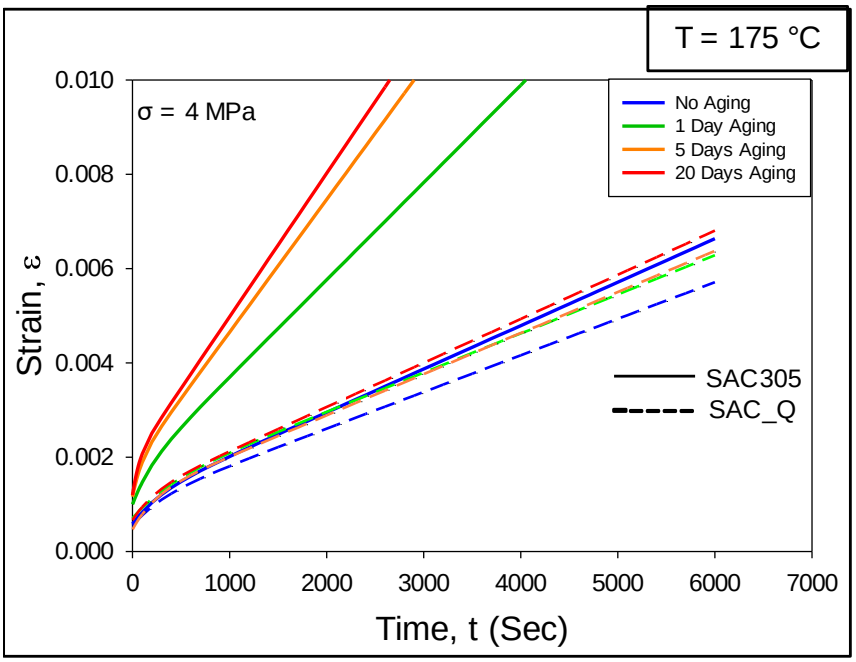

(c)

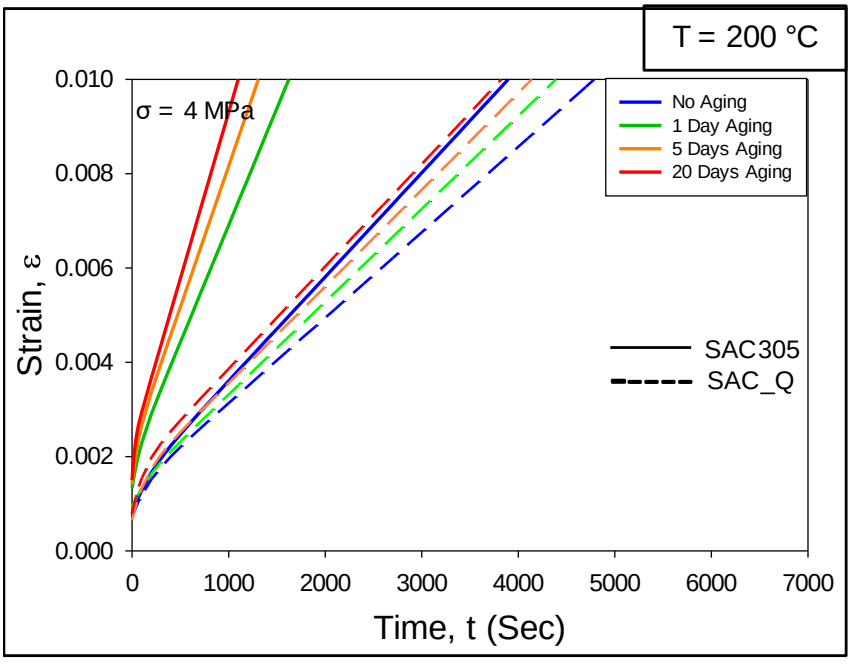

(d)

Figure 5.24 Comparison of Creep Behavior between SAC305 and SAC_Q

The average secondary creep strain rates extracted from the data are tabulated in Table 5.6. The variations of secondary creep strain rate with testing temperature and aging

time of both alloys are plotted in Figure 5.25 for comparison. Each of the graphs shows comparison of secondary creep strain rate of both alloys at different test temperature and aging condition, with various colored curves representing different aging durations (Figure 5.25 (a)) and different test temperatures (Figure 5.25 (b)). The solid curves represent average creep curves for SAC305 and the dashed curves correspond to SAC_Q.

Large aging induced degradation in secondary creep strain rate are evident for SAC305 with a significant increase in 1 day of aging at 125 °C. After that point, the creep rate increases at a much slower rate. On the other hand, the properties of SAC_Q were found to degrade very slowly or remain nearly constant at all aging conditions.

Table 5.6 Secondary Creep Strain Rate of SAC305 and SAC_Q (RF)

Alloy	Test Temperature (°C)	Stress (MPa)	Strain Rate ($x10^{-8}$ sec^{-1})			
			No Aging	1 Day Aging	5 Days Aging	20 Days Aging
SAC305	125	4	6.5	9.1	11.7	14.8
	150		25.2	48.2	60.0	71.2
	175		92.3	206.7	281.3	304.3
	200		220.4	496.4	597.5	705.1
SAC_Q	125		5.45	6.2	6.9	7.7
	150		20.5	22.0	22.4	25.8
	175		77.8	83.1	87.3	93.6
	200		181.2	197.1	205.1	217.3

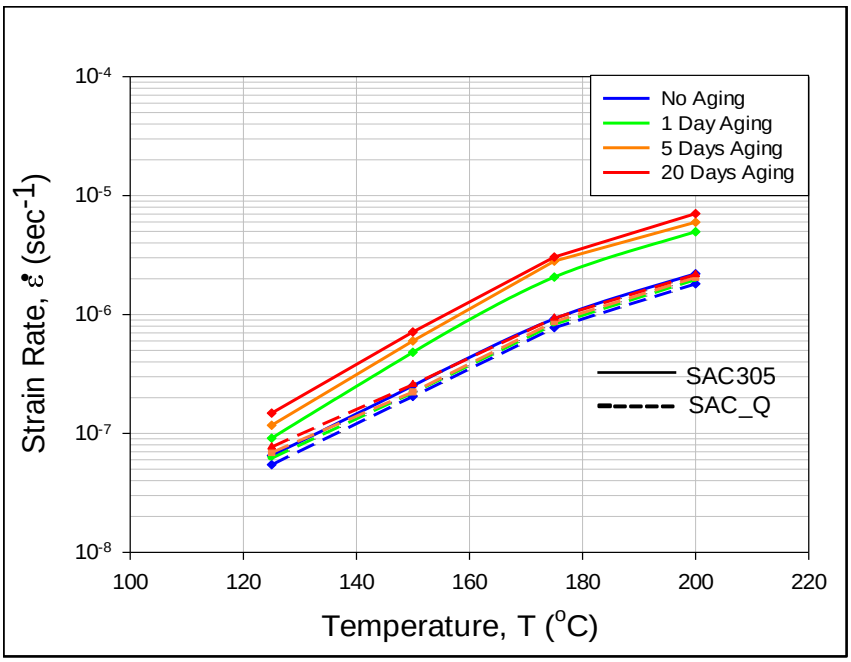

(a)

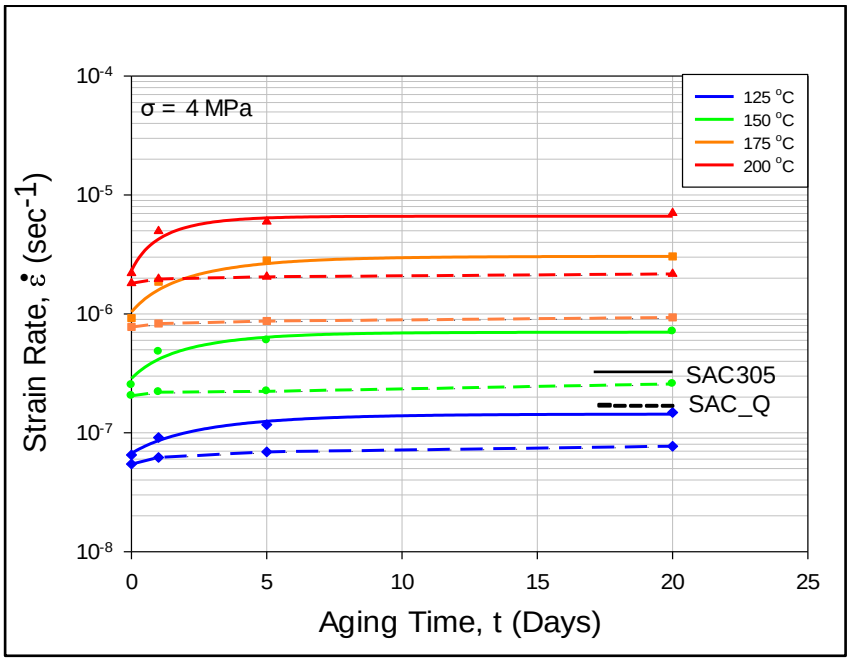

(b)

Figure 5.25 Variation of Creep Strain Rate with Test Temperature and Aging Time

5.7.6 Comparison of Creep Behavior of SAC305 and Innolot

Figure 5.26 illustrates the aging dependent creep curves for SAC305 and Innolot under a fixed stress level of 4 MPa. Each of the graphs shows a comparative analysis of the creep behavior of both alloys at a particular test temperature, with the various colored curves representing the different aging durations (no aging, and 1, 5, and 20 days of aging at T = 125 °C). The solid curves represent average creep curves for SAC305 and the dashed curves correspond to Innolot. In all cases, the creep rates for Innolot are lower than those for SAC305 under comparable test conditions. Comparing the different graphs, we can see significant increases in the secondary creep strain rate for both alloys as the temperature increases. For testing at T = 200 °C, the samples experienced tertiary creep when the load was applied for about 2 hours. Increased dislocation movements occur for the higher creep rates at higher temperatures.

It is observed that SAC305 shows sharp increase of the secondary creep strain rate as the aging time increases. However, the creep rate for Innolot varied only slightly with aging, similar to the small changes observed in the tensile test properties with aging time. In addition, the creep behaviors of Innolot for all aging conditions were comparable to the creep behavior of SAC305 with no aging (the solid blue curve is within all the dashed curves at each test temperature).

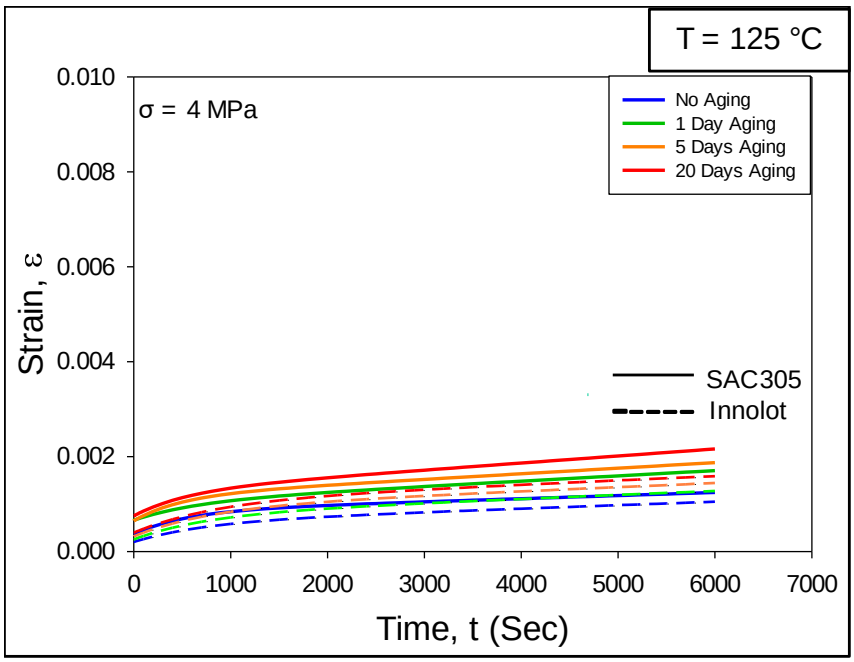
T = 125 °C
σ = 4 MPa
No Aging
1 Day Aging
5 Days Aging
20 Days Aging
SAC305
Innolot
Strain, ε
Time, t (Sec)
0.010
0.008
0.006
0.004
0.002
0.000
0
1000
2000
3000
4000
5000
6000
7000

(a)

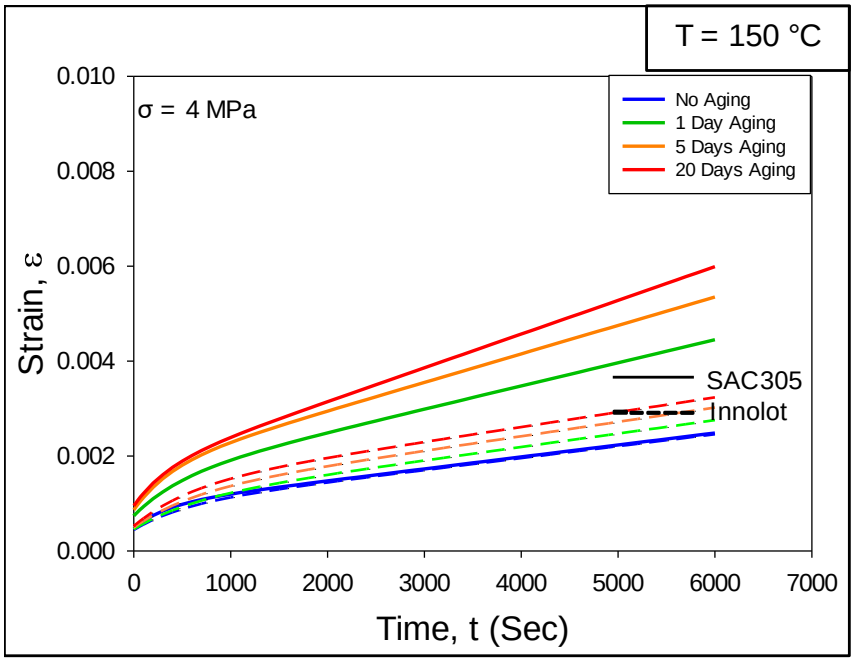
T = 150 °C
σ = 4 MPa
No Aging
1 Day Aging
5 Days Aging
20 Days Aging
SAC305
Innolot
Strain, ε
Time, t (Sec)
0.010
0.008
0.006
0.004
0.002
0.000
0
1000
2000
3000
4000
5000
6000
7000

(b)

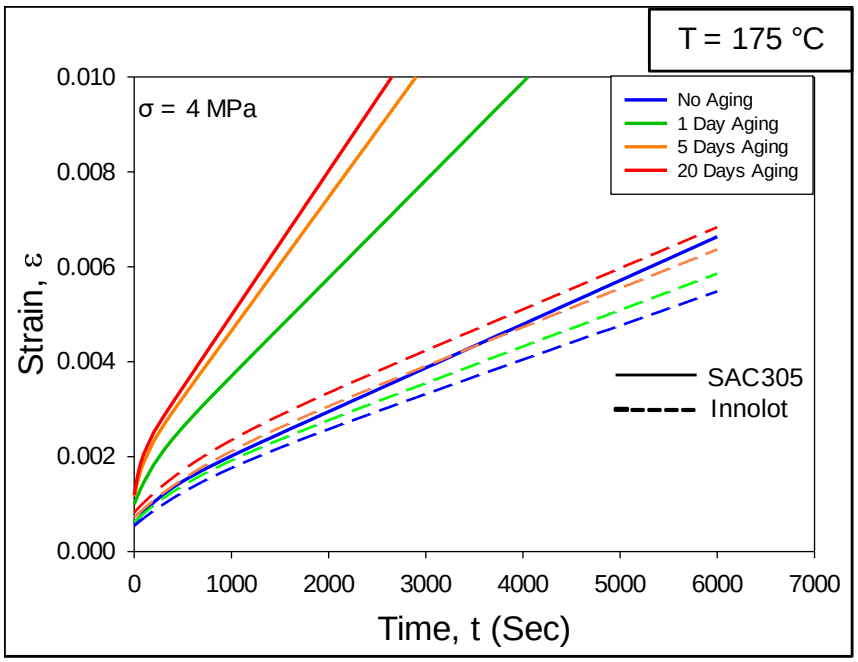

(c)

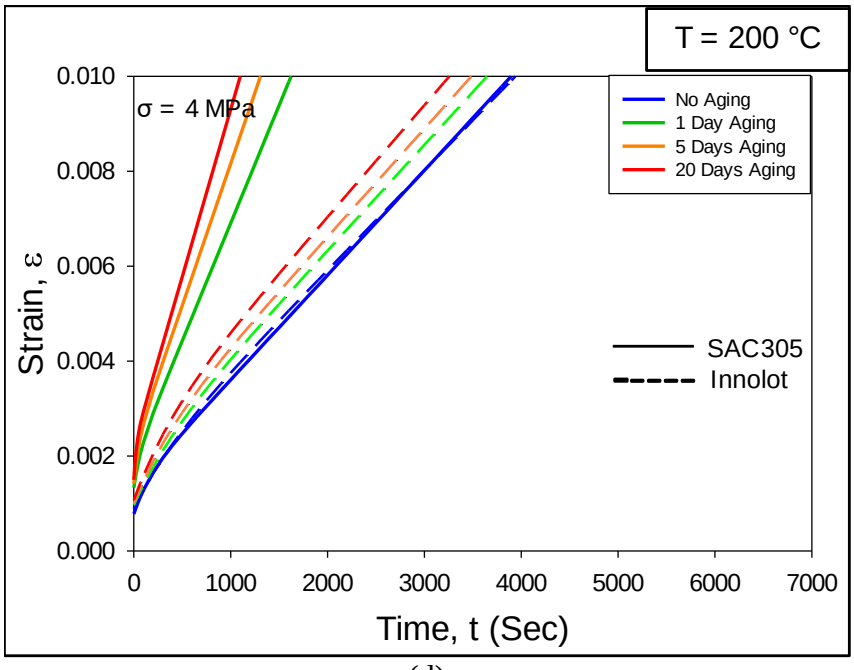

(d)

Figure 5.26 Comparison of Creep Behavior between SAC305 and Innolot

The average secondary creep strain rates of Innolot extracted from the data are tabulated in Table 5.7. The variations of secondary creep strain rate with testing

temperature and aging time of both alloys are plotted in Figure 5.27 for comparison. Each of the graphs shows comparison of secondary creep strain rate of both alloys at different test temperature and aging condition, with various colored curves representing different aging durations (Figure 5.27 (a)) and different test temperatures (Figure 5.27 (b)). The solid curves represent average creep curves for SAC305 and the dashed curves correspond to Innolot.

SAC305 shows large aging induced degradation in secondary creep strain rate with a significant increase in 1 day of aging at 125 °C. After that point, the creep rate increases at a much slower rate. On the other hand, the properties of Innolot were found to degrade very slowly or remain nearly constant at all aging conditions.

Table 5.7 Secondary Creep Strain Rate of SAC305 and Innolot (RF)

Alloy	Test Temperature (°C)	Stress (MPa)	Strain Rate ($x10^{-8}$ sec^{-1})			
			No Aging	1 Day Aging	5 Days Aging	20 Days Aging
SAC305	125	4	6.5	9.1	11.7	14.8
	150		25.2	48.2	60.0	71.2
	175		92.3	206.7	281.3	304.3
	200		220.4	496.4	597.5	705.1
Innolot	125		7.2	8.4	8.6	8.9
	150		25.1	28.2	30.3	31.2
	175		72.2	77.1	81.9	86.6
	200		210.1	222.4	227.3	235.1

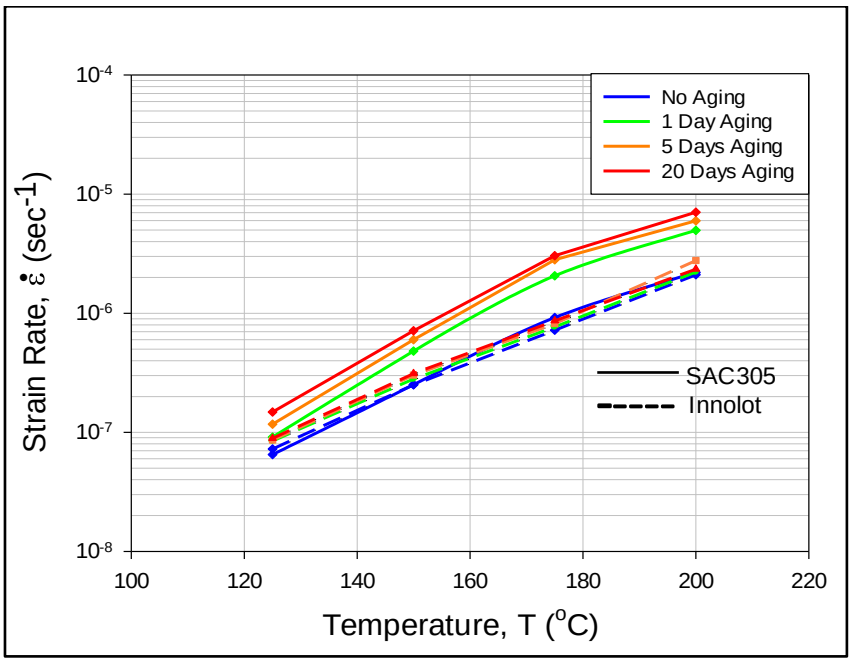

(a)

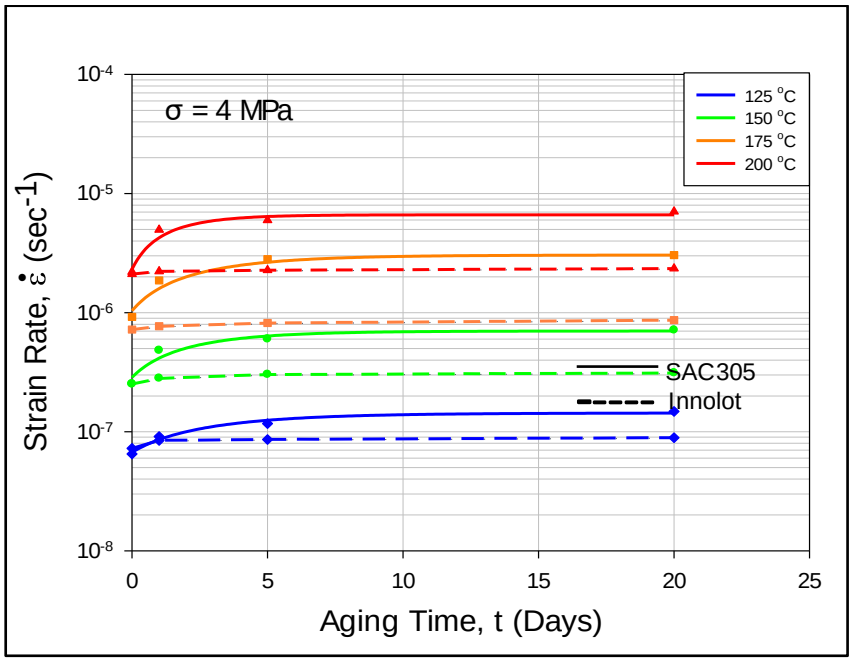

(b)

Figure 5.27 Variation of Creep Strain Rate with Test Temperature and Aging Time

5.8 Summary and Discussion

A comparative study of the aging dependent mechanical behavior of SAC305 SAC_Q, and Innolot solder alloys at extreme high temperatures (T= 125, 150, 175, and 200 °C) were investigated. Before testing, the solder uniaxial specimens were aged (preconditioned) at the extreme high temperature of either T = 125 °C or T = 200 °C, and several different durations of aging were considered (no aging, and 1 day, 5 days, and 20 days of aging). Stress-strain and creep tests were then performed on the aged specimens. Using the measured data, the evolutions of the stress-strain and creep behaviors were determined as a function of aging temperature and aging time, and models describing the evolution of the mechanical properties (effective elastic modulus and ultimate tensile strength, secondary creep strain rate) with extreme aging were established.

Our experimental measurements show that a 40-50% drop in strength and modulus occurred between T = 125 °C and T = 200 °C. Comparisons between SAC305 and SAC_Q indicate that SAC_Q had significantly better mechanical properties at all test temperatures and prior aging conditions. Substantial degradations of the mechanical properties (initial modulus, ultimate tensile strength, and secondary creep strain rate) occur in SAC305 during extreme high temperature aging, whereas, SAC_Q exhibited relatively small variations in its properties during aging. Innolot shows similar mechanical behavior as SAC_Q at all testing and aging conditions.

CHAPTER 6

ANAND VISCOPLASTIC CONSTITUTIVE MODEL FOR SOLDER ALLOYS

6.1 Anand Viscoplastic Constitutive Model

The Anand viscoplastic constitutive model [115] is often used to represent the material behavior of the lead free solders in finite element simulations. This model is defined using nine material parameters, and the reliability prediction results are often highly sensitive to the values of the Anand parameters. There are several publications listing values of Anand parameters for particular solder alloys. For example, Anand parameters for alloys such as Sn-3.5Ag, SAC105, SAC305, and SAC387 have been documented [121, 167-171].

In this chapter, stress-strain data presented in Chapter 4 has been utilized to determine the nine Anand parameters for SAC305 and doped SAC solder alloys (SAC_Q and Innolot) recommended for high reliability applications. Anand parameters were determined for SAC305 with both water quenched and reflowed microstructures. For SAC_Q and Innolot, only reflowed microstructures were explored to determine the Anand parameters.

The nine Anand parameters were determined for each unique solder alloy from a set of uniaxial tensile tests performed at several strain rates and temperatures. Testing conditions included strain rates of 0.001, 0.0001, and 0.00001 (sec^{-1}), and temperatures of

125, 150, 175, and 200 °C. The Anand parameters were calculated from each set of stress-strain data using an established procedure that is described in detail in the chapter.

6.2 Review of Anand Model Equations (1D)

Several authors [167, 168, 172] have previously reviewed the general equations of the Anand constitutive model for one-dimensional (uniaxial) stress states. The theoretical approach is based on a scalar internal variable s, which represents the material resistance to plastic flow. The model includes three equations: (1) stress equation, (2) flow equation, and (3) evolution equation. These expressions unify the rate-independent plastic behavior of the material. The Anand model does not contain an explicit yield condition or a loading/unloading criterion.

The stress equation is expressed as

$$\sigma = cs;\ c < 1 \tag{6.1}$$

where s is the scalar internal valuable. Quantity c is a function of the temperature and strain rate, and is given by

$$c = c(\dot{\varepsilon}_p, T) = \frac{1}{\xi}\sinh^{-1}\left\{\left[\frac{\dot{\varepsilon}_p}{A}e^{\left(\frac{Q}{RT}\right)}\right]^m\right\} \tag{6.2}$$

where $\dot{\varepsilon}_p$ is the plastic strain rate, A is the pre-exponential factor, ξ is the multiplier of stress, m is the strain rate sensitivity, Q is the activation energy, R is the universal gas constant, and T is the absolute temperature. By substitution of Equation 6.2 into Equation 6.1, the reformatted stress equation becomes:

$$\sigma = \frac{s}{\xi} \sinh^{-1}\left\{\left[\frac{\dot{\varepsilon}_p}{A} e^{\left(\frac{Q}{RT}\right)}\right]^m\right\} \tag{6.3}$$

The Anand model flow equation is found by solving for the strain rate in Equation 6.3:

$$\dot{\varepsilon}_p = A\, e^{-\left(\frac{Q}{RT}\right)}\left[\sinh\left(\xi\frac{\sigma}{s}\right)\right]^{\frac{1}{m}} \tag{6.4}$$

The evolution equation describes the variation of internal variable s with time. In its differential form, it can be expressed as:

$$\begin{aligned} \dot{s} &= h(\sigma, s, T)\dot{\varepsilon}_p \\ \dot{s} &= \left[h_o\left(1-\frac{s}{s^*}\right)^a \operatorname{sign}\left(1-\frac{s}{s^*}\right)\right]\dot{\varepsilon}_p; \quad a > 1 \end{aligned} \tag{6.5}$$

The term $h(\sigma, s, T)$ in Equation 6.5 is associated with dynamic hardening and recovery, and its initial value is the hardening constant $h(0) = h_o$. Parameter a is the strain rate sensitivity of the hardening process, and parameter s* is the saturation value of the deformation resistance given by

$$s^* = \hat{s}\left[\frac{\dot{\varepsilon}_p}{A} e^{\left(\frac{Q}{RT}\right)}\right]^n \tag{6.6}$$

where $\hat{s}$ is a coefficient, and n is the strain rate sensitivity. Equation 6.5 can be expressed as

$$ds = h_o\left(1 - \frac{s}{s^*}\right)^a d\varepsilon_p \tag{6.7}$$

for s < s*, and then integrated resulting in an evolution expression for the internal variable s:

$$s = s^* - \left[\left(s^* - s_o\right)^{(1-a)} + (a-1)\left\{(h_o)\left(s^*\right)^{-a}\right\}\varepsilon_p\right]^{\frac{1}{1-a}} \tag{6.8}$$

where the initial value is $s(0) = s_o$ at time t = 0. Combining Equations 6.6 and 6.8 results in an evolution equation for the internal variable s in terms of the plastic strain and plastic strain rate:

$$s = \hat{s}\left[\frac{\dot{\varepsilon}_p}{A}e^{\left(\frac{Q}{RT}\right)}\right]^n - \left[\left(\hat{s}\left[\frac{\dot{\varepsilon}_p}{A}e^{\left(\frac{Q}{RT}\right)}\right]^n - s_o\right)^{(1-a)} + (a-1)\left\{(h_o)\left(\hat{s}\left[\frac{\dot{\varepsilon}_p}{A}e^{\left(\frac{Q}{RT}\right)}\right]^n\right)^{-a}\right\}\varepsilon_p\right]^{\frac{1}{1-a}} \tag{6.9}$$

or

$$s = s(\dot{\varepsilon}_p, \varepsilon_p) \tag{6.10}$$

The final versions of the Anand model equations are the stress equation in Equation 6.3, the flow equation in Equation 6.4, and the integrated evolution equation in Equation 6.9. These expressions include 9 material parameters: A, ξ, Q/R, m in Equations 6.3 and 6.4; and constants h_o, a, s_o, $\hat{s}$, and n in Equation 6.9.

6.3 Uniaxial Stress-Strain Theoretical Response

Equations 6.3 and 6.9 can be combined to give an expression for the uniaxial stress-strain law (post yield) predicted by the Anand model:

$$\sigma = \frac{1}{\xi}\sinh^{-1}\left\{\left[\frac{\dot{\varepsilon}_p}{A}e^{\left(\frac{Q}{RT}\right)}\right]^m\right\}\left(\hat{s}\left[\frac{\dot{\varepsilon}_p}{A}e^{\left(\frac{Q}{RT}\right)}\right]^n - \left[\left(\hat{s}\left[\frac{\dot{\varepsilon}_p}{A}e^{\left(\frac{Q}{RT}\right)}\right]^n - s_o\right)^{(1-a)} + (a-1)\left\{(h_o)\left(\hat{s}\left[\frac{\dot{\varepsilon}_p}{A}e^{\left(\frac{Q}{RT}\right)}\right]^n\right)\right\}^{-a}\right\}\varepsilon_p\right]^{\frac{1}{1-a}}\right)$$

$$\sigma = \sigma(\dot{\varepsilon}_p, \varepsilon_p) \tag{6.11}$$

For a uniaxial tensile test performed at fixed (constant) strain rate $\dot{\varepsilon}_p$ and constant temperature T, this equation represents nonlinear stress-strain behavior in the form of a power law type function after yielding:

$$\sigma = \sigma(\varepsilon_p) \tag{6.12}$$

The yield stress (σ_Y) and the Ultimate Tensile Strength (UTS = maximum or saturation stress) can be obtained from Equation 6.11 by taking the limits for small and large plastic strains. The yield stress is given by the limit as ε_p goes to 0:

$$\sigma_Y = \sigma\big|_{\varepsilon_p \to 0} = cs_0 = \frac{1}{\xi}\sinh^{-1}\left\{\left[\frac{\dot{\varepsilon}_p}{A}e^{\left(\frac{Q}{RT}\right)}\right]^m\right\}\; s_0 = cs_0 \equiv \sigma_0 \tag{6.13}$$

while the UTS is given by the limit as ε_p goes to ∞:

$$UTS = \sigma\big|_{\varepsilon_p \to \infty} = \frac{\hat{s}}{\xi}\left[\frac{\dot{\varepsilon}_p}{A}e^{\left(\frac{Q}{RT}\right)}\right]^n \sinh^{-1}\left\{\left[\frac{\dot{\varepsilon}_p}{A}e^{\left(\frac{Q}{RT}\right)}\right]^m\right\} \equiv \sigma^* \tag{6.14}$$

By substituting Equation 6.14 into Equation 6.11, the stress-strain power law relation after yielding can be expressed as:

$$\sigma = \sigma^* - \left[\left(\sigma^* - c s_0 \right)^{(1-a)} + (a-1) \left\{ (c h_0) (\sigma^*)^{-a} \right\} \varepsilon_p \right]^{1/(1-a)} \tag{6.15}$$

6.4 Procedure for Determining the Anand Model Parameters from Uniaxial Stress Strain data

Anand [115] suggested using stress-strain data measured over a wide range of temperatures and strain rates to determine the 9 parameters (A, ξ, Q/R, m, h_o, a, s_o, $\hat{s}$, and n) in the viscoelastic constitutive relations presented above. Several previous studies [167, 168, 172], have outlined a procedure for performing this task. Values of the saturation stress (σ^* = UTS) can be extracted from the peak stress values on the stress-strain curves for several temperatures and strain rates. Also, stress vs. plastic strain data (σ vs. ε_p) can be extracted from the recorded stress-strain curves (σ, ε) at the various temperatures and strain rates. The conversion of total strain to plastic strain for each data set is performed using:

$$\varepsilon_p = \varepsilon - \frac{\sigma}{E} \tag{6.16}$$

where E is the initial elastic modulus. The sequential procedure for calculating the Anand model parameters consists of:

1. The six Anand parameters $\hat{S}$, ξ, A, Q/R, n and m are determined using a nonlinear least-squares regression fit of Equation 6.14 to the recorded saturation stress (UTS) vs. temperature and strain rate data.

2. The remaining three Anand parameters (s_o, h_o, and a) are found using nonlinear regression fits of Equation 6.15 to the recorded stress vs. plastic strain data at several temperatures and strain rates.

6.5 Anand Model Parameters for SAC305

The Anand model parameters for the SAC305 lead free solder materials, for both water quenched and reflowed microstructures, have been determined from the temperature and strain rate dependent stress-strain data in Figures 4.1 and 4.2. The curves in each Figure were first processed to extract saturation stress (UTS) vs. strain rate and temperature data for each alloy, as well as stress vs. plastic strain data at several strain rates and temperatures for each alloy. From the extracted data from each Figure, the nine Anand parameters were calculated for each alloy using Equations 6.13 and 6.15, and the nonlinear regression analysis procedure discussed in section 6.1.3. The results are tabulated in Table 6.1.

Table 6.1 Anand Parameters for SAC305

Constant Number	Anand Constant	Units	SAC305	
			WQ	RF
1	s_0	MPa	27.2	6.5
2	Q/R	1/K	9380	11500
3	A	sec^{-1}	2800	3700
4	ξ	Dimensionless	4	4
5	m	Dimensionless	0.28	0.47
6	h_o	MPa	150,000	70000
7	$\hat{s}$	MPa	44.67	7.72
8	n	Dimensionless	0.0120	0.0315
9	a	Dimensionless	1.72	1.9

6.6 Correlation between Anand Model Predictions and Experimental Results

Once the Anand constants are determined for each alloy, it is possible to predict the stress (σ) vs. plastic strain (ε_p) curve at a particular set of temperature, strain rate, and alloy using Equation 6.11. This result can be adjusted to a stress (σ) vs. total strain curve (ε) by adding the elastic strain to the plastic strain:

$$\varepsilon = \varepsilon_e + \varepsilon_p \qquad \varepsilon_e = \frac{\sigma}{E} \tag{4.17}$$

where E is the initial elastic modulus at the particular temperature, strain rate, and aging conditions.

Figure 6.1 illustrates the correlation between the model predictions and the experimental stress-strain curves for SAC305 (WQ). In this case, the Anand model constants from Table 6.1 for the alloy SAC305 were utilized. The experimental curves were those shown earlier in Figure 4.1. Good correlations are obtained, with the Anand model able to represent the stress-strain curves accurately over a wide range of temperatures and strain rates. Analogous comparisons for SAC305 (RF) are shown in Figure 6.2. In these cases, the appropriate Anand model constants from Table 6.1 were utilized, along with the experimental curves from Figure 4.2. Again, good correlations were obtained.

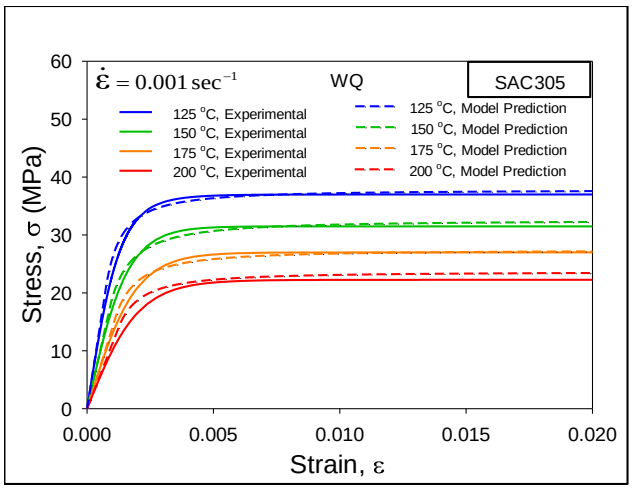

(a)

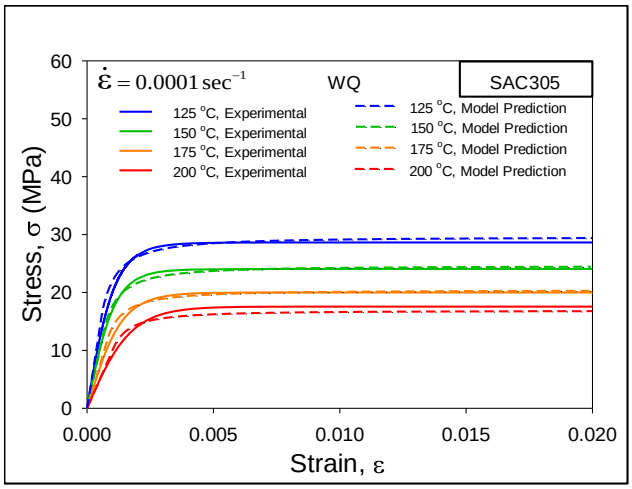

(b)

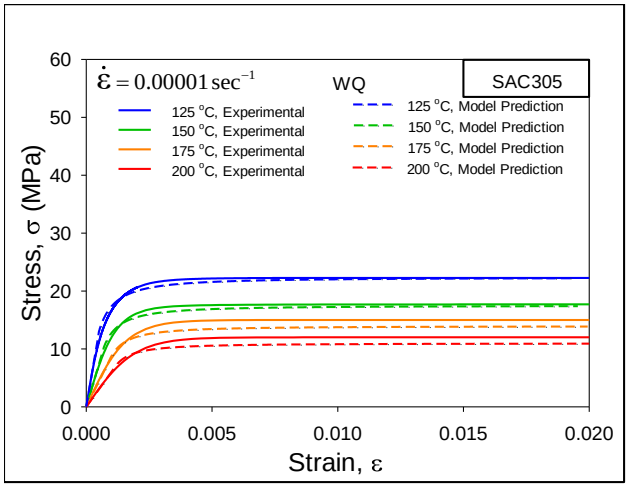

(c)

Figure 6.1 Anand Model Correlation for SAC305 (WQ)

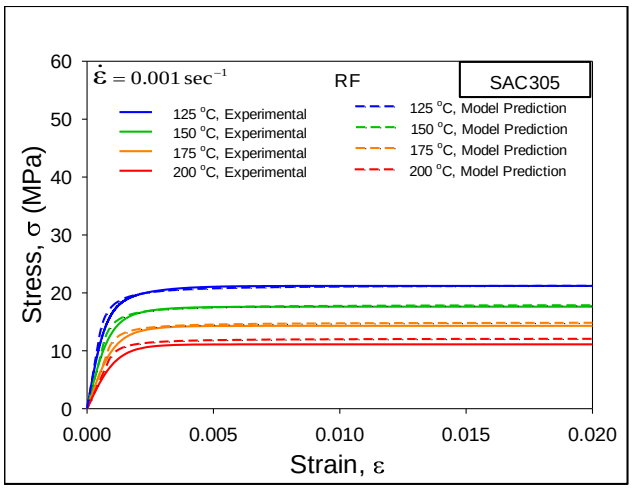

(a)

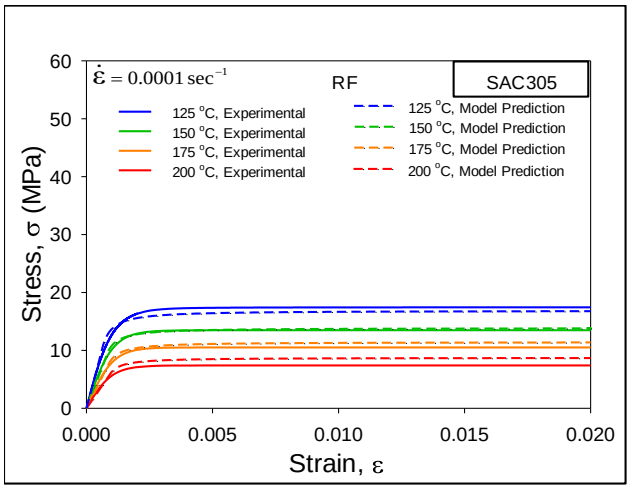

(b)

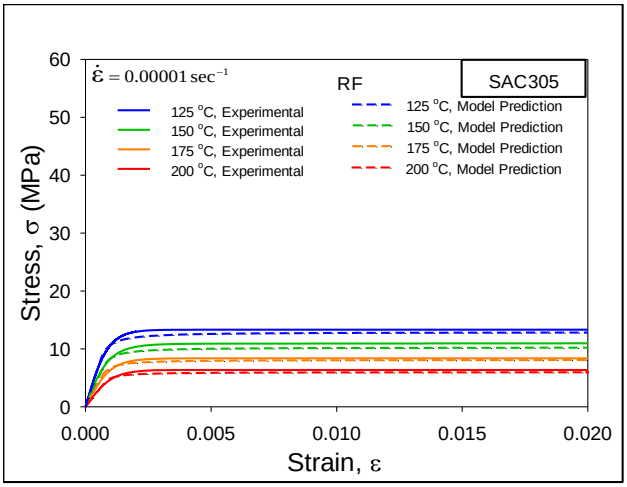

(c)

Figure 6.2 Anand Model Correlation for SAC305 (RF)

6.7 The Anand Parameters for SAC_Q

The data in Figure 4.4 were used to extract the nine Anand parameters for the SAC_Q material. As discussed previously, a least-squares regression fitting procedure was utilized to extract the optimal set of Anand parameters using the stress-strain curves for each pre-test conditions at 4 different temperatures and 3 different strain rates. The calculated Anand parameters are tabulated in Table 6.2.

Table 6.2 Anand Parameters for SAC_Q

Constant Number	Anand Constant	Units	SAC_Q (RF)
1	s_0	MPa	6.2
2	Q/R	1/K	11200
3	A	sec^{-1}	12000
4	ξ	Dimensionless	6
5	m	Dimensionless	0.5
6	h_o	MPa	45000
7	$\hat{s}$	MPa	23.97
8	n	Dimensionless	0.0323
9	a	Dimensionless	1.05

The calculated values of the Anand parameters were used to predict stress-strain behavior for the SAC_Q solder alloy with the various microstructures. For example, the results for SAC_Q are presented in Figures 6.3(a), 6.3(b) and 6.3(c) for 3 different strain rates (i.e. 0.001, 0.0001 and 0.00001 sec^{-1}). Reasonable correlations were found for all of the temperatures.

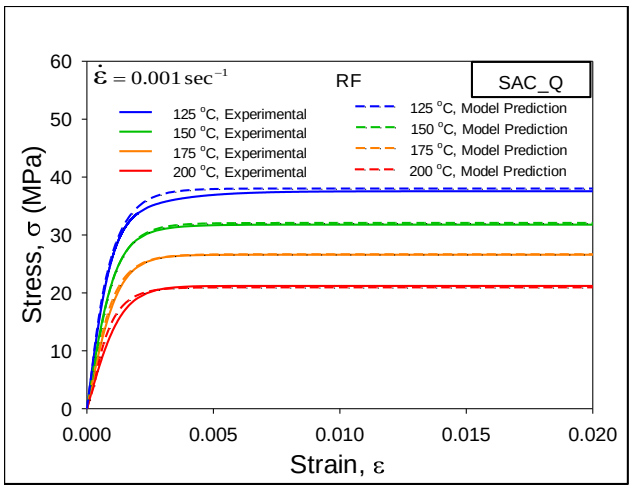

(a)

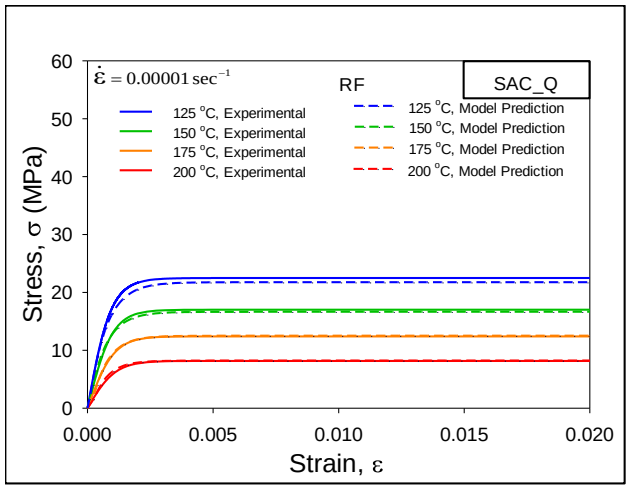

(b)

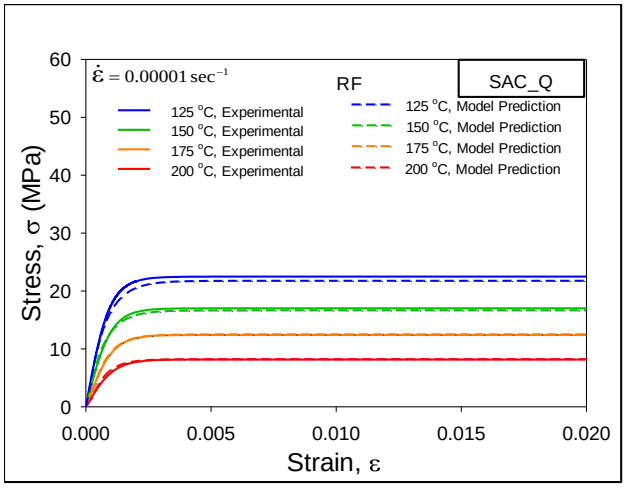

(c)

Figure 6.3 Anand Model Correlation for SAC_Q (RF)

6.8 The Anand Parameters for Innolot

The data in Figure 4.5 were used to extract the nine Anand parameters for the Innolot. As discussed previously, a least-squares regression fitting procedure was utilized to extract the optimal set of Anand parameters using the stress-strain curves for each pre-test conditions at 4 different temperatures and 3 different strain rates. The calculated Anand parameters are tabulated in Table 6.3.

Table 6.3 Anand Parameters for Innolot

Constant Number	Anand Constant	Units	Innolot (RF)
1	s_0	MPa	5.6
2	Q/R	1/K	11200
3	A	sec^{-1}	12000
4	ξ	Dimensionless	6
5	m	Dimensionless	0.48
6	h_o	MPa	48000
7	$\hat{s}$	MPa	24.50
8	n	Dimensionless	0.0305
9	a	Dimensionless	1.15

The calculated values of the Anand parameters were used to predict stress-strain behavior for the Innolot solder alloy with the various microstructures. For example, the results for Innolot are presented in Figures 6.4(a), 6.4(b) and 6.4(c) for 3 different strain rates (i.e. 0.001, 0.0001 and 0.00001 sec^{-1}). Reasonable correlations were found for all of the temperatures.

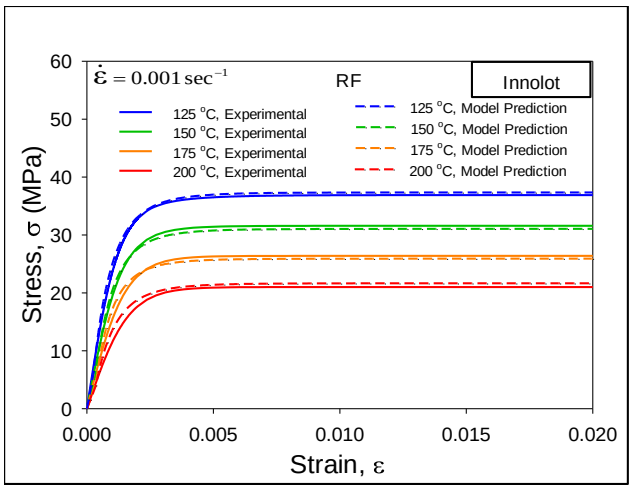

(a)

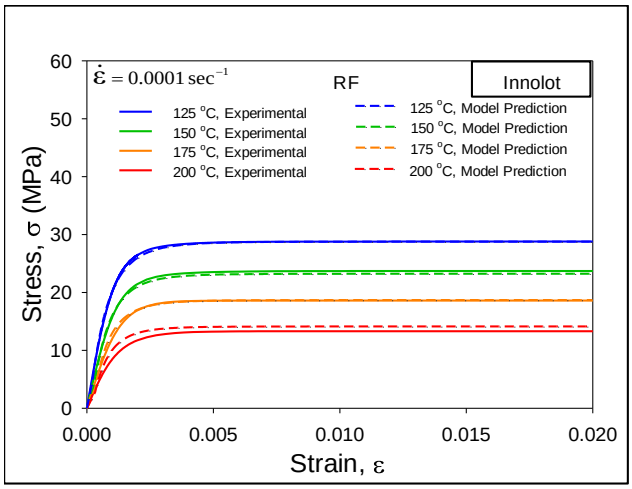

(b)

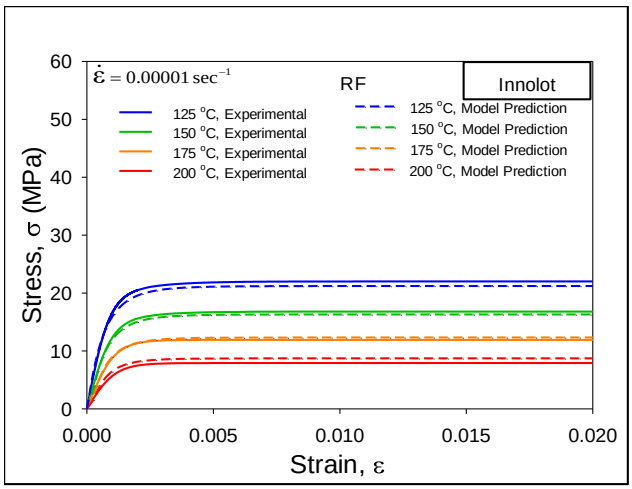

(c)

Figure 6.4 Anand Model Correlation for SAC_Q (RF)

6.9 Summary and Discussion

In this chapter, SAC305, SAC_Q, and Innolot lead free solder materials recommended for high reliability applications have been chemically analyzed and then mechanically tested in order to determine the nine Anand parameters. Test specimens were initially solidified with both water quenched (WQ) and reflowed (RF) cooling profiles. Results from the uniaxial tensile test, performed at three different strain rates (0.001, 0.0001 and 0.00001 sec^{-1}) and four different test temperatures (125, 150, 175, and 200 °C) were used to determine the Anand parameters for all the alloys mentioned before. These parameters were used to predict the stress-strain behavior of the corresponding solder alloy. The experimental results and the model predicted results were compared. A good correlation was found between Anand model predicted and experimentally obtained results. The correlation of experimental results with anand model prediction shows a very small difference (< 10% in most conditions), thus, confirming the applicability of the model for a wide range of temperatures and strain rates.

CHAPTER 7

MECHANICAL BEHAVIOR OF SAC305 SOLDER JOINTS AT EXTREME HIGH TEMPERATURES USING NANOINDENTATION

7.1 Introduction

In this chapter, mechanical behavior, and aging effects of SAC305 (96.5Sn-3.0Ag-0.5Cu) solder joints at several extreme high testing temperatures (T = 125, 150, 175, and 200 °C) have been explored using nanoindentation method. A special high temperature stage and test protocols were used within the nanoindentation system to carefully control the testing temperature, and to make the measurements insensitive to thermal drift problems. Solder joints were extracted from 14 x 14 mm PBGA assemblies (0.8 mm ball pitch, 0.46 mm ball diameter) that were built as part of the iNEMI Characterization of Pb-Free Alloy Alternatives Project. Since the properties of SAC solder joints are highly dependent on crystal orientation, polarized light microscopy was utilized to determine the orientation of the tested joints. For all of the experiments, only single grain solder joints were used to avoid introducing any unintentional variation from changes in the crystal orientation across the joint cross-section. To study the aging effects, solder joints were preconditioned for 0, 1, 5, 10, and 30 days at T = 125 °C in a box oven. Nanoindentation testing was then performed on the aged specimens at four different test temperatures (T = 125, 150, 175, and 200 °C) to extract the elastic modulus, hardness, and creep performance of the aged material. Throughout this study, a constant force of 10 mN was applied for

900 seconds to monitor the creep displacements and measure the creep strain rate as a function of both temperature and prior aging conditions.

As expected, mechanical properties and creep strain rate of solder joints were highly dependent on the test temperature and degrade significantly as the temperature increases. In addition, the effects of aging on solder joints properties become much more significant as the aging time and test temperature increases.

7.2 Sample Preparation for High Temperature Nanoindentation

Sample cross-sectioning and polishing procedure outlined in chapter 3, section 3.5 and 3.6 was followed to prepare samples for high temperature nanoindentation experiments. Since the mechanical behavior of solder alloys depends on crystal orientation, the orientation of the SAC305 solder joints were initially determined using polarized light microscopy. Only single-grain solder joints were identified and used in this study to avoid any variation in properties associated with different crystal orientation. Five different SAC305 solder joints with single grain orientation and uniform IMC distributions were chosen used for the high temperature creep study: one for temperature study and remaining four for aging study. Figures 7.1 shows polarized light images of multi-grain and single grain solder joint samples.

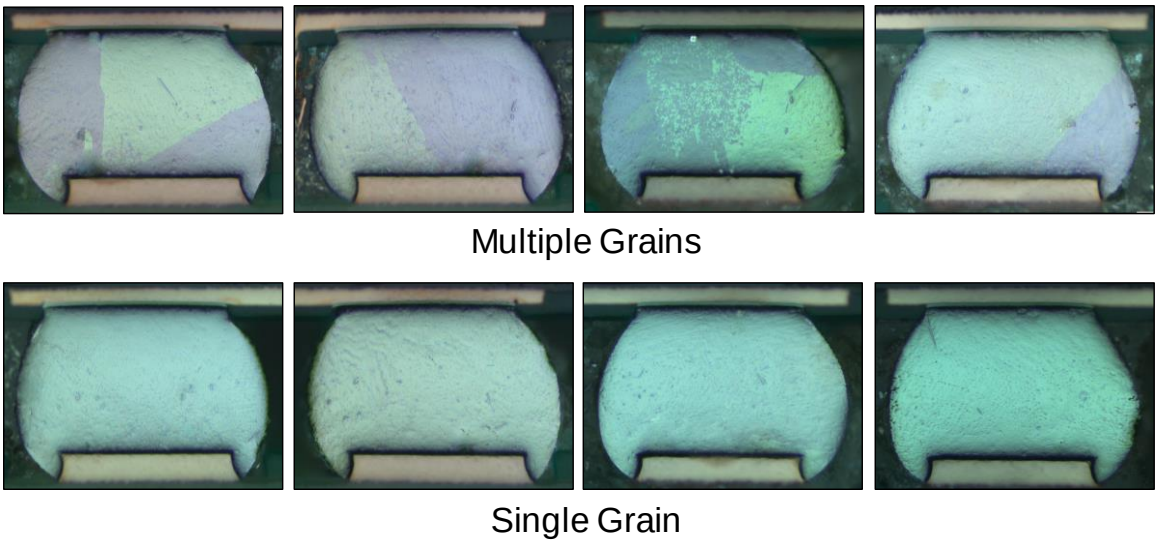

Figure 7.1 Multi-Grain and Single Grain Solder Joint

7.3 High Temperature Nanoindentation System and Test Procedures

Hysitron TI 950 nanoindentation system has been used to perform the nanoindentation creep tests (Figure 3.16). A Berkovich indenter tip was chosen in this work. The extreme high temperature tests were performed in a high temperature stage (xSOL 400). During each indentation experiment, load versus indentation displacement response of the solder material in the direction normal to the cross-sectional surface was measured. Figure 72 shows the high temperature stage within the nanoindentation system, while Figure 7.3 shows images of a test sample in the high temperature stage.

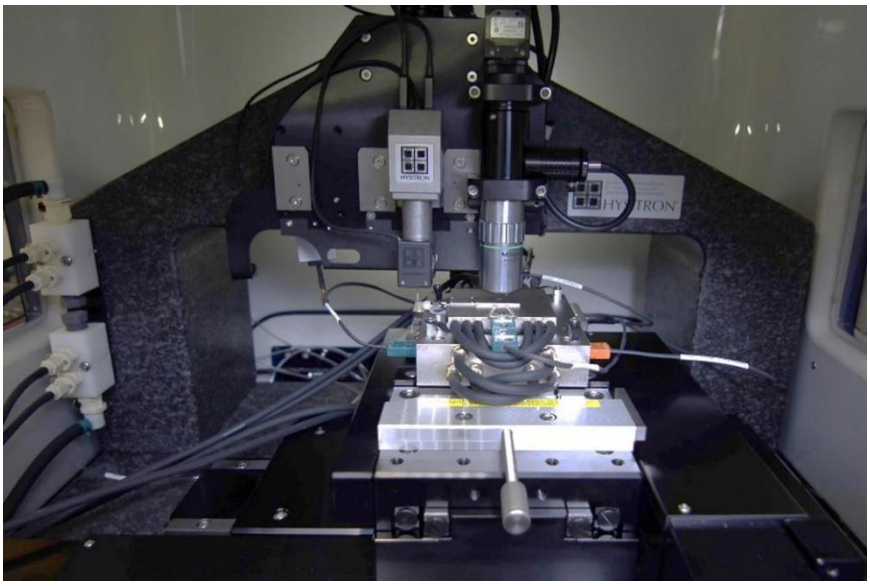

Figure 7.2 High Temperature Nanoindentation System

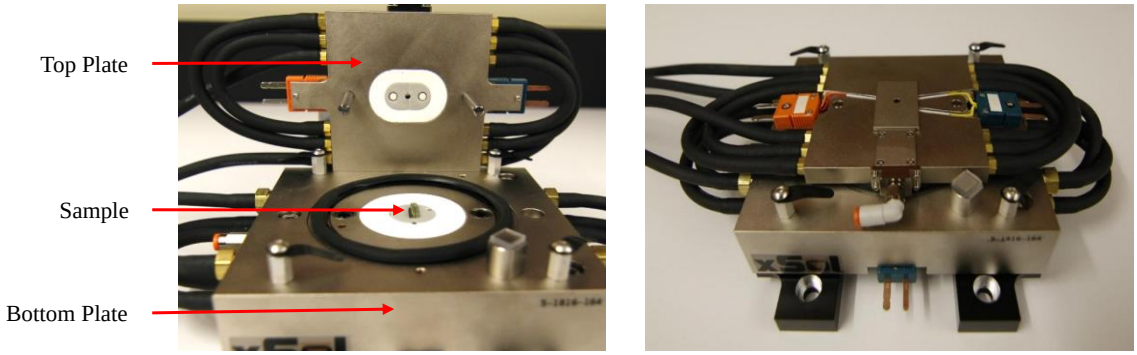

Figure 7.3 Solder Joint Sample in the High Temperature Stage

Typical permanent indentation mark of indent after a nanoindentation experiment is shown in Figure 7.5. At a particular test condition (e.g. temperature and prior aging), about 5-8 indentations were performed, and the average results of all the indents were considered for comparison between different test conditions. The indents were made in 50-80 µm apart to avoid locations that were deformed plastically by the previous indents.

As discussed in the previous section (2.2), all tests in this work were performed on single grain (Sn crystal) solder joints, so that there were no orientation effects caused by

an indentation array covering two or more grain boundaries of grains with different crystal orientations (different material properties).

In all test conditions, as shown in Figure 7.4, the indentation marks were ensured to cover the available phases of the material. Thus, the nanoindentation tests represents the global properties of the solder joints, instead of the localized mechanical properties of the phases (β-Sn dendrites or Ag_3Sn and Cu_6Sn_5 IMC particles). Calibration of the indenter tip shape was performed on a standard fused quartz sample.

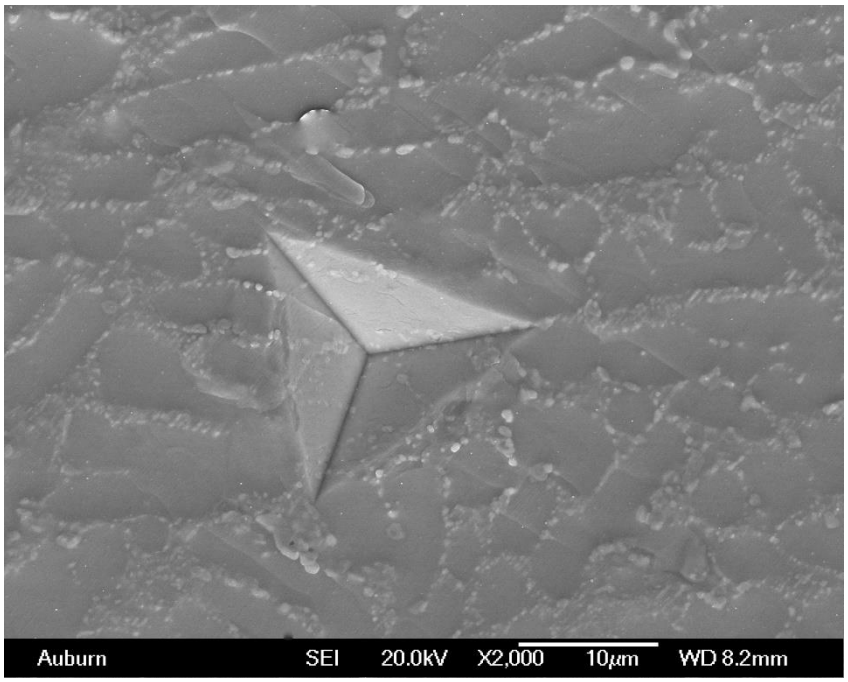

Figure 7.4 Permanent Indentation after Testing

The maximum load of 10 mN was chosen for all the creep tests. Once the peak load reaches to 10 mN, the load was held constant for 900 sec. A load versus time graph for a single indentation test performed in this work is shown in Figure 7.5. As we can see, a small sinusoidal load was introduced with the static load of 10 mN during the start of the dwell period. Thermal drift has negligible effects in the beginning at constant load during

dwell time. Therefore, a "reference segment" of 5 sec duration was introduced at the beginning of the creep deformations. During this reference segment, modulus of the material was calculated from the indentation displacements, which was utilized later to calculate the total area of indent, making the tests quite unaffected by thermal drift problems. Thus, the reference segment makes the experiments relatively insensitive to thermal drift problems. An example of a load vs. indent displacement graph obtained after a nanoindentation creep test is shown in Figure 7.6. The displacement during the Dwell/ Creep region of the curve was utilized to obtain creep properties of the solder joint.

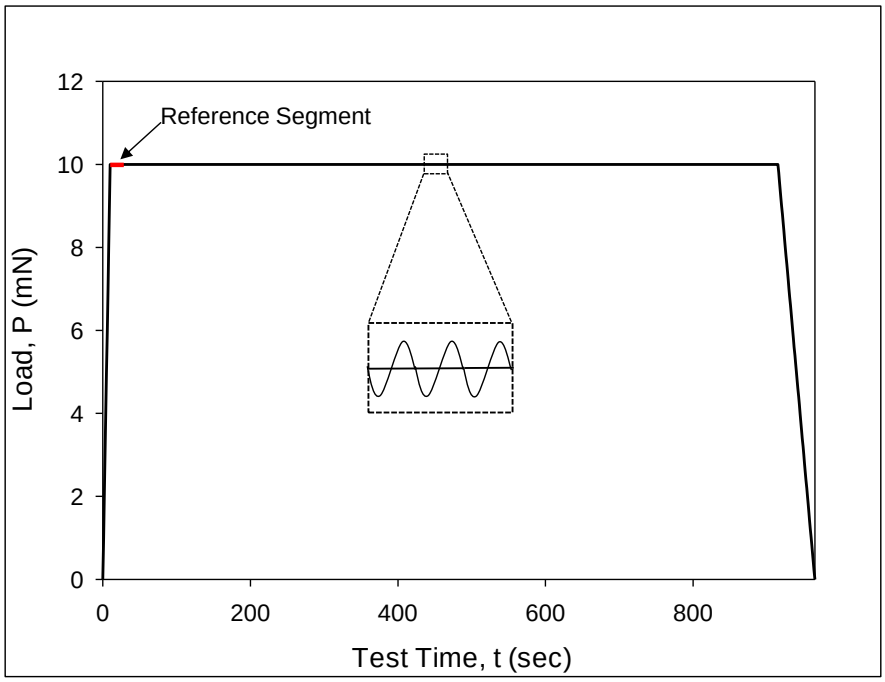

Figure 7.5 Loading Profile Used for Nanoindentation Creep Tests

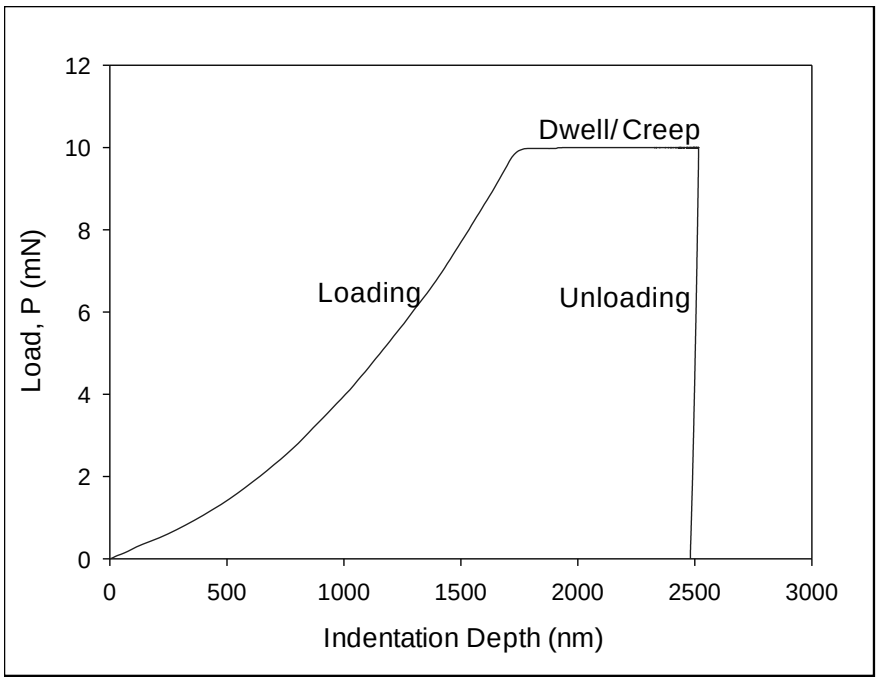

Figure 7.6 Load-Displacement Curve Obtained from a Nanoindentation Creep Test

7.4 Pile-up Correction for High Temperature Nanoindentation Tests

Accumulation of material near the edges of an indent is known as pile-up. Pile-up was observed in the high-temperature tests in this work. From the 3D SPM image of a single indent (Figure 7.7) on SAC305 solder, obtained at high temperature, pile up is apparent. The semi-ellipse method for pile-up correction proposed by Kese, et al. [150] was used here to adjust our nanoindentation creep data. According to this method, the corrected contact area A is given by:

$$A = A_{OP} + A_{PU} = A_{OP} + 5.915 h_c \sum_{i=1}^{3} a_i \tag{7.1}$$

where A_{OP} is the contact area obtained from the normal calculations based on the tip shape, A_{PU} is the additional pile-up area, h_c is contact depth, and a_i (i = 1, 2, 3) are the

height of pile-ups mid-way along the three edges. In this investigation, A_{OP} and h_c were obtained from the normal indentation results reported by the system. In order to determine a_i, the profile of each indent was scanned using SPM imaging. A sample of the topographic SPM image obtained for one typical indent and the location of a_i is shown in Figure 7.8. The surface profile was measured along three different sections as shown in Figure 7.9 to determine the value of a_i along each edges.

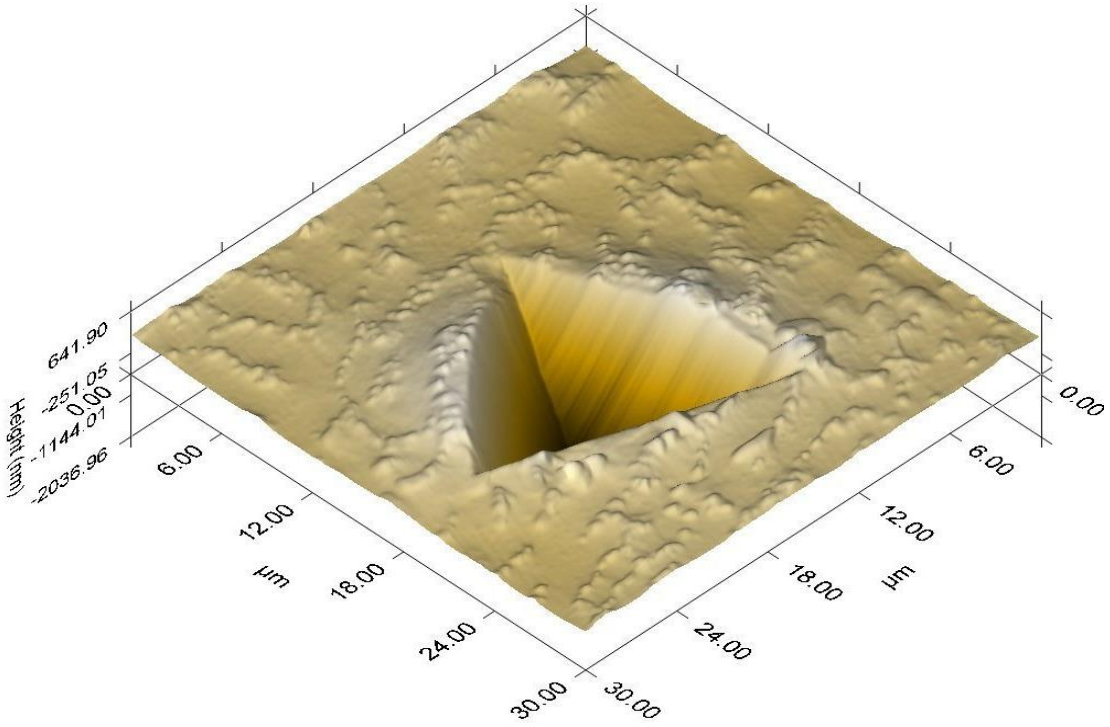

Figure 7.7 3D SPM Image of a Single Indent

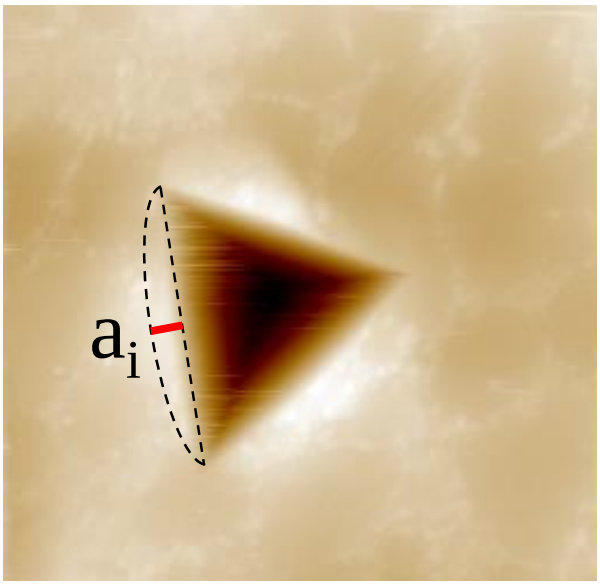

Figure 7.8 2D SPM Topography Data for a Single Indent

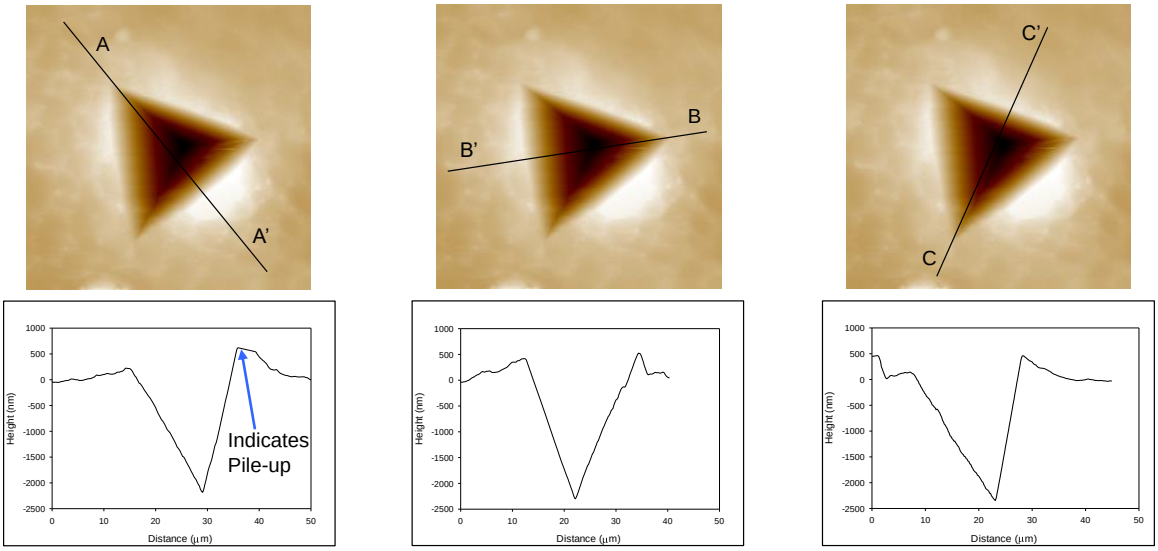

Figure 7.9 SPM Topography Data for a Single Indent and Pile-up Measurement

7.5 Measurement of Creep Behavior

The displacement during the hold period of 900 second at the maximum load of 10 mN was utilized to obtain creep properties of the solder joint. An example of the measured

displacement during the hold period versus time plot, for an array of indents performed on a single grain solder joint under similar test conditions, is presented in Figure 7.10.

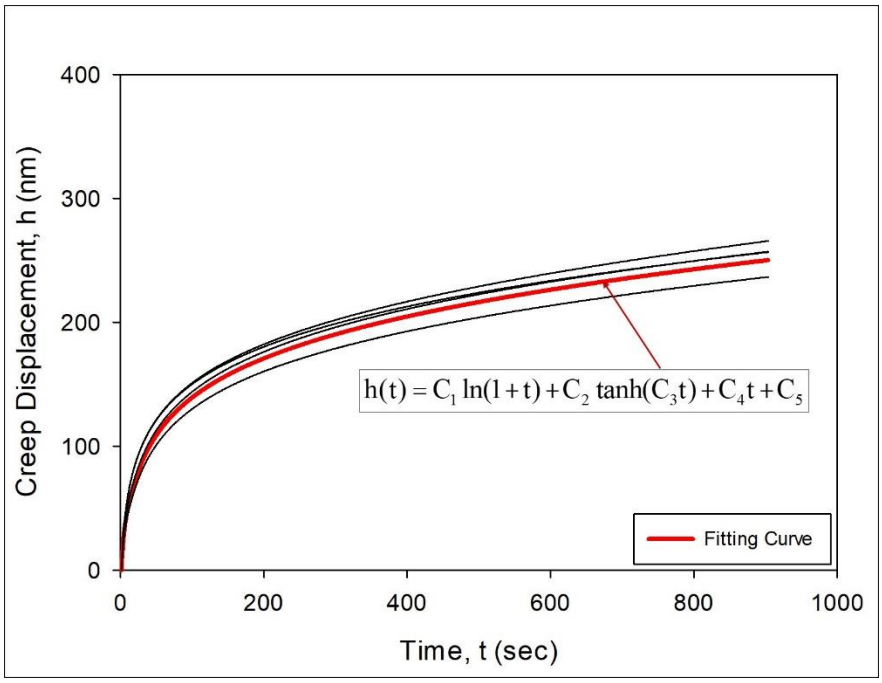

Figure 7.10 Nanoindentation Creep Displacement on SAC305 Joint

The log hyperbolic tangent creep model proposed by Chanda, et al. [173] has been used to fit and model the recorded indentation depth versus time data during the creep loading.

$$h(t) = C_1 \ln(1+t) + C_2 \tanh(C_3 t) + C_4 t + C_5 \tag{7.2}$$

where C_1, C_2, C_3, C_4, and C_5 are fitting constants. All the black curves in Figure 7.10 represents the fit of equation 7.2 to the creep data from several individual indentation experiments whereas the red color curve represents a mathematical average of the series of indentations. In addition, the method for calculating the creep strain rate proposed by

Mayo and Nix [174, 175] has been adopted in this study. According to the method, creep strain rate can be determined from instantaneous creep deformation and deformation rate using the following equation

$$\dot{\varepsilon} = \frac{1}{h}\frac{dh}{dt} \tag{7.3}$$

In order to determine creep strain rate, the derivative of equation 7.2 with respect to time was divided by corresponding instantaneous displacement.

Since the applied load was fixed (10 mN) and the projected area under the indenter tip increases continuously during the creep deformation period, the stress changes over the time. For example, the variation of stress, for the same set of experiments presented in Figure 7.10, as a function of dwell time is presented in Figure 7.11 where the red curve represents an average for the series of indents.

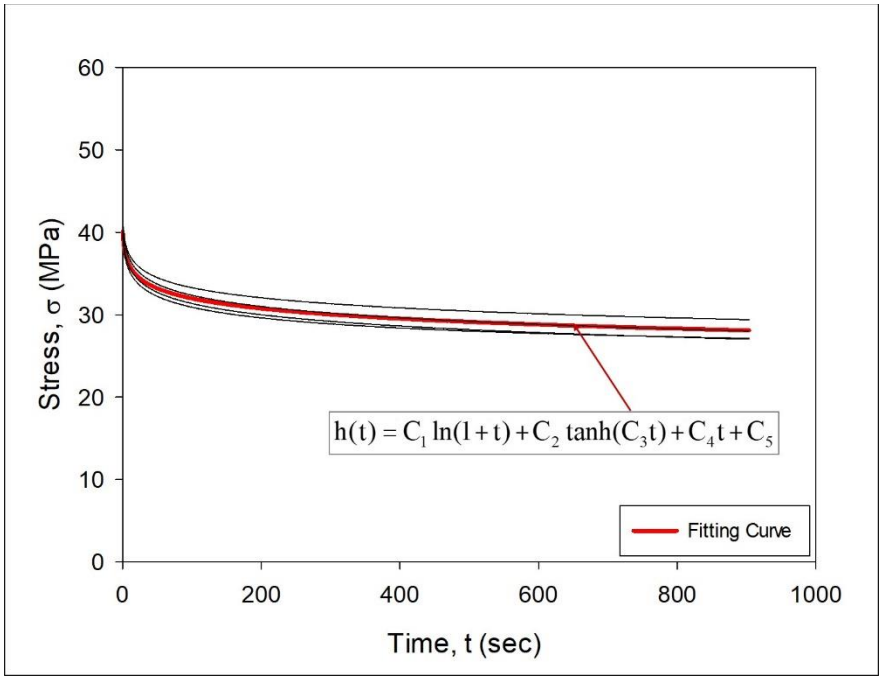

Figure 7.11 Variation of Stress with Holding Time for SAC305 Solder Joint

Data from Figures 7.10-7.11 was combined to generate the creep strain rate versus applied stress plot as shown in Figure 7.12.

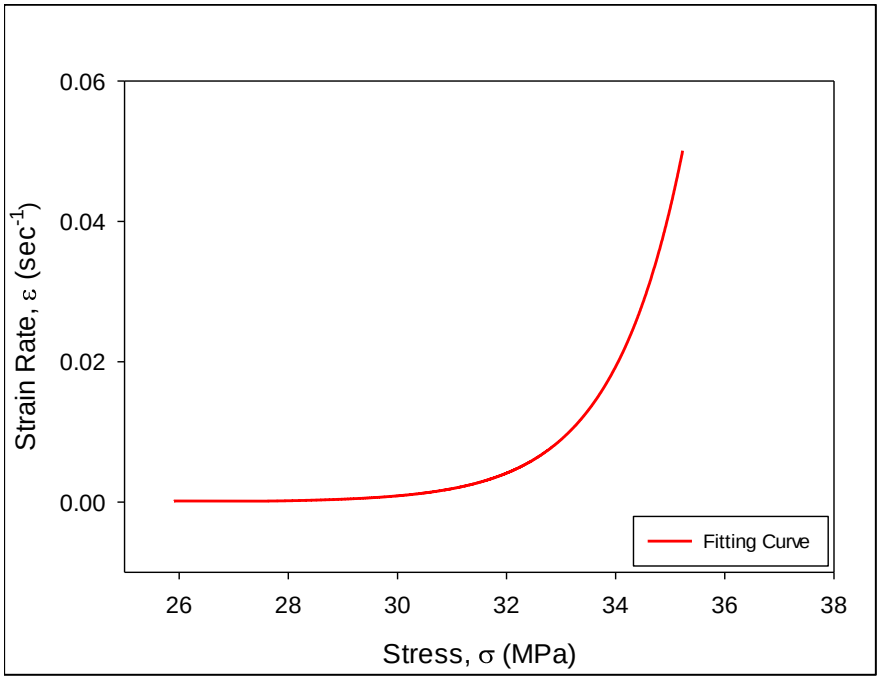

Figure 7.12 Creep Strain Rate vs. Applied Stress Plot

The stress level attained during the test ranges from 26-38 MPa whereas the stress level typically used during high temperature tensile creep experiment of SAC305 solder is 5-10 MPa [69, 85, 86, 103]. Since, the stress applied during the nanoindentation test is compressive in nature, the stress level attained during the test is well above the desired range. The exponential model, as shown in Equation 7.4, was used to extrapolate nanoindentation creep results to a lower stress level.

$$\dot{\varepsilon} = C_1 e^{C_2 \sigma} \tag{7.4}$$

where C_1- C_2 are fitting constants. A log-log plot of strain rate vs. stress for the fitted experimental data (solid red curve) and the extrapolation using the exponential model (blue dotted curve) is presented in Figure 7.13.

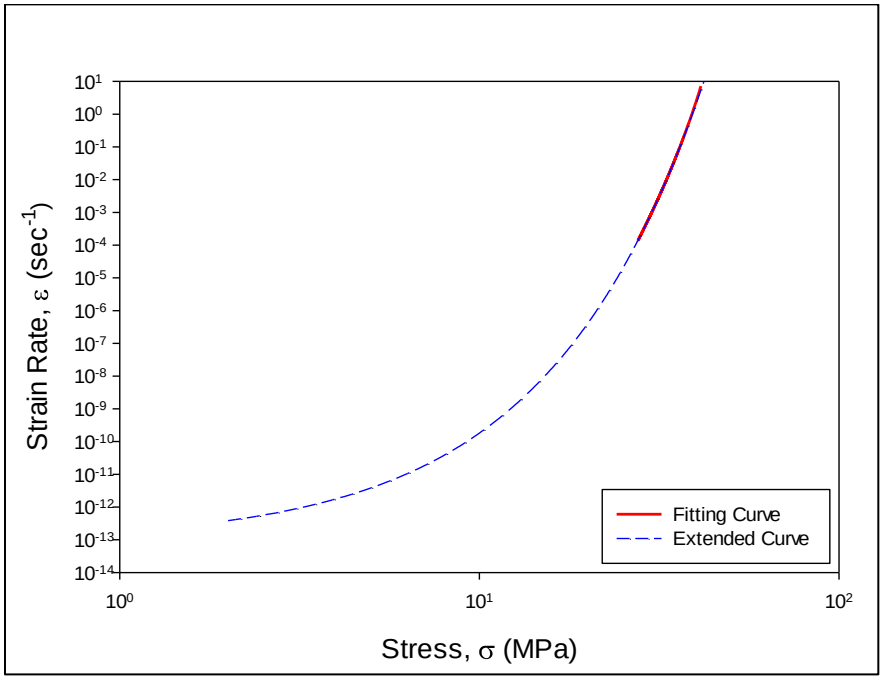

Figure 7.13 Creep Strain Rate vs. Applied Stress Plot (Extended)

7.6 High Temperature Nanoindentation Test Matrix

High temperature tests were performed by placing cross-sectioned and polished single grain solder joint samples into the heating chamber mounted within the nanoindentation system. The test sample set consisted of five single crystal SAC305 solder joints. One joint was used to study only the effect of test temperatures while the rest 4 joints were used to study the combined effect of aging time and test temperatures on the creep properties. The first study involved investigation of the effect of test temperature on the mechanical properties of SAC305 solders. Four different test temperatures (T = 125,

150, 175, and 200 °C) were explored on a single grain joint. For each aging condition and temperature, 6-7 indentations were performed. In the second study, the effect of high temperature aging was explored. For each tested joint and temperature, five unique sets of aging conditions are being explored: no aging; and 1, 5, 10 and 30 days of prior aging at T = 125 °C. Before prior aging, a series of indents were made on 4 single grain SAC305 solder joints at 4 different test temperatures. In this case, test temperature for each joint was kept constant and indents were made at different aging time. After having the initial series of indents in no aging condition, all the joints were kept inside an oven at 125 °C for 1 day. After removing the samples from the aging oven, another series of indents (1 day aging) were made on each joint and then kept them back for the next aging cycle.

7.6.1 Effects of Test Temperature

Using the nanoindentation creep procedures discussed above (sections 7.3-7.5), the effect of test temperatures on the creep response of SAC305 solder joints were explored using the nanoindentation method. At a particular test temperature, a series of indents (6-7) were made with a maximum load of 10 mN for 900 seconds (Figure 7.14). In Figure 5, different rows of indents represents different test temperature, with top row representing 125 °C test temperature and bottom row representing 200 °C test temperature. The size of indent increases with increase in temperature.

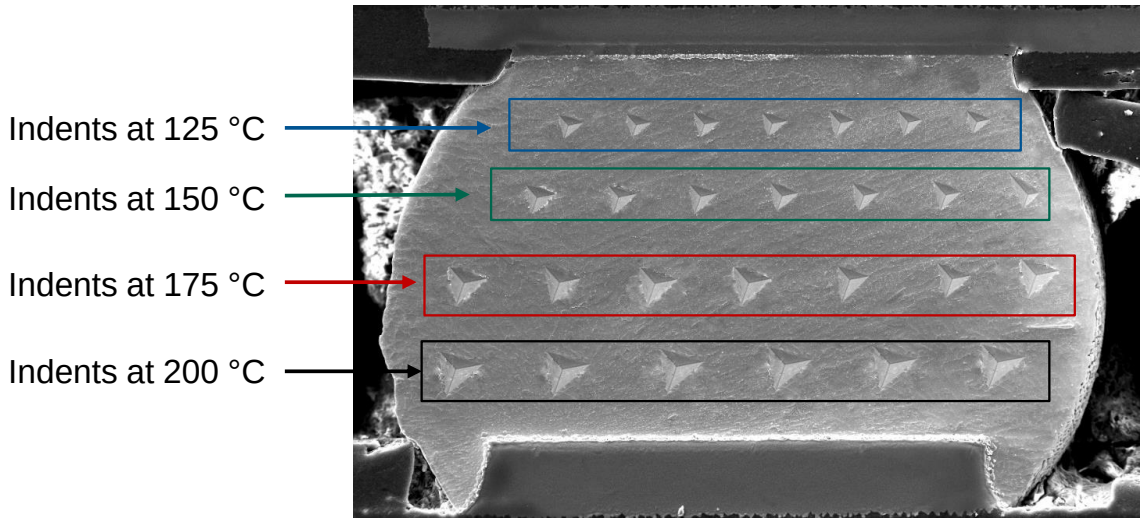

Figure 7.14 SAC305 Solder Joint after Nanoindentation Test at Different Temperatures

Typical load vs. indentation depth curves obtained at different test temperatures are shown in Figure 7.15. Using the recorded creep indentation displacement vs. time data, the creep strain rate vs. applied stress curves were generated. Figure 7.16 represents creep displacement vs. time curves obtained at several extreme high temperatures, ranging from 125 to 200 °C. As expected, the creep displacements increased significantly as test temperature increases.

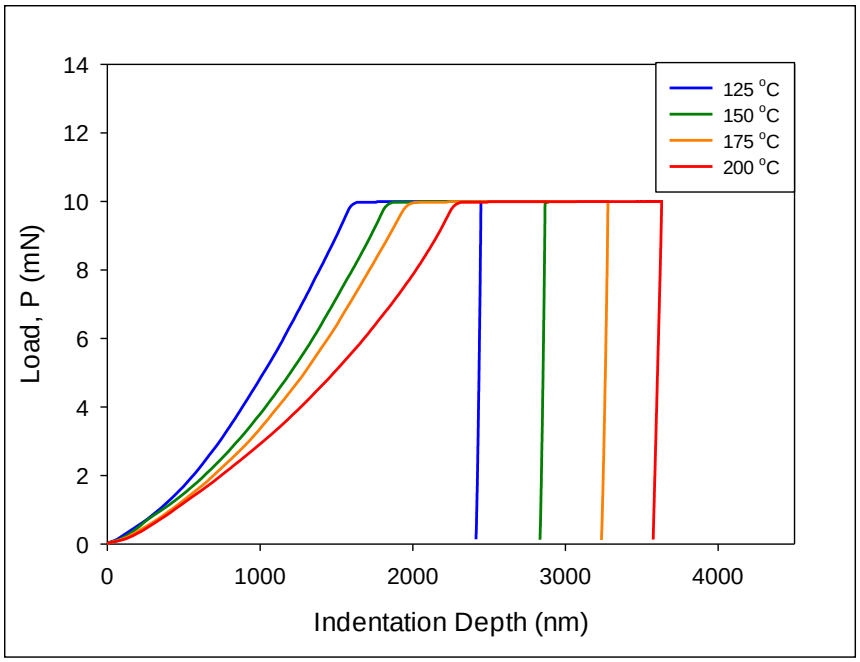

Figure 7.15 Nanoindentation Load vs. Indentation Depth Curves

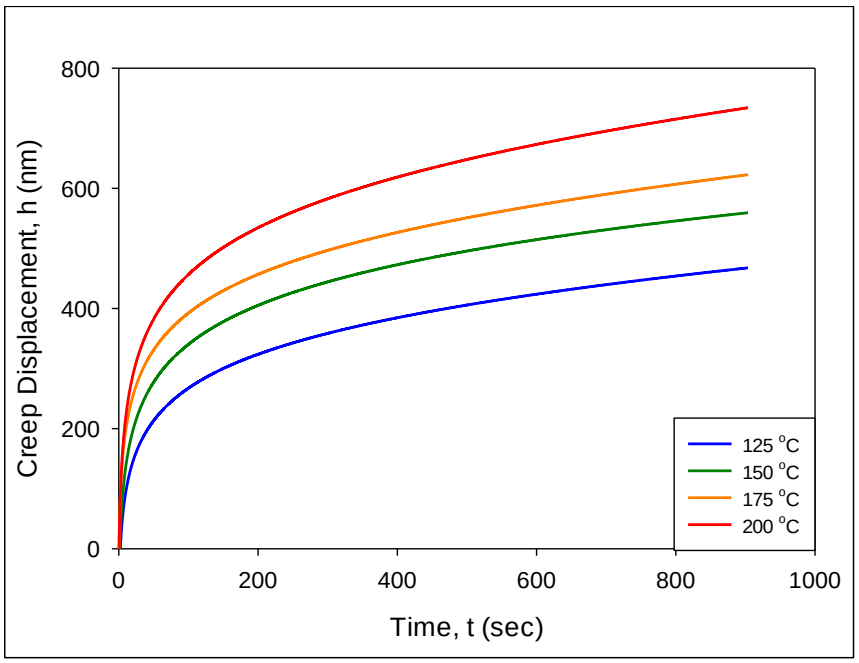

Figure 7.16 Variation of Creep Displacement with Dwell Time

Figure 7.17 shows the variation of applied stress over dwell time at different temperature. A constant load was applied during creep test. However, the contact area under the indenter kept increasing with time, leading to the continuous decrease of stress as time increased. The applied stress further decreased as temperature increased since the contact area increased at higher temperatures.

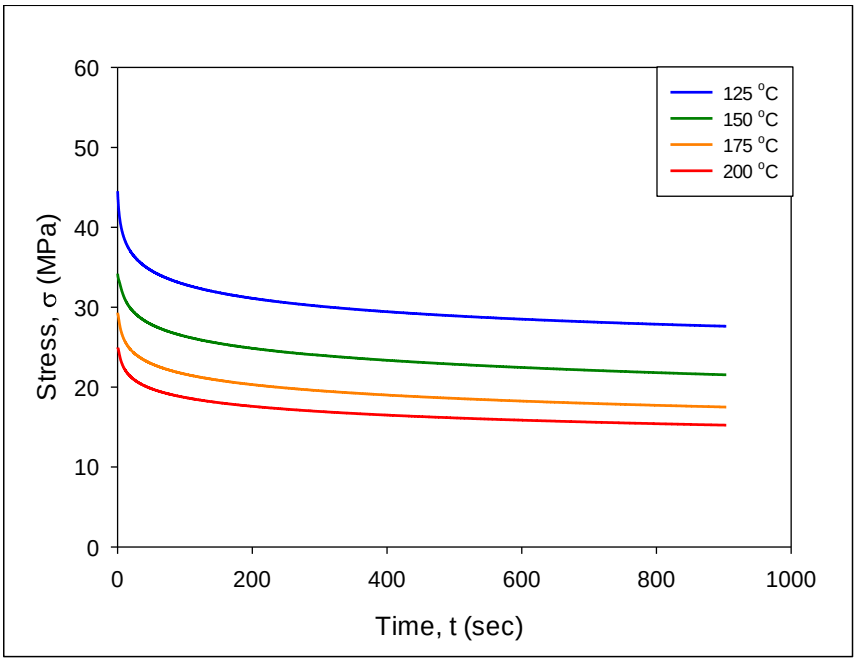

Figure 7.17 Variation of Applied Stress with Dwell Time during Constant Loading

The effect of temperature on the creep strain rate vs. applied stress plot are shown in Figure 7.18. At a fixed applied stress, the creep strain rate changed significantly with test temperature, increasing to several orders of magnitude as temperature increased. The exponential model, as shown in Equation 7.4, was used to extrapolate nanoindentation creep results to a lower stress level. The corresponding extrapolated curves are presented in Figure 7.19. The values of equivalent creep strain rates at 10 MPa stress level for all the test temperatures are tabulated in Table 7.1.

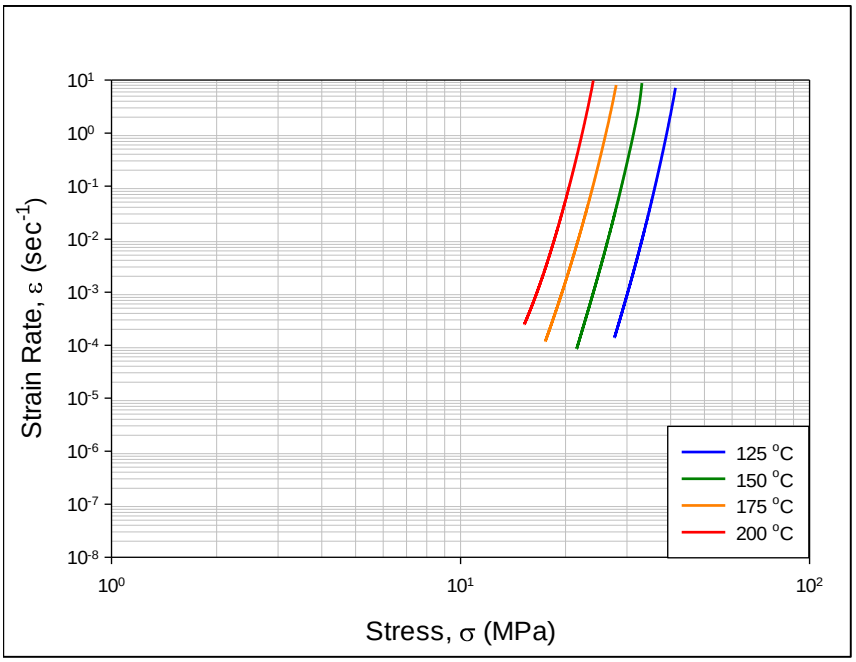

Figure 7.18 Variation of Creep Strain Rate with Applied Stress

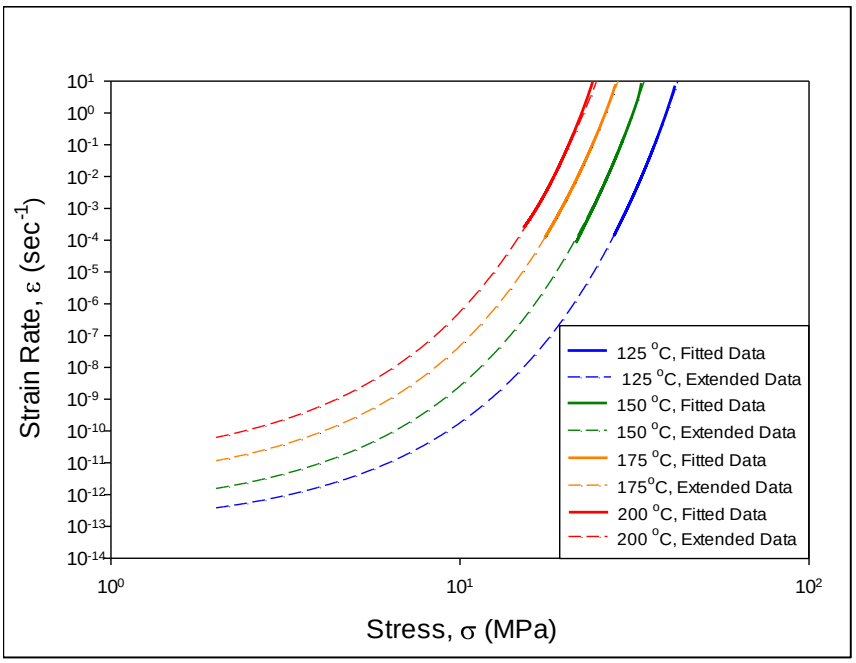

Figure 7.19 Variation of Creep Strain Rate with Applied Stress (Extrapolated to a Lower Stress Level)

Table 7.1 Equivalent Creep Strain Rates at Different Stress Level

Test Temperature (°C)	Strain Rate ($x10^{-8}$)
	10 MPa
125	0.02
150	0.30
175	4.82
200	56.31

Mechanical Properties such as hardness and elastic modulus at different testing temperatures and aging conditions have been collected from the creep experiments and presented in Table 7.2. These properties are plotted with respect to testing temperatures in Figure 7.20.

Table 7.2 Variation of Properties with Testing Temperature

Test Temperature (°C)	Hardness (MPa)	Effective Modulus (GPa)
125	65.5	41.1
150	52.8	27.8
175	41.5	18.8
200	35.5	12.6

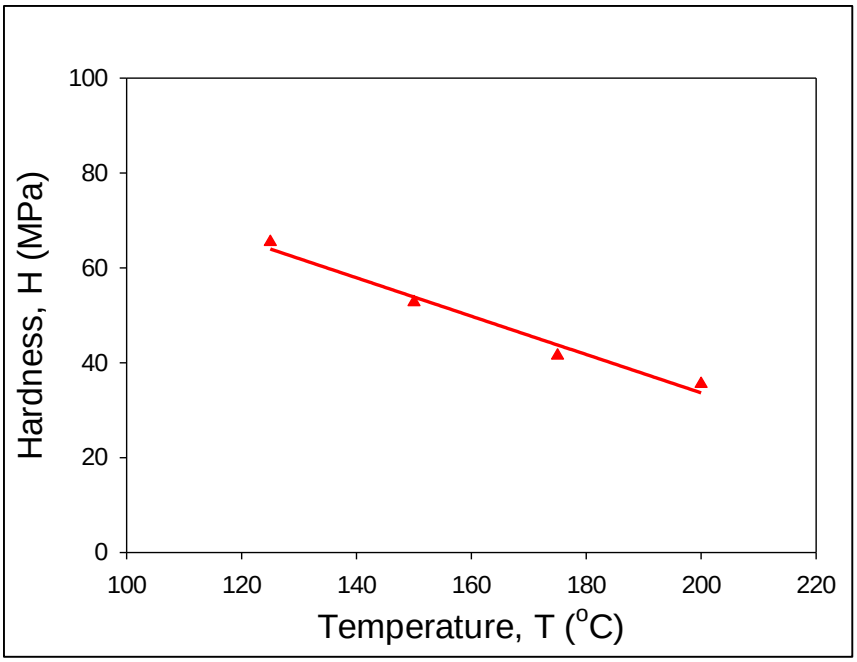

(a)

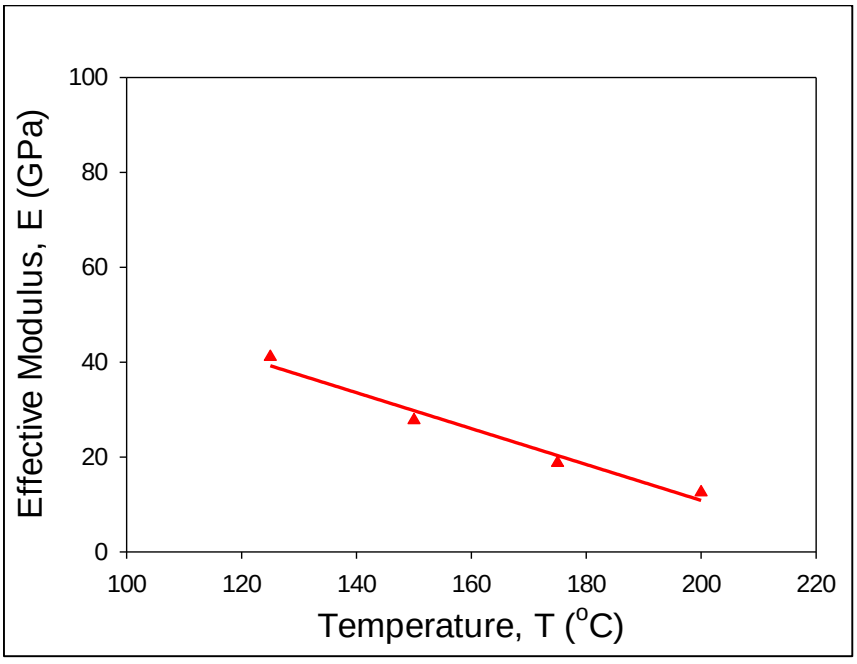

(b)

Figure 7.20 Variation of Properties with Temperature

7.6.2 Effects of Aging

Images of the four single grain solder joints after indentation creep experiments at four different test temperature and five different aging conditions are presented in Figure 7.21. The row of indents on the top of each joint were obtained in no aging condition while the row of indents at the bottom of each joint were obtained after 30 days of aging at 125 °C.

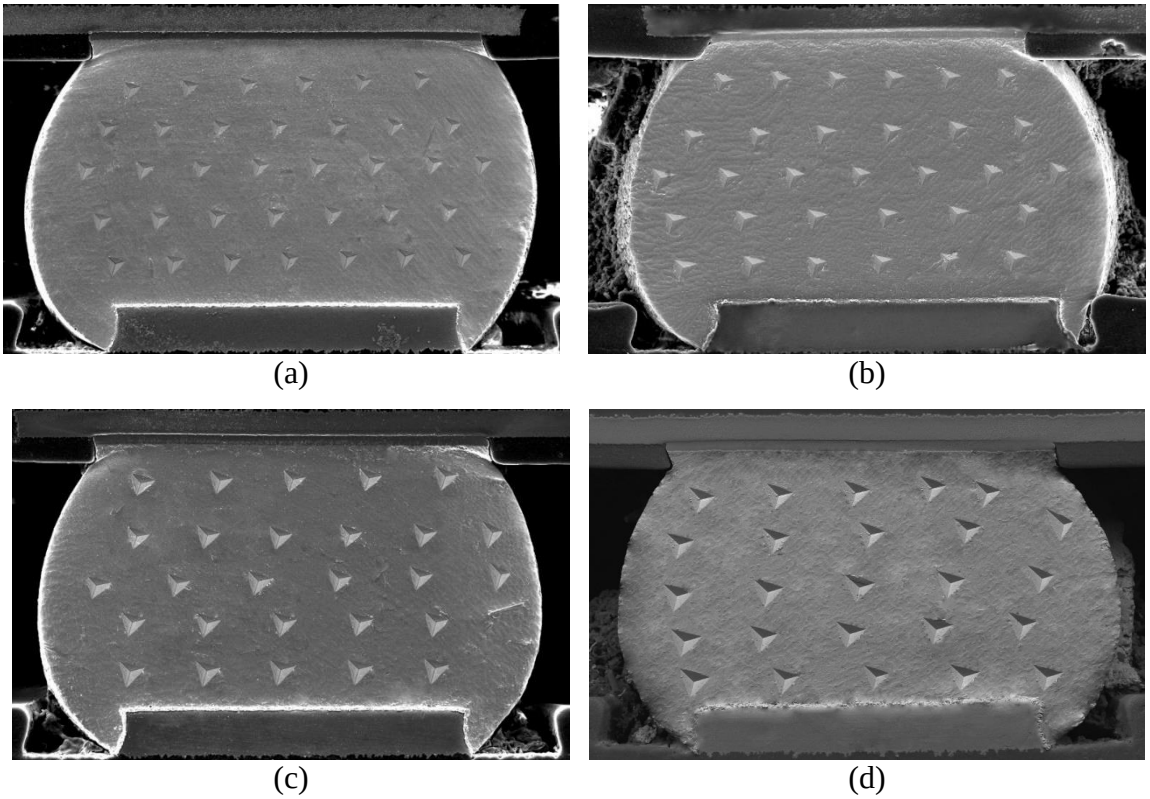

(a) (b)

(c) (d)

Figure 7.21 Indents on SAC305 Solder Joints at Different Aging Conditions Obtained at (a) 125 °C, (b) 150 °C, (c) 175 °C, and (d) 200 °C

Temperature and aging dependent creep results of SAC305 solder joints are shown in Figures 7.22-7.26. In these Figures, each of the five plots for different test temperatures

illustrates the creep behavior at different aging conditions, such as, no aging (blue), 1 day (green), 5 days (orange), 10 days (red) and 30 days(dark red) of prior aging at T = 125 °C.

Figure 7.22 shows typical load vs. total indentation depth curves, and Figure 7.23 shows typical creep displacement vs. time curves for temperatures of T = 125, 150, 175, and 200 °C. As expected, the total and creep displacements increased with increasing aging time at a particular test temperature.

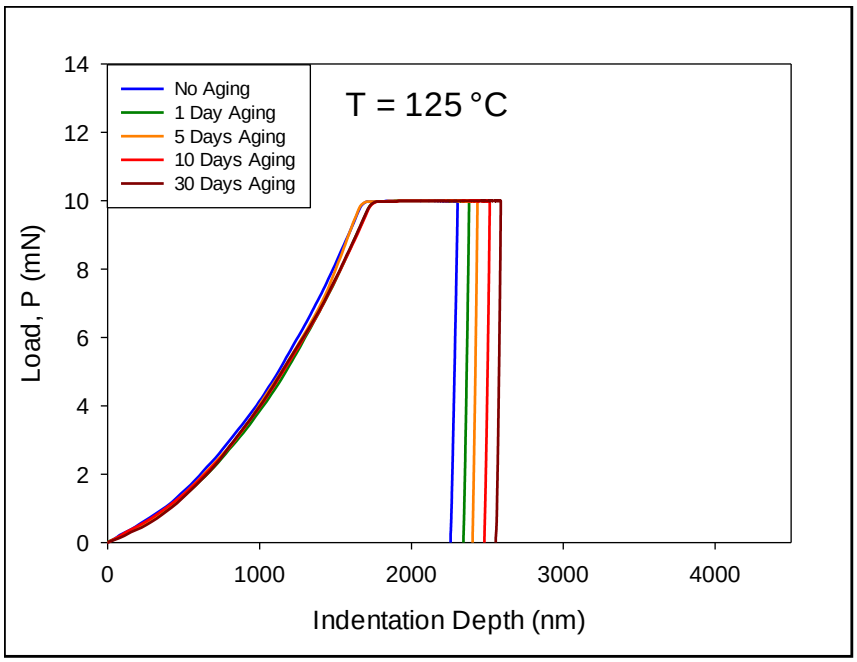
No Aging
1 Day Aging
5 Days Aging
10 Days Aging
30 Days Aging
T = 125 °C
Load, P (mN)
Indentation Depth (nm)
0
2
4
6
8
10
12
14
0
1000
2000
3000
4000

(a)

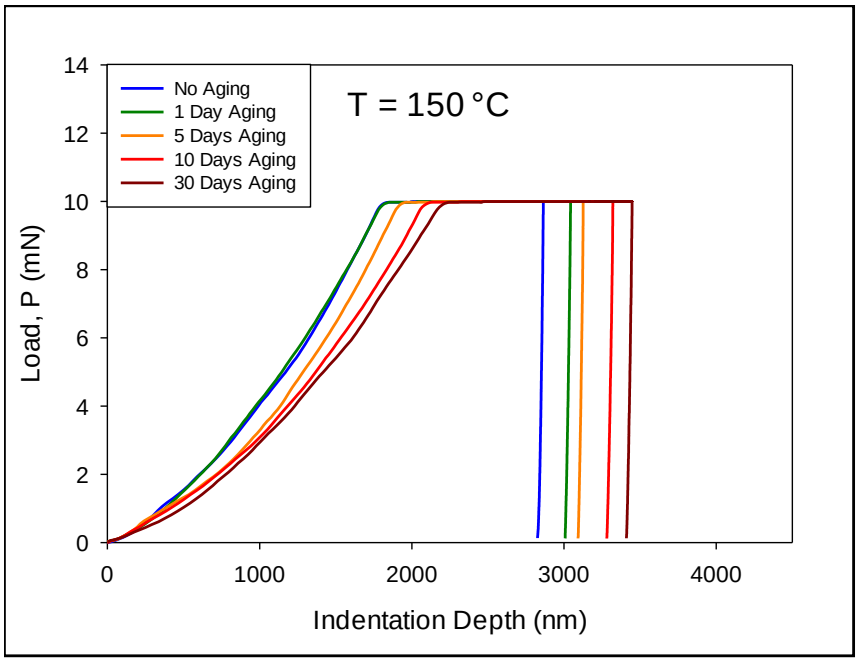
No Aging
1 Day Aging
5 Days Aging
10 Days Aging
30 Days Aging
T = 150 °C
Load, P (mN)
Indentation Depth (nm)
0
2
4
6
8
10
12
14
0
1000
2000
3000
4000

(b)

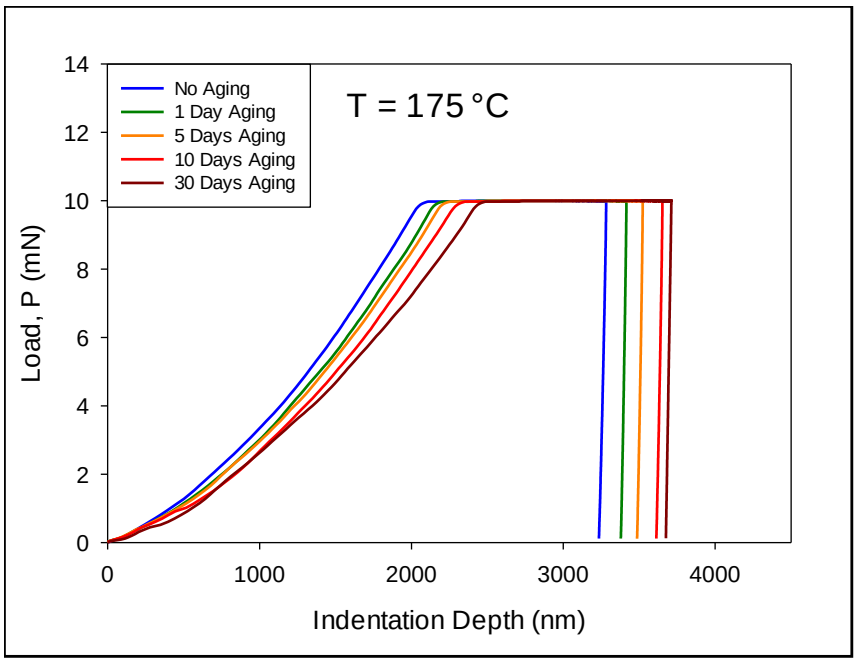

(c)

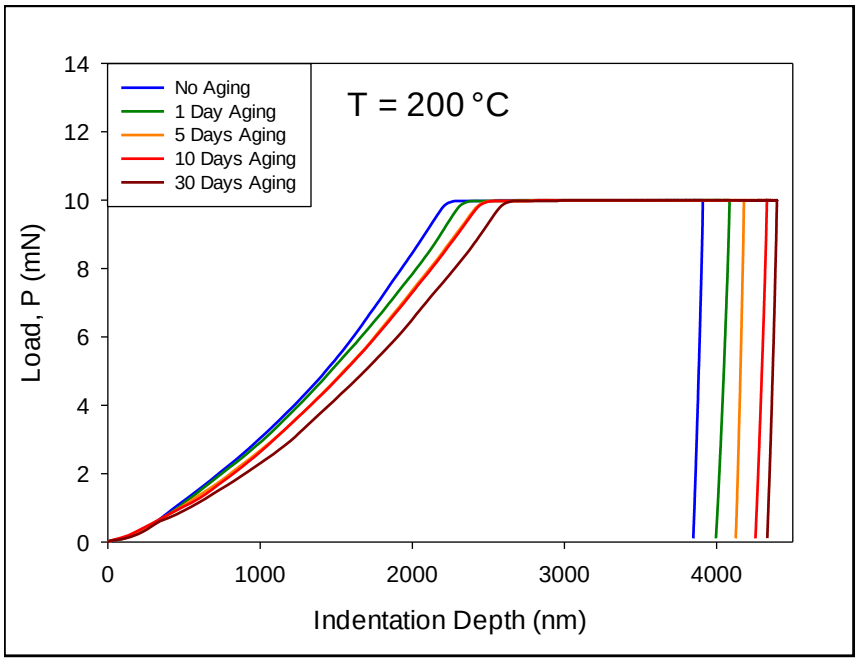

(d)

Figure 7.22 Applied Load vs. Indentation Depth Curves at Different Aging Time

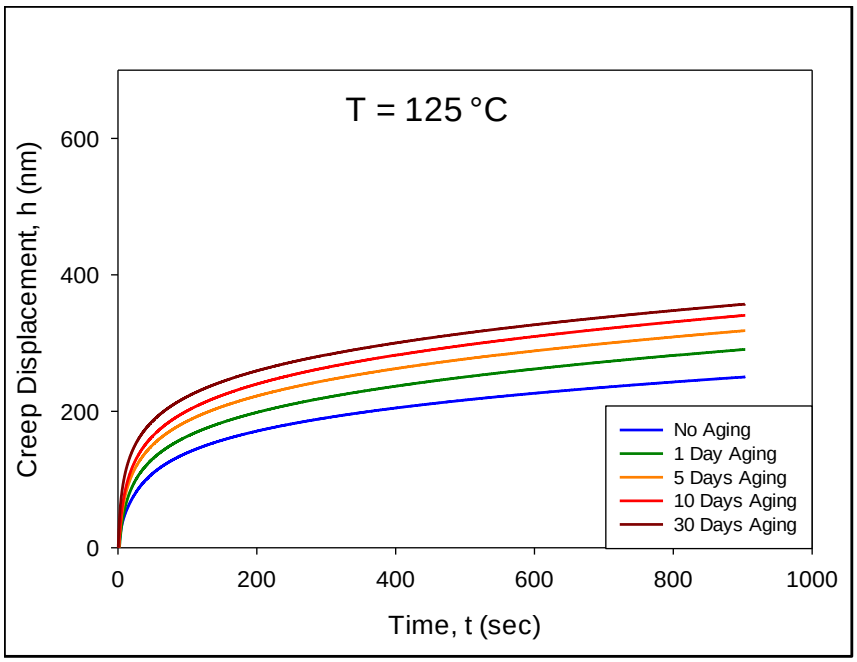
T = 125 °C
Creep Displacement, h (nm)
0
200
400
600
0
200
400
600
800
1000
Time, t (sec)
No Aging
1 Day Aging
5 Days Aging
10 Days Aging
30 Days Aging

(a)

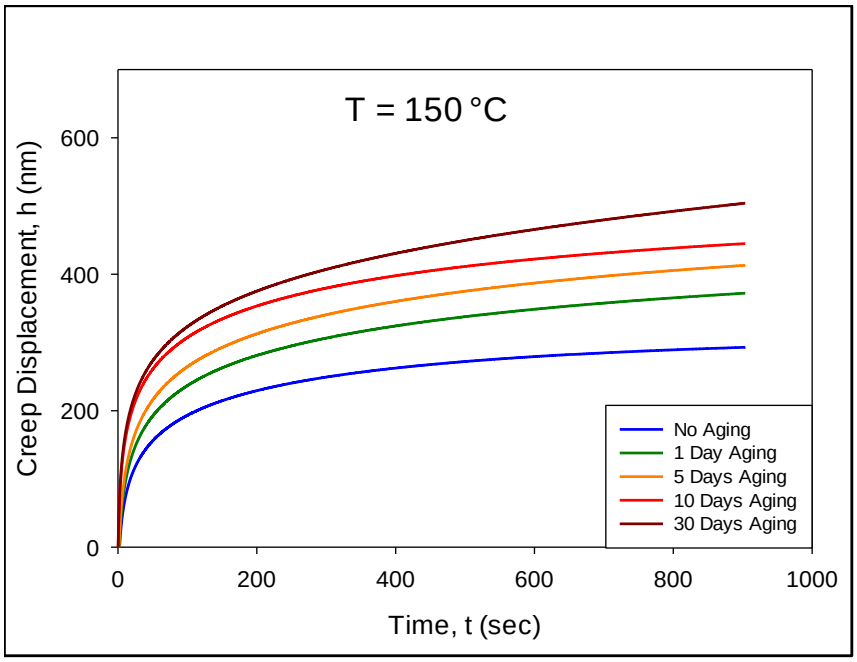
T = 150 °C
Creep Displacement, h (nm)
0
200
400
600
0
200
400
600
800
1000
Time, t (sec)
No Aging
1 Day Aging
5 Days Aging
10 Days Aging
30 Days Aging

(b)

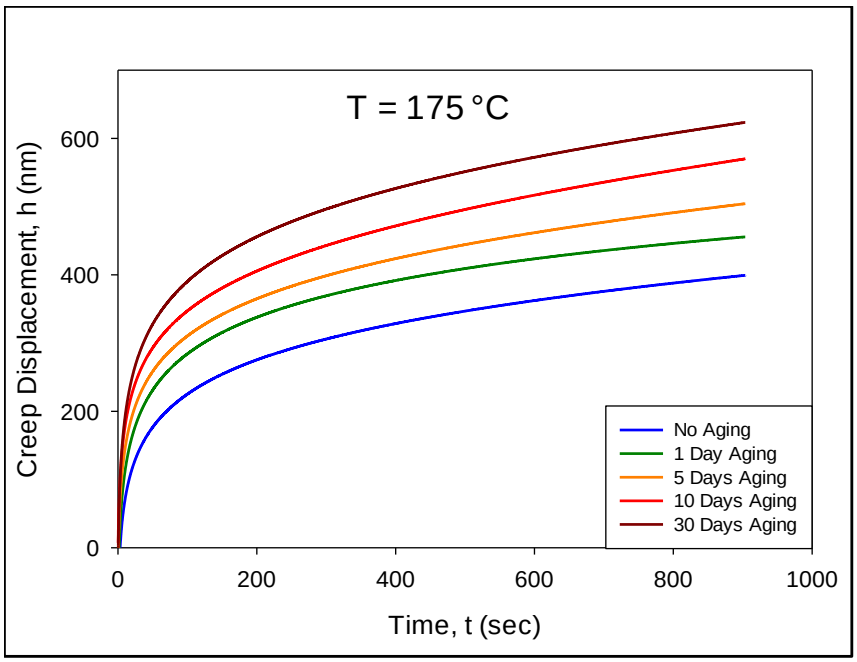

(c)

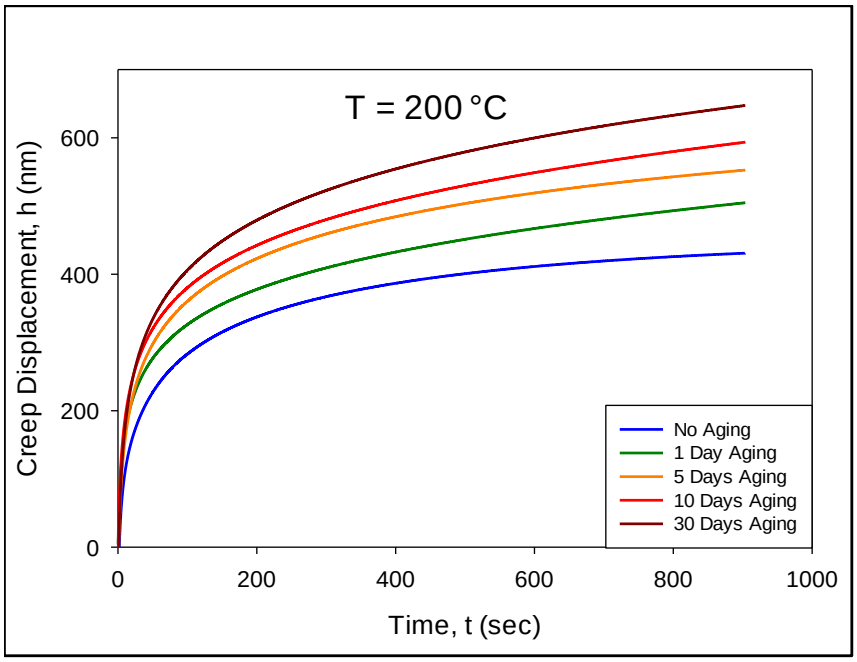

(d)

Figure 7.23 Effects of Aging on Creep Displacement

The effects of aging on the applied stress vs. time curves during the creep deformations are shown in Figure 7.24. Although the applied load was kept constant during the creep tests, the applied stress, at a particular aging condition, under the indenter tip decreased with time due to the contact area continually increasing. Moreover, solder alloy becomes very soft when they are exposed to high temperature aging. So, the indentation depth and the contact area further increased and thus the applied stress is more decreased with aging time.

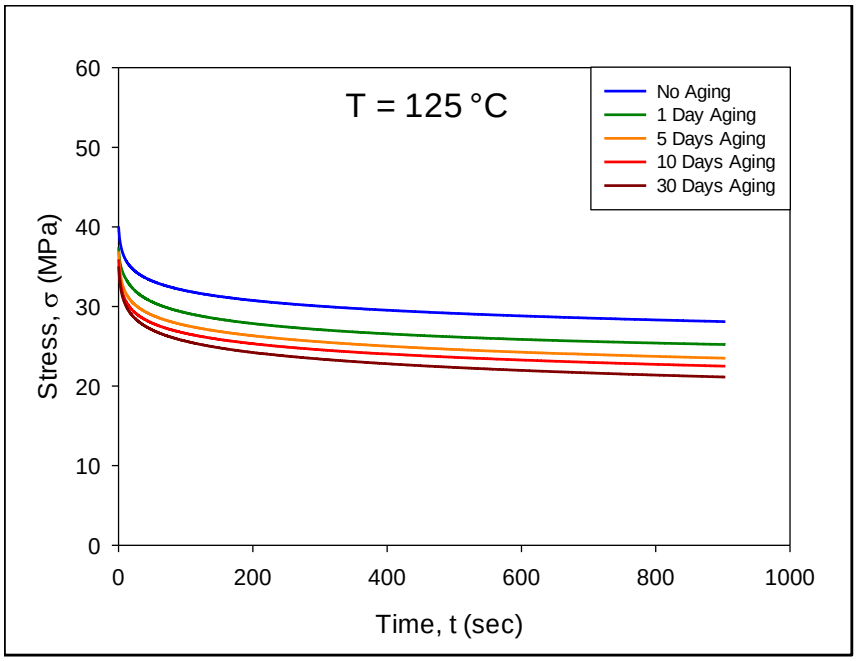

(a)

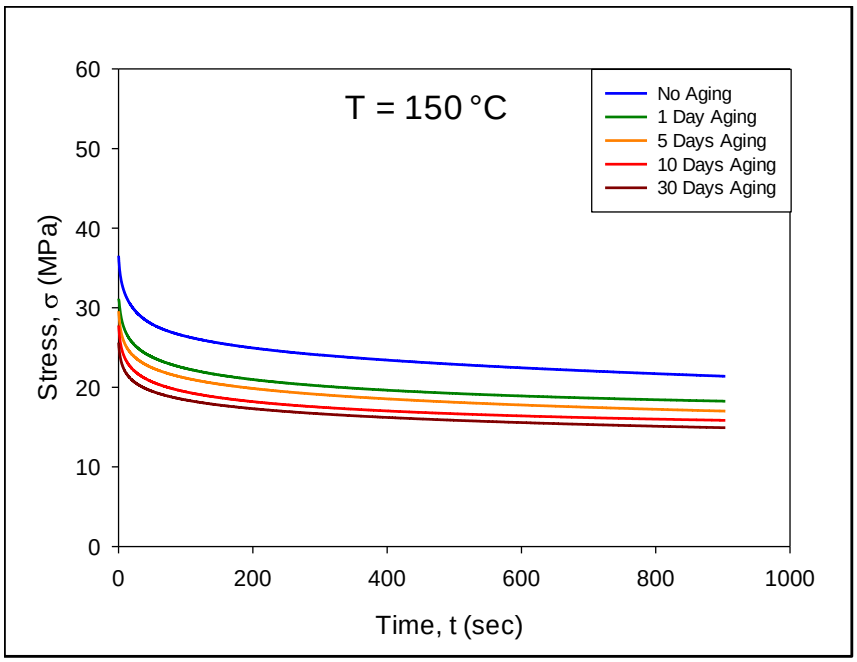
T = 150 °C
No Aging
1 Day Aging
5 Days Aging
10 Days Aging
30 Days Aging
Stress, σ (MPa)
Time, t (sec)
0
10
20
30
40
50
60
0
200
400
600
800
1000

(b)

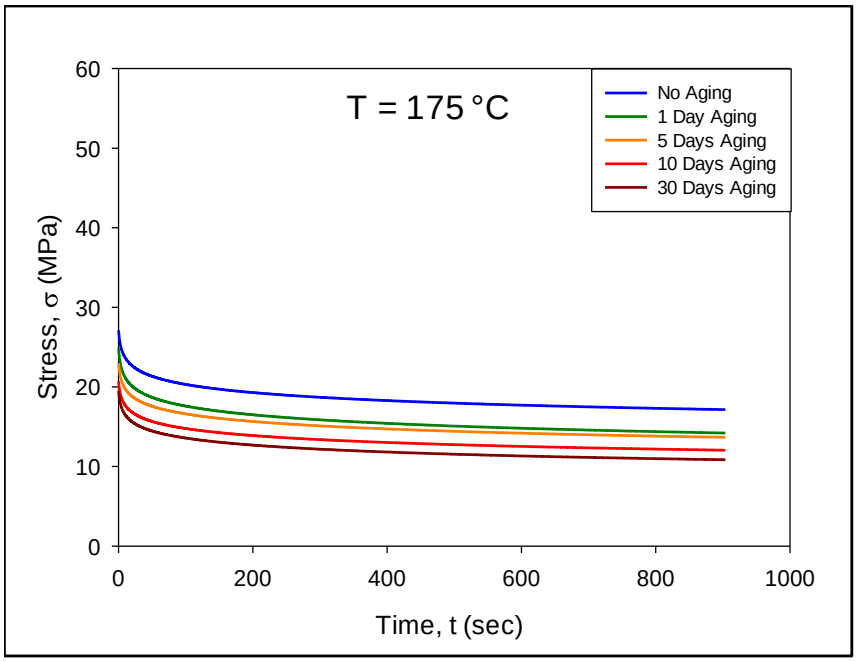
T = 175 °C
No Aging
1 Day Aging
5 Days Aging
10 Days Aging
30 Days Aging
Stress, σ (MPa)
Time, t (sec)
0
10
20
30
40
50
60
0
200
400
600
800
1000

(c)

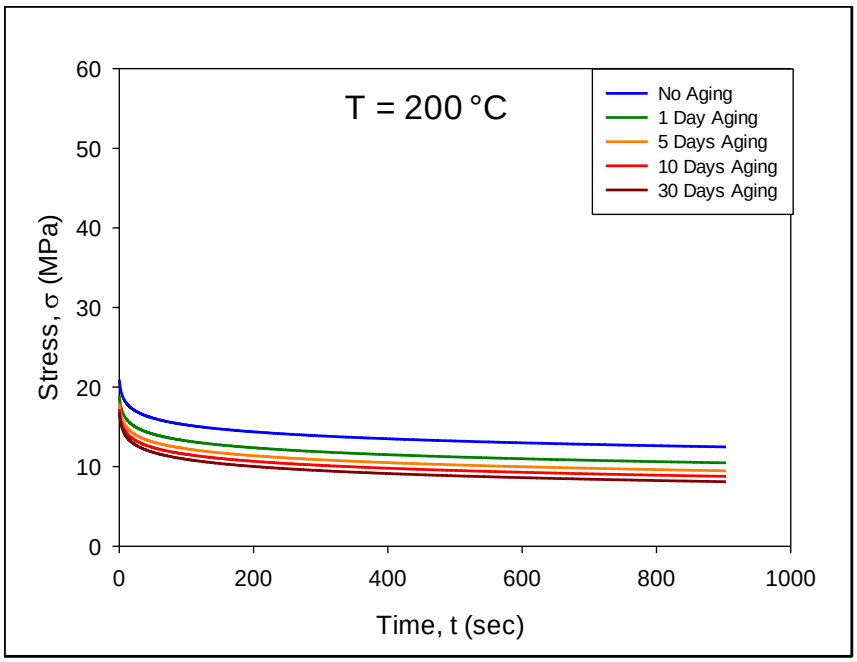

(d)

Figure 7.24 Effects of Aging on Applied Stress

Creep strain rate vs. dwell time plots obtained at different test temperatures and aging conditions are shown in Figure 7.25. Creep strain rate vs. applies stress plots obtained at different test temperatures and aging conditions are shown in Figure 7.26. As expected, aging time had a significant influence on measured creep strain rate, changing it several orders of magnitude for a fixed applied stress level as aging time increases. At any particular test temperature, the strain rate vs. stress curve shifts towards the left with increasing aging time. This indicates that for any fixed stress level, creep strain rate increases with increasing aging time. At high temperature, the creep rates increased significantly with prior aging time. For example, the creep rate at T = 175 °C increased over 10000X at σ = 20 MPa only after 10 days of aging (Figure 7.26 (c)). The effects of aging on the creep rate vs. stress response became larger and larger as the testing temperature increased.

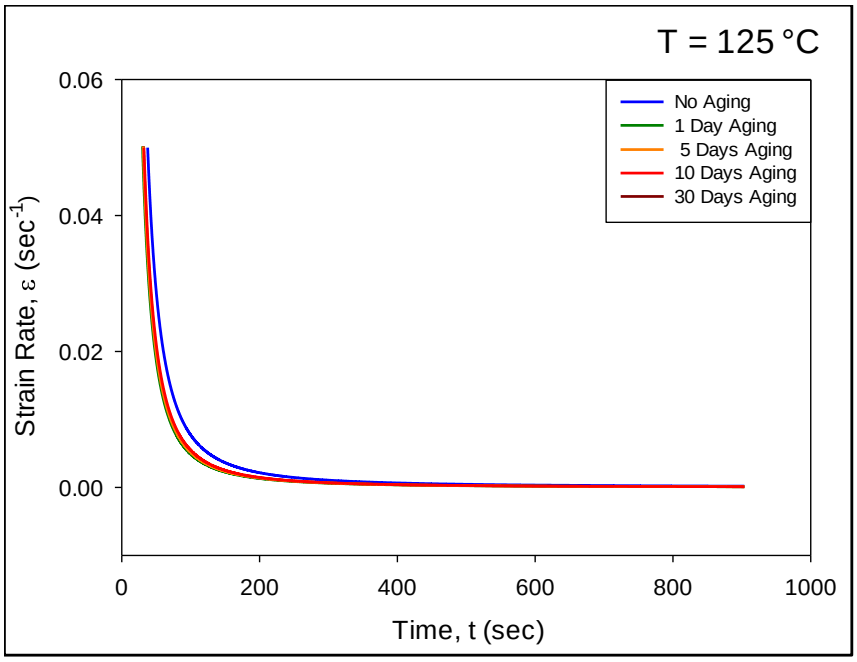
T = 125 °C
No Aging
1 Day Aging
5 Days Aging
10 Days Aging
30 Days Aging
Strain Rate, ε (sec-1)
0.06
0.04
0.02
0.00
0
200
400
600
800
1000
Time, t (sec)

(a)

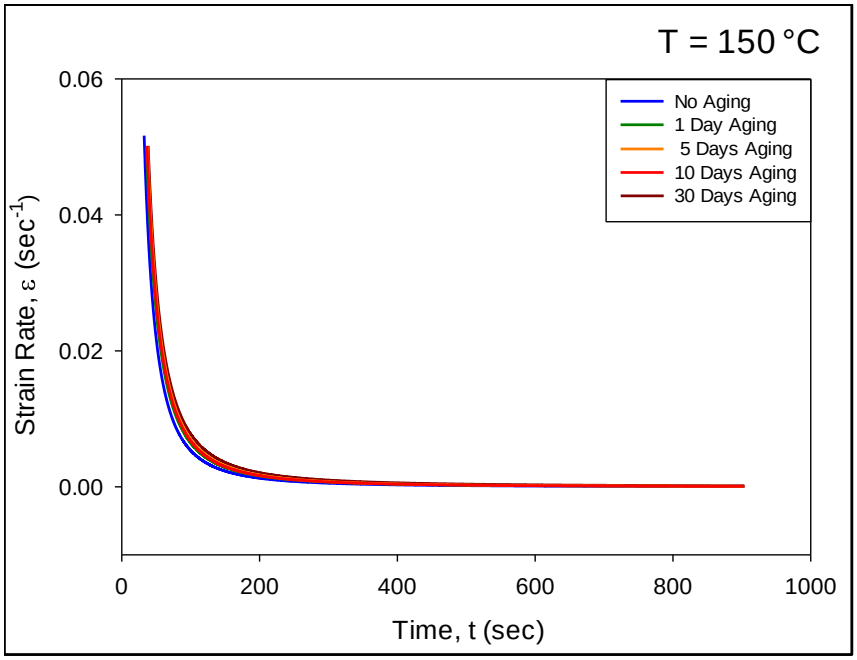
T = 150 °C
No Aging
1 Day Aging
5 Days Aging
10 Days Aging
30 Days Aging
Strain Rate, ε (sec-1)
0.06
0.04
0.02
0.00
0
200
400
600
800
1000
Time, t (sec)

(b)

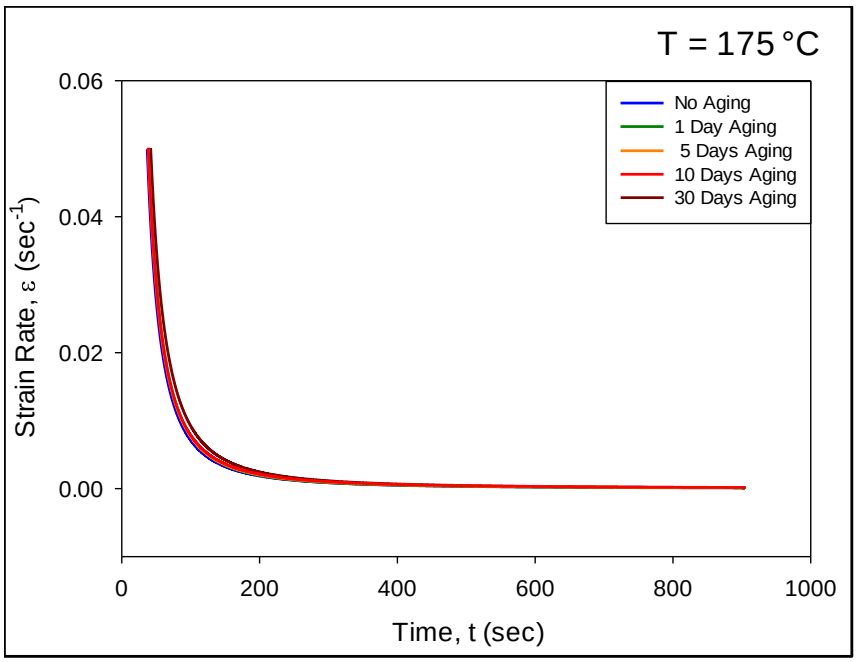

(c)

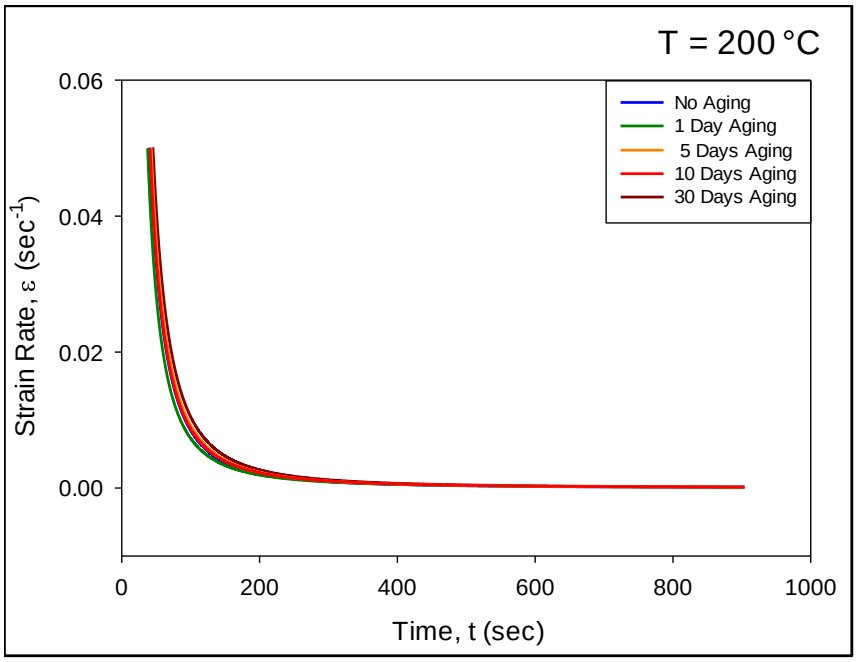

(d)

Figure 7.25 Effects of Aging on Strain Rate vs. Time

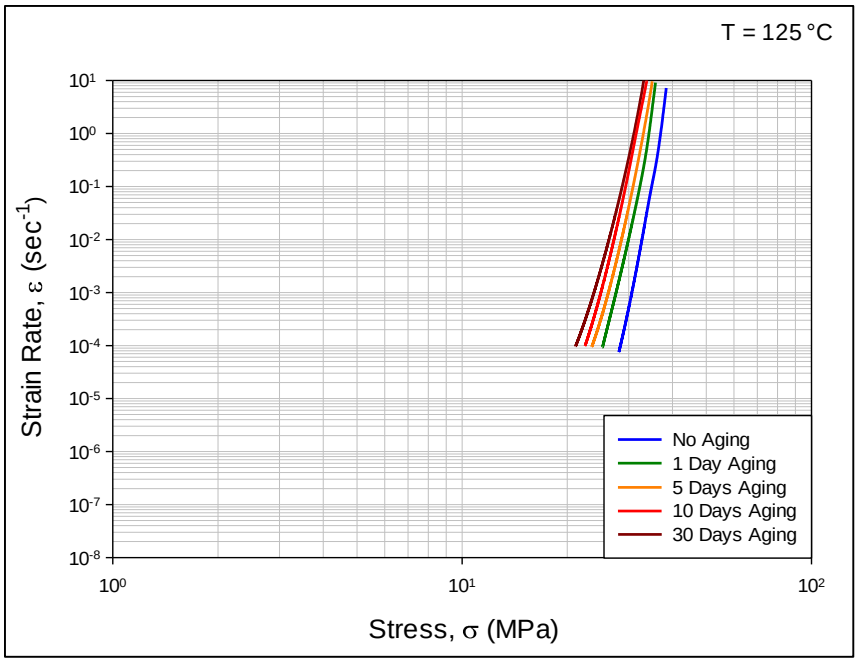
T = 125 °C
Strain Rate, ε (sec-1)
Stress, σ (MPa)
No Aging
1 Day Aging
5 Days Aging
10 Days Aging
30 Days Aging

(a)

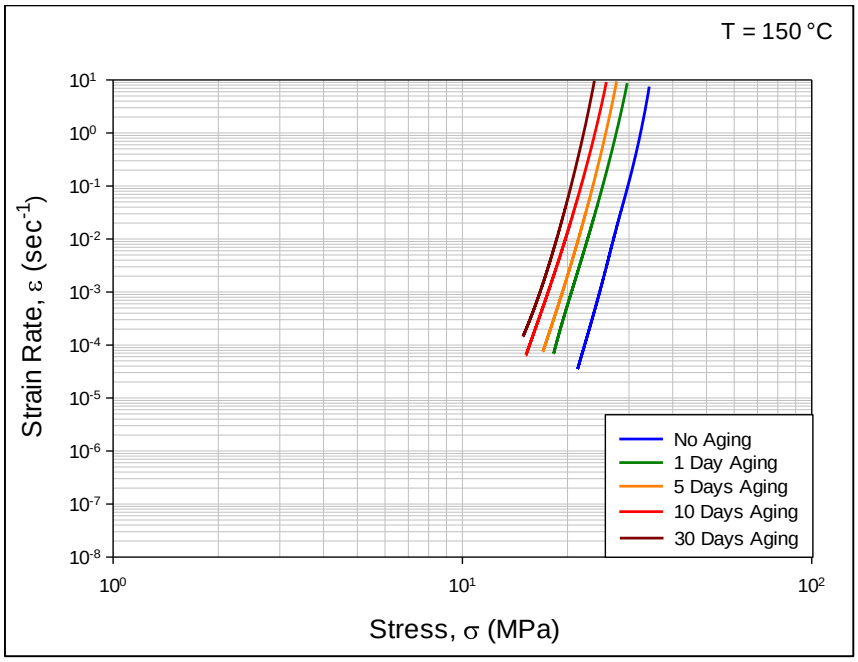
T = 150 °C
Strain Rate, ε (sec-1)
Stress, σ (MPa)
No Aging
1 Day Aging
5 Days Aging
10 Days Aging
30 Days Aging

(b)

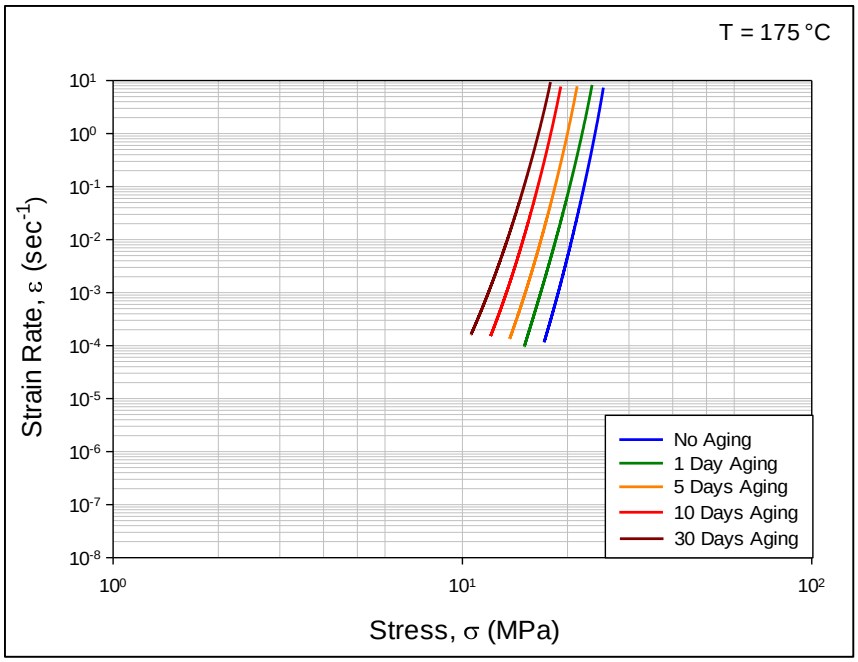

(c)

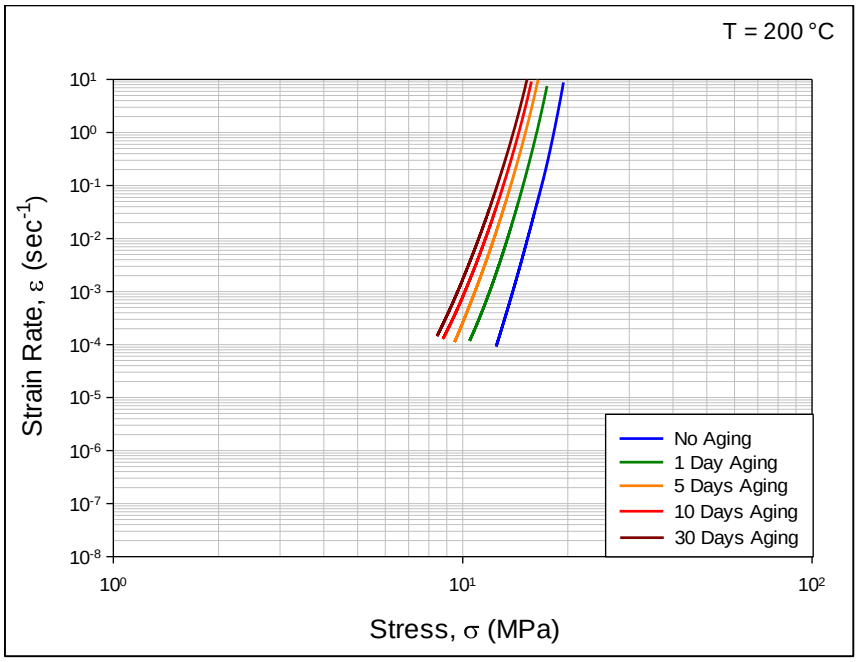

(a)

Figure 7.26 Effects of Aging on Strain Rate vs. Stress Curves

The creep strain rate vs applied stress curves have been extrapolated to the lower stress levels, and are presented in Figure 7.27. The values of equivalent creep strain rates at 10 MPa stress level for all the test temperatures are tabulated in Table 7.3.

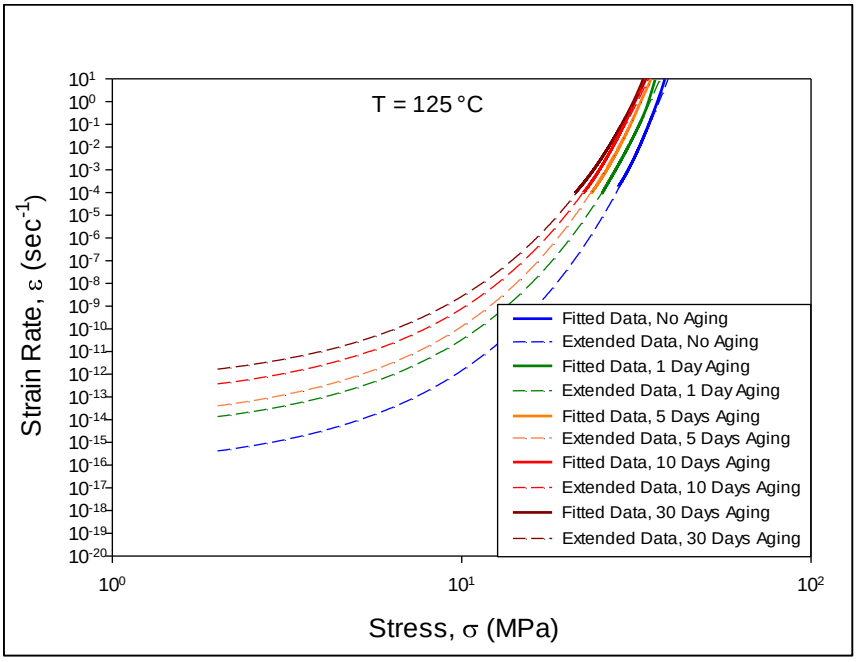

(a)

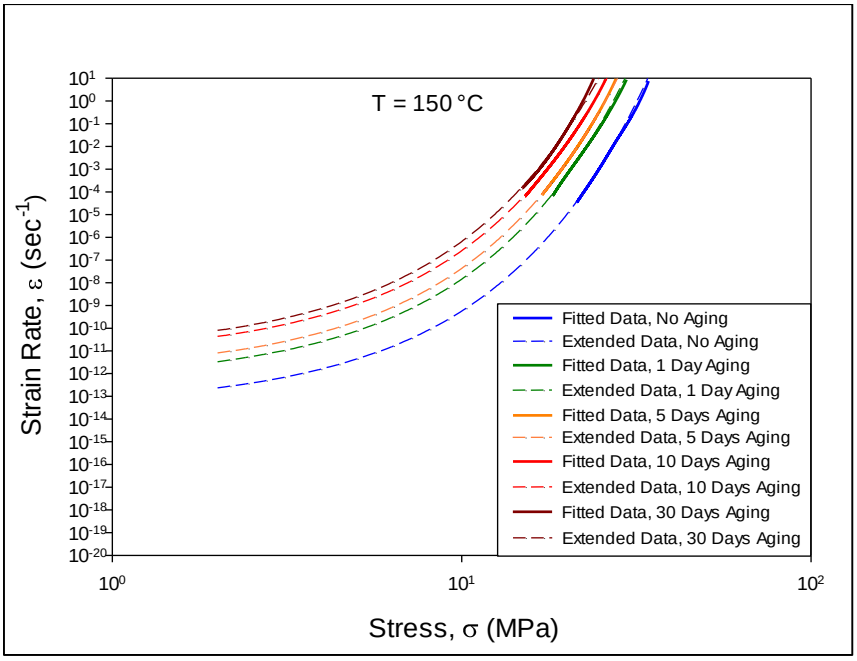

(b)

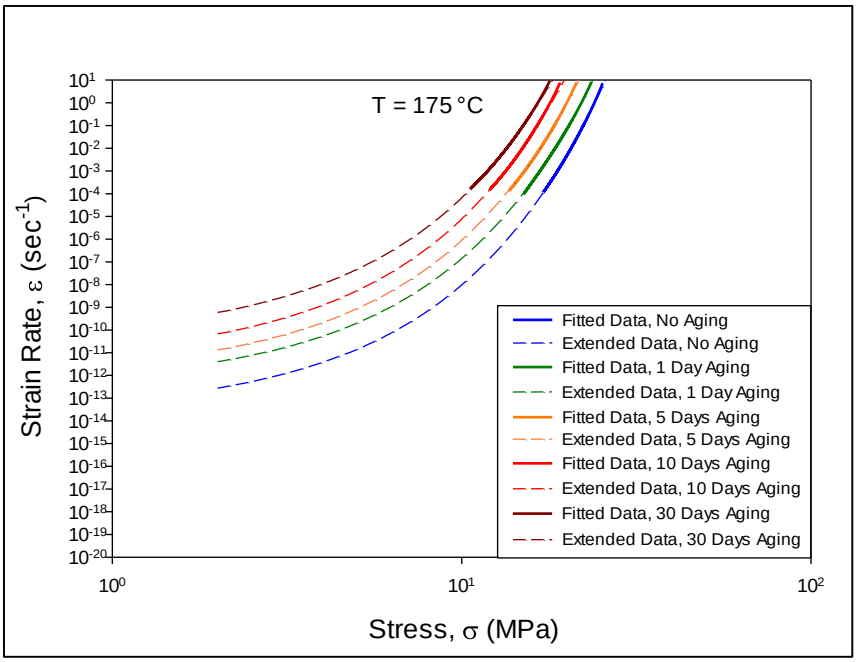

(c)

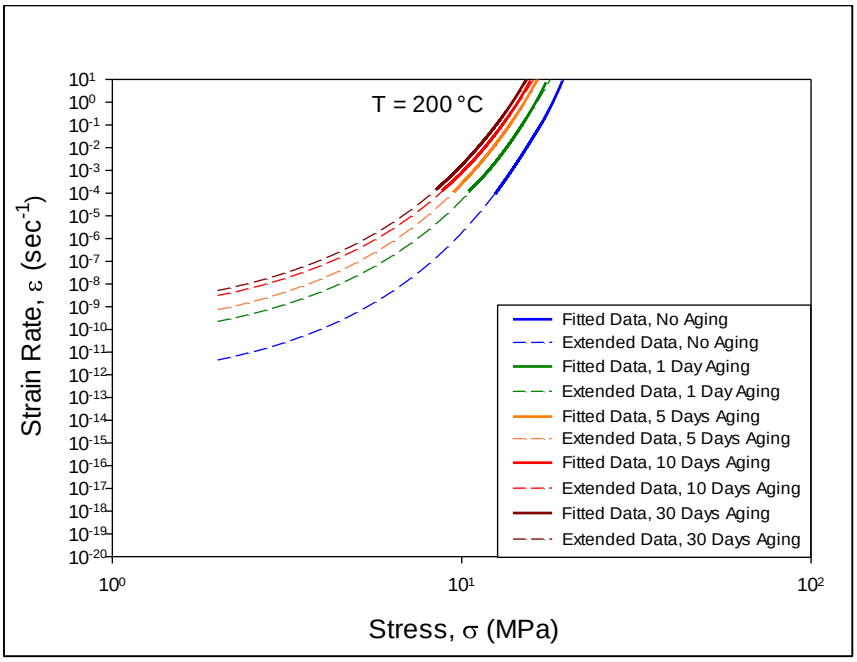

(d)

Figure 7.27 Effects of Aging on Strain Rate vs. Stress Curves (Extended)

Table 7.3 Variation of Creep Strain Rate with Aging Time

Test Temperature (°C)	Aging Time (Days)	Strain Rate ($x10^{-8}$) (Sec^{-1})
		10 MPa
125	0	0.0002
	1	0.0034
	5	0.013
	10	0.0489
	30	0.2722
150	0	0.06
	1	1.47
	5	4.38
	10	26.25
	30	66.62
175	0	0.98
	1	14.26
	5	90.43
	10	777.91
	30	6659.10
200	0	180.51
	1	5000.12
	5	25966.76
	10	79324.48
	30	170492.34

Mechanical Properties such as hardness and elastic modulus at different testing temperatures and aging conditions have been collected from the creep experiments and

presented in Table 7.4. These properties are plotted with respect to aging time for each test temperature in Figure 7.28.

Table 7.4 Variation of Properties with Aging Time

Test Temperature (°C)	Aging Time (Days)	Hardness (MPa)	Effective Modulus (GPa)
125	0	78.1	41.6
	1	63.4	35.7
	5	61.9	33.1
	10	59.9	31.9
	30	58.2	29.1
150	0	47.8	28.7
	1	45.8	27.2
	5	44.4	26.4
	10	42.8	24.6
	30	40.9	23.8
175	0	36.6	20.2
	1	34.8	18.8
	5	33.3	18.3
	10	32.6	17.1
	30	32.1	16.0
200	0	27.3	11.4
	1	25.7	9.9
	5	24.9	9.6
	10	23.9	8.4
	30	22.6	8.3

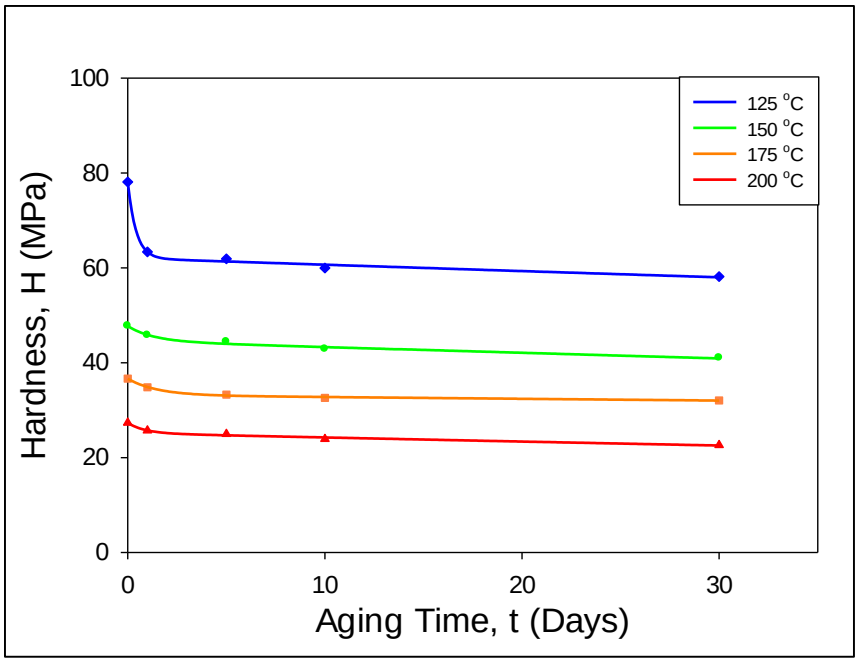

(a)

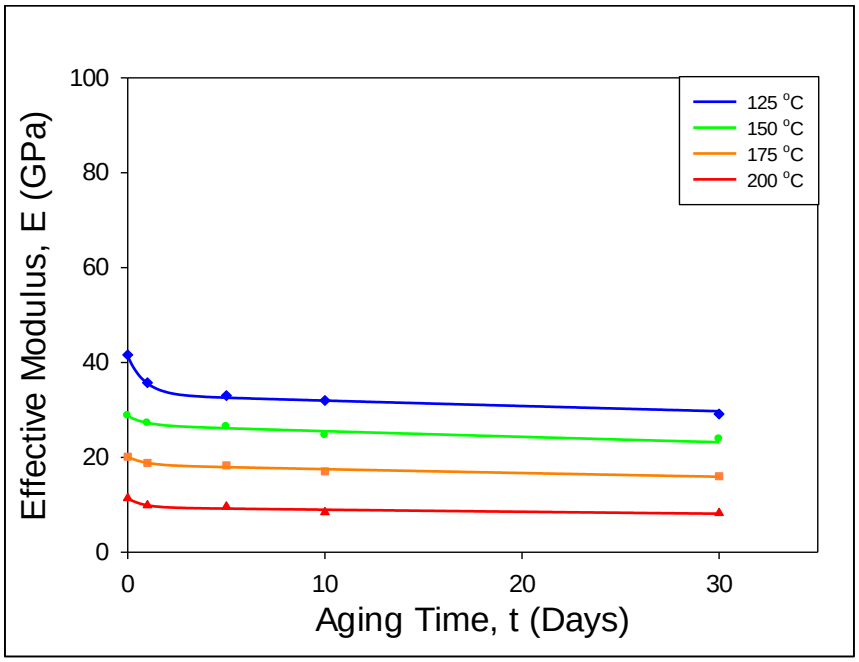

(b)

Figure 7.28 Effects of Aging on Properties

7.7 Summary and Discussion

In this chapter, we have explored the aging dependent mechanical behavior of SAC305 solder joints at extreme high temperatures (T= 125, 150, 175, and 200 °C) using nanoindentation technique. Effect of both test temperatures and aging conditions were investigated. Nanoindentation creep tests were initially performed on SAC305 solder joints at different test temperatures, and temperature dependent mechanical properties, such as creep strain rate, elastic modulus, and hardness were recorded. In addition, Effect of high temperature aging on these properties have been explored. Before testing, four different solder joints were aged (preconditioned) at the high temperature (aging at T = 125 °C), and several different durations of aging were considered (no aging, and 1 day, 5 days, 10 days, and 30 days of aging). Nanoindentation creep tests were performed on these aged specimens, and aging induced degradation of mechanical properties were recorded. A special high temperature test system was used to control the test temperature, and avoid any thermal drift occur during the high temperature tests. Solder joints with single grain crystal structure were chosen to avoid the variation in mechanical properties since solder alloys are highly sensitive to grain orientation.

Our experimental measurements show that mechanical behavior of SAC305 solders are high dependent on test temperature. Mechanical properties, such as creep strain rate, elastic modulus, and hardness degrades significantly with the increase in temperatures. For example, creep rates at 200 °C were about 10000X than those seen at 125 °C. This degradations are more severe when specimens are preconditioned with aging at high temperature for a specific amount of time. At a fixed temperature, creep rate increases,

while modulus and hardness decreases with increasing aging time. The creep properties at high temperature degrades considerably with just a few days of prior aging.

CHAPTER 8

MICROSTRUCTURAL EVOLUTION IN LEAD FREE SOLDERS SUBJECTED TO EXTREME-HIGH TEMPERATURE AGING USING SCANNING ELECTRON MICROSCOPY

8.1 Introduction

The degradation of mechanical properties of solder alloys are result of the microstructural evolution during isothermal aging and high temperature testing. The most well-known and widely observed changes are coarsening of the Ag_3Sn and Cu_6Sn_5 intermetallic compounds (IMCs) present in the eutectic regions between β-Sn dendrites. Some researchers have proposed empirical models to describe the growth of these secondary phase particles as a function of aging temperature and aging time, and related this growth to mechanical property changes. In most of the prior investigations, microstructural changes during aging have been observed by comparing two different solder joints subjected to different aging conditions. Thus, the comparisons made were qualitative in nature (e.g. average IMC particle size) since the two microstructures were from different samples and could not be directly compared.

8.2 Microstructural Evolution of SAC305 Solder

In the current work, the microstructural evolution of SAC305 was investigate for different aging conditions. In particular, aging was performed at T = 125, 150, and 175 °C

for up to 20 days, and the topography of the microstructure of a fixed region was captured using the SEM system. This process generated several images of the microstructure as the aging progressed. These images were used to predict the microstructural evolution in SAC305 solder joints exposed to high temperature aging. Image analysis software was utilized to quantify microstructural changes (total area, number and average diameter of IMC particles, interparticle spacing etc.) with respect to aging time.

The microstructure of SAC305 solder consists of β-Sn dendrites surrounded by eutectic region which is a mixture of Ag_3Sn, Cu_6Sn_5, and β-Sn phase. The IMCs (Ag_3Sn, Cu_6Sn_5) in the eutectic region helps to improve strength of the solder alloy restricting dislocation motion. Due to their low melting temperatures, lead free solders are exposed to high homologous temperatures in most product applications. Thus, there is a continuous state of active diffusion processes in the solder alloys, and their microstructures are inherently unstable and will continually evolve during normal operating temperature conditions of electronic packaging assemblies. Typical microstructure evolution in lead free solders includes coarsening of intermetallic phases and subgrains, breakdown of dendrite structures, as well as potential recrystallization at Sn grain boundaries. Such changes in solder microstructure are accompanied by dramatic changes in mechanical response and failure behavior, and these multifaceted evolutions occurring in the material are typically referred to as solder aging phenomena. An example of SAC305 solder microstructure evolution after 1 year of aging at 100 °C is presented in Figure 8.1.

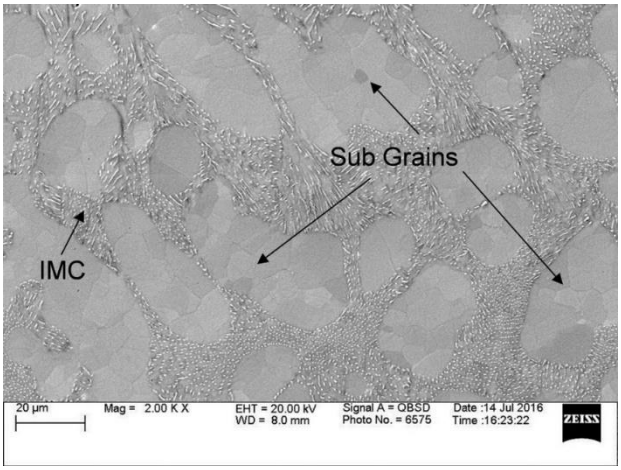

(a)

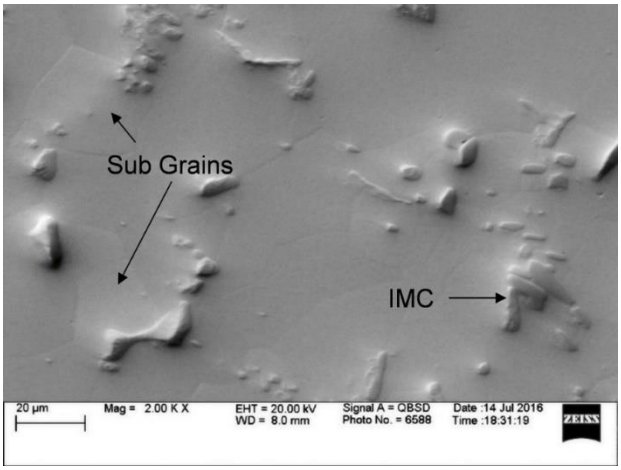

(b)

Figure 8.1 Microstructure of SAC305 Solder (a) Before Aging and (b) After Aging

Many researchers have studied effects of aging on the evolution of solder microstructure. The most well-known and widely observed changes are coarsening of the Ag_3Sn and Cu_6Sn_5 IMCs present in the eutectic regions between β-Sn dendrites. Several researchers [57, 61, 70, 154, 157, 176-179] have also proposed empirical models to describe the growth of IMC particles or layers as a function of aging temperature and aging time. In many studies on the effects of aging on solder microstructure, observations were made on two different solder joints (one non-aged and one aged). Thus, the comparisons

made were often qualitative in nature since the two microstructures were from different samples and could not be directly compared. Figure 8.2 represents the variations of SAC305 microstructure based on the locations of the same sample. All the images were taken at the same magnification from the same sample but in different locations or regions. It is evident from all the images in Figure 8.2 (a-d) that the microstructure of SAC305 is also dependent on the locations. As a result, in order to avoid region based variation in the microstructure, aging study should conduct at a fixed location of the same sample (not different sample). This kind of careful studies are expected to produce a more realistic quantitative analysis results for aging induced IMC coarsening experiments.

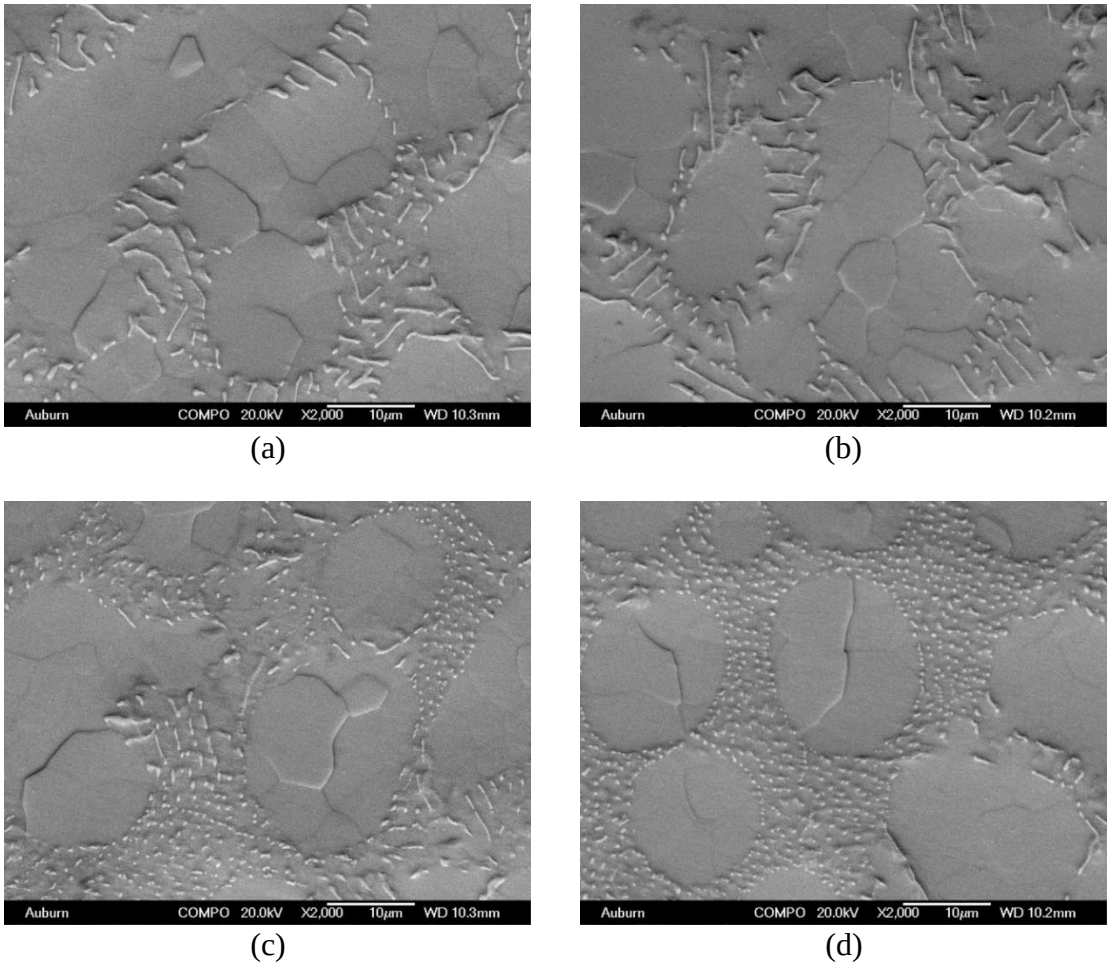

Figure 8.2 Location Based Variation in the Microstructure of SAC305 Solder

8.3 Experimental Procedure

The procedure mentioned in section 3.5 was used in this work. In brief, scanning electron microscopy was utilized to examine microstructural changes in lead free solder joints occurring due to aging. SAC305 solder joint samples were prepared using a nine-zone reflow oven and a typical lead free BGA temperature profile. Solder joint cross-sectional specimens were encapsulated in epoxy molds and polished using industry standard procedures. As shown in Figures 8.3 and 8.4, small indentation marks were added to the cross-sections to facilitate subsequent locating of the same regions in the solder joints. These consisted of β-Sn dendrites surrounded by interdendritic eutectic regions incorporating a fine dispersion of Ag_3Sn and Cu_6Sn_5 intermetallic particles in β-Sn. Pyramidal idents were placed near the corners of the regions of interest using a nanoindentation system. As shown in Figure 8.3, the indents were placed suitably away from the region of interest to minimize any influence on the microstructure evolution. In this case, the region of interest was approximately 60 x 40 μm, while the center-to-center spacing between the indentation marks was approximately 90 μm.

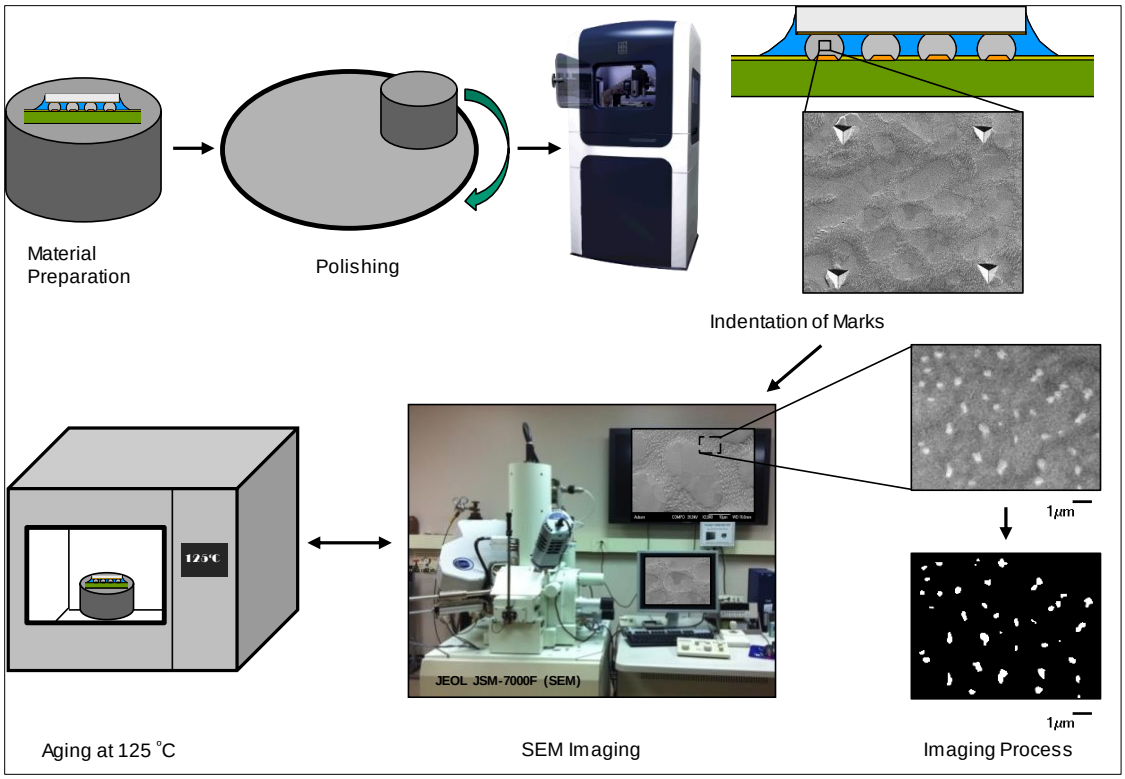

Figure 8.3 Flow Chart of Experimental Procedure (Including JEOL JSM-7000F and Hysitron TI 950).

SEM analysis of the selected regions was then performed on the non-aged as-polished samples. The same samples were then aged at three different extreme high temperatures (T= 125, 150, and 175 ºC) for four different durations of aging (0, 1, 5, and 20 Days). The microstructures of the selected regions were captured after each aging interval. One SAC305 solder joint was prepared for each of the three aging temperatures, and three regions were studied in each joint.

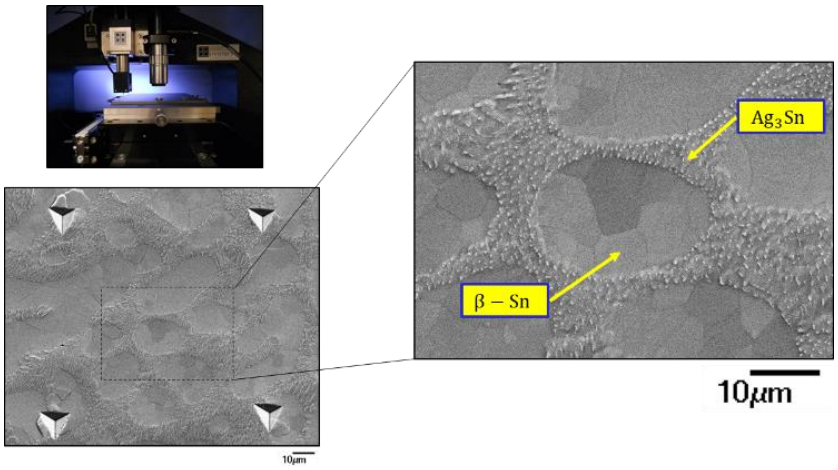

Figure 8.4 Example Region of Interest and Nanoindentation Markers.

The SEM images of the selected regions at different aging conditions are shown in Figure 8.5. A diffusion based IMC coarsening occurs, and larger particles are produced at the expense of smaller particles (Ostwald Ripening) [180-183]. Coarsening of intermetallic particles occurred due to aging. Some IMC particles grew in size, some split into several smaller particles, and some decreased in size and disappeared in the end. In other words, the number of IMC particles decreased, the average particle size increased, and the average particle separation distance increased. Also, the particles shifted to more spherical shapes. The shape and size of the dendrites remained nearly unchanged.

This coarsening and coalescing of IMC particles during aging is known to play a critical role in the degradations of solder mechanical properties. IMC particles will pin and block the movement of dislocations. However, aging leads to both a smaller number of larger IMC particles, and increased spacing between the particles. This results in dislocations being able to pass more easily through the material, decreasing both the yield stress and strength.

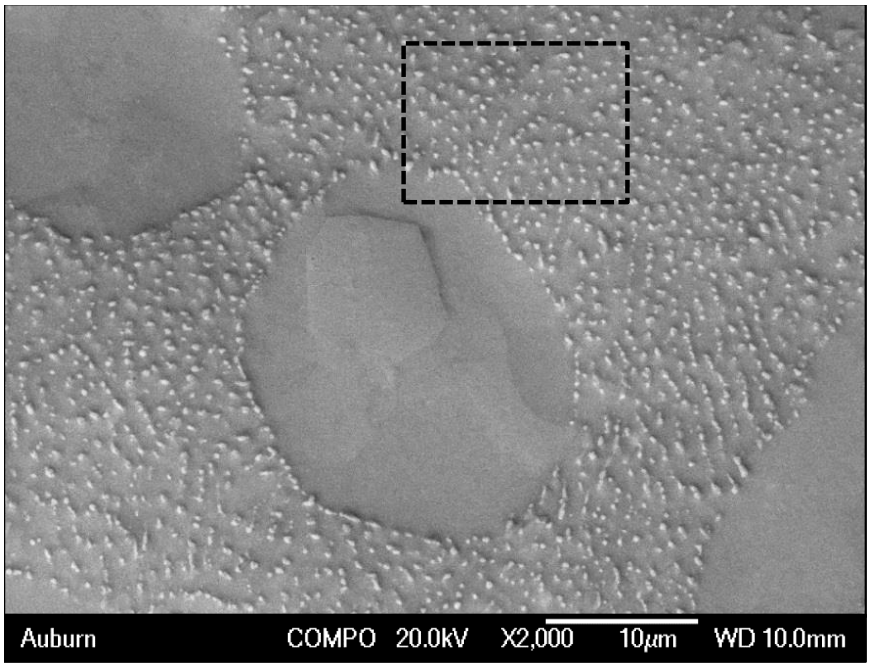

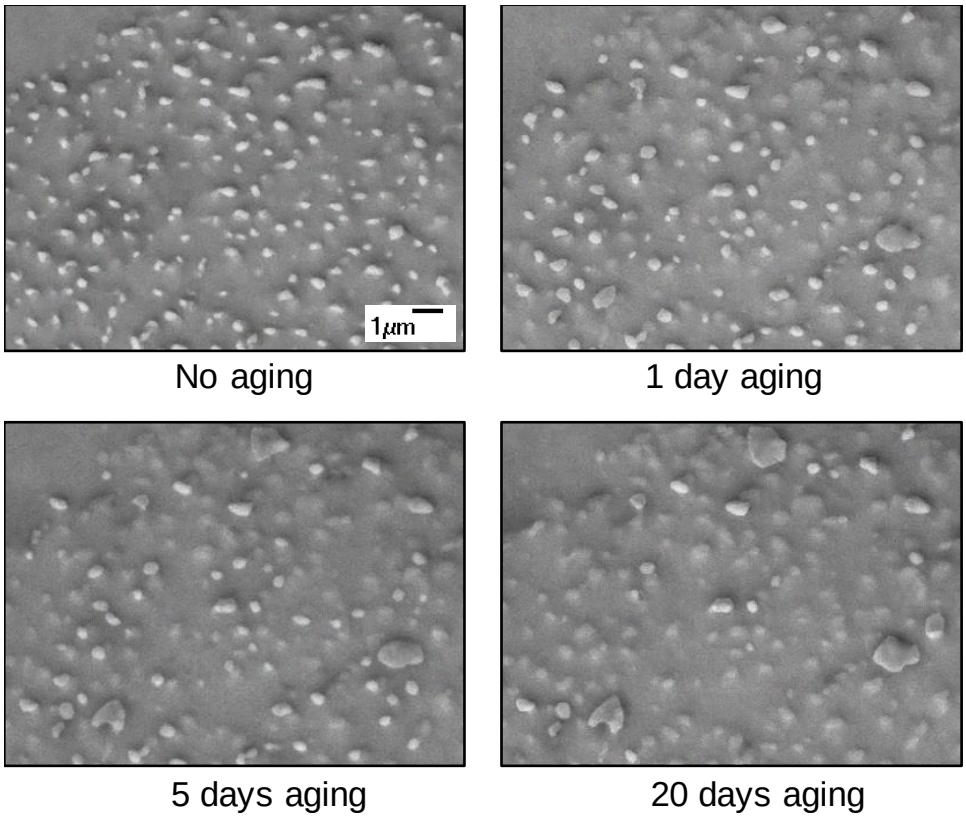

(a) Aging T = 125 ºC (Region 1)

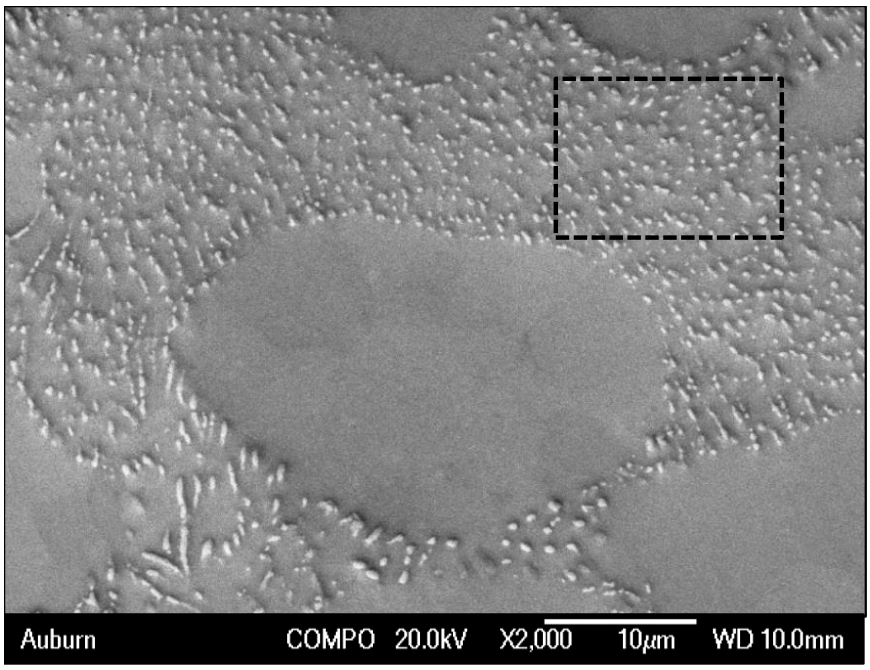

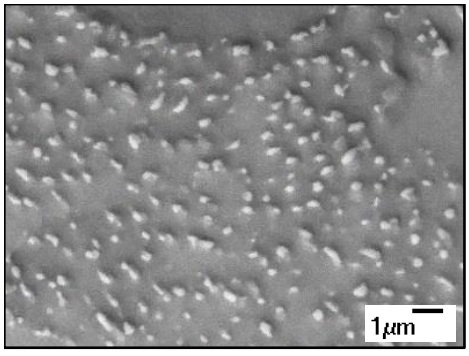

No aging

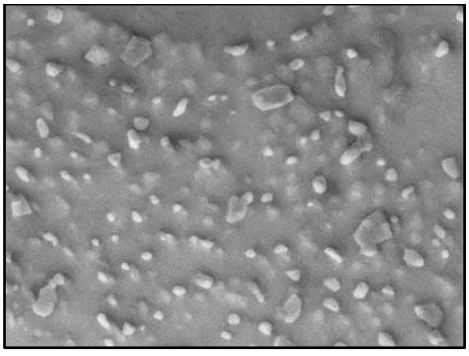

1 day aging

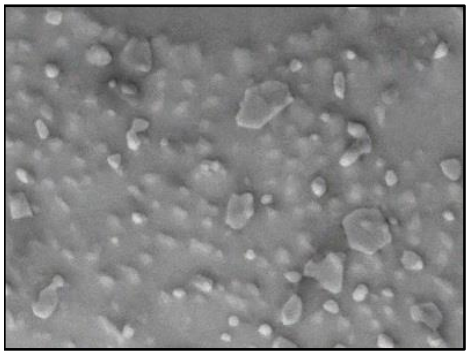

5 days aging

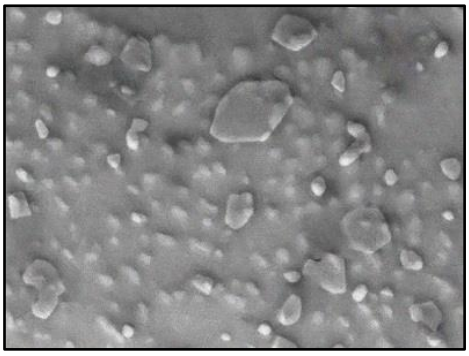

20 days aging

(b) Aging T = 125 ºC (Region 2)

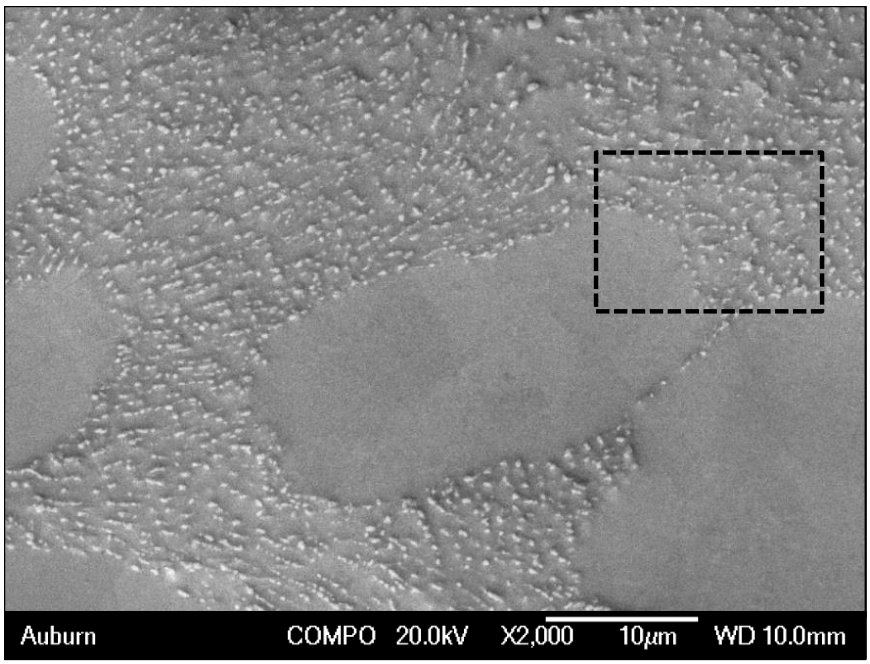

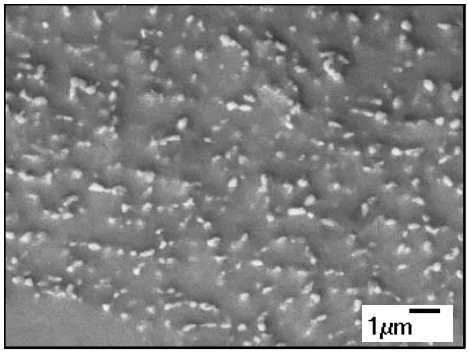

No aging

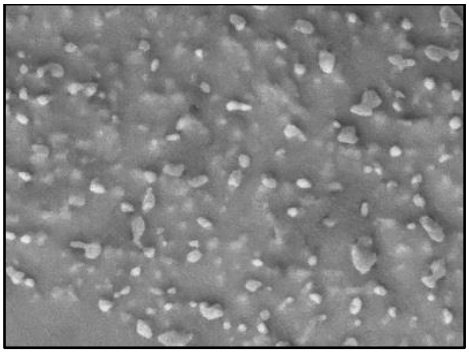

1 day aging

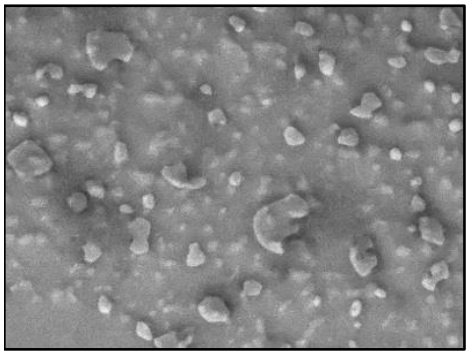

5 days aging

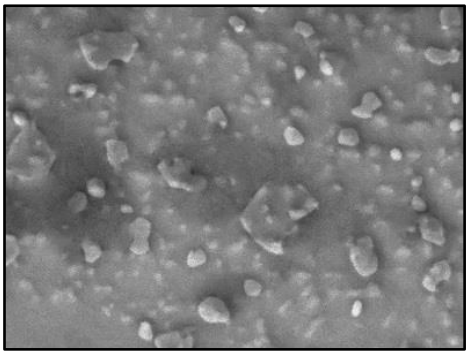

20 days aging

(c) Aging T = 125 ºC (Region 3)

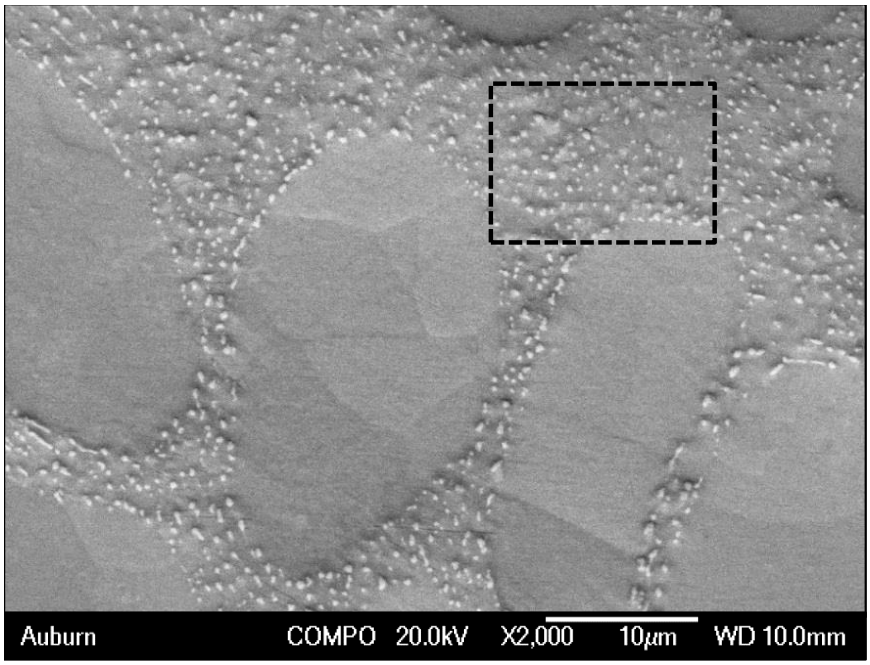

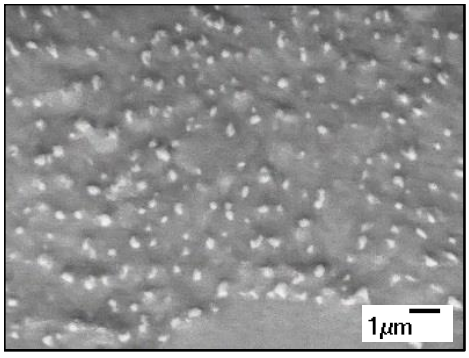

No aging

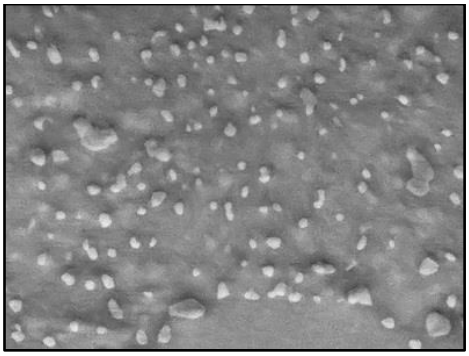

1 day aging

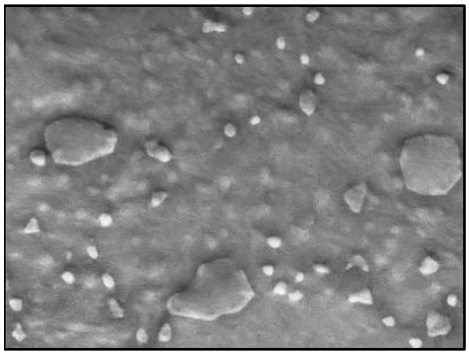

5 days aging

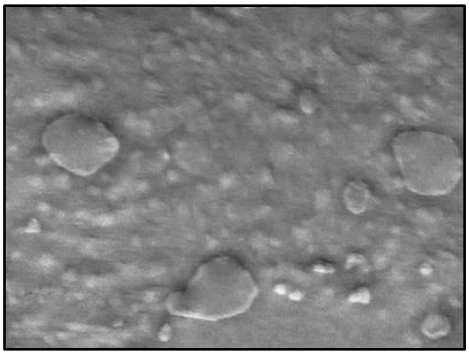

20 days aging

(d) Aging T = 150 ºC (Region 1)

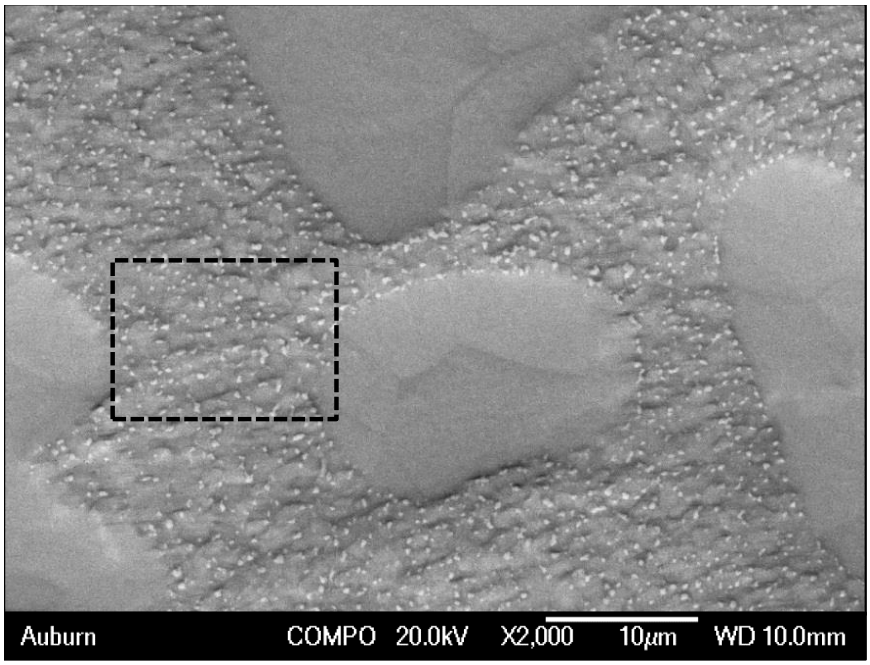

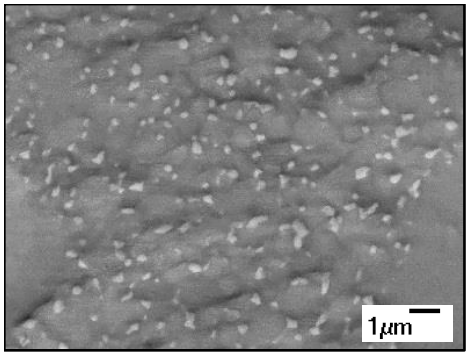

No aging

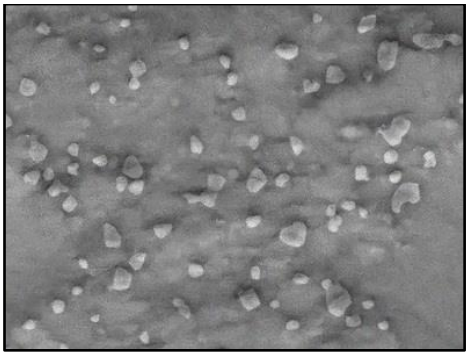

1 day aging

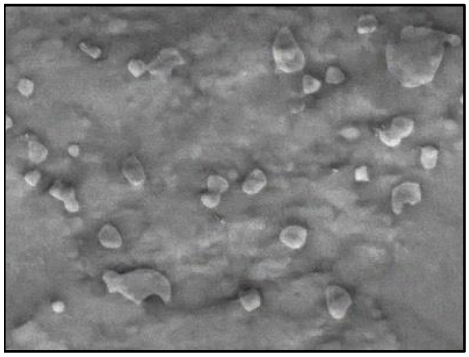

5 days aging

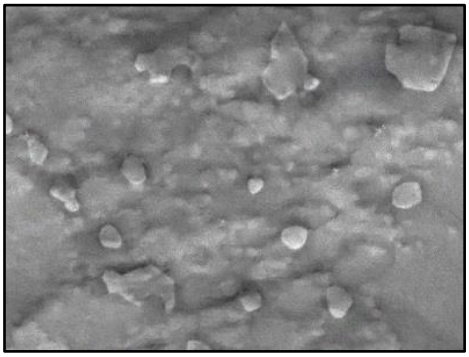

20 days aging

(e) Aging T = 150 ºC (Region 2)

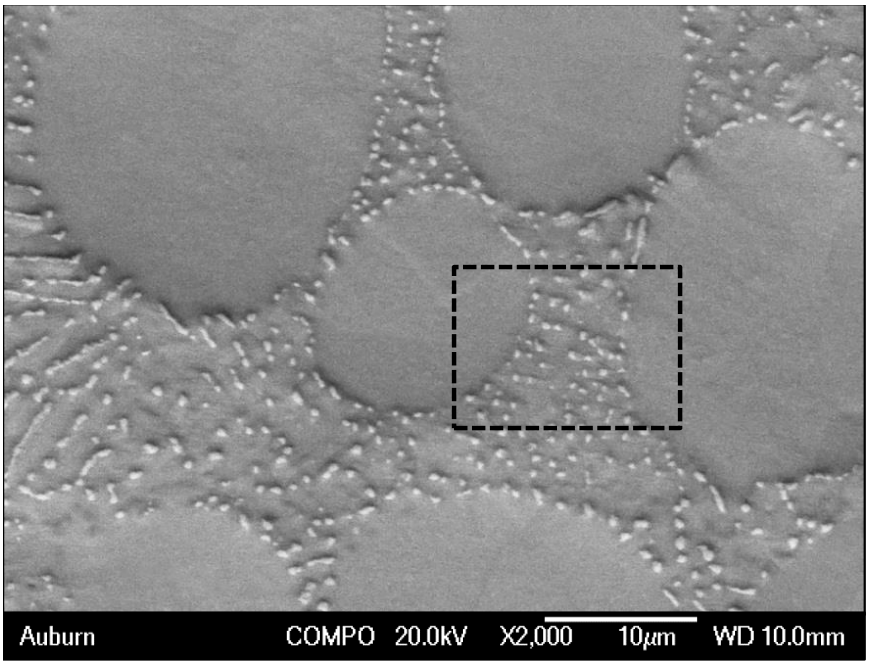

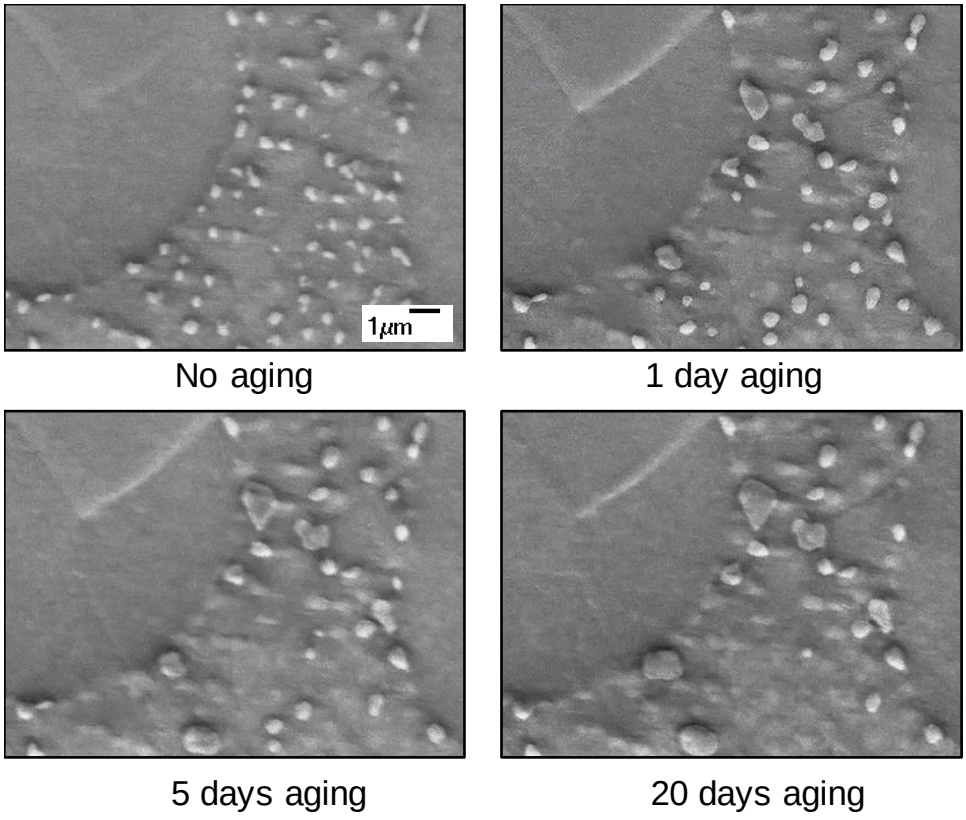

(f) Aging T = 150 ºC (Region 3)

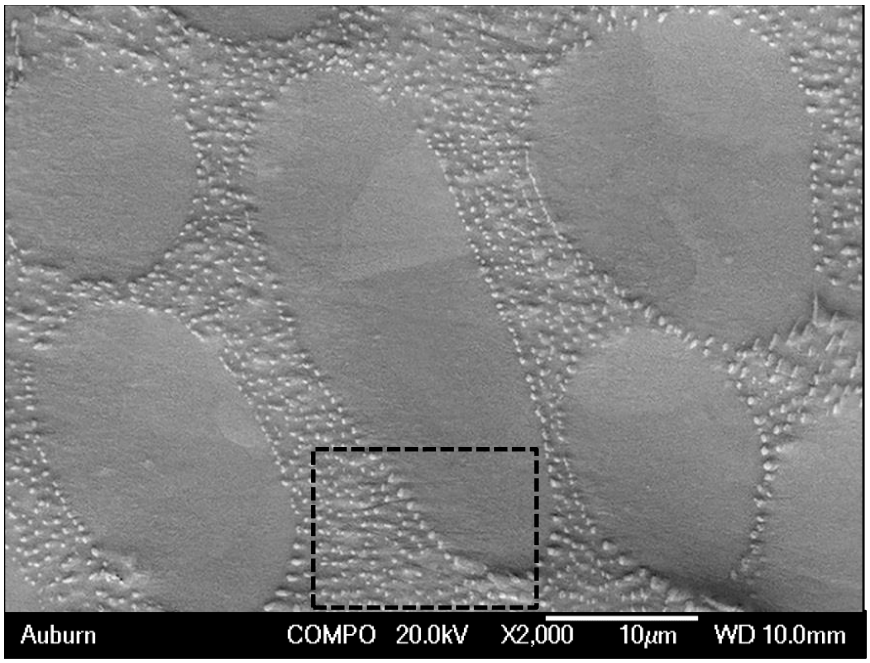

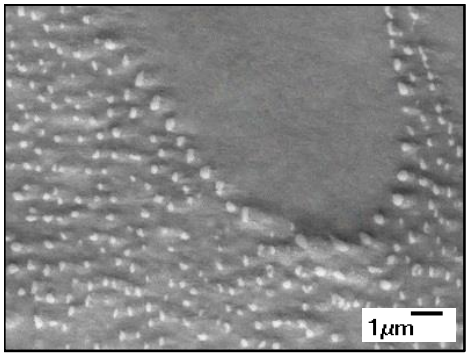

No aging

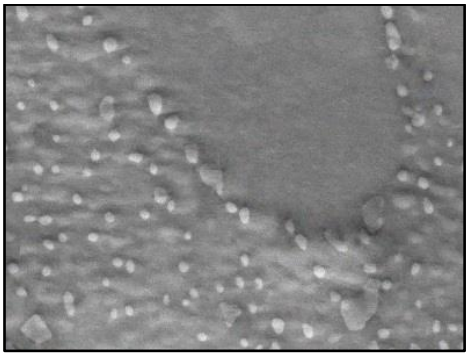

1 day aging

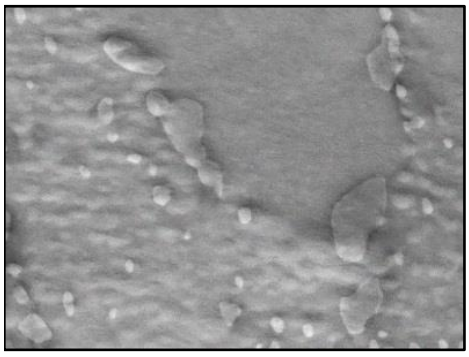

5 days aging

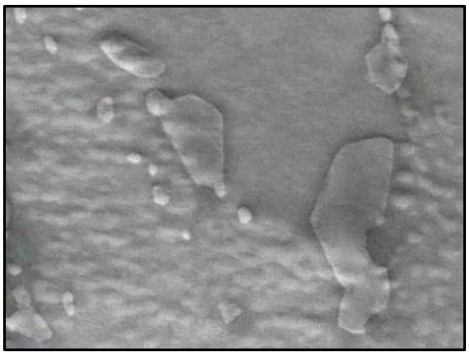

20 days aging

(g) Aging T = 175 ºC (Region 1)

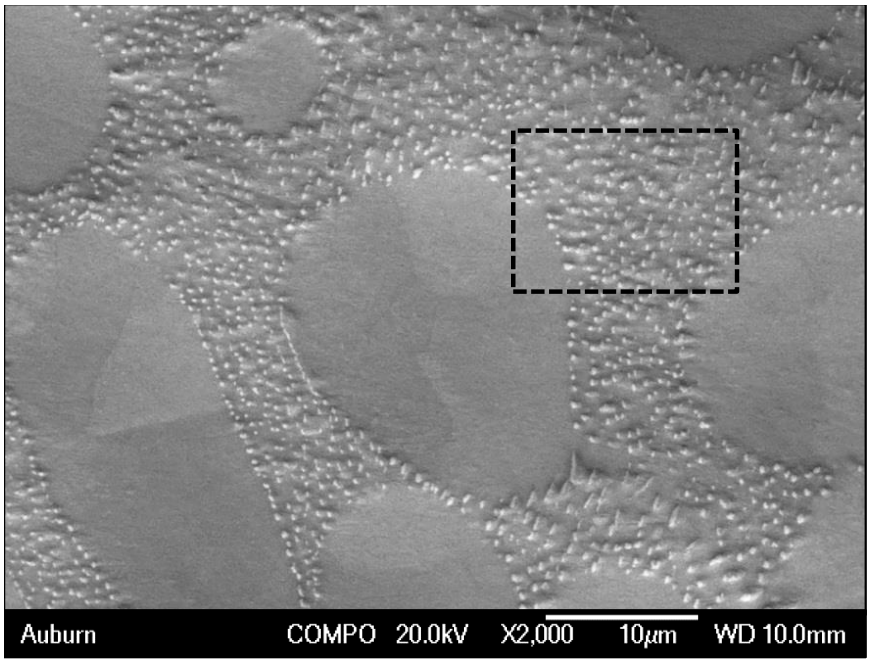

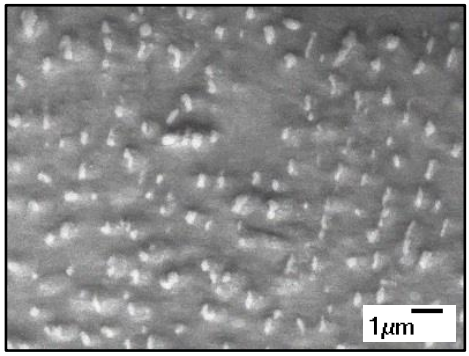

No aging

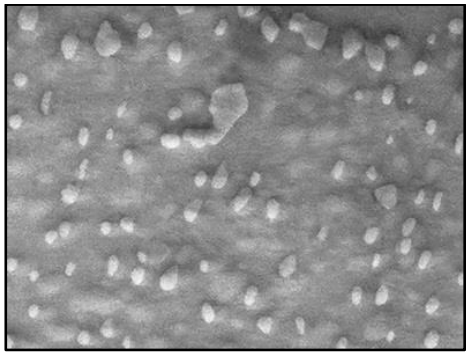

1 day aging

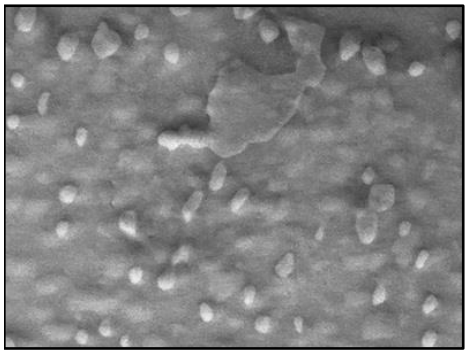

5 days aging

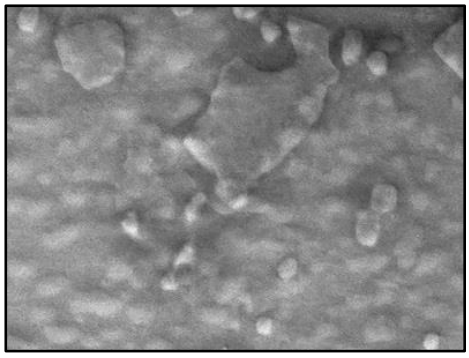

20 days aging

(h) Aging T = 175 ºC (Region 2)

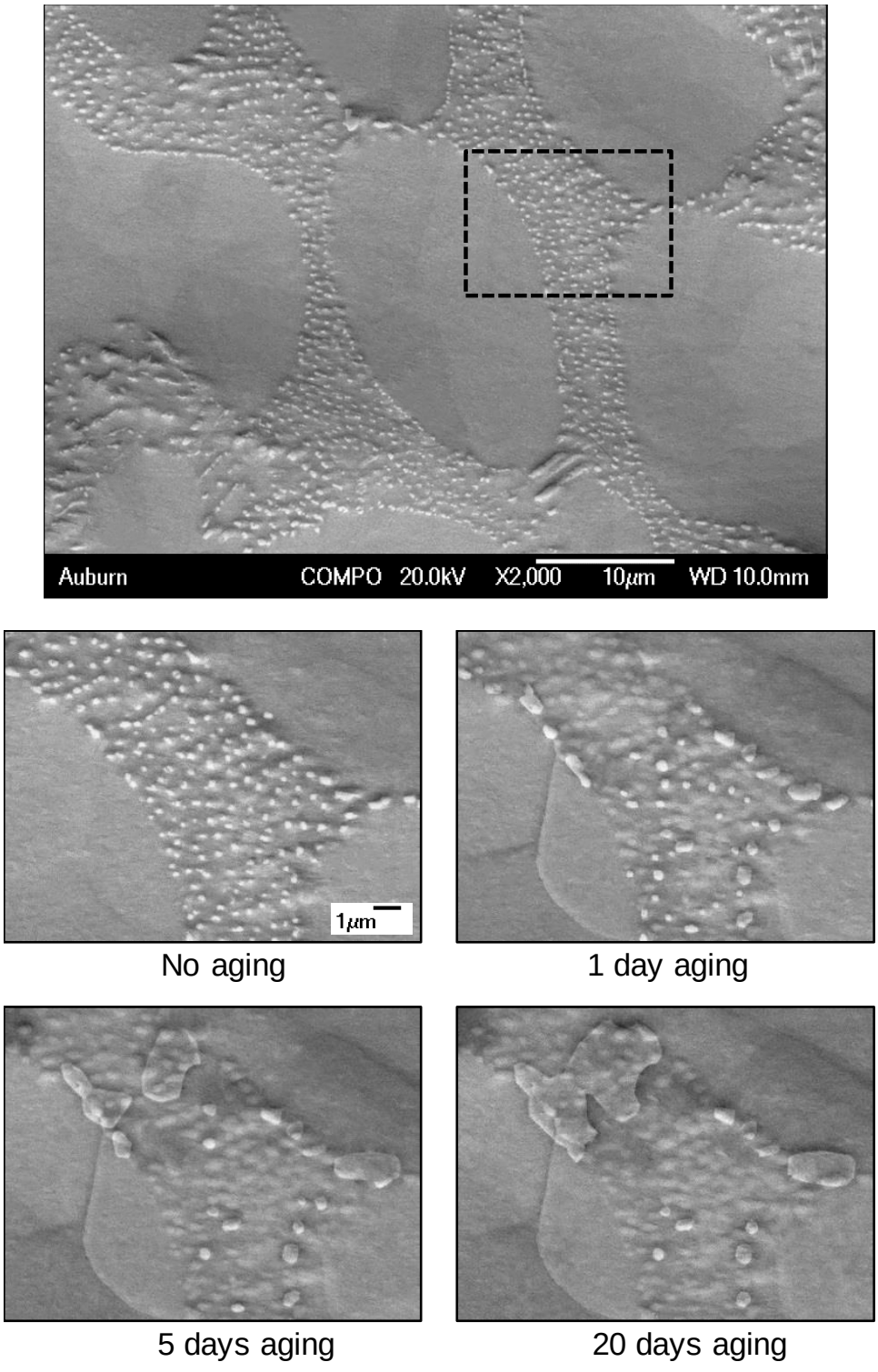

(i) Aging T = 175 ºC (Region 3)

Figure 8.5 Microstructural Evolution in SAC305 Subjected to Extreme High Temperature Aging

8.4 Measurement of Area and Number of IMC

Quantitative analyses of the size metrics of the IMC particles were performed with all of the SEM images at different aging times and aging temperatures for the IMC particle evolutions. The analyzed regions were typically chosen to be interdendritic regions with a heavy concentration of IMC particles. For example, the images shown in Figure 8.6, were taken from a subregion of the images in Figure 8.5. The area of each particle, the total area of all of the particles, and the total number of particles in each selected region and aging time were determined using image analysis software (ImageJ and Adobe Photoshop) and Matlab. The particle size measurement process involves 3 major steps. First, all the particles were outlined in Adobe Photoshop. Then the gray scale image were converted into a binary image. Lastly, the average area of the particles (White spots), in the binary image, were calculated using MATLAB and the number of particles were determined using image analysis software (ImageJ). An example of image analysis process is shown in Figure 8.6. An SEM image with all the IMC particles are presented in Figure 8.6 (a). Figure 8.6 (b) represents the corresponding binary image with the outlined particles that was obtained after conversion. This image was used to calculate the area of particles in MATLAB. Figure 8.6 (c) shows the image obtained from the ImageJ software representing particles numbers. It is evident from this image that the software was capable to accurately identify all the individual particle in the field of view.

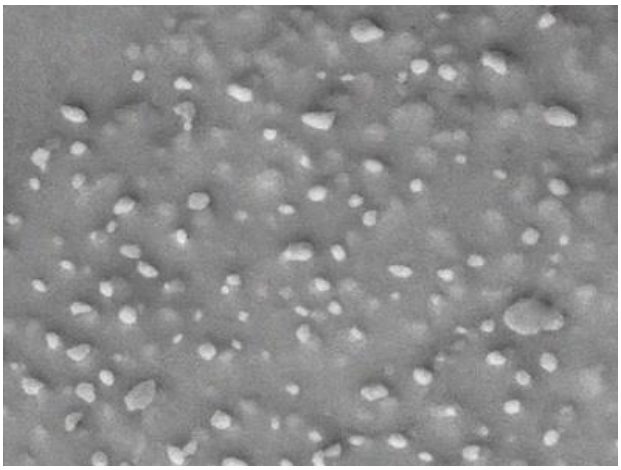

(a)

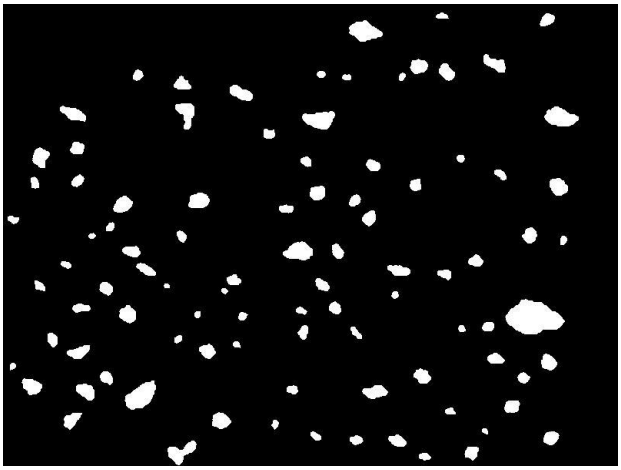

(b)

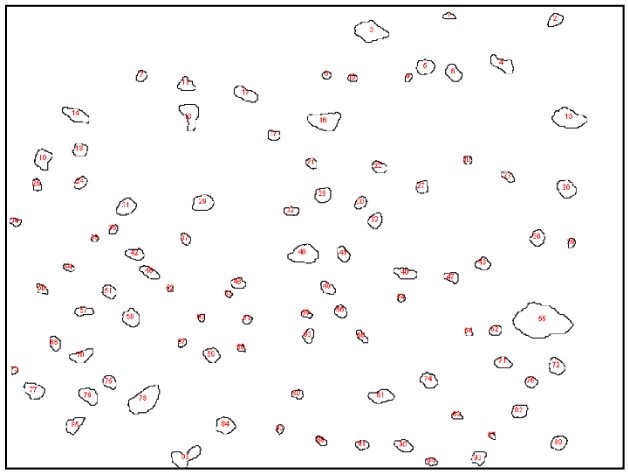

(c)

Figure 8.6 Image Processing Steps for IMC Particle Area Calculations (a) After Outlining All the Particles (b) Binary Image and (c) Final Image from ImageJ.

8.5 Measurement of Particle Diameter

As shown for an ideal spherical IMC particle in Figure. 8.7, the amount of the particle that is visible on the polished cross-sectional surface is actually unknown. Here, the black portion of the particle represents the portion on IMC exposed on the polished surface, while the gray shaded portion is the portion of the IMC below the surface. As indicated in Figures. 8.7 and 8.8, the observed particle diameter (apparent diameter) for a particle is actually less than or equal to the actual particle diameter. Thus, the measured (apparent) average particle diameter must be adjusted to calculate the actual average particle diameter.

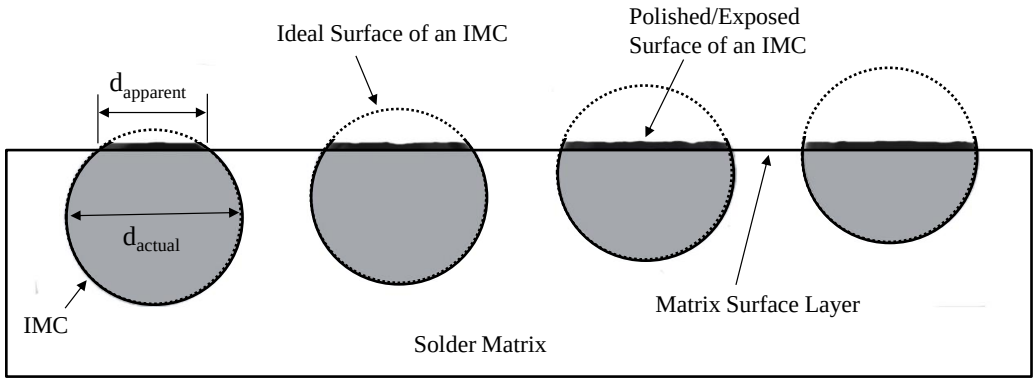

Figure 8.7 A Schematic Representation of an IMC with Several Possible Exposed Area above the Surface Layer.

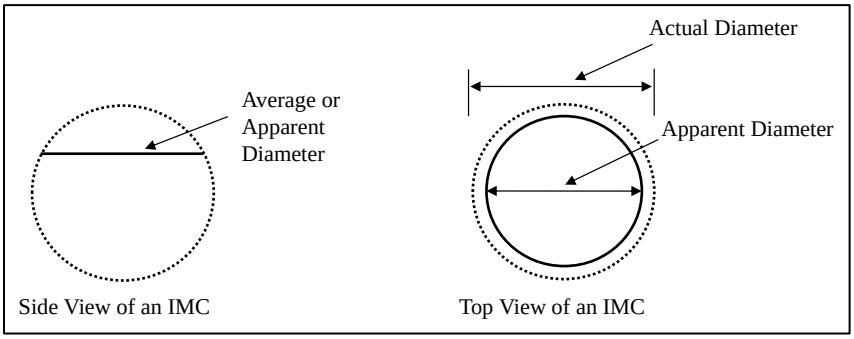

Figure 8.8 Side and Top View of an Ideal Spherical IMC Particle Showing Actual and Apparent Diameters.

For a fixed particle with diameter d, the apparent/measured particle diameter $d_{apparent}$ can be several different values based on the vertical position of the particle (Figure 8.7). The average value of $d_{apparent}$ can be found mathematically by averaging all possible values obtained from all possible vertical positions for the particle:

$$(d_{apparent})_{ave} = 2 \times (R_{apparent})_{ave} = \frac{2}{R} \int_0^R \sqrt{(R^2 - x^2)} dx \tag{8.1}$$

$$(d_{apparent})_{ave} = \frac{2}{R} \times \frac{\pi R^2}{4} = \frac{\pi}{4} d_{actual} \tag{8.2}$$

$$d_{actual} = \frac{4}{\pi} (d_{apparent})_{ave} \tag{8.3}$$

Equation 8.3 was used to estimate the actual diameter of each particle by adjusting the measured (apparent) diameter.

If the particles are spherical, the apparent diameter of the exposed surface of each particle can be calculated by assuming a circular relation between particle surface area and apparent diameter:

$$A_{apparent} = \pi R^2 = \frac{\pi}{4} (d_{apparent})^2 \tag{8.4}$$

$$d_{apparent} = \frac{2}{\sqrt{\pi}} \sqrt{A_{apparent}} \tag{8.5}$$

Combining of Equations (8.3, 8.5) yields the relation for the particle diameter in terms of the measured/particle surface area:

$$d_{actual} = \frac{4}{\pi}(d_{apparent})_{ave} = \frac{8}{\pi^{3/2}}\sqrt{(A_{apparent})_{ave}} \quad (8.6)$$

In addition to the averaging assumptions made above, this analysis also assumes that the particle does not move vertically during the aging process.

8.6 Changes in IMC Particle Diameter during Aging

Image processing and analysis steps as outlined before in sections 1.3 and 1.4 were followed to calculate the number and average diameter of the IMC particles of all the images (presented in Figure 8.5). The quantitative analysis results are summarized in Table 8.1. Table 8.1 represents the variations in particle numbers and average particle diameters with aging. These values were used to estimate the variation of the average particle diameter with aging time. The variations of the average IMC particle diameter and the number of IMC particles with aging time are shown in Figures 8.9 and 8.10. It is evident that the average size of the particles increases while the number of the particles decreases with increasing aging time. The data were fitted using a two term exponential relation

$$\frac{d}{d_o} = k_1 e^{k_2 t} + k_3 e^{k_4 t} \quad (8.7)$$

where d is the average diameter of all particles at time t, d_o is the average diameter of all particles at time t = 0, and K_1, K_2, K_3, and K_4 are fitting constants.

Table 8.1 IMC Particle Diameter of Different Locations after Different Aging Duration

Aging Temperature (°C)	Aging Time (Days)	No. of Particles				Avg. Diameter (nm)			
		R- 1	R- 2	R- 3	Avg	R- 1	R- 2	R- 3	Avg
125	0	178	205	273	218	390	374	328	364
	1	94	88	101	94	550	645	587	537
	5	69	44	47	53	651	930	968	850
	20	60	35	33	42	753	1132	1225	1036
150	0	75	209	230	171	504	356	329	396
	1	45	130	69	81	660	513	719	631
	5	30	41	25	32	894	1045	1289	1076
	20	21	20	18	19	1084	1563	1578	1409
175	0	252	193	151	198	326	292	428	349
	1	90	54	73	72	547	595	805	649
	5	32	18	35	28	1171	1359	1401	1310
	20	17	11	12	13	1975	2171	2328	2158

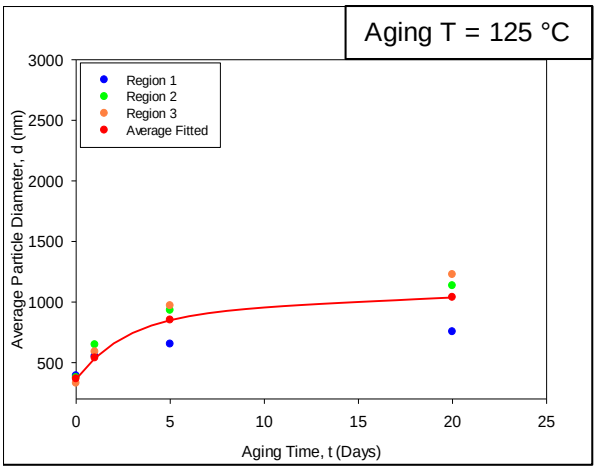

(a)

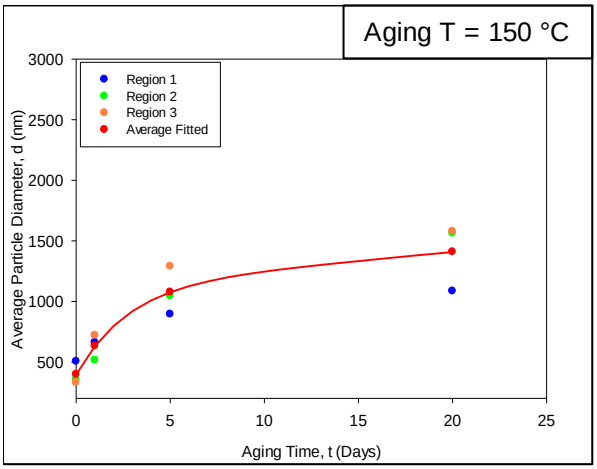

(b)

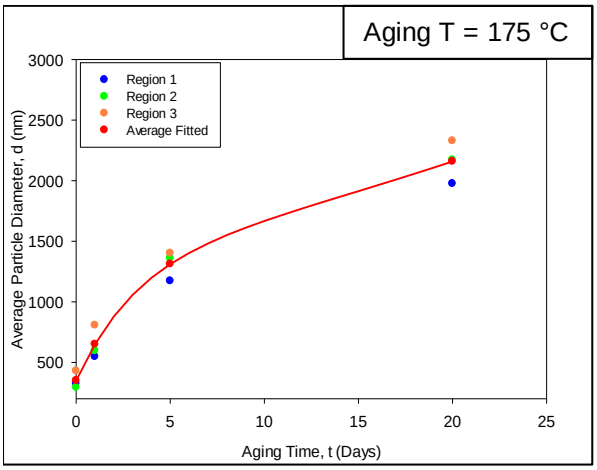

(c)

Figure 8.9 Changes in IMC Particle Diameter with Aging Time

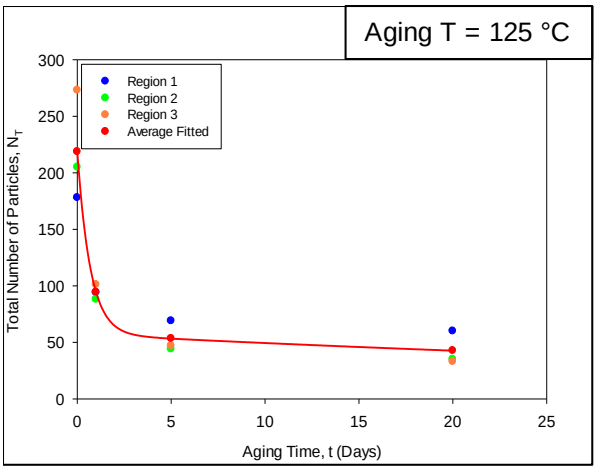

(a)

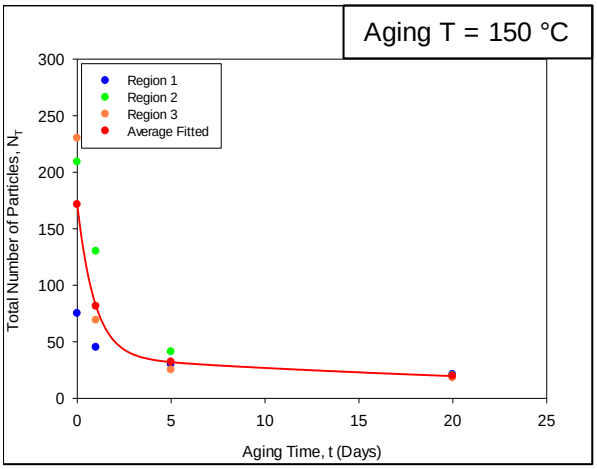

(b)

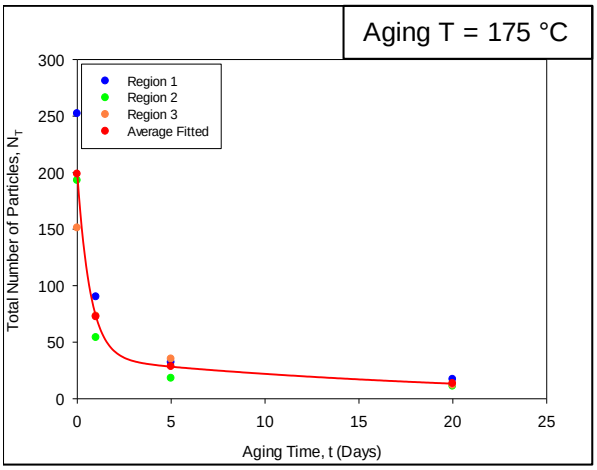

(c)

Figure 8.10 Changes in IMC Particle Number with Aging Time

The average fitted curves for particle size and particle numbers for different aging temperatures are plotted in the same graph for comparison (Figure 8.11). The colors of the data points and associated fitting curves indicate the aging temperature.

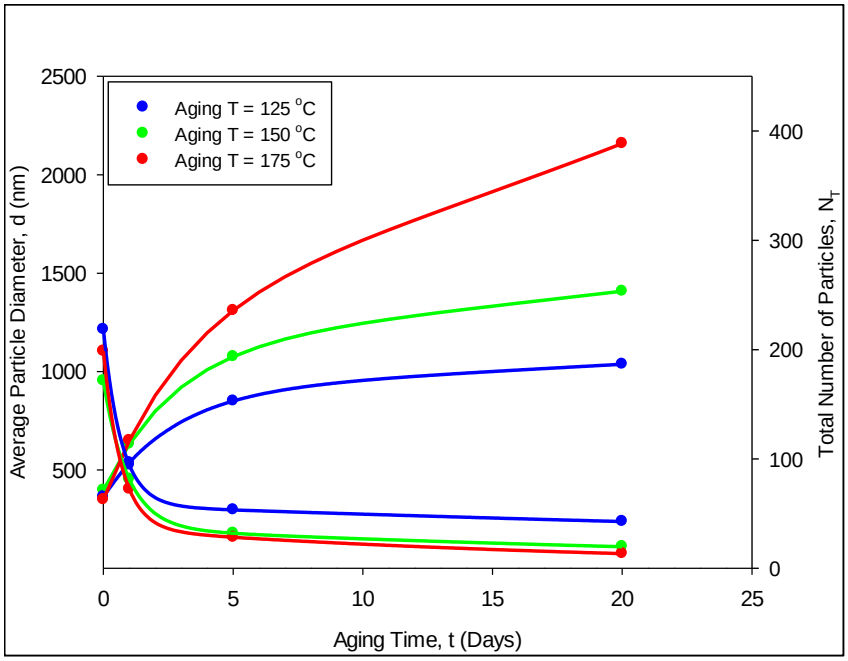

(a)

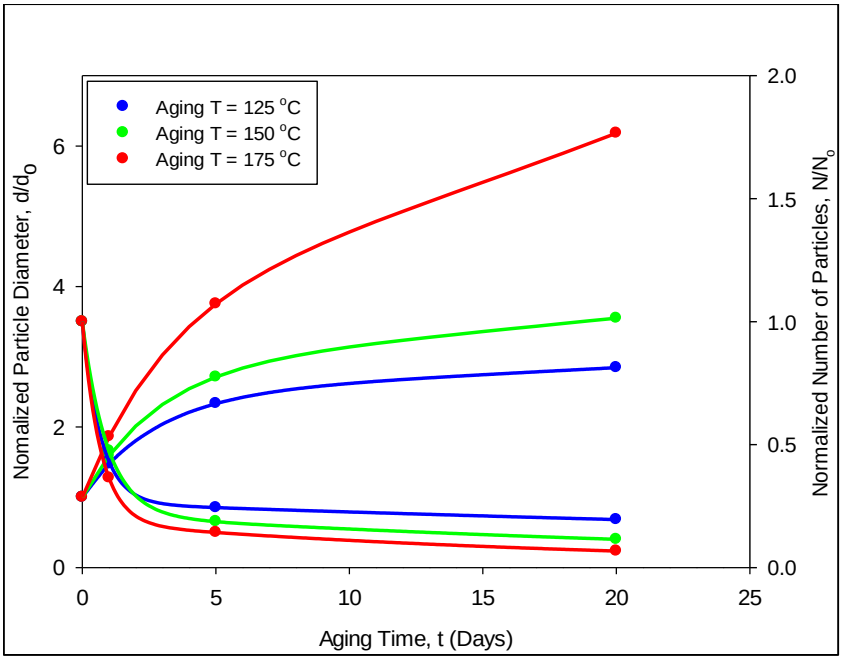

(b)

Figure 8.11 Variation in Total IMC Particle Area with Aging Time

8.7 Microstructure Analysis of SAC-Bi Alloy

As Mentioned in section 8.1, the microstructure of SAC305 is mainly composed of a β-Sn matrix and two different intermetallic compounds (IMC) namely, Ag_3Sn and Cu_6Sn_5. The reduction of strength of SAC305 after aging can be attributed to 2 major facts. First, aging causes coarsening of the Ag_3Sn and Cu_6Sn_5 intermetallic compounds and hence reduces their ability to block dislocation movements. Second, the β-Sn phase also coarsens/grows with aging, and hence reduces the strength of the alloy.

For the SAC-Bi alloy, the additional Bi content doesn't form any IMC with Sn. Therefore, the only IMCs that should present in microstructure of SAC_Q and Innolot are Ag_3Sn and Cu_6Sn_5. However, Bi remains as a separate phase in the microstructure enhance the strength of the SAC-Bi alloys. Also, from the Sn-Bi phase diagram (see Figure 8.12), it is observed that Bi has a good (~1.8%) solid solubility in Sn at room temperature. Hence Bi contributes more enhancement in strength of the SAC-Bi alloy before aging by the solid solution strengthening mechanism.

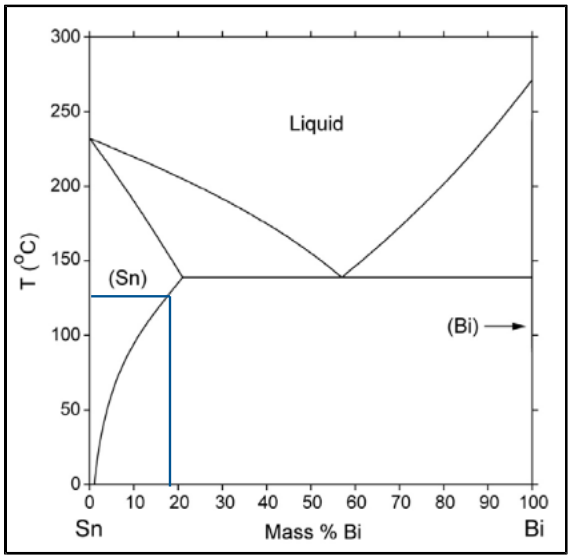

Figure 8.12 Sn-Bi Phase Diagram (http://www.metallurgy.nist.gov/)

Cai and coworkers [51] have demonstrated that additional Bi will go into solution in the β-Sn matrix during the aging of SAC-Bi alloys. As seen in Figure 8.12, the solid solution solubility of Bi increases from 1.8% at T = 25 °C, to about 17% at 125 °C. Thus, the Bi present in the as solidified microstructure of SAC-Bi alloys as a separate Bi phase will have the tendency to go into the solution with the β-Sn matrix during aging. This will lead to additional solid solution strengthening of the SAC-Bi alloy. A hypothesis was developed to explain the experimental observation. According to the hypothesis, the observed negligible variations in strength of SAC_Q and Innolot before and after aging tis due to the increases in strength from solid solution strengthening exceeding any reductions in strength caused by the evolution of microstructure during high temperature aging.

To support the proposed mechanism for mitigation of aging effects in SAC-Bi alloys, a study on the microstructure of SAC_Q was performed. At first, three different locations in a SAC_Q microstructure with β-Sn dendrites surrounded by interdendritic regions with IMC particles were selected and captured in SEM. The sample was then preconditioned with aging at 150 °C for 1 day and 5 days, and the images of the same locations were recaptured. These images were compared to see the effect of aging on the microstructure (Figure 8.13). The comparison shows that both the β-Sn dendrites and IMC particles presents in the microstructure of SAC_Q remains unaffected after aging in each of these three locations. These findings validate the experimental results of SAC-Bi alloys reported in this dissertation where the mechanical properties of SAC_Q and Innolot showed negligible variations after aging.

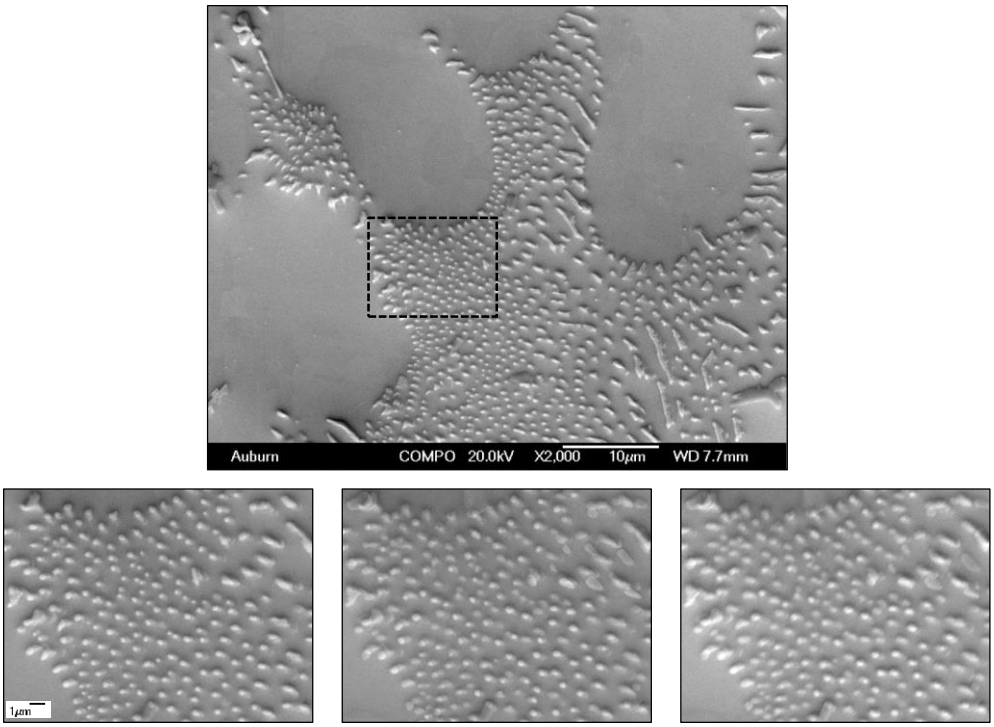

No Aging | 1 Day Aging | 5 Days Aging

(a) SAC_Q - Region 1

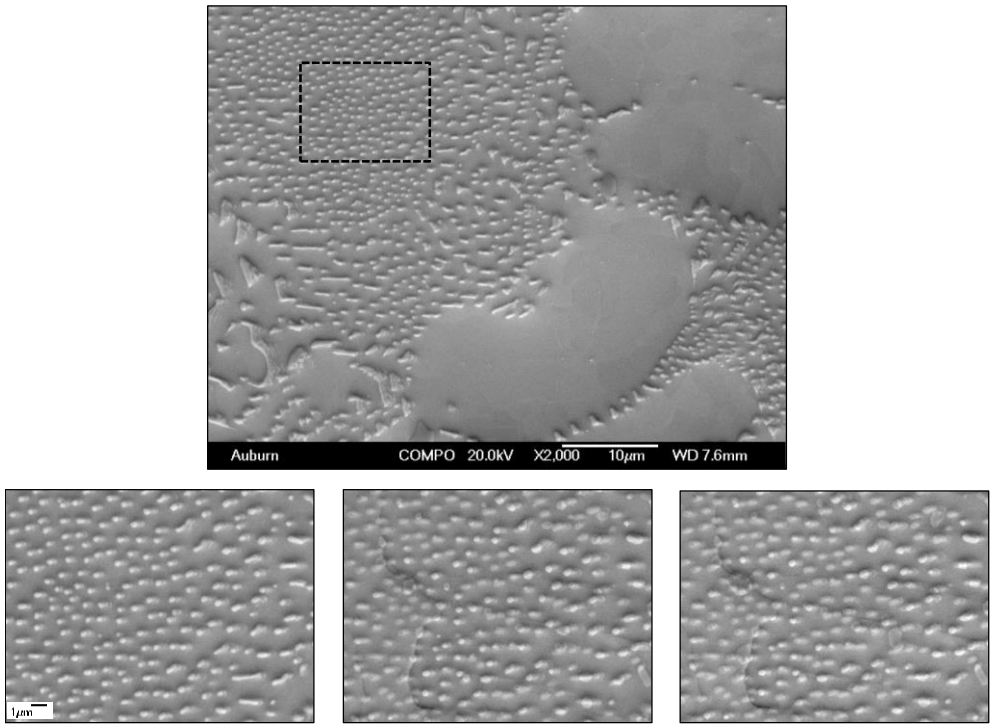

No Aging | 1 Day Aging | 5 Days Aging

(a) SAC_Q - Region 2

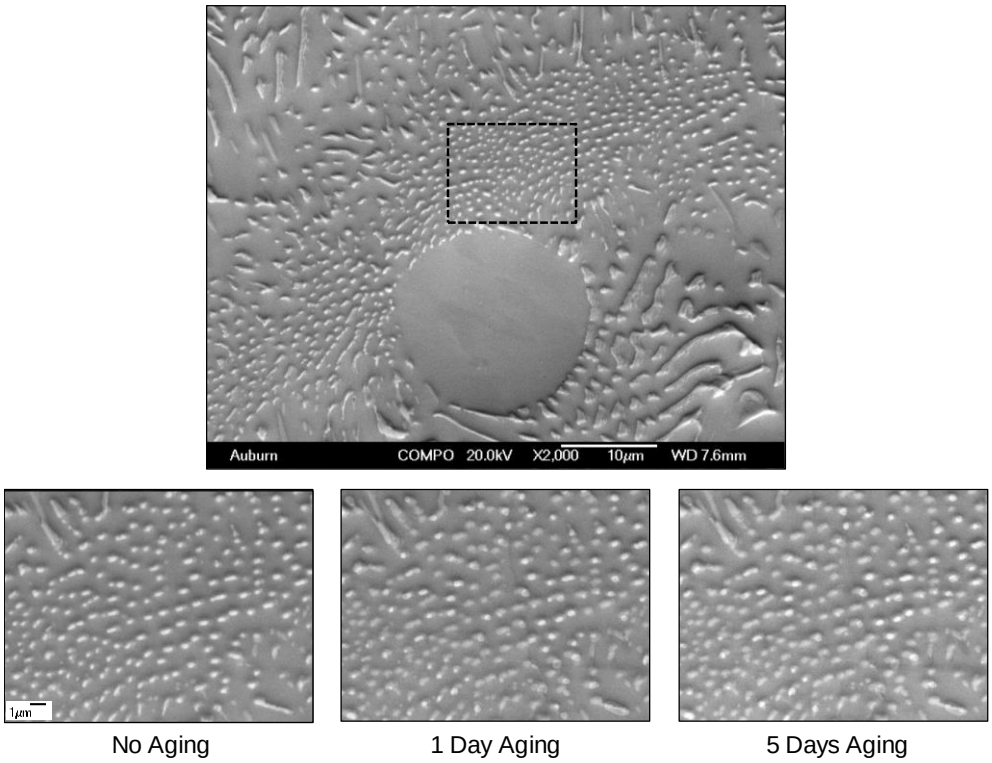

(a) SAC_Q - Region 3

Figure 8.13 Microstructures of SAC_Q Subjected to Extreme High Temperature Aging (Aging T = 150 °C)

Figure 8.14 contains images of three Bi-rich regions illustrating example microstructural evolutions of the bismuth rich phases in SAC_Q joints subjected to isothermal aging at T = 150 °C for 1 day. The images in the left sides were taken immediately after reflow. It exhibits a distribution of white Bi-rich phases throughout the lead free microstructure. EDS analysis of these white particles has confirmed that they are Bi rich phases with more than 80% of Bi. During aging (images in the right side), bismuth was observed to go into solution within the β-Sn dendrites and also in the intermetallic rich regions between dendrites. As discussed previously, this leads to strengthening of the solder during aging by the mechanism of solid solution strengthening.

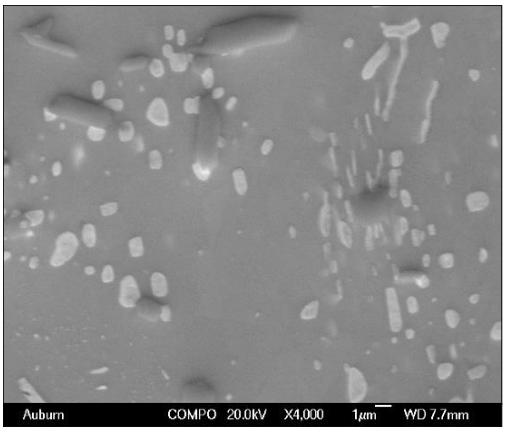

No Aging

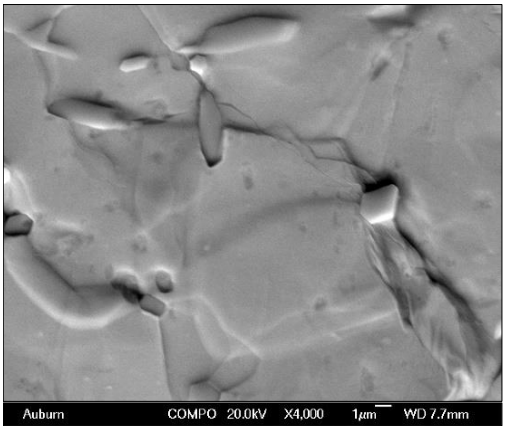

1 Day Aging

(a) Region 1

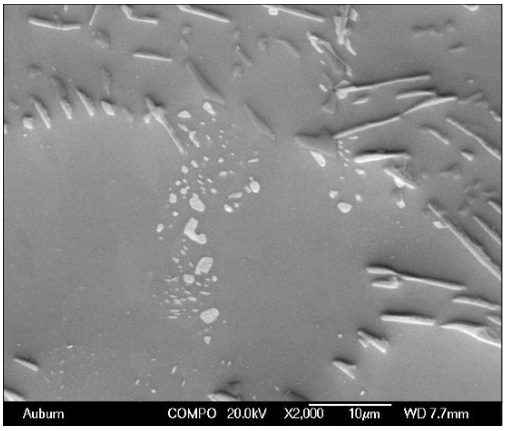

No Aging

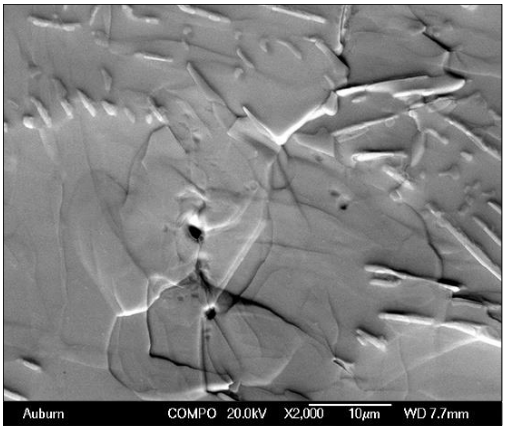

1 Day Aging

(a) Region 2

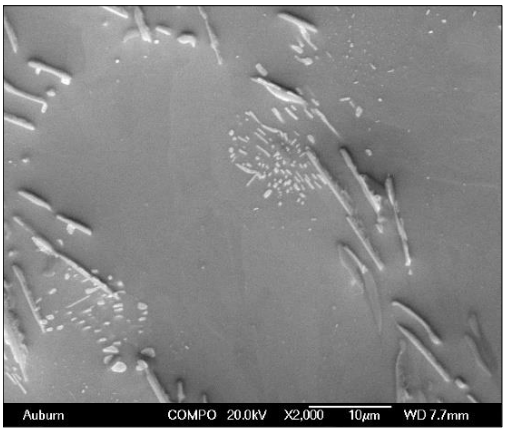

No Aging

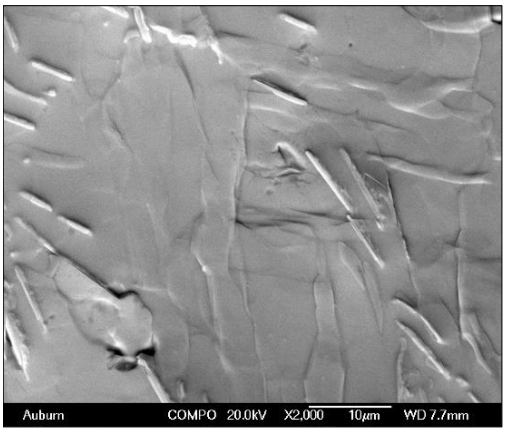

1 Day Aging

(a) Region 3

Figure 8.14 Dissolving of Bismuth Rich Phases in β-Sn Matrix during Aging

8.8 Discussion on Evolution of IMC Particles during Aging

Typically, IMC particles tend to become more round (spherical) with aging. Atoms on the surface of a particle have higher energy than the atoms inside a particle due to unsatisfied bonds in the surface atoms. A cylindrical or elongated particle has a higher fraction of surface atoms (or higher surface to volume ratio) compared to a spherical (round) particle with the same volume. As a result, the free energy per atom of an elongated particle or several small particle is higher than a big round particle with equal volume. This free energy difference is the driving force that causes the transition of IMC particles from smaller to a bigger size as seen in Figure 8.5.

This IMC coarsening phenomenon is also known as Ostwald Ripening. According to the Gibbs-Thompson effect [181, 182], an increase in particle size is accompanied by a decrease of the solute concentration in the matrix surrounding the particle. This leads to a concentration gradient, and solute atoms near smaller particles will diffuse towards the larger particles where the reductions in solute concentration has occurred. In addition, atoms from the smaller particles will go back into solution. The overall effects are shrinkage of smaller particles, and growth of larger particles. A schematic of the variation of solute concentration around a small and a large particles is shown in Figure 8.15. Since Ostwald Ripening is a diffusion-based process, use of higher aging temperatures will increase the rate of coarsening significantly.

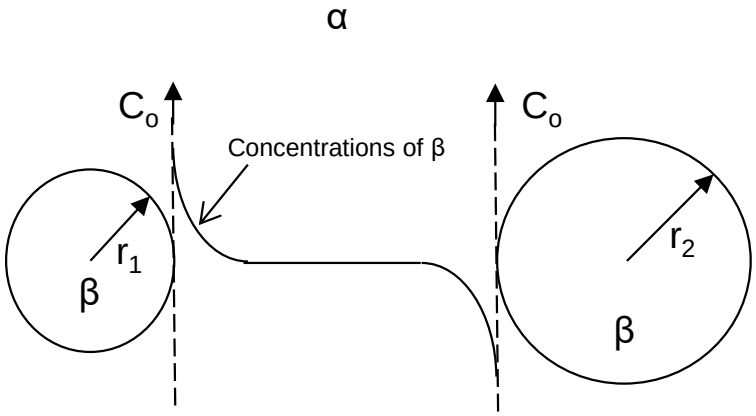

Figure 8.15 Schematic of Solute Concentration in Front of Particle [181].

The coarsening and coalescing of IMC particles during aging is known to play a critical role in the degradations of solder mechanical properties. IMC particles will pin and block the movement of dislocations. However, aging leads to both a smaller number of larger IMC particles and increased spacing between the IMC particles. The interparticle spacing λ can be calculated from the following equation:

$$\lambda = \frac{4(1-f)r}{3f} \tag{8.8}$$

where f is the volume fraction of the particles and r is the particle radius. Hence for a fixed volume fraction of the IMC particles, spacing between the particles increases with increasing particle diameter. Orowan proposed a mechanism that when a dislocation crosses incoherent precipitate particles (like the IMC particles in present case), it will bow and leave a loop of stress field around the particle [181, 182, 184]. A schematic of the interaction between a dislocation and IMC particles is shown in Figure 8.16.

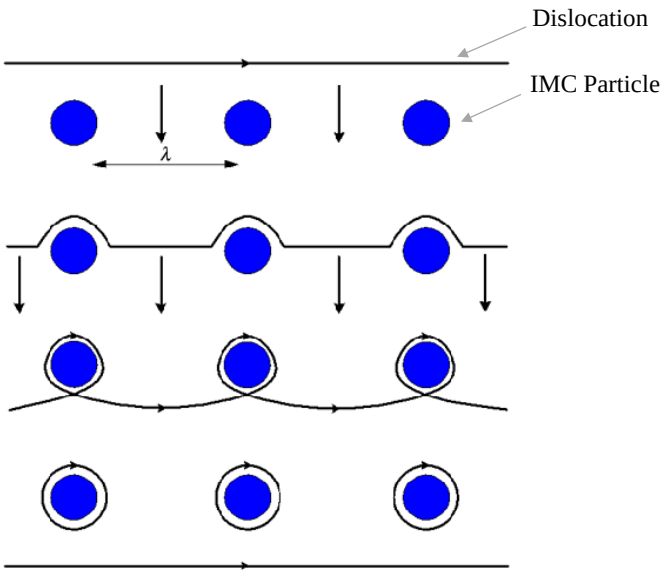

Figure 8.16 Schematic of a Dislocation Passing IMCs (Orowan Looping)

The yield stress and strength of a material depends on the shear stress (also known as the Orowan stress) that is required for a dislocation to pass through the particles. This shear stress will decrease as the inter-particle spacing increases during aging as shown in Equation 8.9 [180-182].

$$\tau_o = \frac{Gb}{\lambda} \tag{8.9}$$

where τ_o is the shear stress required for a dislocation to pass through the particles, G is the shear modulus, and b is the magnitude of the burgers vector. Therefore, aging leads to the coarsening of the IMC particles which causes to increase the interparticle spacing (Equation 8.8). The yield stress and strength of a material decrease after aging due to the increased interparticle spacing.

8.9 Summary

Microstructural evolution of SAC305 lead free solder have been performed using SEM system. SAC305 samples were aged at different temperatures and different durations in a box oven for the aging study on the microstructures. In particular, aging was performed at T = 125, 150, and 175 °C for 1, 5 and 20 days, and the topography of the microstructure of nine different fixed regions (three region for each aging temperature) were captured using the SEM system after each aging interval. This process generated several images of the microstructure as the aging progressed. Image analysis software was utilized to quantify microstructural changes (total area, number and average diameter of IMC particles, etc.) with respect to aging time. Quantitative analysis of the microstructures has shown that the number of IMC particles decreases during aging, while the average diameter of the particles increases significantly.

CHAPTER 9

CONCLUSIONS

9.1 Literature Review

The mechanical properties of a solder are strongly influenced by its microstructure, which is controlled by its thermal history including its solidification rate and thermal exposures after solidification. Aging of lead free solders leads to degradations in their constitutive and failure behaviors. For example, research in the literature has shown that aging leads to large reductions in solder material properties including shear strength, elastic modulus, nanoindentation joint modulus and hardness, high strain rate mechanical behavior, creep response, and Anand model parameters. Other studies have shown that aging causes severe degradations in uniaxial cyclic stress-strain curves and fatigue life, shear cyclic stress-strain curves and fatigue life, fracture behavior, drop reliability, and thermal cycling reliability.

Dopants have been found to strongly influence the properties and behaviors of lead free solders. For Example, Bi helps to reduce solidification temperature, increases strength by means of precipitation hardening, helps to reduce IMC (Intermetallic Compound) layer thickness, and also reduce aging induced degradation of mechanical properties in lead free solder materials. Ni helps to improve thermal fatigue life and drop test performance by refining Sn grain size and reducing the IMC layer formation near the Cu pad. The effects of rear earth (RE) elements and nanoparticle addition on the properties of lead free solder was also discussed in this chapter.

Nanoindentation methods have shown great potential for characterizing solder materials and aging effects at the joint scale. Nanoindentation is mainly used to extract elastic modulus and hardness of solder joints. Some of the prior works have also used nanoindentation technique to characterize the creep properties although most of the nanoindentation experiments, on solder joints, were conducted at room temperature.

The changes in solder mechanical behavior are a result of the evolution of the SAC solder microstructure that occurs during aging. The most well-known and widely observed changes are coarsening of the Ag_3Sn and Cu_6Sn_5 intermetallic compounds (IMCs) present in the eutectic regions between beta-Sn dendrites. Several researchers have proposed empirical models to describe the growth of these secondary phase particles as a function of aging temperature and aging time, and related this growth to mechanical property changes.

9.2 Experimental Procedures

All the experimental procedures and the data processing steps were presented in chapter 3. Micro-scale uniaxial tensile specimens were prepared in a rectangular shaped hollow glass tube using a vacuum suction method. Typical dimension of the uniaxial tensile specimens were 80 (length) $\times$ 3 (width) $\times$ 0.5 (height) mm. Uniaxial tensile tests were performed using a micro tension torsion testing system. Nanoindentation experiments were conducted on actual solder joints which were typically extracted from 14 x 14 mm PBGA assemblies (0.8 mm ball pitch, 0.46 mm ball diameter). Nanoindentation experiments were performed using Hysitron TI950 TriboIndenter.

9.3 High Temperature Mechanical Behavior of SAC and SAC+X Lead Free Solders

In this work, the mechanical behavior of several SAC and SAC+X lead free solder alloys at extreme high temperatures up to 200 °C has been investigated. The studied alloys included SAC305 (96.5Sn-3.0Ag-0.5Cu), SAC_R (96.6Sn-0.9Cu-2.5Bi), SAC_Q (92.8Sn-3.4Ag-0.5Cu-3.3Bi), and Innolot (90.95Sn-3.8Ag-0.7Cu-3.0Bi-0.15Ni-1.4Sb). The solder uniaxial test specimens were formed in high precision rectangular cross-section glass tubes using a vacuum suction process. The samples were initially cooled in a water bath and were later reflowed. The reflow profile was chosen to closely mimic profiles used for BGA assemblies, so that the obtained microstructures were similar to those found in typical solder joints.

For each of 4 elevated temperatures (T = 125, 150, 175, and 200 °C), tensile stress-strain tests were performed at three strain rates (SR = 0.001, 0.0001, and 0.00001 sec-1). For each alloy and testing temperature, the stress-strain curve shape and high temperature tensile properties (initial modulus, yield stress, and ultimate tensile strength) of the solders were measured and compared. As expected, the results have shown significant degradations of the mechanical properties of lead-free solders at higher temperatures. However, it was found that the addition of dopants (e.g. Bi, Ni, and Sb) in the SAC+X alloys improved their high temperature properties significantly. Both SAC_Q and Innolot alloys significantly outperformed SAC305 and SAC_R at all temperature levels.

9.4 Effects of Extreme High Temperature Aging on the Mechanical Behavior of SAC and SAC+X Solder Alloys

A comparative study of the aging dependent mechanical behavior of SAC305 SAC_Q, and Innolot solder alloys at extreme high temperatures (T= 125, 150, 175, and 200 °C) were

investigated. Before testing, the solder uniaxial specimens were aged (preconditioned) at the extreme high temperature of either T = 125 °C or T = 200 °C, and several different durations of aging were considered (no aging, and 1 day, 5 days, and 20 days of aging). Stress-strain and creep tests were then performed on the aged specimens. Using the measured data, the evolutions of the stress-strain and creep behaviors were determined as a function of aging temperature and aging time, and models describing the evolution of the mechanical properties (effective elastic modulus and ultimate tensile strength, secondary creep strain rate) with extreme aging were established.

Our experimental measurements show that a 40-50% drop in strength and modulus occurred between T = 125 °C and T = 200 °C. Comparisons between SAC305 and SAC_Q indicate that SAC_Q had significantly better mechanical properties at all test temperatures and prior aging conditions. Substantial degradations of the mechanical properties (initial modulus, ultimate tensile strength, and secondary creep strain rate) occur in SAC305 during extreme high temperature aging, whereas, SAC_Q exhibited relatively small variations in its properties during aging. Innolot shows similar mechanical behavior as SAC_Q at all testing and aging conditions.

9.5 Anand Viscoplastic Constitutive Model for Solder Alloys

SAC305, SAC_Q, and Innolot lead free solder materials recommended for high reliability applications have been chemically analyzed and then mechanically tested in order to determine the nine Anand parameters. Test specimens were initially solidified with both water quenched (WQ) and reflowed (RF) cooling profiles. Results from the uniaxial tensile test, performed at three different strain rates (0.001, 0.0001 and 0.00001 sec-1) and four different test temperatures (125, 150, 175, and 200 °C) were used to determine the Anand parameters for all the alloys mentioned before. These parameters were used to predict the stress-strain behavior of the corresponding

solder alloy. The experimental results and the model predicted results were compared. A good correlation was found between Anand model predicted and experimentally obtained results. The correlation of experimental results with anand model prediction shows a very small difference (< 10% in most conditions), thus, confirming the applicability of the model for a wide range of temperatures and strain rates.

9.6 Mechanical Behavior of SAC305 Solder Joints at Extreme High Temperatures Using Nanoindentation

Nanoindentation methods were used to explore the creep behavior, and aging effects of SAC305 solder joints at several extreme high testing temperatures from 125 to 200 °C. A special high temperature stage and test protocol was used within the nanoindentation system to carefully control the testing temperature, and make the measurements insensitive to thermal drift problems. Since the properties of SAC solder joints are highly dependent on crystal orientation, only single grain solder joints were used to avoid introducing any unintentional variation from changes in the crystal orientation across the joint cross-section.

Nanoindentation creep testing was performed on the non-aged and aged solder joint specimens at four different testing temperatures (T = 125, 150, 175, and 200 °C). As expected, the results have shown that indent/testing temperature has a significant impact on the mechanical properties and creep strain rate of solder joints. The measured data have also shown that the effects of aging on solder joint creep response are highly temperature dependent. At any particular temperature, creep rate increases with increasing aging time. The creep rates at high temperature increased significantly with just a few days of prior aging. In particular, the aging induced degradation rates at high temperatures (200 °C) were about 10000X than those seen at 125 °C.

The effects of aging on the creep rate vs. stress response became larger and larger as the testing temperature increased. Nanoindentation pile-up effects, observed during high-temperature testing and corrections were made to limit their influence on the test results.

9.7 Microstructural Evolution in Lead Free Solders Subjected to Extreme-High Temperature Aging Using Scanning Electron Microscopy

Microstructural evolution of SAC305 lead free solder have been performed using SEM system. SAC305 samples were aged at different temperatures and different durations in a box oven for the aging study on the microstructures. In particular, aging was performed at T = 125, 150, and 175 °C for 1, 5 and 20 days, and the topography of the microstructure of nine different fixed regions (three region for each aging temperature) were captured using the SEM system after each aging interval. This process generated several images of the microstructure as the aging progressed. Image analysis software was utilized to quantify microstructural changes (total area, number and average diameter of IMC particles, etc.) with respect to aging time. Quantitative analysis of the microstructures has shown that the number of IMC particles decreases during aging, while the average diameter of the particles increases significantly.

9.8 Summary

In this Dissertation, several SAC and SAC+X lead free solder alloys have been characterized and the reliability of these alloys in harsh environment applications have been investigated. These alloys were subjected to very high testing temperature up to 200 °C and mechanical properties, such as elastic modulus, ultimate tensile strength, and yield stress were recorded. It was found that mechanical properties of lead free solder alloys degrade significantly

at higher temperature. About 40-50% Decrease in Strength has been Observed between Testing Temperatures of T = 125 and T = 200 °C for all the Alloys. In addition, In addition, the high temperature tensile properties of the solders were compared. Comparison of the results for different solders has shown that the addition of dopants (e.g. Bi, Ni, and Sb) in the traditional SAC alloys improved their high temperature properties significantly. Also, this study considered aging effects in lead free solder aged at extreme high temperatures. Previous studies on solder aging has considered aging temperatures in the range of T = 25-125 °C. This work is the first study of extreme high temperature aging effects. The evolution of the stress-strain and creep behavior with aging temperature and time was determined, and models describing the evolution of the mechanical properties with extreme aging were established. The results suggested that there are large challenges to obtaining solder joint reliability when the joints are exposed to long-term high temperature aging. The addition of dopants (e.g. Bi, Ni, and Sb) in the traditional SAC alloys significantly mitigated the high temperature aging induced degradations in the mechanical properties. Previous studies reported a significant degradation of mechanical properties of SAC solders during aging due to the coarsening of the microstructure. In this study, it was found that Bi can help the solder alloy to become resistant to aging induced degradation. The improved aging resistance of SAC-Bi alloys is due to solid solution strengthening where the Bi-phases go into the solution in the β-Sn matrix during aging and enhance strength. This enhancement in strength of the alloy balances any reduction of strength during aging caused by the grain coarsening. To understand the effect of aging on the actual solder joint at elevated temperatures, a test procedure was developed to perform high temperature creep experiments using nanoindentation tool. It was found that the creep strain rate decreases with increasing test temperature and aging time. The

negative effect of aging was found to be even more pronounced when the joints were tested at extreme high temperatures, e.g., 200 °C.

The Anand viscoplastic constitutive model is often used to represent the material behavior of the solder in finite element simulations, and the reliability prediction results are often highly sensitive to the Anand parameters. The nine Anand parameters were determined for each unique solder alloy from a set of uniaxial tensile tests performed at several strain rates and extreme high temperatures (125 to 200 °C).

Since IMC coarsening is the main reason for the mechanical property degradation during aging, the coarsening of the IMCs, with aging, was correlated with the degradation of the mechanical strength of SAC305 solder.

Future Work

Following future work can be performed to extend the findings of this dissertation:

- High temperature stress-strain behavior of SAC and SAC+X alloys subjected to aging at various high temperatures can be explored at various strain rates (such as, 10^{-4} and 10^{-5} sec^{-1}).
- High temperature creep behavior of various SAC and SAC+X alloys subjected to aging at very high temperature (such as, up to 200 °C) can be investigated.
- Anand parameters for several lead free solder alloys were included in this dissertation. This work can be extended to explore the effect of high temperature aging on Anand parameters.
- The effects of test temperatures and aging conditions on the creep properties of SAC305 solder joints were investigated from 125-200 °C temperature range using nanoindentation system. This project can be continued for other SAC and SAC-Bi lead free solder alloys.
- The microstructure evolution study presented in this dissertation can be extended to a higher aging time. Based on the short and long term aging induced IMC coarsening data, a mathematical model can be developed to predict solder joint reliability as a function of aging time and temperature.
- The evolution of the microstructure of SAC-Bi alloys with aging can also be performed to understand how the changes in the microstructure making them resistant to aging induced degradations.

REFERENCES

[1] M. Abtew and G. Selvaduray, "Lead-Free Solders in Microelectronics," *Materials Science and Engineering: R: Reports*, vol. 27, no. 5, pp. 95-141, 2000.

[2] P. T. Vianco, "Development of Alternatives to Lead-Bearing Solders," *Proceedings of the Technical Program on Surface Mount Technical Association International Conference*, 1993.

[3] J. S. Hwang, *Implementing Lead-Free Electronics*. McGraw-Hill, New York, 2005.

[4] Q. Zhang, A. Dasgupta, and P. Haswell, "Creep and High-Temperature Isothermal Fatigue of Pb-Free Solders," *Proceedings of ASME InterPACK*, no. 36908a, pp. 955-960, 2003.

[5] NCMS, "Lead-Free Solder Project Final Report," *NCMS Report 0401RE96*, 1997.

[6] N. C. Lee, "Getting Ready for Lead-Free Solders," *Soldering & Surface Mount Technology*, vol. 9, no. 2, pp. 65-69, 1997.

[7] K. S. Kim, S. H. Huh, and K. Suganuma, "Effects of Intermetallic Compounds on Properties of Sn–Ag–Cu Lead-Free Soldered Joints," *Journal of Alloys and Compounds*, vol. 352, no. 1, pp. 226-236, 2003.

[8] J.-W. Yoon, S.-W. Kim, and S.-B. Jung, "IMC Morphology, Interfacial Reaction and Joint Reliability of Pb-Free Sn–Ag–Cu Solder on Electrolytic Ni BGA Substrate," *Journal of Alloys and Compounds*, vol. 392, no. 1, pp. 247-252, 2005.

[9] D. Q. Yu and L. Wang, "The Growth and Roughness Evolution of Intermetallic Compounds of Sn–Ag–Cu/Cu Interface During Soldering Reaction," *Journal of Alloys and Compounds*, vol. 458, no. 1, pp. 542-547, 2008.

[10] C. M. L. Wu, D. Q. Yu, C. M. T. Law, and L. Wang, "Properties of Lead-Free Solder Alloys with Rare Earth Element Additions," *Materials Science and Engineering: R: Reports*, vol. 44, no. 1, pp. 1-44, 2004.

[11] Y. C. Chan and D. Yang, "Failure Mechanisms of Solder Interconnects under Current Stressing in Advanced Electronic Packages," *Progress in Materials Science*, vol. 55, no. 5, pp. 428-475, 2010.

[12] C.-h. Wang and S.-w. Chen, "Sn–0.7wt.%Cu/Ni Interfacial Reactions at 250°C," *Acta Materialia*, vol. 54, no. 1, pp. 247-253, 2006.

[13] G. Zeng, S. D. McDonald, Q. F. Gu, K. Sweatman, and K. Nogita, "Effects of Element Addition on the β→α Transformation in Tin," *Philosophical Magazine Letters*, vol. 94, no. 2, pp. 53-62, 2014.

[14] W. J. Plumbridge, "Tin Pest Issues in Lead-Free Electronic Solders," in *Lead-Free Electronic Solders: A Special Issue of the Journal of Materials Science: Materials in Electronics*, pp. 307-318, 2007.

[15] S. Cheng, C.-M. Huang, and M. Pecht, "A Review of Lead-Free Solders for Electronics Applications," *Microelectronics Reliability*, vol. 75, pp. 77-95, 2017.

[16] M. Hasnine, B. Tolla, and M. Karasawa, "Effect of Ge Addition on Wettability, Copper Dissolution, Microstructural and Mechanical Behavior of SnCu–Ge Solder Alloy," *Journal of Materials Science: Materials in Electronics*, vol. 28, no. 21, pp. 16106-16119, 2017.

[17] Q. B. Tao, L. Benabou, L. Vivet, V. N. Le, and F. B. Ouezdou, "Effect of Ni and Sb Additions and Testing Conditions on the Mechanical Properties and Microstructures of Lead-Free Solder Joints," *Materials Science and Engineering: A*, vol. 669, pp. 403-416, 2016.

[18] J. Glazer, "Metallurgy of Low Temperature Pb-Free Solders for Electronic Assembly," *International Materials Reviews,* vol. 40, no. 2, pp. 65-93, 1995.
[19] M. McCormack, S. Jin, G. W. Kammlott, and H. S. Chen, "New Pb-Free Solder Alloy with Superior Mechanical Properties," *Applied Physics Letters,* vol. 63, no. 1, pp. 15-17 1993.
[20] K. Nogita, "Stabilisation of Cu_6Sn_5 by Ni in Sn-0.7 Cu-0.05 Ni Lead-Free Solder Alloys," *Intermetallics,* vol. 18, no. 1, pp. 145-149, 2010.
[21] F. X. Che, J. E. Luan, and X. Baraton, "Effect of Silver Content and Nickel Dopant on Mechanical Properties of Sn-Ag-Based Solders," *Proceedings of the 58th IEEE Electronic Components and Technology Conference,* pp. 485-490, 2008.
[22] F. Guo, J. Lee, S. Choi, J. P. Lucas, T. R. Bieler, and K. N. Subramanian, "Processing and Aging Characteristics of Eutectic Sn-3.5 Ag Solder Reinforced with Mechanically Incorporated Ni Particles," *Journal of Electronic Materials,* vol. 30, no. 9, pp. 1073-1082, 2001.
[23] Z. G. Chen, Y. W. Shi, Z. D. Xia, and Y. F. Yan, "Study on the Microstructure of a Novel Lead-Free Solder Alloy SnAgCu-Re and Its Soldered Joints," *Journal of Electronic Materials,* vol. 31, no. 10, pp. 1122-1128, 2002.
[24] F. Gao, S. Mukherjee, Q. Cui, and Z. Gu, "Synthesis, Characterization, and Thermal Properties of Nanoscale Lead-Free Solders on Multisegmented Metal Nanowires," *Journal of Physical Chemistry C,* vol. 113, no. 22, pp. 9546-9552, 2009.
[25] C. M. T. Law and C. M. L. Wu, "Microstructure Evolution and Shear Strength of Sn-3.5 Ag-Re Lead-Free BGA Solder Balls," *Proceedings of the 6th IEEE CPMT Conference on High Density Microsystem Design and Packaging and Component Failure Analysis,* pp. 60-65, 2004.
[26] N.-C. Lee, "Lead-Free Soldering-Where the World Is Going," *Advancing Microelectronics,* vol. 26, no. 5, pp. 29-35, 1999.
[27] A. Pirondi, "Mechanical Failure in Microelectronic Packaging," 2008.
[28] S. Wiese, A. Schubert, H. Walter, R. Dukek, F. Feustel, E. Meusel, and B. Michel, "Constitutive Behaviour of Lead-Free Solders vs. Lead-Containing Solders-Experiments on Bulk Specimens and Flip-Chip Joints," *Proceedings of the 51st IEEE Electronic Components and Technology Conference,* pp. 890-902, 2001.
[29] R. J. McCabe and M. E. Fine, "Athermal and Thermally Activated Plastic Flow in Low Melting Temperature Solders at Small Stresses," *Scripta Materialia,* vol. 39, no. 2, pp. 189-195, 1998.
[30] J. H. Lau, "Solder Joint Reliability of Flip Chip and Plastic Ball Grid Array Assemblies under Thermal, Mechanical, and Vibrational Conditions," *IEEE Transactions on Components, Packaging, and Manufacturing Technology, Part B,* vol. 19, no. 4, pp. 728-735, 1996.
[31] K. M. Ralls, Courtney, T. H., Wulff, J, *Introduction to Materials Science and Engineering*. Wiley & Sons, 1976.
[32] R. W. Hertzberg, R. P. Vinci, and J. L. Hertzberg, *Deformation and Fracture Mechanics of Engineering Materials*. Wiley New York, 1996.
[33] H. Ma and J. C. Suhling, "A Review of Mechanical Properties of Lead-Free Solders for Electronic Packaging," *Journal of Materials Science,* vol. 44, no. 5, pp. 1141-1158, 2009.
[34] J. H. Lau and Y.-H. Pao, *Solder Joint Reliability of* BGA, *CSP, Flip Chip, and Fine Pitch SMT Assemblies,* McGraw-Hill New York, 1997.
[35] R. W. Evans and B. Wilshire, "Creep of Metals and Alloys," 1985.

[36] M. F. Ashby, "A First Report on Deformation-Mechanism Maps," *Acta Metallurgica,* vol. 20, no. 7, pp. 887-897, 1972.
[37] J. Weertman, "Steady-State Creep through Dislocation Climb," *Journal of Applied Physics,* vol. 28, p. 362, 1957.
[38] R. L. Coble, "A Model for Boundary Diffusion Controlled Creep in Polycrystalline Materials," *Journal of Applied Physics,* vol. 34, p. 1679, 1963.
[39] C. Herring, "Diffusional Viscosity of a Polycrystalline Solid," *Journal of Applied Physics,* vol. 21, pp. 437-445, 1950.
[40] A. C. Fischer-Cripps, *Nanoindentation,* Third ed. Springer, 2011.
[41] P. McCluskey, R. Grzybowski, and T. Podlesak, "High Temperature Electronics," CRC Press, 1997.
[42] S. Ganesan and M. Pecht, *Lead-Free Electronics*. John Wiley and Sons, 2006.
[43] R. W. Johnson, J. L. Evans, P. Jacobsen, J. R. Thompson, and M. Christopher, "The Changing Automotive Environment: High-Temperature Electronics," *IEEE Transactions on Electronics Packaging Manufacturing,* vol. 27, no. 3, pp. 164-176, 2004.
[44] M. Hattori, "Needs and Applications of High-Temperature Lsis for Automotive Electronic Systems," *Proceedings of the International Conference on High Temperature Electronics,* pp. 37-43, 1999.
[45] B. Parmentier, O. Vermesan, and L. Beneteau, "Design of High Temperature Electronics for Well Logging Applications," *Proceedings of the International Conference on High Temperature Electronics,* 2003.
[46] H. Ma, J. C. Suhling, P. Lall, and M. J. Bozack, "Reliability of the Aging Lead Free Solder Joint," *Proceeding of the 56th IEEE Electronic Components and Technology Conference,* pp. 849-864, 2006.
[47] H. Ma, J. C. Suhling, Y. Zhang, P. Lall, and M. J. Bozack, "The Influence of Elevated Temperature Aging on Reliability of Lead Free Solder Joints," *Proceeding of the 57th IEEE Electronic Components and Technology Conference,* pp. 653-668, 2007.
[48] Y. Zhang, Z. Cai, J. C. Suhling, P. Lall, and M. J. Bozack, "The Effects of Aging Temperature on SAC Solder Joint Material Behavior and Reliability," *Proceedings of the 58th IEEE Electronic Components and Technology Conference,* pp. 99-112, 2008.
[49] I. E. Anderson and J. L. Harringa, "Elevated Temperature Aging of Solder Joints Based on Sn-Ag-Cu: Effects on Joint Microstructure and Shear Strength," *Journal of Electronic Materials,* vol. 33, no. 12, pp. 1485-1496, 2004.
[50] I. E. Anderson, J. W. Walleser, J. L. Harringa, F. Laabs, and A. Kracher, "Nucleation Control and Thermal Aging Resistanceof near-Eutectic Sn-Ag-Cu-X Solder Jointsby Alloy Design," *Journal of Electronic Materials,* vol. 38, no. 12, pp. 2770-2779, 2009.
[51] Z. Cai, Y. Zhang, J. C. Suhling, P. Lall, R. W. Johnson, and M. J. Bozack, "Reduction of Lead Free Solder Aging Effects Using Doped SAC Alloys," *Proceedings of the 60th IEEE Electronic Components and Technology Conference,* pp. 1493-1511, 2010.
[52] S. Choi, T. R. Bieler, J. P. Lucas, and K. N. Subramanian, "Characterization of the Growth of Intermetallic Interfacial Layers of Sn-Ag and Sn-Pb Eutectic Solders and Their Composite Solders on Cu Substrate During Isothermal Long-Term Aging," *Journal of Electronic Materials,* vol. 28, no. 11, pp. 1209-1215, 1999.
[53] C. M. Chuang, T. S. Lui, and L. H. Chen, "Effect of Aluminum Addition on Tensile Properties of Naturally Aged Sn-9Zn Eutectic Solder," *Journal of Materials Science,* vol. 37, no. 1, pp. 191-195, 2002.

[54] R. Darveaux, "Shear Deformation of Lead Free Solder Joints," *Proceedings of the 55th IEEE Electronic Components and Technology Conference*, pp. 882-893, 2005.
[55] R. Darveaux and K. Banerji, "Fatigue Analysis of Flip Chip Assemblies Using Thermal Stress Simulations and a Coffin-Manson Relation," *Proceedings of the 41st IEEE Electronic Components & Technology Conference*, pp. 797-805, 1991.
[56] Y. Ding, C. Wang, Y. Tian, and M. Li, "Influence of Aging Treatment on Deformation Behavior of 96.5Sn3.5Ag Lead-Free Solder Alloy During in Situ Tensile Tests," *Journal of Alloys and Compounds*, vol. 428, no. 1, pp. 274-285, 2007.
[57] I. Dutta, D. Pan, R. A. Marks, and S. G. Jadhav, "Effect of Thermo-Mechanically Induced Microstructural Coarsening on the Evolution of Creep Response of SnAg-Based Microelectronic Solders," *Materials Science and Engineering: A*, vol. 410-411, pp. 48-52, 2005.
[58] T.-C. Hsuan and K.-L. Lin, "Effects of Aging Treatment on Mechanical Properties and Microstructure of Sn–8.5Zn–0.5Ag–0.01Al–0.1Ga Solder," *Materials Science and Engineering: A*, vol. 456, no. 1, pp. 202-209, 2007.
[59] K.-S. Kim, C.-H. Yu, and J.-M. Yang, "Aging Treatment Characteristics of Solder Bump Joint for High Reliability Optical Module," *Thin Solid Films*, vol. 462-463, pp. 402-407, 2004.
[60] B. Lampe, "Room Temperature Aging Properties of Some Solder Alloys," *Welding Journal*, vol. 55, no. 10, pp. 330-340, 1976.
[61] X. Luhua, J. H. L. Pang, K. H. Prakash, and T. H. Low, "Isothermal and Thermal Cycling Aging on IMC Growth Rate in Lead-Free and Lead-Based Solder Interface," *IEEE Transactions on Components and Packaging Technologies*, vol. 28, no. 3, pp. 408-414, 2005.
[62] A. S. Medvedev, "Aging of Tin-Lead Solders and Joints Soldered by Them," *Metallovedenie I Obrabotka Metallov*, vol. 7, pp. 16-23, 1956.
[63] K. Mysore, D. Chan, D. Bhate, G. Subbarayan, I. Dutta, V. Gupta, J. Zhao, and D. Edwards, "Aging-Informed Behavior of Sn3.8Ag0.7Cu Solder Alloys," *Proceedings of IEEE ITherm*, pp. 870-875, 2008.
[64] J. H. L. Pang, T. H. Low, B. S. Xiong, X. Luhua, and C. C. Neo, "Thermal Cycling Aging Effects on Sn–Ag–Cu Solder Joint Microstructure, IMC and Strength," *Thin Solid Films*, vol. 462-463, pp. 370-375, 2004.
[65] S. Wiese and K. J. Wolter, "Creep of Thermally Aged SnAgCu-Solder Joints," *Microelectronics Reliability*, vol. 47, no. 2, pp. 223-232, 2007.
[66] Q. Xiao, H. J. Bailey, and W. D. Armstrong, "Aging Effects on Microstructure and Tensile Property of Sn3.9Ag0.6Cu Solder Alloy," *Journal of Electronic Packaging*, vol. 126, no. 2, pp. 208-212, 2004.
[67] J.-W. Yoon, C.-B. Lee, and S.-B. Jung, "Growth of an Intermetallic Compound Layer with Sn-3.5Ag-5Bi on Cu and Ni-P/Cu During Aging Treatment," *Journal of Electronic Materials*, vol. 32, no. 11, pp. 1195-1202, 2003.
[68] Y. Zhang, "The Effects of Aging on the Mechanical Behavior of Lead Free and Mixed Formulation Solder Alloys," PhD, Mechanical Engineering, Auburn University, Auburn, AL, 2010.
[69] Y. Zhang, Z. Cai, J. C. Suhling, P. Lall, and M. J. Bozack, "The Effects of SAC Alloy Composition on Aging Resistance and Reliability," *Proceedings of the 59th IEEE Electronic Components and Technology Conference* pp. 370-389, 2009.

[70] S. L. Allen, M. R. Notis, R. R. Chromik, and R. P. Vinci, "Microstructural Evolution in Lead-Free Solder Alloys: Part I. Cast Sn–Ag–Cu Eutectic," *Journal of Materials Research,* vol. 19, no. 5, pp. 1417-1424, 2004.

[71] A. Bansal, T. Lee, K. Liu, and J. Xue, "Effects of Isothermal Aging and in-Situ Current Stress on the Reliability of Lead-Free Solder Joints," *Proceedings of 60th IEEE Electronic Components and Technology Conference,* pp. 1529-1535, 2010.

[72] S. Chavali, Y. Singh, P. Kumar, G. Subbarayan, I. Dutta, and D. R. Edwards, "Aging Aware Constitutive Models for SnAgCu Solder Alloys," *Proceedings of the 61st IEEE Electronic Components and Technology Conference* pp. 701-705, 2011.

[73] W. M. Chen, P. McCloskey, and S. C. O'Mathuna, "Isothermal Aging Effects on the Microstructure and Solder Bump Shear Strength of Eutectic Sn37Pb and Sn3.5Ag Solders," *Microelectronics Reliability,* vol. 46, no. 5, pp. 896-904, 2006.

[74] R. Gagliano, "Shear Testing of Solder Joints: The Effect of Various Parameters on the Maximum Shear Stress of Eutectic Tin-Lead Solder," *Advanced Materials for the 21st Century: Proceedings of the 1999 Julia R. Weertman Symposium,* pp. 107-116, 1999.

[75] M. Hasnine, M. Mustafa, J. C. Suhling, B. C. Prorok, M. J. Bozack, and P. Lall, "Characterization of Aging Effects in Lead Free Solder Joints Using Nanoindentation," *Peoceedings of the 63rd IEEE Electronic Components and Technology Conference,* pp. 166-178, 2013.

[76] S. W. R. Lee, Y.-K. Tsui, X. Hunag, and E. C. C. Yan, "Effects of Room Temperature Storage Time on the Shear Strength of PBGA Solder Balls," *International Mechanical Engineering Congress and Exposition,* pp. 259-262, 2002.

[77] Y. Miyazawa and T. Ariga, "Influences of Aging Treatment on Microstructure and Hardness of Sn-(Ag, Bi, Zn) Eutectic Solder Alloys," *Materials Transactions,* vol. 42, no. 5, pp. 776-782, 2001.

[78] M. Mustafa, Z. Cai, J. C. Suhling, and P. Lall, "The Effects of Aging on the Cyclic Stress-Strain Behavior and Hysteresis Loop Evolution of Lead Free Solders," *Proceedings of the 61st IEEE Electronic Components and Technology Conference*, pp. 927-939, 2011.

[79] J. Wilde, A. R. Fix, and W. Nüchter, "Microstructural Changes of Lead-Free Solder Joints During Long-Term Ageing, Thermal Cycling and Vibration Fatigue," *Soldering & Surface Mount Technology*, vol. 20, no. 1, pp. 13-21, 2008.

[80] M. Motalab, M. Mustafa, J. C. Suhling, J. Zhang, J. Evans, M. J. Bozack, and P. Lall, "Correlation of Reliability Models Including Aging Effects with Thermal Cycling Reliability Data," *Proceedings of the 63rd IEEE Electronic Components and Technology Conference*, pp. 986-1004, 2013.

[81] J. Zhang, Z. Hai, S. Thirugnanasambandam, J. L. Evans, M. Bozack, R. Sesek, Y. Zhang, and J. C. Suhling, "Correlation of Aging Effects on Creep Rate and Reliability in Lead Free Solder Joints," *Journal of SMT,* vol. 25, no. 3, pp. 19-28, 2012.

[82] T. Lee and H. Ma, "Aging Impact on the Accelerated Thermal Cycling Performance of Lead-Free BGA Solder Joints in Various Stress Conditions," *Proceedings of the 62nd IEEE Electronic Components and Technology Conference*, pp. 477-482, 2012.

[83] L. Yin, M. Meilunas, B. Arfaei, L. Wentlent, and P. Borgesen, "Effect of Microstructure Evolution on Pb-Free Solder Joint Reliability in Thermomechanical Fatigue," *Proceedings of the 62nd IEEE Electronic Components and Technology Conference*, pp. 493-499, 2012.

[84] T. Zhang, J. Evans, C. Mitchell, Z. Z. Li, E. Crandall, a. J. Ridenour, and F. Xie, "Reliability of Lead-Free BGA with SnPb Solder Paste for Harsh Environments," *Proceedings of SMTA/CAVE Symposium on AIMS Harsh Environment Electronics,* 2009.

[85] M. Hongtao, J. C. Suhling, P. Lall, and M. J. Bozack, "Reliability of the Aging Lead Free Solder Joint," *Peoceedings of the 56th IEEE Electronic Components and Technology Conference,* pp. 849-864, 2006.

[86] Z. Yifei, C. Zijie, J. C. Suhling, P. Lall, and M. J. Bozack, "The Effects of Aging Temperature on SAC Solder Joint Material Behavior and Reliability," *Proceedings of the 58th IEEE Electronic Components and Technology Conference*, pp. 99-112, 2008.

[87] R. J. Coyle, P. P. Solan, A. J. Serafino, and S. A. Gahr, "The Influence of Room Temperature Aging on Ball Shear Strength and Microstructure of Area Array Solder Balls," *Proceedings of the 50th IEEE Electronic Components and Technology Conference*, pp. 160-169, 2000.

[88] T.-K. Lee, H. Ma, K.-C. Liu, and J. Xue, "Impact of Isothermal Aging on Long-Term Reliability of Fine-Pitch Ball Grid Array Packages with Sn-Ag-Cu Solder Interconnects: Surface Finish Effects," *Journal of Electronic Materials,* vol. 39, no. 12, pp. 2564-2573, 2010.

[89] M. A. Whitmore, A. C. Chilton, and W. B. Hampshire, "Fatigue Failure in a Model SMD Joint," *Soldering & Surface Mount Technology,* vol. 1, no. 3, pp. 21-24, 1989.

[90] L. Ming, K. Y. Lee, D. R. Olsen, W. T. Chen, B. T. C. Tan, and S. Mhaisalkar, "Microstructure, Joint Strength and Failure Mechanisms of SnPb and Pb-Free Solders in BGA Packages," *IEEE Transactions on Electronics Packaging Manufacturing,* vol. 25, no. 3, pp. 185-192, 2002.

[91] J.-M. Koo and S.-B. Jung, "Effect of Displacement Rate on Ball Shear Properties for Sn–37Pb and Sn–3.5Ag BGA Solder Joints During Isothermal Aging," *Microelectronics Reliability,* vol. 47, no. 12, pp. 2169-2178, 2007.

[92] R. Darveaux, "Shear Deformation of Lead Free Solder Joints," *Proceedings of the 55th Electronic Components and Technology Conference*, pp. 882-893, 2005.

[93] J. R. Oliver, J. Liu, and Z. Lai, "Effect of Thermal Ageing on the Shear Strength of Lead-Free Solder Joints," *Proceedings of the International Symposium on Advanced Packaging Materials Processes, Properties and Interfaces*, pp. 152-157, 2000.

[94] H. L. J. Pang, K. H. Tan, X. Q. Shi, and Z. P. Wang, "Microstructure and Intermetallic Growth Effects on Shear and Fatigue Strength of Solder Joints Subjected to Thermal Cycling Aging," *Materials Science and Engineering: A,* vol. 307, no. 1, pp. 42-50, 2001.

[95] T. Lee, B. Zhou, and T. R. Bieler, "Impact of Isothermal Aging and Sn Grain Orientation on the Long-Term Reliability of Wafer-Level Chip-Scale Package Sn–Ag–Cu Solder Interconnects," *IEEE Transactions on Components, Packaging and Manufacturing Technology,* vol. 2, no. 3, pp. 496-501, 2012.

[96] R. C. J. Smetana, P. Read, R. Popowich, D. Fleming, and T. Sack, "Variations in Thermal Cycling Response of Pb-Free Solder Due to Isothermal Preconditioning," *Proceedings of SMTA International Conference,* pp. 641-654, 2011.

[97] L. Anand, "Constitutive Equations for Hot-Working of Metals," *International Journal of Plasticity,* vol. 1, no. 3, pp. 213-231, 1985.

[98] S. B. Brown, K. H. Kim, and L. Anand, "An Internal Variable Constitutive Model for Hot Working of Metals," *International Journal of Plasticity,* vol. 5, no. 2, pp. 95-130, 1989.

[99] J.-P. Clech, "An Obstacle-Controlled Creep Model for Sn-Pb and Sn-Based Lead-Free Solders," *Proceedings of SMTA International Conference*, 2004.
[100] Y. Hong, P. Deane, P. Magill, and K. L. Murty, "Creep Deformation of 96.5Sn-3.5Ag Solder Joints in a Flip Chip Package," *Peoceedings of the 46th IEEE Electronic Components and Technology Conference*, pp. 1136-1142, 1996.
[101] X. Q. Shi, Z. P. Wang, Q. J. Yang, and H. L. J. Pang, "Creep Behavior and Deformation Mechanism Map of Sn-Pb Eutectic Solder Alloy," *Journal of Engineering Materials and Technology*, vol. 125, no. 1, pp. 81-88, 2002.
[102] S. Wiese, M. Roellig, and K. Wolter, "Creep of Eutectic SnAgCu in Thermally Treated Solder Joints," *Proceedings of the 55th IEEE Electronic Components and Technology Conference*, vol. 2, pp. 1272-1281, 2005.
[103] H. Ma, J. C. Suhling, Y. Zhang, P. Lall, and M. J. Bozack, "The Influence of Elevated Temperature Aging on Reliability of Lead Free Solder Joints," *Proceedings of the 57th IEEE Electronic Components and Technology Conference*, pp. 653-668, 2007.
[104] J. H. Lau, "Solder Joint Reliability of Flip Chip and Plastic Ball Grid Array Assemblies under Thermal, Mechanical, and Vibrational Conditions," *IEEE Transactions on Components, Packaging, and Manufacturing Technology: Part B*, vol. 19, no. 4, pp. 728-735, 1996.
[105] W. K. Jones, Y. Q. Liu, M. A. Zampino, and G. L. Gonzalez, "The at-Temperature Mechanical Properties of Lead-Tin Based Alloys," in *Microelectronic Interconnections and Assembly*, Springer Netherlands, pp. 53-58, 1998.
[106] Y. L. W. K. Jones, M. A. Zampino, G. Gonzalez, and M. Shah, "Design and Reliability of Solders and Solder Interconnections," *TMS Annual Meeting*, 1997.
[107] X. Q. Shi, W. Zhou, H. L. J. Pang, and Z. P. Wang, "Effect of Temperature and Strain Rate on Mechanical Properties of 63Sn/37Pb Solder Alloy," *Journal of Electronic Packaging*, vol. 121, no. 3, pp. 179-185, 1999.
[108] F. Lang, H. Tanaka, O. Munegata, T. Taguchi, and T. Narita, "The Effect of Strain Rate and Temperature on the Tensile Properties of Sn–3.5Ag Solder," *Materials Characterization*, vol. 54, no. 3, pp. 223-229, 2005.
[109] L. H. Dai and S.-W. R. Lee, "Characterization of Strain Rate-Dependent Behavior of 63sn-37Pb Solder Alloy," *Proceedings of ASME InterPACK*, pp. 307-313, 2001.
[110] H. Nose, M. Sakane, Y. Tsukada, and H. Nishimura, "Temperature and Strain Rate Effects on Tensile Strength and Inelastic Constitutive Relationship of Sn-Pb Solders," *Journal of Electronic Packaging*, vol. 125, no. 1, pp. 59-66, 2003.
[111] W. J. Plumbridge and C. R. Gagg, "Effects of Strain Rate and Temperature on the Stress–Strain Response of Solder Alloys," *Journal of Materials Science: Materials in Electronics*, vol. 10, no. 5, pp. 461-468, 1999.
[112] J. H. L. Pang, B. S. Xiong, and F. X. Che, "Modeling Stress Strain Curves for Lead-Free 95.5Sn-3.8Ag-0.7Cu Solder," *Proceedings of the 5th International Conference on Thermal and Mechanical Simulation and Experiments in Microelectronics and Microsystems*, pp. 449-453, 2004.
[113] J. G. Harper, L. A. Shepard, and J. E. Dorn, "Creep of Aluminum under Extremely Small Stresses," *Acta Metallurgica*, vol. 6, no. 7, pp. 509-518, 1958.
[114] F. Garofalo and D. B. Butrymowicz, "Fundamentals of Creep and Creep-Rupture in Metals," *Physics Today*, vol. 19, no. 5, pp. 100-102, 1966.

[115] L. Anand, "Constitutive Equations for the Rate-Dependent Deformation of Metals at Elevated Temperatures," *Journal of Engineering Materials and Technology*, vol. 104, no. 1, pp. 12-17, 1982.
[116] F. X. Che, H. L. J. Pang, W. H. Zhu, W. Sun, and A. Y. S. Sun, "Modeling Constitutive Model Effect on Reliability of Lead-Free Solder Joints," *Proceedings of the 7th International Conference on Electronic Packaging Technology*, pp. 1-6, 2006.
[117] M. Pei and J. Qu, "Constitutive Modeling of Lead-Free Solders," *Proceedings of International Symposium on Advanced Packaging Materials: Processes, Properties and Interfaces*, pp. 45-49, 2005.
[118] K. Mysore, G. Subbarayan, V. Gupta, and R. Zhang, "Constitutive and Aging Behavior of Sn3.0Ag0.5Cu Solder Alloy," *IEEE Transactions on Electronics Packaging Manufacturing*, vol. 32, no. 4, pp. 221-232, 2009.
[119] M. Motalab, Z. Cai, J. C. Suhling, and P. Lall, "Determination of Anand Constants for SAC Solders Using Stress-Strain or Creep Data," *Proceedings of IEEE ITherm*, pp. 910-922, 2012.
[120] N. Bai, X. Chen, and H. Gao, "Simulation of Uniaxial Tensile Properties for Lead-Free Solders with Modified Anand Model," *Materials & Design*, vol. 30, no. 1, pp. 122-128, 2009.
[121] M. Amagai, M. Watanabe, M. Omiya, K. Kishimoto, and T. Shibuya, "Mechanical Characterization of Sn–Ag-Based Lead-Free Solders," *Microelectronics Reliability*, vol. 42, no. 6, pp. 951-966, 2002.
[122] Y. Kim, H. Noguchi, and M. Amagai, "Vibration Fatigue Reliability of BGA -IC Package with Pb-Free Solder and Pb–Sn Solder," *Microelectronics Reliability*, vol. 46, no. 2, pp. 459-466, 2006.
[123] M. L. Huang and L. Wang, "Effects of Cu, Bi, and in on Microstructure and Tensile Properties of Sn-Ag-X(Cu, Bi, in) Solders," *Metallurgical and Materials Transactions A*, vol. 36, no. 6, pp. 1439-1446, 2005.
[124] M. Matahir, L. Chin, K. Tan, and A. Olofinjana, "Mechanical Strength and Its Variability in Bi-Modified Sn-Ag-Cu Solder Alloy," *Journal of Achievement in Materials and Manufacturing Engineering*, vol. 46, pp. 50-56, 2011.
[125] R. S. Pandher, B. G. Lewis, R. Vangaveti, and B. Singh, "Drop Shock Reliability of Lead-Free Alloys - Effect of Micro-Additives," *Proceedings of the 57th IEEE Electronic Components and Technology Conference*, pp. 669-676, 2007.
[126] Z. Zhenqing, W. Lei, X. Xiaoqiang, W. Qian, and L. Jaisung, "The Influence of Low Level Doping of Ni on the Microstructure and Reliability of SAC Solder Joint," *Proceedings of International Conference on Electronic Packaging Technology & High Density Packaging*, pp. 1-5, 2008.
[127] I. d. Sousa, D. W. Henderson, L. Parry, S. K. Kang, and D. Shih, "The Influence of Low Level Doping on the Thermal Evolution of SAC Alloy Solder Joints with Cu Pad Structures," *Proceedings of the 56th IEEE Electronic Components and Technology Conference*, pp. 1454-1461, 2006.
[128] J. H. Lee, S. Kumar, H. J. Kim, Y. W. Lee, and J. T. Moon, "High Thermo-Mechanical Fatigue and Drop Impact Resistant Ni-Bi Doped Lead Free Solder," *Proceedings of the 64th IEEE Electronic Components and Technology Conference*, pp. 712-716, 2014.

[129] T. Yeung, H. Sze, K. Tan, J. Sandhu, C. Neo, and E. Law, "Material Characterization of a Novel Lead-Free Solder Material — SACQ," *Proceedings of the 64th IEEE Electronic Components and Technology Conference*, pp. 518-522, 2014.
[130] L. Sun and L. Zhang, "Properties and Microstructures of Sn-Ag-Cu-X Lead-Free Solder Joints in Electronic Packaging," *Advances in Materials Science and Engineering*, vol. 2015, no. 639028, 2015.
[131] M. Sadiq, R. Pesci, and M. Cherkaoui, "Impact of Thermal Aging on the Microstructure Evolution and Mechanical Properties of Lanthanum-Doped Tin-Silver-Copper Lead-Free Solders," *Journal of Electronic Materials*, vol. 42, no. 3, pp. 492-501, 2013.
[132] H. Lee, Y. Chen, T. Hong, K. Shih, and C. Hsu, "Microstructural Evolution of Sn-3.5Ag Solder with Lanthanum Addition," *International Conference on Electronic Packaging Technology & High Density Packaging*, pp. 617-622, 2009.
[133] H. Hao, Y. Shi, Z. Xia, Y. Lei, and F. Guo, "Microstructure Evolution of SnAgCu Lead-Free Solders under High Temperature Aging," *Journal of Electronic Materials*, vol. 37, no. 1, pp. 2-8, 2008.
[134] D. Witkin, "Influence of Microstructure on Mechanical Behavior of Bi-Containing Pb-Free Solders," *Proceedings of IPC APEX EXPO Conference and Exhibition*, vol. 1, pp. 540-560, 2013.
[135] A. Delhaise, D. Perovic, and P. Snugovsky, "The Effects of Bi and Aging on the Microstructure and Mechanical Properties of Sn-Rich Alloys," *Proceedings of the International Conference on Soldering and Reliability*, 2015.
[136] R. R. Chromik, R. P. Vinci, S. L. Allen, and M. R. Notis, "Measuring the Mechanical Properties of Pb-Free Solder and Sn-Based Intermetallics by Nanoindentation," *JOM*, vol. 55, no. 6, pp. 66-69, 2003.
[137] X. Deng, N. Chawla, K. K. Chawla, and M. Koopman, "Deformation Behavior of (Cu, Ag)–Sn Intermetallics by Nanoindentation," *Acta Materialia*, vol. 52, no. 14, pp. 4291-4303, 2004.
[138] F. Gao, H. Nishikawa, T. Takemoto, and J. Qu, "Mechanical Properties Versus Temperature Relation of Individual Phases in Sn–3.0Ag–0.5Cu Lead-Free Solder Alloy," *Microelectronics Reliability*, vol. 49, no. 3, pp. 296-302, 2009.
[139] Y. D. Han, H. Y. Jing, S. M. L. Nai, L. Y. Xu, C. M. Tan, and J. Wei, "Temperature Dependence of Creep and Hardness of Sn-Ag-Cu Lead-Free Solder," *Journal of Electronic Materials*, vol. 39, no. 2, pp. 223-229, 2010.
[140] M. Hasnine, J. C. Suhling, B. C. Prorok, M. J. Bozack, and P. Lall, "Exploration of Aging Induced Evolution of Solder Joints Using Nanoindentation and Microdiffraction," *Peoceedings of the 64th IEEE Electronic Components and Technology Conference*, pp. 379-394, 2014.
[141] M. Hasnine, J. C. Suhling, B. C. Prorok, M. J. Bozack, and P. Lall, "Nanomechanical Characterization of SAC Solder Joints - Reduction of Aging Effects Using Microalloy Additions," *Peoceedings of the 65th IEEE Electronic Components and Technology Conference*, pp. 1574-1585, 2015.
[142] M. Hasnine, J. C. Suhling, B. C. Prorok, M. J. Bozack, and P. Lall, "Anisotropic Mechanical Properties of SAC Solder Joints in Microelectronic Packaging and Prediction of Uniaxial Creep Using Nanoindentation Creep," *Experimental Mechanics*, vol. 57, no. 4, pp. 603-614, 2017.

[143] S. Lotfian, J. M. Molina-Aldareguia, K. E. Yazzie, J. Llorca, and N. Chawla, "Mechanical Characterization of Lead-Free Sn-Ag-Cu Solder Joints by High-Temperature Nanoindentation," *Journal of Electronic Materials,* vol. 42, no. 6, pp. 1085-1091, 2013.
[144] V. M. F. Marques, C. Johnston, and P. S. Grant, "Nanomechanical Characterization of Sn–Ag–Cu/Cu Joints—Part 1: Young's Modulus, Hardness and Deformation Mechanisms as a Function of Temperature," *Acta Materialia,* vol. 61, no. 7, pp. 2460-2470, 2013.
[145] V. M. F. Marques, B. Wunderle, C. Johnston, and P. S. Grant, "Nanomechanical Characterization of Sn–Ag–Cu/Cu Joints—Part 2: Nanoindentation Creep and Its Relationship with Uniaxial Creep as a Function of Temperature," *Acta Materialia,* vol. 61, no. 7, pp. 2471-2480, 2013.
[146] H. Rhee, J. P. Lucas, and K. N. Subramanian, "Micromechanical Characterization of Thermomechanically Fatigued Lead-Free Solder Joints," *Journal of Materials Science: Materials in Electronics,* vol. 13, no. 8, pp. 477-484, 2002.
[147] M. Sadiq, J.-S. Lecomte, and M. Cherkaoui, "Individual Phase Mechanical Properties at Different Temperatures of Sn–Ag–Cu Lead-Free Solders Incorporating Special Pileup Effects Using Nanoindentation," *Journal of Electronic Packaging,* vol. 137, no. 3, pp. 031005-031005-5, 2015.
[148] Y. Sun, J. Liang, Z.-H. Xu, G. Wang, and X. Li, "Nanoindentation for Measuring Individual Phase Mechanical Properties of Lead Free Solder Alloy," *Journal of Materials Science: Materials in Electronics,* vol. 19, no. 6, pp. 514-521, 2008.
[149] J. L. Hay and G. M. Pharr, "Instrumented Indentation Testing," *Mechanical Testing and Evaluation,* vol. 8, 2000.
[150] K. O. Kese, Z. C. Li, and B. Bergman, "Method to Account for True Contact Area in Soda-Lime Glass During Nanoindentation with the Berkovich Tip," *Materials Science and Engineering: A,* vol. 404, no. 1, pp. 1-8, 2005.
[151] M. Cabibbo, D. Ciccarelli, and S. Spigarelli, "Nanoindentation Hardness Measurement in Piling up SiO_2 Coating," *Physics Procedia,* vol. 40, pp. 100-112, 2013.
[152] G. J. S. Chou, "Microstructure Evolution of Snpb and SnAg/Cu BGA Solder Joints During Thermal Aging," *Proceedings of the 8th International Advanced Packaging Materials Symposium,* pp. 39-46, 2002.
[153] R. L. J. M. Ubachs, P. J. G. Schreurs, and M. G. D. Geers, "Microstructure Evolution of Tin-Lead Solder," *IEEE Transactions on Components and Packaging Technologies,* vol. 27, no. 4, pp. 635-642, 2004.
[154] U. Sahaym, B. Talebanpour, S. Seekins, I. Dutta, P. Kumar, and P. Borgesen, "Recrystallization and Ag_3Sn Particle Redistribution During Thermomechanical Treatment of Bulk Sn–Ag–Cu Solder Alloys," *IEEE Transactions on Components, Packaging and Manufacturing Technology,* vol. 3, no. 11, pp. 1868-1875, 2013.
[155] M. Maleki, J. Cugnoni, and J. Botsis, "Isothermal Ageing of SnAgCu Solder Alloys: Three-Dimensional Morphometry Analysis of Microstructural Evolution and Its Effects on Mechanical Response," *Journal of Electronic Materials,* vol. 43, no. 4, pp. 1026-1042, 2014.
[156] A. U. Telang, T. R. Bieler, J. P. Lucas, K. N. Subramanian, L. P. Lehman, Y. Xing, and E. J. Cotts, "Grain-Boundary Character and Grain Growth in Bulk Tin and Bulk Lead-Free Solder Alloys," *Journal of Electronic Materials,* vol. 33, no. 12, pp. 1412-1423, 2004.

[157] P. Kumar, B. Talenbanpour, U. Sahaym, C. H. Wen, and I. Dutta, "Microstructural Evolution and Some Unusual Effects During Thermo-Mechanical Cycling of Sn-Ag-Cu Alloys," *Proceedings of IEEE ITherm*, pp. 880-887, 2012.
[158] P. Chauhan, S. Mukherjee, M. Osterman, A. Dasgupta, and M. Pecht, "Effect of Isothermal Aging on Microstructure and Creep Properties of SAC305 Solder: A Micromechanics Approach," *Proceedings of ASME InterPACK*, pp. V001T07A009, 2013.
[159] W. Yang, R. W. Messler, and L. E. Felton, "Microstructure Evolution of Eutectic Sn-Ag Solder Joints," *Journal of Electronic Materials*, vol. 23, no. 8, pp. 765-772, 1994.
[160] C. Tz-Cheng, Z. Kejun, R. Stierman, D. Edwards, and K. Ano, "Effect of Thermal Aging on Board Level Drop Reliability for Pb-Free BGA Packages," *Proceedings of the 54th IEEE Electronic Components and Technology Conference*, vol. 2, pp. 1256-1262, 2004.
[161] S. Ahat, M. Sheng, and L. Luo, "Microstructure and Shear Strength Evolution of SnAg/Cu Surface Mount Solder Joint During Aging," *Journal of Electronic Materials*, vol. 30, no. 10, pp. 1317-1322, 2001.
[162] W. K. Choi and H. M. Lee, "Effect of Soldering and Aging Time on Interfacial Microstructure and Growth of Intermetallic Compounds between Sn-3.5Ag Solder Alloy and Cu Substrate," *Journal of Electronic Materials*, vol. 29, no. 10, pp. 1207-1213, 2000.
[163] A. M. Z. Akhtar, K. H. Wirda, I. S. R. Aisha, and I. Mahadzir, "Microstructure Evolution at the Solder Joint During Isothermal Aging," *Proceedings of the 36th International Electronics Manufacturing Technology Conference*, pp. 1-5, 2014.
[164] M. Berthou, P. Retailleau, H. Frémont, A. Guédon-Gracia, and C. Jéphos-Davennel, "Microstructure Evolution Observation for SAC Solder Joint: Comparison between Thermal Cycling and Thermal Storage," *Microelectronics Reliability*, vol. 49, no. 9, pp. 1267-1272, 2009.
[165] W. C. Oliver and G. M. Pharr, "An Improved Technique for Determining Hardness and Elastic Modulus Using Load and Displacement Sensing Indentation Experiments," *Journal of Materials Research*, vol. 7, no. 6, pp. 1564-1583, 1992.
[166] D. Tabor, *The Hardness of Metals*, Oxford University Press, 2000.
[167] M. Motalab, Z. Cai, J. C. Suhling, J. Zhang, J. L. Evans, M. J. Bozack, and P. Lall, "Improved Predictions of Lead Free Solder Joint Reliability That Include Aging Effects," *Proceedings of the 62nd IEEE Electronic Components and Technology Conference*, pp. 513-531, 2012.
[168] M. Motalab, M. Mustafa, J. C. Suhling, J. Zhang, J. Evans, M. J. Bozack, and P. Lall, "Correlation of Reliability Models Including Aging Effects with Thermal Cycling Reliability Data," *Proceedings of the 63rd IEEE Electronic Components and Technology Conference*, pp. 986-1004, 2013.
[169] D. Herkommer, J. Punch, and M. Reid, "A Reliability Model for SAC Solder Covering Isothermal Mechanical Cycling and Thermal Cycling Conditions," *Microelectronics Reliability*, vol. 50, no. 1, pp. 116-126, 2010.
[170] G. Z. Wang, Z. N. Cheng, K. Becker, and J. Wilde, "Applying Anand Model to Represent the Viscoplastic Deformation Behavior of Solder Alloys," *Journal of Electronic Packaging*, vol. 123, no. 3, pp. 247-253, 2001.
[171] D. Bhate, D. Chan, G. Subbarayan, T. C. Chiu, V. Gupta, and D. R. Edwards, "Constitutive Behavior of Sn3. 8Ag0. 7Cu and Sn1. 0Ag0. 5Cu Alloys at Creep and Low Strain Rate Regimes," *IEEE Transactions on Components and Packaging Technologies*, vol. 31, no. 3, pp. 622-633, 2008.

[172] M. Motalab, Z. Cai, J. C. Suhling, and P. Lall, "Determination of Anand Constants for SAC Solders Using Stress-Strain or Creep Data," *Proceedings of ITherm*, pp. 910-922, 2012.
[173] N. J. Chhanda, J. C. Suhling, and P. Lall, "Experimental Characterization and Viscoplastic Modeling of the Temperature Dependent Material Behavior of Underfill Encapsulants," *Proceedings of ASME InterPACK* no. 44625, pp. 749-761, 2011.
[174] M. Mayo and W. Nix, "A Micro-Indentation Study of Superplasticity in Pb, Sn, and Sn-38 Wt% Pb," *Acta Metallurgica*, vol. 36, no. 8, pp. 2183-2192, 1988.
[175] M. Mayo, R. Siegel, A. Narayanasamy, and W. Nix, "Mechanical Properties of Nanophase TiO_2 as Determined by Nanoindentation," *Journal of Materials Research*, vol. 5, no. 5, pp. 1073-1082, 1990.
[176] P. Borgesen, "Microstructurally Adaptive Constitutive Relations and Reliability Assessment Protocols for Lead Free Solder," in "SERDP Project WP-1752 Final Report," 2015.
[177] I. Dutta, "A Constitutive Model for Creep of Lead-Free Solders Undergoing Strain-Enhanced Microstructural Coarsening: A First Report," *Journal of Electronic Materials*, vol. 32, no. 4, pp. 201-207, 2003.
[178] I. Dutta, P. Kumar, and G. Subbarayan, "Microstructural Coarsening in Sn-Ag-Based Solders and Its Effects on Mechanical Properties," *JOM*, vol. 61, no. 6, pp. 29-38, 2009.
[179] P. Kumar, Z. Huang, S. C. Chavali, D. K. Chan, I. Dutta, G. Subbarayan, and V. Gupta, "Microstructurally Adaptive Model for Primary and Secondary Creep of Sn-Ag-Based Solders," *IEEE Transactions on Components, Packaging and Manufacturing Technology*, vol. 2, no. 2, pp. 256-265, 2012.
[180] G. E. Dieter and D. J. Bacon, *Mechanical Metallurgy*, 3rd ed., Mc Graw-Hill New York, 1986.
[181] R. Boistelle and J. P. Astier, "Crystallization Mechanisms in Solution," *Journal of Crystal Growth*, vol. 90, no. 1, pp. 14-30, 1988.
[182] R. E. Smallman, *Modern Physical Metallurgy*, 4th ed., Elsevier, 2016.
[183] D. A. Porter, K. E. Easterling, and M. Sherif, "Phase Transformations in Metals and Alloys, (Revised Reprint)," CRC press, 2009.
[184] Y. D. Han, H. Y. Jing, S. M. L. Nai, C. M. Tan, J. Wei, L. Y. Xu, and S. R. Zhang, "A Modified Constitutive Model for Creep of Sn–3.5Ag–0.7Cu Solder Joints," *Journal of Physics D: Applied Physics*, vol. 42, no. 12, p. 125411, 2009.

Appendix

A.1 Variation of Temperature inside the Temperature Chamber

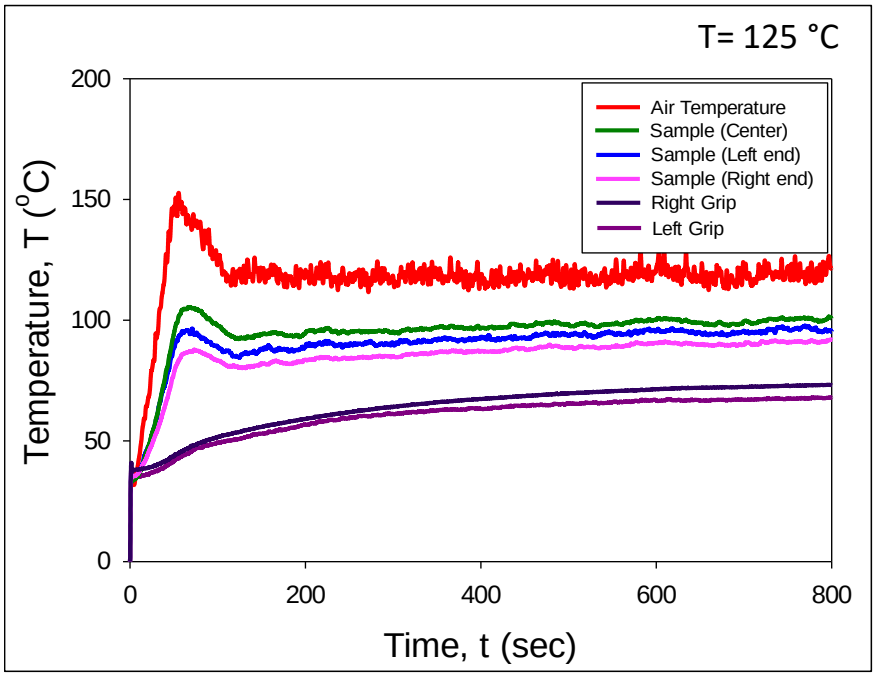

(a) T = 125 °C

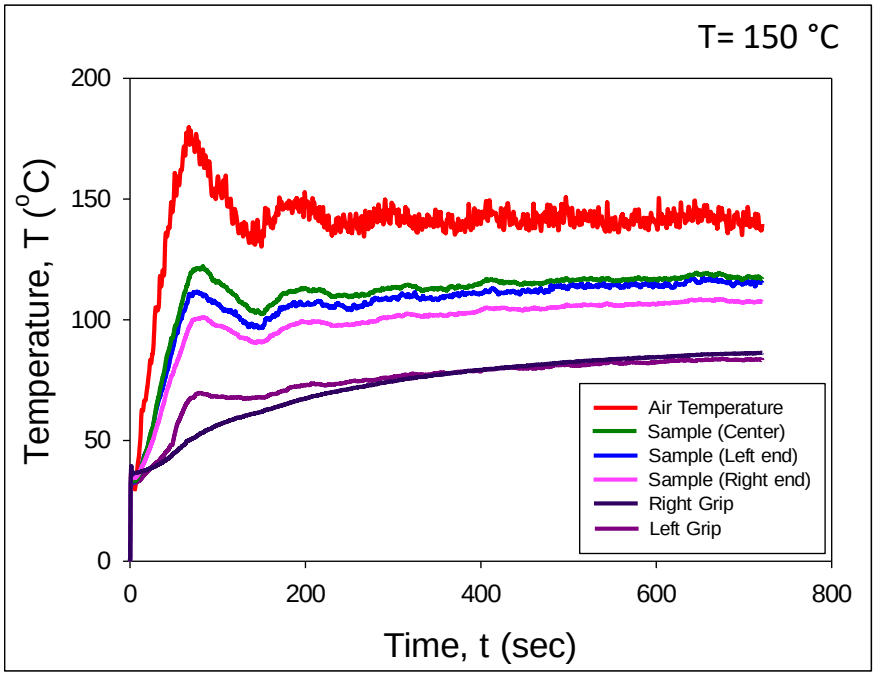

(b) T = 150 °C

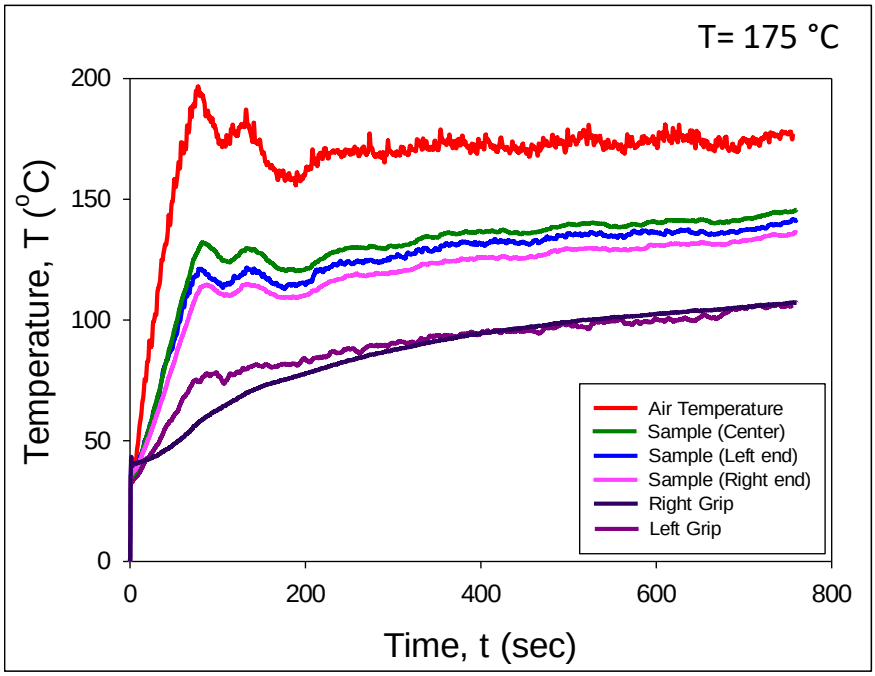

(c) T = 175 °C

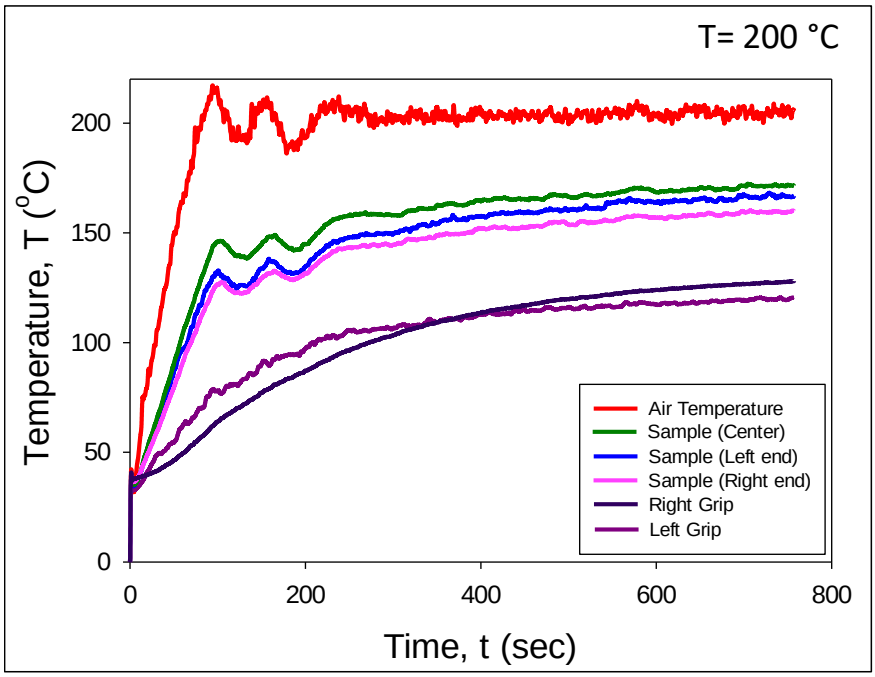

(d) T = 200 °C

Figure A.1 Variation of Temperature inside the Temperature Chamber

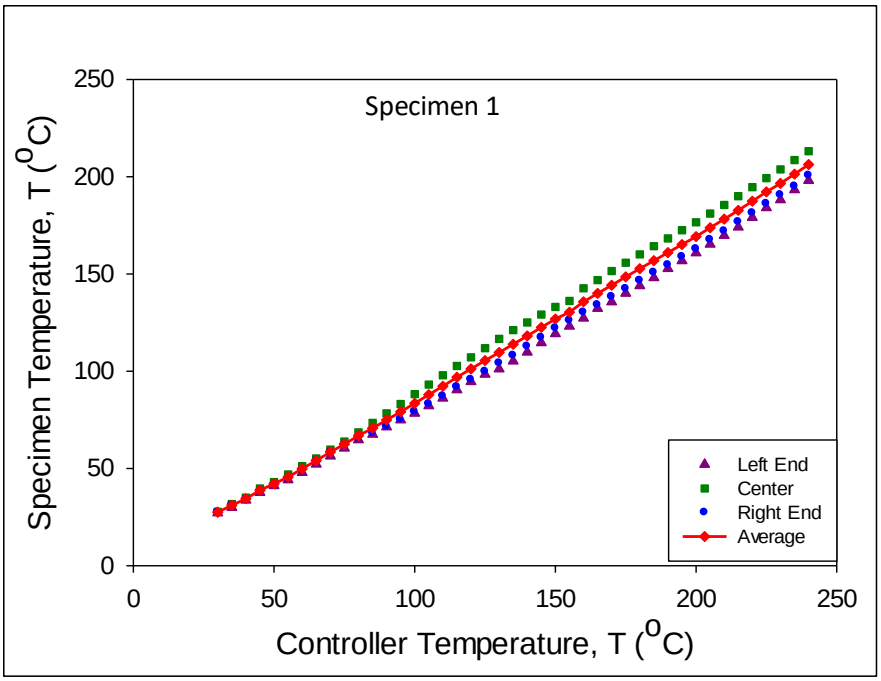

(a) Specimen 1

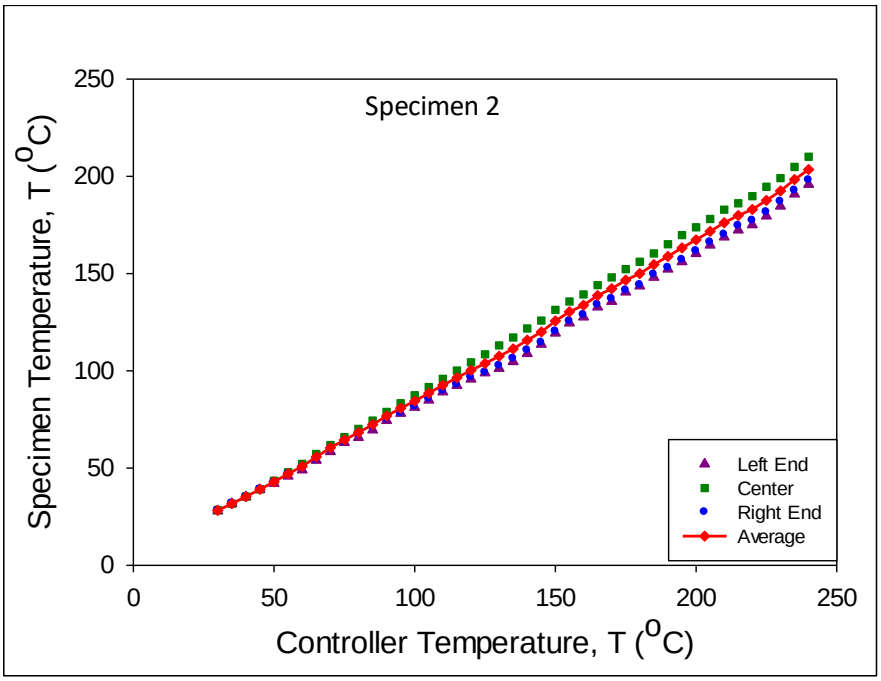

(b) Specimen 2

Figure A.2 Relationship between Specimen Temperature and Controller Temperature

Controller (°C)	Left End (°C)	Center (°C)	Right End (°C)	Average (°C)		Controller (°C)	Left End (°C)	Center (°C)	Right End (°C)	Average (°C)
35	29.9	31.7	30.9	31.1		140	109.8	125.1	112.8	118.2
40	33.7	35	33.9	34.4		145	114.7	129.2	117.4	122.6
45	37.6	39.7	38.1	38.8		150	119.3	133.1	122.2	126.9
50	41.1	43	41.4	42.1		155	123.2	136.2	126.1	130.4
55	44.1	46.9	44.3	45.6		160	127.3	142.7	130.3	135.8
60	47.9	51.2	48.9	49.8		165	132.3	146.9	134.1	140.1
65	52.2	55.1	53.7	54.0		170	135.7	151.5	138.3	144.3
70	56.3	59.7	58.2	58.5		175	140.1	155.8	142.5	148.6
75	60.4	63.8	61.9	62.5		180	144	160.1	146.7	152.7
80	64.7	68.5	65.5	66.8		185	148.1	164.3	150.8	156.9
85	67.5	73.4	68.4	70.7		190	152.8	168.3	154.7	161.0
90	71.3	78.3	71.7	74.9		195	156.8	172.5	158.9	165.2
95	74.9	83.1	75.2	79.1		200	160.9	176.6	162.9	169.3
100	78.3	88.2	79.2	83.5		205	165.3	181.1	167.7	173.8
105	82.2	93.1	83.1	87.9		210	169.8	185.5	172.1	178.2
110	86.1	97.9	87.2	92.3		215	174.1	190	176.8	182.7
115	90.4	102.7	91.9	96.9		220	179.1	194.7	181.4	187.5
120	94.6	107.2	95.7	101.2		225	184.1	199.3	186.2	192.2
125	98.4	111.9	99.8	105.5		230	188.2	203.8	190.7	196.6
130	101.1	116.7	104.1	109.7		235	193.3	208.6	195.1	201.4
135	105.2	121.2	108.1	113.9		240	198.1	213.2	200.7	206.3

Table A.1 Variation of Temperature in Different Locations of the Specimen (Specimen 1)

Controller (°C)	Left End (°C)	Center (°C)	Right End (°C)	Average (°C)		Controller (°C)	Left End (°C)	Center (°C)	Right End (°C)	Average (°C)
35	31.6	31.7	31.8	31.7		140	108.9	121.8	110.7	115.8
40	35.1	35.3	35.2	35.2		145	113.7	125.9	114.6	120.0
45	38.8	39.1	39.1	39.0		150	119.4	131.4	120.4	125.7
50	42.1	43.5	42.5	42.9		155	124.6	135.7	125.6	130.4
55	45.8	47.8	46.8	47.1		160	127.7	139.3	128.8	133.8
60	49	52.1	50	50.8		165	132.8	144.1	134.1	138.8
65	54	57.2	54.2	55.7		170	135.7	148.1	137.1	142.3
70	58.4	61.8	59.5	60.4		175	140.5	152.3	141.5	146.7
75	63.1	65.9	63.1	64.5		180	143.6	156.1	144.2	150.0
80	65.7	70.1	67.2	68.3		185	148.1	160.4	149.7	154.7
85	69.5	74.4	70.9	72.3		190	152.3	165.1	153.1	158.9
90	74.4	78.8	75.1	76.8		195	156.1	169.8	157.2	163.2
95	78.1	83.3	78.2	80.7		200	160.3	173.8	161.7	167.4
100	81.2	87.4	81.6	84.4		205	164.7	178.1	166.2	171.8
105	84.9	91.6	85.7	88.5		210	168.8	182.9	170.2	176.2
110	89.1	95.8	89.8	92.6		215	172.4	186.2	174.7	179.9
115	92.5	100.1	93	96.4		220	175.1	189.8	177.3	183.0
120	95.7	104.3	96.8	100.3		225	179.6	194.7	181.7	187.7
125	98.9	108.5	99.2	103.8		230	184.7	199.1	187.1	192.5
130	101.2	113.1	102.6	107.5		235	190.9	204.9	192.8	198.4
135	104.7	117.2	106.3	111.4		240	195.9	210.1	198.1	203.6

Table A.2 Variation of Temperature in Different Locations of the Specimen (Specimen 2)

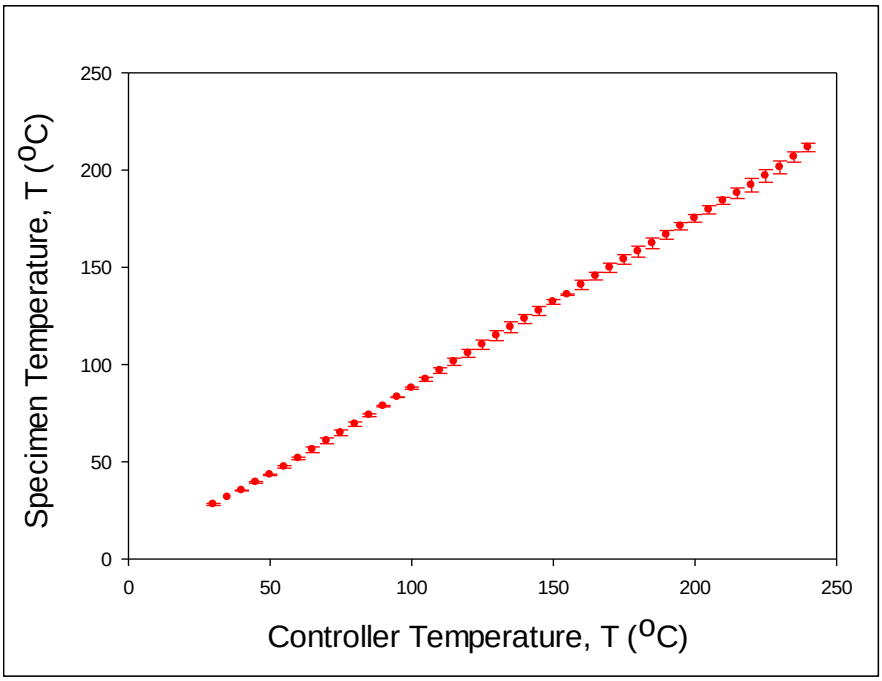

(a)

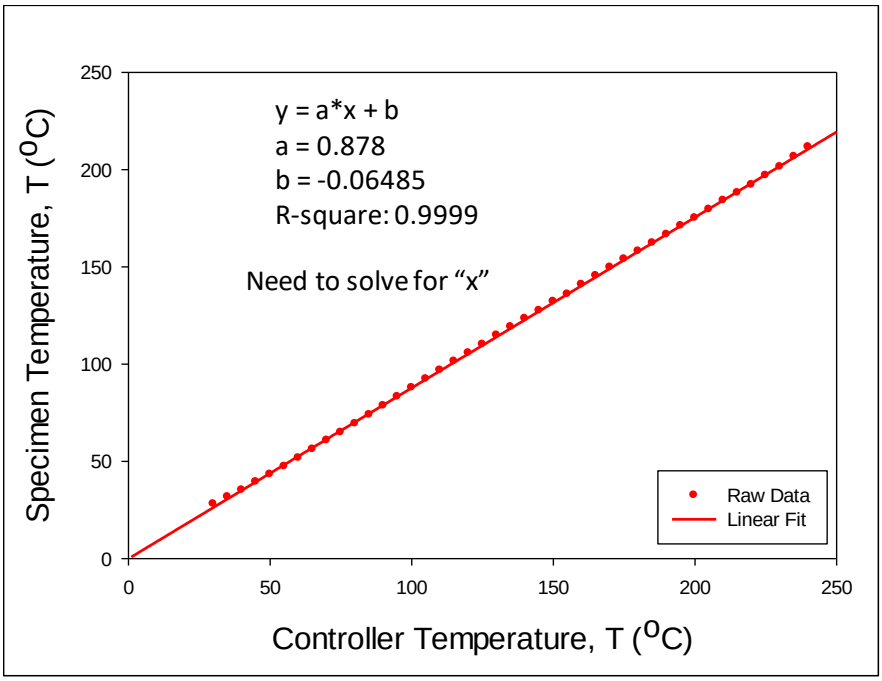

(b)

Figure A.3 Relationship between Specimen Temperature and Controller Temperature (Average Fitted)

Specimen Temperature (°C)	Controller Temperature (°C)		Specimen Temperature (°C)	Controller Temperature (°C)
35	39.9		140	159.5
40	45.6		145	165.2
45	51.3		150	170.9
50	57.0		155	176.6
55	62.7		160	182.3
60	68.4		165	188.0
65	74.1		170	193.7
70	79.8		175	199.4
75	85.5		180	205.1
80	91.2		185	210.8
85	96.9		190	216.5
90	102.6		195	222.2
95	108.3		200	227.9
100	114.0		205	233.6
105	119.7		210	239.3
110	125.4		215	244.9
115	131.1		220	250.6
120	136.7		225	256.3
125	142.4		230	262.0
130	148.1		235	267.7
135	153.8		240	273.4

Table A.3 Calibrated Temperature Table

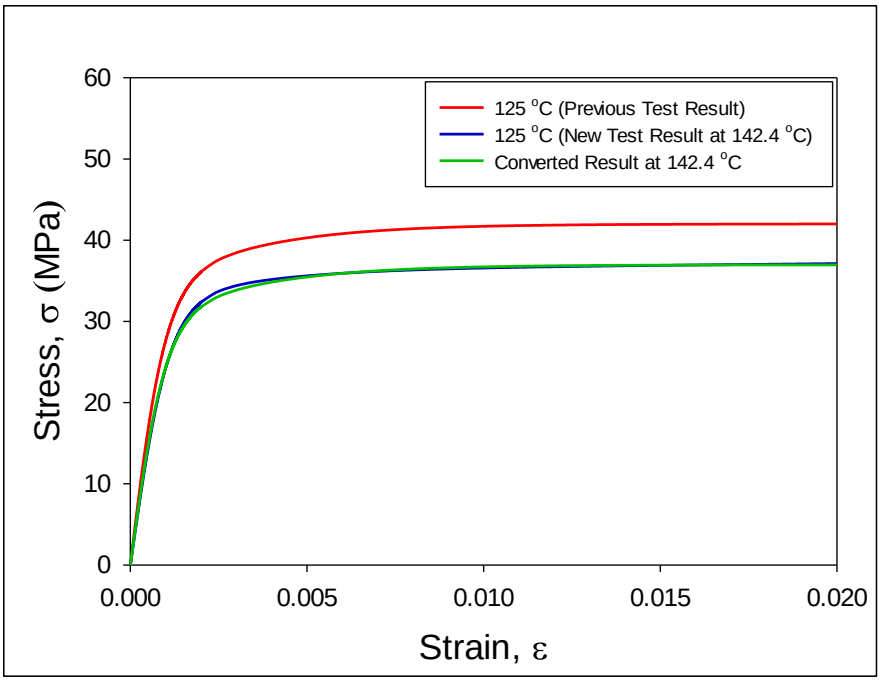

Figure A.4 Comparison between Previous Results and Converted (Corrected) Results